

Thèse de Doctorat

Mohammad ONEISSI

*Mémoire présenté en vue de l'obtention du
grade de Docteur de l'Université d'Angers
sous le sceau de l'Université Bretagne Loire*

École doctorale : ED 498 SPIGA - Sciences Pour l'Ingénieur, Géosciences, Architecture

Discipline : *Energétique, thermique, combustion*

Spécialité : *Physique*

Unité de recherche : LARIS EA 7315

Soutenue le 23 Janvier 2017

Thèse N° :

Analysis of the flow structure and heat transfer enhancement in a rectangular channel with longitudinal vortices

JURY

Rapporteurs :	M. Christophe GOURDON , Professeur, Université de Toulouse - LGC Mme Hasna LOUAHLIA , Professeur, Université de Caen - LUSAC
Examineurs :	M. Daniel BOUGEARD , Maître Assistant HDR, Mines Douai M. Michel EL HAYEK , Professeur étranger, Notre Dame University - Louaize (Liban) M. Hassan PEERHOSSAINI , Professeur, Université Paris Diderot - APC
Directeur de Thèse :	M. Thierry LEMENAND , Maître de Conférences HDR, Université d'Angers - LARIS
Co-encadrants de Thèse :	M. Charbel HABCHI , Professeur Assistant étranger, Notre Dame University - Louaize (Liban) M. Serge RUSSEIL , Maître Assistant, Mines Douai



*A little body thyself thou deem, while
the great universe in thee dwells.*

Imam Ali (AS)



Contents

GENERAL INTRODUCTION	VII
LIST OF FIGURES	IX
NOMENCLATURE.....	XIII
ACKNOWLEDGEMENT	XVII
PUBLICATIONS	XIX
1 LITERATURE REVIEW	1
1.1 INTRODUCTION	1
1.2 ENHANCED HEAT EXCHANGERS EHE	2
1.3 HEAT TRANSFER CHARACTERIZATION.....	5
1.3.1 Colburn and Fanning friction factor	6
1.3.2 Goodness factor	7
1.4 HEAT TRANSFER ENHANCEMENT USING ACTIVE TECHNIQUES.....	11
1.4.1 Mechanical aids.....	11
1.4.2 Surface vibration	11
1.4.3 Fluid vibration.....	12
1.4.4 Electrostatic fields	13
1.4.5 Injection.....	13
1.4.6 Suction.....	14
1.4.7 Jet impingement.....	15
1.5 HEAT TRANSFER ENHANCEMENT USING PASSIVE TECHNIQUES	16
1.5.1 Treated surfaces.....	16
1.5.2 Rough surfaces.....	17
1.5.3 Additives for liquids	18
1.5.4 Additives for gases	19

1.5.5	<i>Surface tension devices</i>	19
1.5.6	<i>Displaced enhancement devices</i>	20
1.5.7	<i>Coiled tubes</i>	20
1.5.8	<i>Swirl flow devices</i>	22
1.5.9	<i>Extended surfaces</i>	23
1.6	COMPOUND TECHNIQUES.....	24
1.7	VORTEX GENERATORS	25
1.8	OBJECTIVE AND OUTLINE OF THIS RESEARCH WORK	33
2	METHODS AND MATERIALS	37
2.1	INTRODUCTION	37
2.2	COMPUTATIONAL FLUID DYNAMICS	37
2.2.1	<i>Governing equations</i>	39
2.2.2	<i>Turbulence models</i>	40
2.2.3	<i>Numerical error sources</i>	44
2.3	EXPERIMENTAL STUDY.....	45
2.3.1	<i>Instrumentation</i>	46
2.3.2	<i>Experimental test benches</i>	53
2.3.3	<i>Experimental error sources</i>	57
2.4	CONCLUSION	58
3	ANALYSE EXPÉRIMENTALE PAR PIV STÉRÉOSCOPIQUE DU DÉVELOPPEMENT DE TOURBILLONS LONGITUDINAUX À L'AVANT D'AILETTES RECTANGULAIRES	61
4	ÉTUDE COMPARATIVE DE SIMULATIONS NUMÉRIQUES ET MESURES EXPÉRIMENTALES DE GÉNÉRATEURS DE VORTICITÉ À PAIRES D'AILETTES RECTANGULAIRES	100
5	CONCEPTION NOUVELLE D'UN GÉNÉRATEUR DE VORTICITÉ À PAIRES D'AILETTES TRIANGULAIRES POUR L'AMÉLIORATION DU TRANSFERT DE CHALEUR	130
6	OPTIMISATION DE L'ANGLE D'INCLINAISON DU GÉNÉRATEUR DE VORTICITÉ IPWP « INCLINED PROJECTED WINGLET PAIR »	142

7	INTENSIFICATION DES TRANSFERTS THERMIQUES D'UN NOUVEAU TYPE DE GÉNÉRATEUR DE VORTICITÉ À PAIRES D'AILETTES EN DELTA MUNI DE PROTRUSIONS DANS UN ÉCHANGEUR DE CHALEUR À PLAQUE ET AILETTE	180
8	CONCLUSION AND PERSPECTIVES	221

Introduction générale

Ce travail de thèse propose une conception innovante d'une nouvelle configuration de générateur de vorticité (VG) utilisée pour améliorer le transfert de chaleur dans des échangeurs de chaleur à plaques et ailettes. Les techniques passives d'intensification des transferts sont couramment utilisées dans les échangeurs de chaleur de par leur efficacité, leur économie, leur facilité de fabrication et leur faible maintenance. Les générateurs de vorticité sont une des techniques passives qui créent des écoulements secondaires, cassent la croissance de la couche limite et créent des écoulements tourbillonnants qui améliorent l'échange entre les parois et le fluide, améliorant ainsi le transfert de chaleur.

Le manuscrit de la thèse est organisé en huit chapitres.

Le chapitre 1 est consacré à l'examen de la littérature dans laquelle un aperçu des différents types d'échangeurs de chaleur intensifiés est mis en évidence. La caractérisation du transfert de chaleur est également présentée dans ce chapitre, de nombreuses options existent pour évaluer l'amélioration du transfert de chaleur. De plus, les techniques d'amélioration du transfert de chaleur et de masse sont présentées, et classées comme méthodes actives, passives et combinées. La revue de la littérature sur les générateurs de vorticité est mise en évidence tout au long de ce chapitre 1.

Le chapitre 2 présente les outils scientifiques utilisés dans ce travail, à la fois numériques et expérimentaux dans le domaine de la mécanique des fluides. D'une part, la simulation numérique (CFD) est présentée avec les équations générales et les modèles de turbulence utilisés, ainsi que les sources d'erreurs numériques. D'autre part, la partie expérimentale est présentée via les différentes instrumentations utilisées dans le domaine des échangeurs de

chaleur et de la mécanique des fluides, les bancs expérimentaux utilisés, ainsi que les sources d'erreurs expérimentales.

Les cinq chapitres suivants présentent des résultats et analyses sous la forme d'articles publiés, soumis ou prêts à soumettre.

Le chapitre 3 est un article intitulé "Experimental analysis by stereo-PIV of the development of streamwise vortices downstream of rectangular winglets", à soumettre à Experiments in Fluids.

Le chapitre 4 est un article intitulé "Comparison between numerical simulation and experimental study of rectangular-winglet pair vortex generator", à soumettre à Computers and Fluids.

Le chapitre 5 est l'article "Novel design of delta-winglet pair vortex generator for heat transfer enhancement", publié dans International Journal of Thermal Sciences en 2016.

Le chapitre 6 est un article intitulé "Inclination angle optimization for Inclined Projected Winglet Pair vortex generator", à soumettre à International Journal of Heat and Mass Transfer.

Le chapitre 7 est un article intitulé "Heat transfer enhancement of a novel delta winglet pair vortex generator with protrusions in parallel plate-fin heat exchanger", à soumettre à Applied Thermal Engineering.

Le chapitre 8 est consacré aux conclusions et perspectives.

List of Figures

FIGURE 1 TYPES OF CONVENTIONAL COMPACT HEAT EXCHANGERS AND THEIR TYPICAL TEMPERATURE LIMITS [1].	3
FIGURE 2 (A) ROTATING HEAT EXCHANGER [20], (B) SCRAPED SURFACE HEAT EXCHANGER [21].	11
FIGURE 3 PIEZOELECTRIC ELEMENTS WITH FIXTURE USED IN SURFACE VIBRATING HEAT EXCHANGERS [23].	12
FIGURE 4 FLUID VIBRATION HEAT EXCHANGER [26].	12
FIGURE 5 ELECTROSTATIC FIELD APPARATUS FOR ENHANCING HEAT TRANSFER [27].	13
FIGURE 6 A GENERAL VIEW OF AIR BUBBLE INJECTION METHOD FOR HEAT TRANSFER INTENSIFICATION [29].	14
FIGURE 7 3D VIEW OF A TUBE WITH SUCTION PASSAGES EMBEDDED ON ITS MATERIAL VOLUME [30].	14
FIGURE 8 PHYSICAL MODEL OF A SINGLE PULSED SLOT IMPINGING JET [31].	15
FIGURE 9 (A) SCHEMATIC DIAGRAM OF THE 5×5 ARRAY OF JET ORIFICES POSITIONED OVER A SMOOTH FLAT SURFACE, (B) LOCAL HEAT TRANSFER DISTRIBUTION DURING LIQUID IMPINGEMENT FROM THE JET ARRAY [32].	16
FIGURE 10 (A) SURFACE PROTRUSIONS ON CURVED SURFACES, (B) ARRAY OF SIMULTANEOUSLY PROTRUSIONS [40].	17
FIGURE 11 (A-B) IMAGES OF THE SURFACES OF THE PLAIN AND POROUS-LAYER COATED TUBES, RESPECTIVELY. (C) ISOMETRIC VIEW OF THE POROUS-LAYER COATED TUBE WITH 75 MM DIAMETER COPPER PARTICLES. (D-E) SCANNING ELECTRON MICROSCOPE (SEM) IMAGES OF THE POROUS-LAYER COATING [41].	17
FIGURE 12 SURFACE MORPHOLOGICAL CHARACTERIZATION OF FLAT SAMPLES: (A, C, E) BY 3D OPTICAL SCANNER REFERRING TO THE FLUID-DYNAMIC PLANE AND (B, D, F) BY FIELD EMISSION SCANNING ELECTRON MICROSCOPE [43].	18
FIGURE 13 MICROGRAPHS OF NANO ₂ Cu PARTICLES-TRANSFORMER OIL AT DIFFERENT SUSPENSIONS [44].	19
FIGURE 14 (A) SCHEMATIC VIEW OF VERTICAL FLUTED TUBE [47], (B) SURFACE TENSION DRAINAGE FROM THE FLUTES INTO DRAINAGE CHANNELS.	20
FIGURE 15 DISPLACED INSERT DEVICES: (A) SPACED DISK DEVICES, (B) SPACED STREAMLINE-SHAPE DEVICES, (C) DISPLACED WIRE-COIL INSERT [48].	20

FIGURE 16 DEAN VORTICES: (A) CHANNEL GEOMETRY [52], (B) FLOW PATTERNS AT $DE < 150$, (C) FLOW PATTERNS AT $DE > 150$ [51].....	21
FIGURE 17 (A) TWISTED PIPE DESIGN [53],(B) HELICAL COILED TUBE HEAT EXCHANGER [54].....	21
FIGURE 18 SWIRL FLOW DEVICES: (A) TWISTED TAPE INSERTS [56]; (B) HELICAL STRIP INSERTS [57].....	22
FIGURE 19 SOME TYPES OF EXTENDED SURFACES [48]: (A) OFFSET STRIP FIN, (B) INTEGRAL STRIP-FINNED TUBE, (C) LOUVERED FINS, (D) LONGITUDINAL FINNED TUBES.....	23
FIGURE 20 SCHEMATIC DIAGRAM OF PLATE FIN WITH COMMON LONGITUDINAL VORTEX GENERATORS [58].....	24
FIGURE 21 NATURALLY AND PASSIVELY GENERATED VORTICES AND VORTEX GENERATORS FOR HEAT EXCHANGER APPLICATIONS: (A) NATURAL GENERATION OF A LAMINAR HORSESHOE VORTEX AT FIN-TUBE JUNCTION; (B) PASSIVELY GENERATED LONGITUDINAL VORTICES; (C) COMMON HEAT EXCHANGER VORTEX GENERATORS [71]..	26
FIGURE 22 SOME TYPES OF SURFACE PROTRUSIONS: CUBE, HEMISPHERE AND CONE [71].....	28
FIGURE 23 SCHEMATIC SHOWING THE LONGITUDINAL VORTICES CONFIGURATIONS: (A) COMMON FLOW DOWN (COMMON INFLOW PAIR) AND (B) COMMON FLOW UP (COMMON OUTFLOW PAIR) [71].....	29
FIGURE 24 MODIFIED RECTANGULAR WINGLET [88].....	31
FIGURE 25 SOME CFD APPLICATIONS IN INDUSTRIAL AND ENVIRONMENTAL FIELDS: (A) AEROSPACE [101], (B) AUTOMOTIVE [102], (C) TURBOMACHINERY [103], (D) INTERNAL COMBUSTION ENGINES [104], (E) WIND FARM PLANNING [105].....	39
FIGURE 26 A SCHEME OF PILLARS OF BASIC RESEARCH IN FLUID MECHANICS [123].	46
FIGURE 27 MEASUREMENT PRINCIPLE OF LDA BY DANTEC DYNAMICS© [126].....	48
FIGURE 28 THE PROBE AND PROBE VOLUME BY DANTEC DYNAMICS© [126].	49
FIGURE 29 PIV MEASUREMENT PRINCIPLE BY DANTEC DYNAMICS© [127].	51
FIGURE 30 CORRELATION OF TWO INTERROGATION AREAS OF THE PIV SYSTEM BY DANTEC DYNAMICS© [127].	51
FIGURE 31 TWO CAMERAS TECHNIQUE FOR SPIV SYSTEM BY DANTEC DYNAMICS© [127].....	53
FIGURE 32 ALPHA-1 EXPERIMENTAL TEST BENCH: (1) SEEDING ROOM; (2) PARTICLES GENERATOR; (3) HONEYCOMB; (4) CONVERGENT SECTION; (5) UPSTREAM CHANNEL; (6) TEST SECTION (LATERAL AND UPPER GLAZED WINDOWS); (7) CONVERGENT 90° BEND; (8) ABSOLUTE PRESSURE TRANSDUCER; (9) LAMINAR FLOWMETER;	

(10) TEMPERATURE PROBE; (11) PVC SUCTION PIPE; (12) CENTRIFUGAL FAN; (13) WIRINGS AND CABLES; (14) MICRO-MANOMETER; THE CYAN ARROW INDICATES THE AIR FLOW DIRECTION.	55
FIGURE 33 ALPHA-3 EXPERIMENTAL TEST BENCH: (1) SEEDING ROOM; (2) PARTICLES GENERATOR; (3) ENTRANCE PIPE; (4) BELL-SHAPE CONVERGENT SECTION; (5) SWIVEL DISK; (6) TEST SECTION (LATERAL, LOWER AND UPPER PLEXIGLAS WALLS); (7) SWIVEL HINGE; (8) ABSOLUTE PRESSURE TRANSDUCER; (9) DIAPHRAGM FLOWMETER; (10) TEMPERATURE PROBE; (11) PVC SUCTION PIPE; (12) CENTRIFUGAL FAN; (13) WIRINGS AND CABLES; (14) MICRO-MANOMETER; THE CYAN ARROW INDICATES THE AIR FLOW DIRECTION.	56
FIGURE 34 DETAILED VIEW FOR ALPHA-3 SWIVEL TEST SECTION.	57

Nomenclature

A	Surface wetted area, m^2
A_c	Cross sectional area, m^2
C_{\min}	Heat capacity rate
C_p	Specific heat at constant pressure, $J (kgK)^{-1}$
D	Diameter, m
D_e	Dean number, dimensionless
D_h	Hydraulic diameter, m
E	Total energy
E_{st}	Pumping power per unit heat transfer surface area
f	Fanning friction factor, dimensionless
h	Convective heat transfer coefficient, $W (m^2K)^{-1}$
j	Colburn factor, dimensionless
R	Channel radius of curvature, m
St	Stanton number, dimensionless
L	Channel length, m
\dot{m}	Mass flow rate, $kg s^{-1}$
Nu	Nusselt number, dimensionless
Nu_x	Local Nusselt number, dimensionless
\dot{V}	Volumetric flow rate, $m^3 s^{-1}$
Pr	Prandtl number, dimensionless
ΔP	Pressure drop, Pa
q''_x	local wall heat flux

q''_{0-L}	Averaged wall heat flux
Re	Reynolds number, dimensionless
T	Temperature magnitude, K
T_b	Bulk temperature, K
$T_{i,b}$	Inlet bulk temperature, K
$T_{o,b}$	Outlet bulk temperature, K
T_w	Wall temperature, K
T_{avg}	Average temperature, K
U	Velocity magnitude, $m\ s^{-1}$
u	Local flow velocity in x direction, $m\ s^{-1}$
$\overline{u'_i u'_j}$	Reynolds stress tensor

Greek letters

μ	Dynamic viscosity, Pa s
ρ_f	Fluid density, $kg\ m^{-3}$
τ	Local shear stress
λ	Thermal conductivity, $W(mK)^{-1}$
λ_{eff}	Effective thermal conductivity, $W(mK)^{-1}$
η	Thermal enhancement factor, dimensionless
Σ	Modulus of the mean strain rate tensor

Abbreviations

CAD	Computer Aided Drawing
CFD	Common Flow Down
CFD	Computational Fluid Dynamics

CFU	Common Flow Up
DES	Detached Eddy Simulation
DWP	Delta Winglet Pair
EHE	Enhanced Heat Exchanger
FDM	Finite Difference Method
FVM	Finite Volume Method
IPWP	Inclined Projected Winglet Pair
LCT	Liquid Crystal Thermography
LDA	Laser Doppler Anemometry
LDV	Laser Doppler Velocimetry
LES	Large Eddy Simulation
LVG	Longitudinal Vortex Generator
NTU	Number of Transfer Units
PIV	Particle Image Velocimetry
RANS	Reynolds Averaged Navier-Stokes
RNG	Renormalization-Group
RSM	Response Surface Methodology
RSM	Reynolds Stress Model
RWP	Rectangular Winglet Pair
SPIV	Stereoscopic Particle Image Velocimetry
SST	Shear-Stress Transport
TEF	Thermal Enhancement Fraction, dimensionless
TVG	Transverse Vortex Generator
VG	Vortex Generator

- 2D Two Dimensional
- 3D Three Dimensional
- 2C Two Components
- 3C Three Components

Acknowledgement

In the name of God, the Almighty, I dwelled into this challenge with trust in him and confidence in myself and the team I am working with. It would be my first obligation to thank God for his guidance and provision throughout this whole journey. He not only gave me the will and power to achieve success, but also gifted me the possibility to work with a wonderful team that will always be part of my future. I would like to express special thanks to the wonderful team of Dr. Thierry Lemenand, Dr. Charbel Habchi, Dr. Serge Russeil and Dr. Daniel Bougeard for your endless support and cooperation as well as your motivation and patience. Working with you was a pleasure as much as it was an honor.

Moreover, I would like to thank Prof. Christophe Gourdon, Prof. Hasna Louahlia, Prof. Michel El Hayek, and Prof. Hassan Peerhossaini for serving as my committee members, whose comments, suggestions and remarks not only enlightened my defense, but also made it a gratifying experience.

Last but not least, I cannot forget to thank my family members who were there for me in every step to the dream. My parents, brother and sister who spared no effort to embrace my ambitions and succor it any way possible. Eventually, I would like to send special thanks to my partner in success, my wife Nour, who happens to be celebrating her 22nd birthday today, and to whom I dedicate this significant milestone in our lives.

At last, if I were to individually mention all those who aided in my achievement, the list would be long. However, my sincere apologies and my ultimate gratitude to all those who helped from behind the curtains, and who I could not manage to mention in person.

Publications

ACL publié

Novel Design of Delta Winglet Pair Vortex Generator for Heat Transfer Enhancement. **Oneissi M.**, Habchi C., Russeil S., Bougeard D., Lemenand T. International Journal of Thermal Science. 109, 1-9, 2016.

ACL en rédaction

"Experimental analysis by stereo-PIV of the development of streamwise vortices downstream of rectangular winglets", à soumettre à Experiments in Fluids.

"Comparison between numerical simulation and experimental study of rectangular-winglet pair vortex generator", à soumettre à Computers and Fluids.

"Inclination angle optimization for Inclined Projected Winglet Pair vortex generator", à soumettre à International Journal of Heat and Mass Transfer.

"Heat transfer enhancement of a novel delta winglet pair vortex generator with protrusions in parallel plate-fin heat exchanger", à soumettre à Applied Thermal Engineering.

ACTI

Novel design of triangular delta winglet pair for heat transfer enhancement. **Oneissi M.**, Habchi C., Russeil S., Bougeard D., Lemenand T. LAAS21 International Science Conference 2015. Beirut, Lebanon, April 15-17, 2015.

Novel design of delta winglet pair vortex generator for heat transfer enhancement. **Oneissi M.**, Habchi C., Russeil S., Bougeard D., Lemenand T. Eurotherm Seminar 106 "Physical and Chemical Phenomena in Heat Exchangers and Multifunctional Reactors for Sustainable Technology", Paris (France), 10-11 Oct 2016.

Intensification des transferts par génération de vorticit . **Oneissi M.**, Khanjian A., Bougeard D., Habchi C., Russeil S., Lemenand T. CIFQ2017, St-L , France, 22-24 mai 2017.

Chapter 1

Literature Review

1.1 Introduction

Energy employment, conversion and reclamation in any industrial application involve a heat exchange process. Heat exchange is a process where heat is transferred between two or more fluids, between a solid surface and a fluid, or between solid particulates and a fluid. This exchange process is dominated by convection which is the transfer of heat from one place to another by the fluid movement. Convective heat transfer encompasses the combined processes of conduction (heat diffusion) and advection (heat transfer by bulk fluid flow). It is a naturally occurring phenomenon that can be greatly enhanced with the aid of forcing devices that lead to forced convection heat transfer. In industrial world, units responsible for the heat exchange process are named heat exchangers which are used in various industrial and commercial applications. Their scope of applications extends to power plants (boilers, condensers and nuclear fuel rods), air conditioning and refrigeration, waste-heat recovery, turbomachinery systems, sensible heating and cooling of sensitive products processing (chemical and pharmaceutical industries) and cooling of electrical machines and electronic devices. Since modern technology is characterized by the tendency to package larger power conversion or transfer devices in smaller volumes, and due to the crucial role and high demands for less expensive heat exchangers, efforts have been made to produce more efficient heat exchangers by employing various methods of heat transfer enhancement. Thermal efficiency and the expenses of design and operation can considerably be improved with enhanced heat exchange; consequently, heat transfer enhancement is the process of

increasing the effectiveness of heat exchanger. The study of improved heat transfer is referred to as heat transfer enhancement, augmentation, or intensification.

The objective of this chapter is to provide information about the following topics:

- An overview of enhanced heat exchangers (EHE).
- Heat transfer characterization.
- Heat and mass transfer enhancement using active methods.
- Heat and mass transfer enhancement using passive methods.

1.2 Enhanced heat exchangers EHE

Heat exchangers were initially developed to use plain heat transfer surfaces, where these types of heat exchangers, named as conventional heat exchangers, are limited to specific uses. Figure 1 shows some types of conventional metallic heat exchangers and their typical temperature limits [1]. The conventional heat exchangers working range differs in type with the working temperature regime. For low temperature uses, such as electronic cooling, plate heat exchangers may be used. For higher temperature regime, plate-fin, tube-fin or plane tube heat exchangers can be implemented. In addition, savings in materials and energy use also provide strong motivation for the development of improved methods of enhancement. Thus, enhancing heat exchangers performance is a necessity in order to expand their usage for industrial and residential applications. To provide this intensification, special surface geometries which provide a higher thermal performance should be employed. The use of relatively complex geometries was initially limited by industrial manufacturing technologies. However, new manufacturing methods such as complex punching machines and 3D-printer techniques ease the manufacturing process for advanced complex geometries.

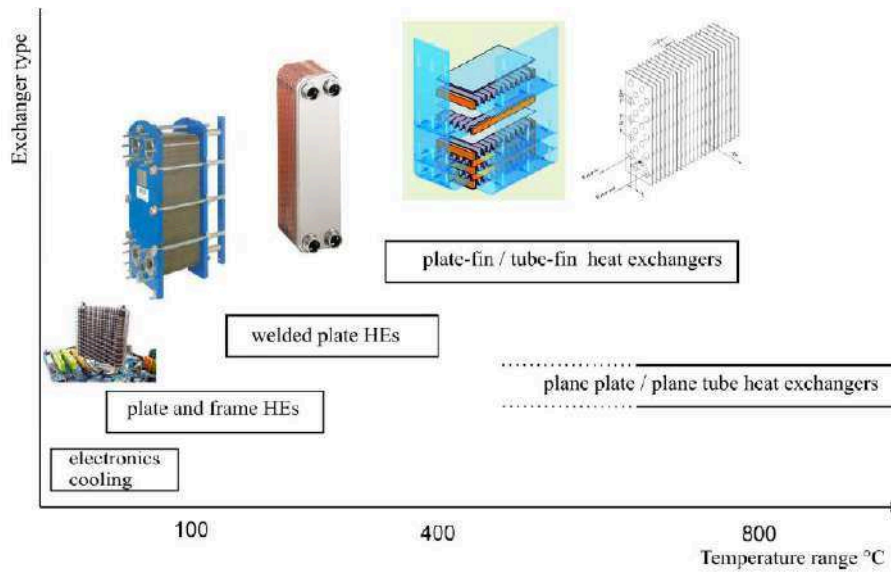


Figure 1 Types of conventional compact heat exchangers and their typical temperature limits [1].

In general, enhanced heat transfer surfaces that increase the thermodynamic process efficiency can be used for three purposes:

1. Compactness, thus reducing the heat exchanger overall volume and possibly its cost.
2. Energy saving by reduce the pumping power required for a given heat transfer process.
3. Decreasing the overall heat transfer resistance $(KA)^{-1}$ value of the heat exchanger (where K is the overall heat transfer coefficient $[W/m^2K]$ and A is the surface wetted area $[m^2]$). This can be achieved in either of two ways:
 - Increasing the heat exchange rate for a fixed fluid temperature, or
 - Reduce the mean temperature difference for the heat exchange.

Enhanced methods essentially reduce the thermal resistance in a conventional heat exchanger by promoting higher convective heat transfer coefficient. Enhancement techniques

can be separated into two categories: passive and active [2]. Passive methods require no direct application of external power, in which special surface geometries or fluid additives are employed. Active techniques do require external power to operate such as electromagnetic fields and surface vibration. Under these two categories, sixteen different enhancement techniques have been identified by Bergles et al. [3, 4]. Table 1 summarizes this classification of heat transfer enhancement techniques.

Table 1 Classification of various heat transfer enhancement techniques.

Passive Techniques	Active Techniques
Treated surfaces	Mechanical aids
Rough surfaces	Surface vibration
Extended surfaces	Fluid vibration
Displaced enhancement devices	Electrostatic fields
Swirl flow devices	Injection
Coiled tubes	Suction
Surface tension devices	Jet impingement
Additives for liquids	
Additives for gases	
Compound Enhancement	
Two or more passive and/or active techniques employed together	

Detailed definitions and descriptions of these techniques are presented in the forthcoming sections. These methods are used with heat exchangers and especially with single-phase heat exchangers enrolled in this study. Single-phase heat exchange is the simplest form of heat transfer, where all the media stay in the same phase throughout the process.

1.3 Heat transfer characterization

Many options exist for evaluating the heat transfer enhancement for a surface geometry. Nusselt number (Nu), which is defined as the ratio of convective to conductive heat transfer across a boundary, has to be calculated in order to evaluate the heat transfer performance. Nusselt number is calculated locally, Eq. (1.1), for local inspection and globally, Eq. (1.2), to evaluate global performance along a boundary and respectively defined as:

$$Nu_x = \frac{q''_x D_h}{\lambda (T_w - T_{x,b})} \quad (1.1)$$

$$Nu = Nu_{0-L} = \frac{q''_{0-L} D_h}{\lambda (T_w - T_{avg})} \quad (1.2)$$

where q''_x and q''_{0-L} are respectively the local wall heat flux and the heat flux averaged from $x=0$ to the overall heat exchanger length L , D_h is the hydraulic diameter of the studied geometry, λ is the thermal conductivity of the working fluid, T_w is the wall or surface temperature, $T_{avg} = \frac{T_{o,b} + T_{i,b}}{2}$ is the average temperature between the inlet and outlet, $T_{i,b}$ and $T_{o,b}$ are respectively the bulk temperatures at the heat exchanger inlet and outlet, and the bulk temperature T_b is defined over a cross sectional area A as:

$$T_b = \frac{\int_A U(x) T(x, y, z) dA}{\int_A U(x, y, z) dA} \quad (1.3)$$

where U and T are the velocity and temperature magnitude at a specific position (x, y, z) in the heat exchanger.

In order to account for the pressure drop in a heat exchanger, the Fanning friction factor is computed and defined as:

$$f = \frac{2D_h}{4L} \frac{\Delta P}{\rho_f \bar{U}_{f,in}^2} \quad (1.4)$$

where ρ_f is the working fluid density, $\bar{U}_{f,in}$ is the average flow velocity at the heat exchanger inlet, ΔP is the pressure drop between the inlet and outlet of the heat exchanger.

Judging the relative heat transfer enhancement by comparing the heat transfer coefficients or dimensionless heat transfer parameters, such as Nusselt number, Stanton number (St) or others, affords an insufficient indication of performance, because the benefits gained from heat transfer enhancement may not be great enough to offset the increase friction losses. Thus, the enhancing term has to compromise between heat transfer rate and pressure losses. This balance is difficult to quantify in a manner that allows straightforward comparisons among various enhanced surface geometries. In order to quantify the enhancing performance of surface geometries, many methods have been proposed, described in the following paragraphs.

1.3.1 Colburn and Fanning friction factor

Many researches use the Colburn factor (j) and Fanning friction factor (f) versus the Reynolds number (Re) analogy to evaluate the enhancement performance of compact surfaces [5, 6, 7]. Colburn factor quantifies the ratio of the thermal power transferred to the mechanical power consumed. It is considered as a frequent tool for presenting performance results for heat transfer surface geometries. Ghanem et al. [5] judged the energy efficiency friction losses of multifunctional heat exchanger (MHE) upon evaluating the Colburn and Fanning friction factors. Jonghyeok and Kwan-Soo [6] performed numerical simulations, validated by experiments and then determined correlations of Colburn factor and Fanning friction factor. Kays and London [8] presented a large number of compact surfaces based on Colburn and Fanning friction factors as a function of Reynolds number, in addition to innumerable works and studies done in this field. The Colburn factor which allows comparing the energy efficiency of the heat exchanger is defined as:

$$j = \frac{Nu}{Re_{D_h} Pr^{1/3}} \quad (1.5)$$

where Pr is the Prandtl number and Re_{D_h} is the Reynolds number calculated based on the hydraulic diameter of the studied configuration. The Fanning friction (f) defined as ratio between local shear stress and local flow kinetic energy density is given by:

$$f = \frac{\tau}{\rho_f \frac{u^2}{2}} \quad (1.6)$$

where τ and u are respectively the local shear stress and local flow velocity.

However, the Colburn and Fanning friction curves plotted as a function of Reynolds number tend to vary in magnitude and slope over a wide range [9]. This variation complicates the relative performance comparison of several geometry surfaces. LaHaye et al. [9] suggested a new way of presenting the heat transfer data. The proposed track lead to a dimensionless performance plot between a “heat transfer performance factor” and a “pumping power factor” with a non-dimensional “flow length between major boundary layer disturbances” as a varying parameter. The developed plot permitted quick estimation and comparison of various heat transfer geometries. LaHaye’s performance plot was restricted only for turbulent flow regime and the data plotted were widely scattered, which did not exhibited a visible trend. This leads to conclude that plotting Colburn and Fanning friction factors as a function of the non-dimensional flow length does not serve as a beneficial norm for comparison.

1.3.2 Goodness factor

Since the performance description of both; Colburn and Fanning friction factors; is not satisfactory, another performance criterion introduced by London and Ferguson [10, 11]

represented by two performance parameters, which are also commonly used, are the area goodness factor and the volume goodness factor.

1.3.2.1 Area goodness factor

The area goodness factor presented by London [10] is defined as the ratio of the Colburn factor to the Fanning friction factor. This criterion ensures a direct comparison between Colburn and Fanning friction factors, since it depend on plotting the ratio of the two factors as a function of Reynolds number.

$$\frac{j}{f} = \frac{Nu Pr^{-1/3}}{f Re_{D_h}} = \frac{1}{A_c^2} \left(\frac{Pr^{2/3} NTU \dot{m}^2}{2\rho \Delta P} \right) \quad (1.7)$$

where A_c is the cross sectional area of the heat exchanger, \dot{m} is the mass flow rate across the heat exchanger and NTU is the Number of Transfer Units defined as:

$$NTU = \frac{U A}{C_{min}} \quad (1.8)$$

where C_{min} is the heat capacity rate which is the mass flow rate multiplied by the minimum specific heat of the fluids and A is the heat transfer surface wetted area.

In Eq. (1.7), the area goodness factor is inversely proportional to the square of the cross-sectional area. Thus, minimal frontal area of the heat exchanger is required if higher value of the area goodness factor is preferred. Thus, when comparing different geometry surfaces based on this criterion, and since both factors are independent of the hydraulic diameter, the impact of the cross-sectional shape is revealed regardless of the geometry scale [12].

1.3.2.2 Volume goodness factor

Volume goodness factor introduced by London and Ferguson [11] permits the comparison in terms of core volume. It is defined as the convective heat transfer coefficient (h_{st}) at a standard set of liquid properties and plotted against the pumping power per unit heat transfer surface area (E_{st}):

$$h_{st} = \frac{\lambda}{D_h} Nu = \frac{\mu \cdot c_p}{Pr^{2/3}} \frac{1}{D_h} j Re_{D_h} \quad (1.9)$$

$$E_{st} = \frac{P}{A} = \frac{\mu^3}{2\rho^2} \frac{1}{D_h^3} f Re_{D_h}^3 \quad (1.10)$$

where μ is the fluid dynamic viscosity and c_p is the fluid specific heat capacity.

At a specific pumping power per unit heat transfer surface area, the higher the convective heat transfer coefficient, the smaller the required heat exchanger volume for constant contraction area and D_h . On the contrary to the area goodness factor, the volume goodness factor is strongly dependent on the hydraulic diameter. Therefore, the choice of same hydraulic diameters of the compared heat exchangers is obligatory in order to perform a valid volume goodness comparison [13].

As well as the Colburn and Fanning friction factors, difficulties are present for the goodness factors when comparing surface geometries. A fixed fluid pressure drop must be fixed for valid area goodness factor comparison between geometry surfaces, while hydraulic diameter must be fixed for the volume goodness criterion. Cowell [14] indicated that neither goodness comparison is totally quantitative. Even London [10] confesses that: “These surface goodness factors are not infallible.” Also, Shah and London [12] declare that: “These factors are easy to understand and apply, and may serve a function of screening the selection of surfaces before other design criteria are applied.”

In addition to these factors, modifications of the volume goodness factor exist which are independent of the hydraulic diameter [15]. Detailed information regarding the performance evaluation criteria for compact heat exchangers may be found in Stone [13], Cowell [14] and Webb [16].

1.3.2.3 Thermal enhancement factor

Since most of the previous performance evaluation criteria are suspicious and relative comparison between geometry surfaces may append some restrictions, another comparison technique is highlighted. This method compares the heat transfer efficiency of different configurations for constant pumping power. Thence, a thermal enhancement factor (η) is introduced, defined as the ratio of the heat exchanger convective heat transfer (h) to that in a straight empty flow (h_0) at a constant pumping power [17, 18] indicated by pp index:

$$\eta = \frac{h}{h_0} \Big|_{pp} = \frac{Nu}{Nu_0} \Big|_{pp} \quad (1.11)$$

where Nu_0 is the Nusselt number for empty (no geometry surfaces inside) heat exchanger flow. For equal pumping power:

$$\dot{V}_0 \Delta P_0 = \dot{V} \Delta P \quad (1.12)$$

where \dot{V} is the volumetric flow rate and the index 0 corresponds to empty heat exchanger flow. It follows from Eqs. (1.4) and (1.12):

$$f_0 Re_0^3 = f Re^3 \quad (1.13)$$

$$\frac{Re}{Re_0} = \left(\frac{f}{f_0}\right)^{-1/3} \quad (1.14)$$

At constant pumping power, the thermal enhancement factor can be written as follows:

$$\eta = \left(\frac{Nu}{Nu_0}\right) \left(\frac{f}{f_0}\right)^{-1/3} \quad (1.15)$$

From the definition of the thermal enhancement factor (Eq. (1.11)), one can obtain η from Eq. (1.11) where Nu_0 is evaluated at Reynolds number corresponding to $f = f_0$. And η may be calculated directly from Eq. (1.15) where Nu_0 and f_0 are evaluated at the same Reynolds number corresponding to Nu and f , where both methods give the same result. More details are given in [17, 18].

1.4 Heat transfer enhancement using active techniques

One of the heat transfer enhancement techniques classifications are the active methods. Active techniques usage are limited to few specific applications and rarely used in compact heat exchangers, due to power necessity. Some applications of these methods are found in heat exchangers used in space shuttles and others in airplane wings. In this section, some of active enhancement techniques used in flow augmentation are presented from open literature.

1.4.1 Mechanical aids

They are normally applied to a liquid and involve stirring the fluid by mechanical means or by rotating surface [19]. This category includes rotating tube and scraped-surface heat exchangers as shown in Figure 2. They are widely used for viscous liquids in the chemical process industry.

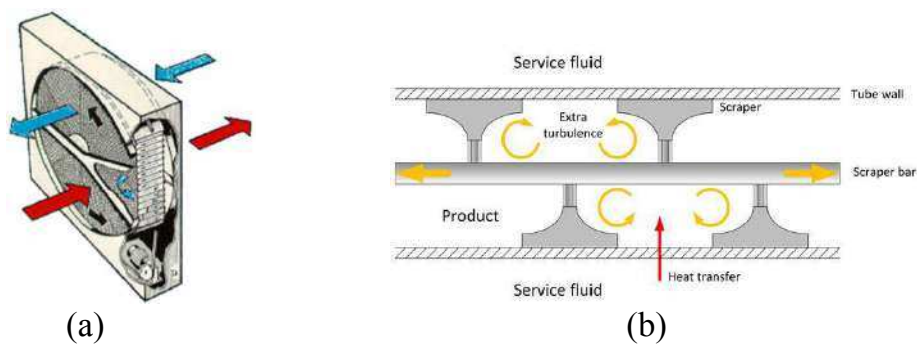


Figure 2 (a) Rotating heat exchanger [20], (b) Scraped surface heat exchanger [21].

1.4.2 Surface vibration

This type of exchangers has been used at either low or high frequency, in single-phase flows to obtain higher convective heat transfer coefficient [22]. Piezoelectric vibrators, as

shown in Figure 3, may also be a source for surface vibrating heat exchangers [23], they may be used in spray cooling process.

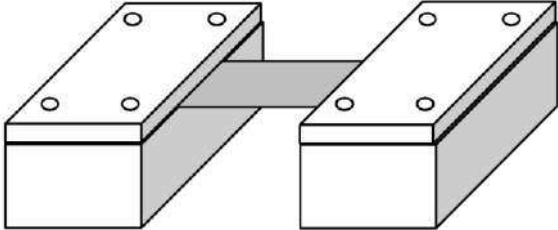


Figure 3 Piezoelectric elements with fixture used in surface vibrating heat exchangers [23].

1.4.3 Fluid vibration

Since it is much easier to excite the fluid than to create vibrations in heat exchangers themselves, fluid is excited with vibrations ranging from 1 Hz to ultrasound (1 MHz). Fluid vibration is used primarily in single-phase flows and considered to be the most practical type of vibration enhancement techniques. Also, fluid pulsation (variation of the mass flow rate) is a source for fluid vibration that intensifies the heat transfer in heat exchangers [24]. Such technique is used in some industrial and biological applications in relation to blood flows and also in curved pipes to trigger dean flow [25]. Figure 4 represents a schematic of this process.

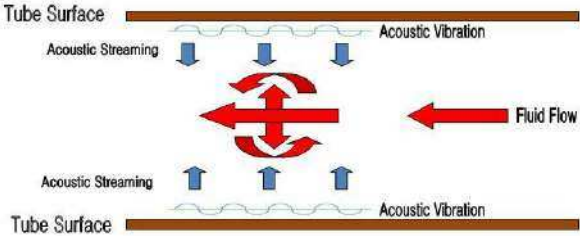
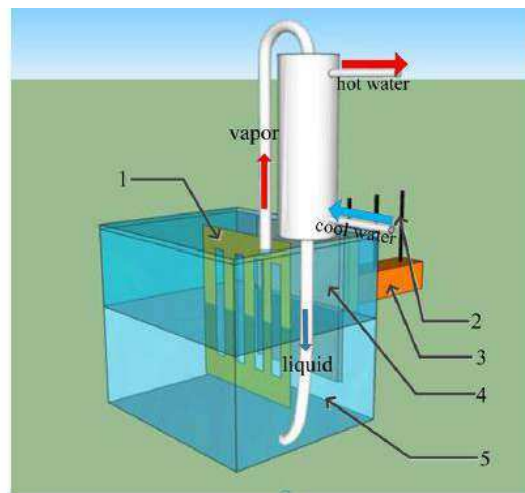


Figure 4 Fluid vibration heat exchanger [26].

1.4.4 Electrostatic fields

This technique could be in the form of electric or magnetic fields, or a combination of the two [27]. It can be directed to cause greater bulk mixing of fluid in the vicinity of the heat transfer surface. The main use of this type of heat exchangers is space, where gravity is reduced and thus specific weights of fluid and vapor becomes equal. Figure 5 shows a schematic of assembled micro evaporator that uses high voltage electrodes to produce the electric field [27].



1- Positive electrode; 2- Thermocouple; 3- Heating block;
4- Copper plate with sintered mesh screen; 5- Working fluid

Figure 5 Electrostatic field apparatus for enhancing heat transfer [27].

1.4.5 Injection

Injection is utilized by supplying gas through a porous heat transfer surface to a flow of liquid or by injecting the same liquid upstream of the heat transfer section. The injected gas intensifies single-phase flow heat transfer [28] and widely used in automotive cooling systems. Figure 6 shows the formation of many small bubbles inside the heat exchanger due to the air flow exit from tiny holes.

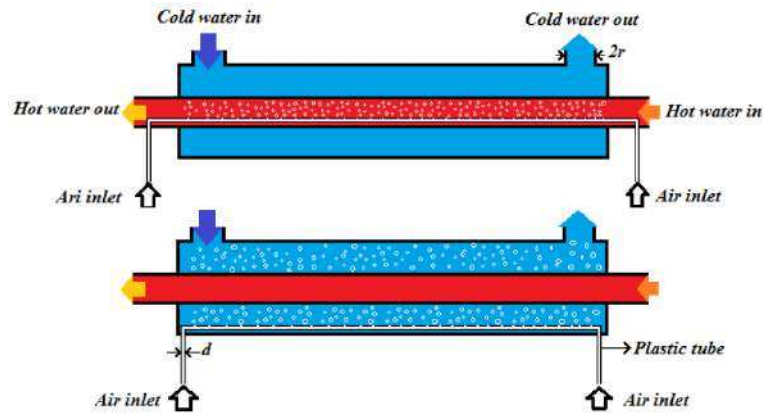


Figure 6 A general view of air bubble injection method for heat transfer intensification [29].

1.4.6 Suction

Suction involves either vapor removal through a porous heated surface in nucleate or film boiling, or fluid withdrawal through a porous heated surface in single-phase flow. Many applications benefit from such techniques such as transpiration cooling, controlling boundary layers over airplane wings surfaces, turbomachinery, lubrication of permeable bearing and many others [30]. Figure 7 shows an isometric view of a permeable tube that is used for suction applications.

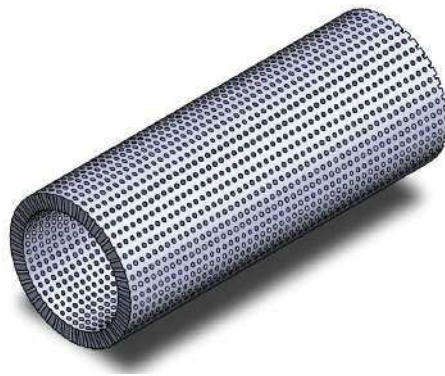


Figure 7 3D view of a tube with suction passages embedded on its material volume [30].

1.4.7 Jet impingement

This technique forces a cooling or heating fluid normally or obliquely toward the heat transfer surface. Single or multiple jets may be used in both single-phase and boiling applications. Jet impingement provides an effective way to enhance heat and mass transfer due to its thin hydrodynamic and thermal boundary layers in the stagnation region. Jet impingement technique is commonly employed for various cooling, heating and drying applications in many industrial fields ranging from thermal drying of continuous sheets of materials and foodstuffs, electronic component and gas turbine blade cooling, manufacture of printed wiring boards and metal sheets, printing processes, deicing or aircraft wings as well as tempering of glass and nonferrous metal sheets [31]. Figure 8 shows a two dimensional symmetric impinging jet configuration model [31]. Figure 9 (a) shows the impinging jet orifices where liquid flow towards the heated surface, while Figure 9 (b) presents the local heat transfer coefficient from an array of 25 jets impinging on a smooth surface undergoing boiling [32].

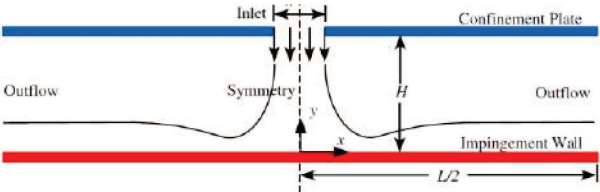


Figure 8 Physical model of a single pulsed slot impinging jet [31].

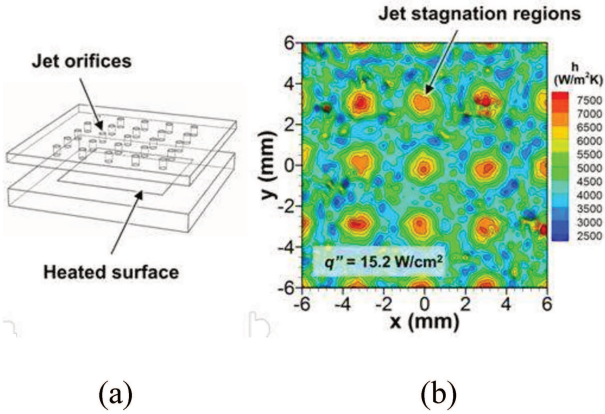


Figure 9 (a) Schematic diagram of the 5×5 array of jet orifices positioned over a smooth flat surface, (b) local heat transfer distribution during liquid impingement from the jet array [32].

1.5 Heat transfer enhancement using passive techniques

Consequent to energy consumption and design complexity of the active techniques used in enhanced heat exchangers, passive techniques are more widely used in many engineering fields. These applications may vary from micro-cooling used in microchannel heat sinks to reaction fuel rod bundles in nuclear power plants [33, 34]. Also, other industrial applications have benefited from passive enhancing techniques such as oil refining, catalytic process, dust removal, calendaring process and many others fields [35, 36, 37, 38]. Plenty of passive geometry surfaces have been studied and tested over decades. In this section, passive enhancement techniques, as given by Bergles [39], used in heat transfer augmentation are discussed from open literature.

1.5.1 Treated surfaces

They are surfaces which have a relatively fine scale alteration to the surface finish, or have a coating applied. This alteration increases the heat transfer surface area. It can be introduced in either continuous or discontinuous manner and changes are generally used to promote enhancement of boiling or condensation, in addition to other industrial applications [40, 41]. Figure 10 shows the micro surface protrusions made on the surface to increase the heat transfer surface area, and Figure 11 illustrates micro-copper coating to a surface.

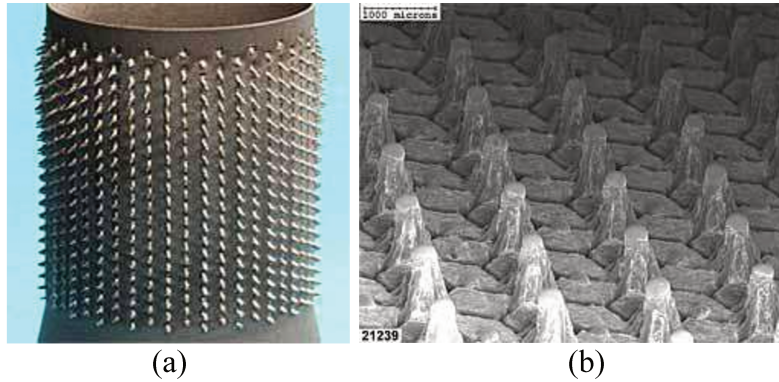


Figure 10 (a) Surface protrusions on curved surfaces, (b) Array of simultaneously protrusions [40]

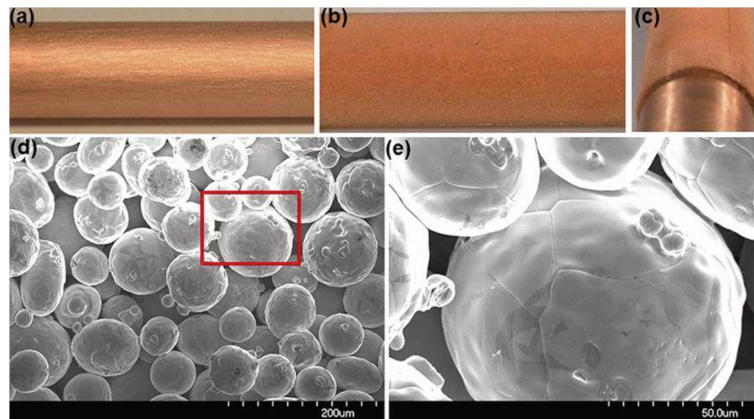


Figure 11 (a-b) images of the surfaces of the plain and porous-layer coated tubes, respectively. (c) Isometric view of the porous-layer coated tube with 75 μm diameter copper particles. (d-e) Scanning Electron Microscope (SEM) images of the porous-layer coating [41].

1.5.2 Rough surfaces

These surface modifications do not increase the heat transfer area but they promote turbulence in the flow field. They may either be complementary to the surface, or by placing adjacent roughness to it. Integral roughness may be generated by machining or restricting the surface. The resulting heat transfer enhancement of the scale roughed surface is surprisingly good compared to rib roughed and dimpled surfaces [42]. Figure 12 shows different surface roughnesses that were used to study the effect of heat transfer [43].

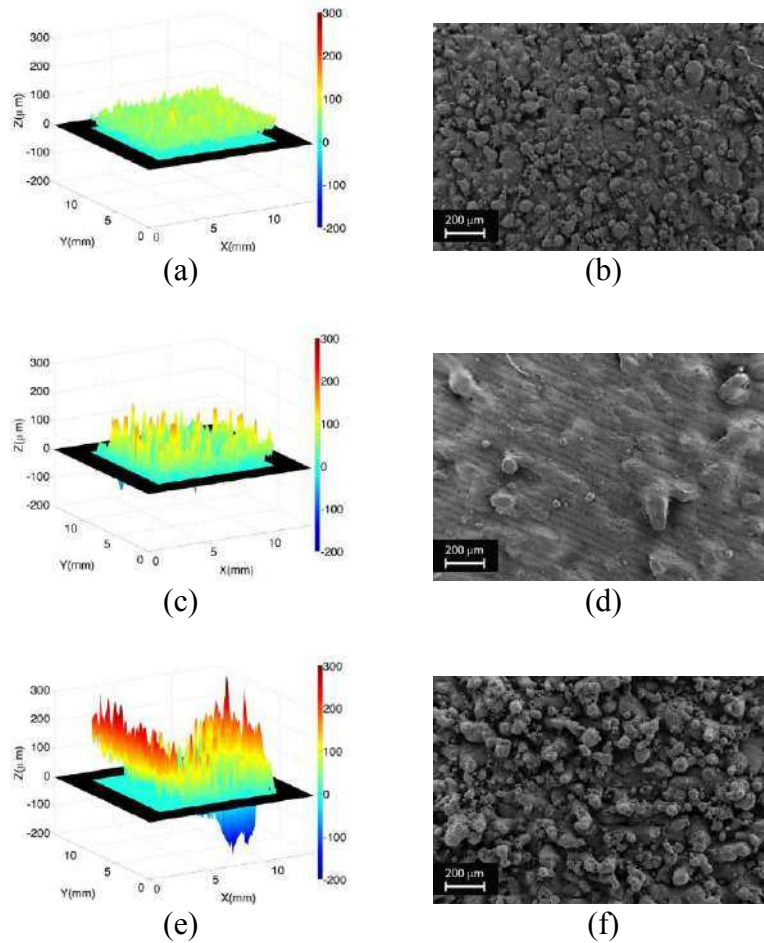


Figure 12 Surface morphological characterization of flat samples: (a, c, e) by 3D optical scanner referring to the fluid-dynamic plane and (b, d, f) by Field Emission Scanning Electron Microscope [43].

1.5.3 Additives for liquids

For single-phase flows, this technique involves the addition of solid particles, soluble trace additives and gas bubbles. While for boiling systems, it is limited to involve trace additives which usually depress the surface tension of the liquid. Figure 13 shows a transmission electron microscopy (TEM) images of suspension of transformer oil-Cu particles used to study the effects of nanofluid on heat transfer [44].

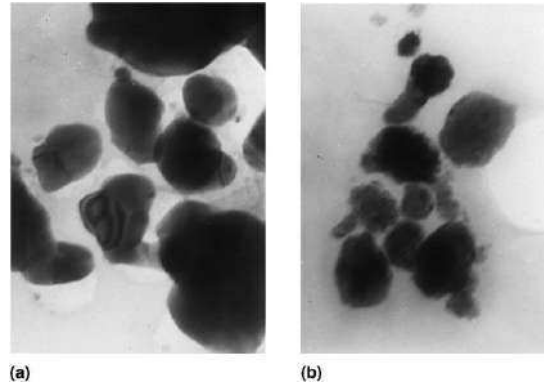


Figure 13 Micrographs of nanoCu particles-transformer oil at different suspensions [44].

1.5.4 Additives for gases

They are liquid droplets or solid particles in single-phase heat exchangers in either dilute-phase (gas-solid suspensions) or dense phase (fluidized beds). This method is widely used in circulating fluidized bed process, pneumatic conveying process, chemical process, drying process and others [44, 45].

1.5.5 Surface tension devices

They use surface tension forces to drain or transport liquid film in boiling and condensing surfaces and consist of wicking or grooved surfaces. Such devices are used for phase transforming heat exchangers [46]. The flute shape presented in Figure 14 promotes condensate drainage from the surface by surface tension forces.

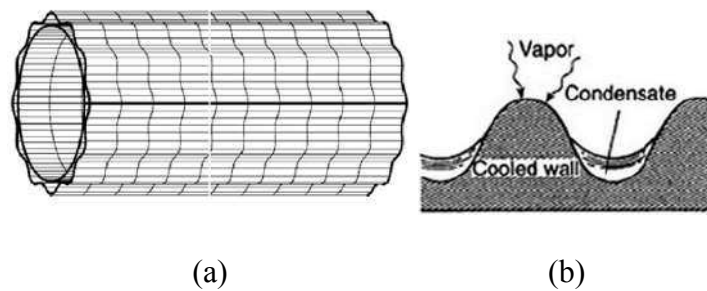


Figure 14 (a) Schematic view of vertical fluted tube [47], (b) surface tension drainage from the flutes into drainage channels.

1.5.6 Displaced enhancement devices

They are insert techniques that are used primarily in confined forced convection which improve the energy transport by displacing fluid from heated or cooled surface to the core flow [46]. Figure 15 shows different displaced insert devices used for main flow mixing in addition to that in the wall region (a) and others used to promote mixing within the boundary layer without significant effect on the main flow [48].

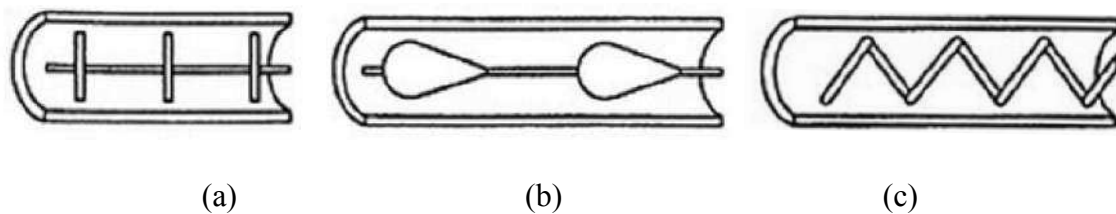


Figure 15 Displaced insert devices: (a) Spaced disk devices, (b) spaced streamline-shape devices, (c) displaced wire-coil insert [48].

1.5.7 Coiled tubes

Coiled tubes produce secondary flows or dean vortices which promote higher heat transfer coefficient. This technique is suitable for relatively more compact heat exchangers. The flow field inside a curved pipe was first described and analyzed by Dean [49] and has been studied through various works as reported by Berger et al. [50]. The flow is characterized by the Dean number (De):

$$De = Re_{Dh} \cdot \sqrt{\frac{D}{R}} \quad (1.16)$$

where D is the pipe diameter and R is the channel radius of curvature. Figure 16 illustrates the concept of Dean vortices in a closed circular channel with a rectangular cross section. At high Dean number $De > 150$, two pairs of vortices appear [51]. Figure 17 shows a twisted pipe design and a helical coiled tube heat exchanger used in industrial applications.

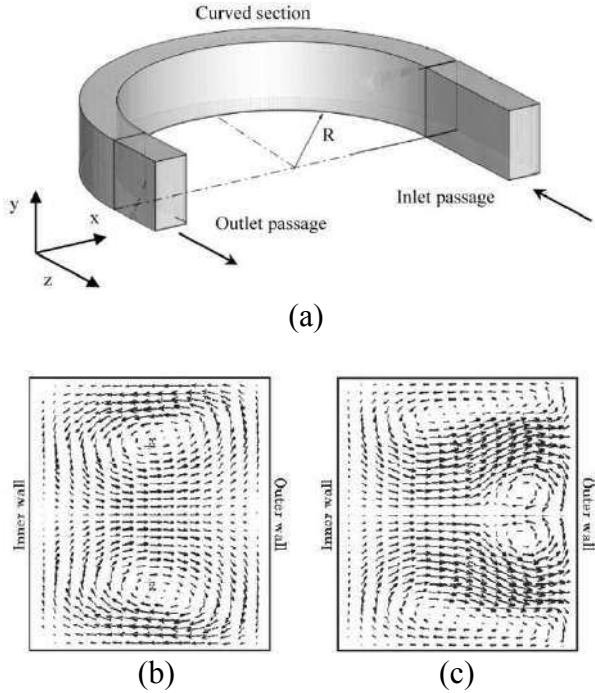


Figure 16 Dean vortices: (a) Channel geometry [52], (b) flow patterns at $De < 150$, (c) flow patterns at $De > 150$ [51].

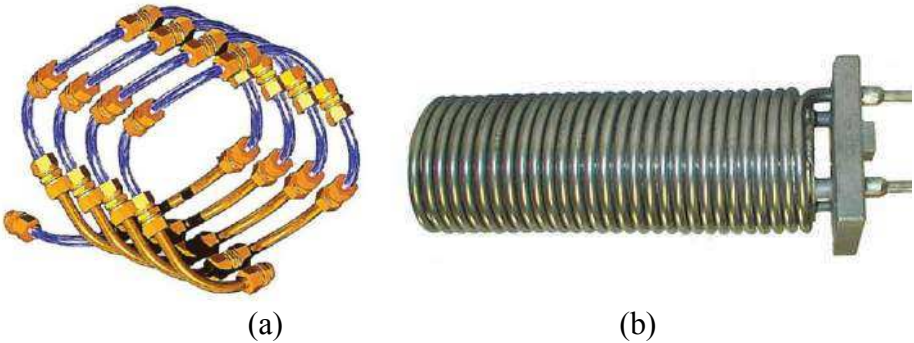


Figure 17 (a) Twisted pipe design [53],(b) helical coiled tube heat exchanger [54].

1.5.8 Swirl flow devices

This technique may be used for both, single and two-phase flows. These devices produce and superimpose swirl or secondary recirculation on the channel axial flow. They include helical strips, twisted tapes shown in Figure 18 in addition to other forms. They have been examined for enhancing condensation, where up to 60% improvements in heat transfer were recorded, at a constant pressure drop penalty [55].

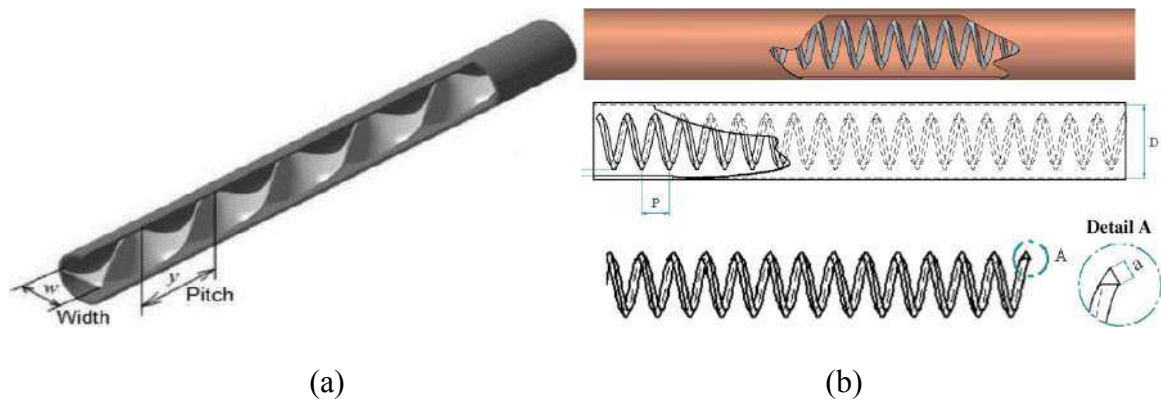


Figure 18 Swirl flow devices: (a) Twisted tape inserts [56]; (b) helical strip inserts [57].

1.5.9 Extended surfaces

Extended or finned surfaces are the most commonly used of all enhancement techniques. Their applications cover a broad spectrum of heat exchange devices including finned tubes for shell-and-tube heat exchangers, plate fins for compact heat exchangers and many others. Figure 19 presents some of the extended surfaces types used in fin-type heat exchangers. In addition to these surfaces, developed finned surfaces with protuberances are also used for further heat transfer enhancements by disturbing the flow field in addition to increasing the surface area. These protuberances alter the heat exchange by secondary flow enhancement.

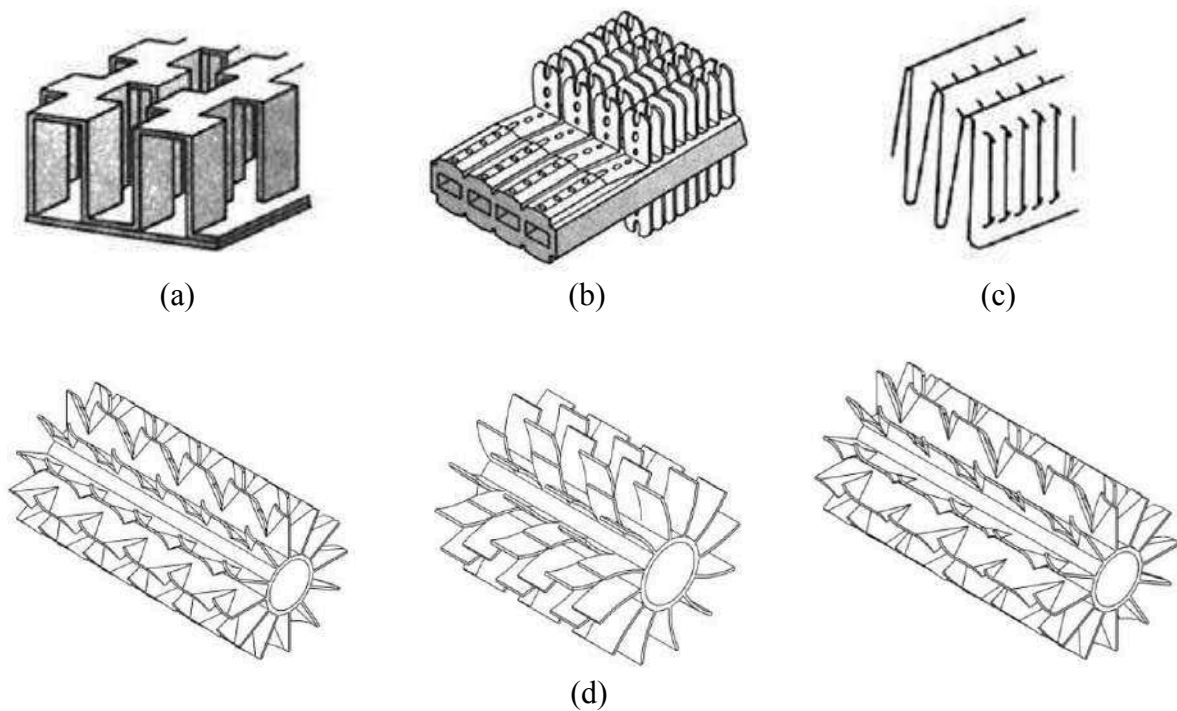


Figure 19 Some types of extended surfaces [48]: (a) Offset strip fin, (b) Integral strip-finned tube, (c) louvered fins, (d) longitudinal finned tubes.

Figure 20 represents some common vortex generators (VG) and the associated geometrical definitions. Many studies were done on this enhanced technique and will be presented in details in a separated section in this chapter.

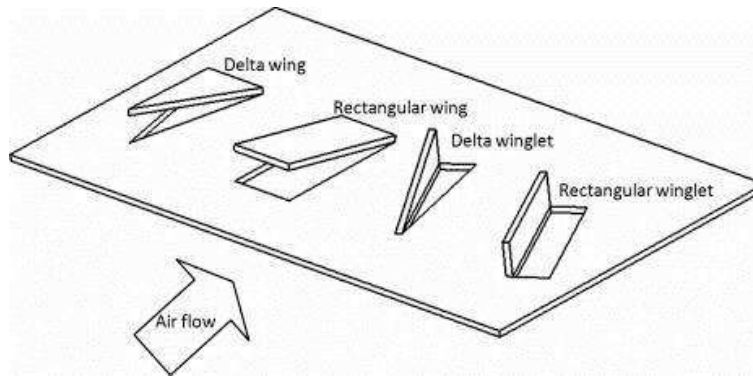


Figure 20 Schematic diagram of plate fin with common longitudinal vortex generators [58].

In addition to these vortex generators, a new technique of passive-dynamic vortex generators is introduced by Ali et al. [59]. This method increases the efficiency of high efficiency vortex mixers by using flexible vortex generators which are dynamic and passively controlled. This technique eliminates the need of external source of energy and reduces the complexity of actively controlled VGs. Ali et al. [59] provided designs for self-sustained oscillations of flexible vortex generators using numerical simulations. Also, and as a future work, this type of VGs can be used to harvest energy and not only saving power by using piezoelectric materials in manufacturing these flexible vortices.

1.6 Compound techniques

Compound enhancement refers to the technique where two or more passive and/or active techniques are used in conjunction. This enhanced technology offers a way to further elevate heat transfer coefficients [60]. Many combinations for two or more enhancement techniques have been studied and suggested. Ribbed roughness and vortex generators have been used in rotating duct [61, 62], while Manglik and Bergles [63] used twisted tape inserts in a rotating tube. Zhang et al. [64] and Zimparov [65] have experimentally investigated the ribbed duct with twisted tape inserts, while Usui et al. [66] and Zhou et al. [67] investigated

internally finned tubes with twisted tape inserts. Das et al. [68] studied the effect of rough tube with treated surface to promote steam condensation. Nishimura et al. [69] investigated the effect of mass transfer enhancement in finned channel with flow pulsations. Also, air pulsation with air-particle suspension heat transfer effects had been studied by Bhattacharya and Harrison [70]. Various combinations of different techniques have been studied and may be combined together to reach higher heat intensification performance of heat exchangers.

1.7 Vortex generators

Heat transfer enhancement is classified as main and secondary flow enhancements. Gross flow characteristics are altered for the main flow enhancement by geometric changes, pressure variations and other means, while local flow structures are introduced in secondary flow enhancement and shown in Figure 21 [71]. For this intention, two enhancement methods can be implemented: the active VG method and the passive VG method [46]. Passive VG are more commonly used since they are characterized by their efficiency, economy, manufacturing simplicity and maintenance ease, opposite to active VG which are energy consumers and less easy to implement. Decreasing the thermal resistance of the sublayer adjacent to the wall, where viscous effects are dominant, is one of the effective passive methods for increasing the heat transfer coefficient. This can be performed by disrupting the growth of the boundary layer using vortex generators (VG) which also promote secondary swirling flow. Flow swirl causes an exchange between the core and wall adjacent fluid that enhances heat transfer between fluid and channel walls. Vortex generators are relatively new types of passive enhancement devices and an optimum geometry has not yet been stated, since it exist plenty of boundary conditions and geometrical parameters to take into account.

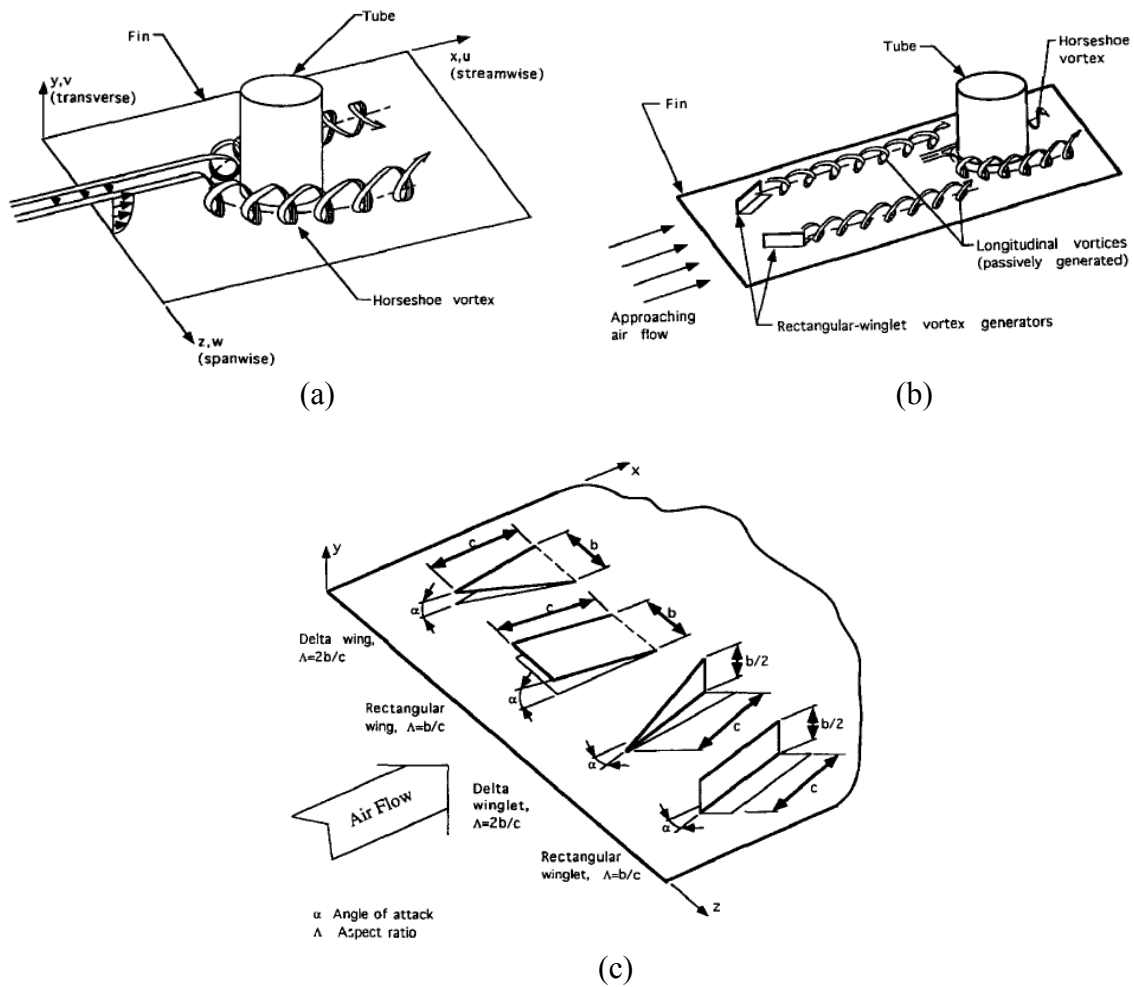


Figure 21 Naturally and passively generated vortices and vortex generators for heat exchanger applications: (a) Natural generation of a laminar horseshoe vortex at fin-tube junction; (b) passively generated longitudinal vortices; (c) common heat exchanger vortex generators [71].

Two types of vortex generators can be distinguished according to the type of the generated vortices: transverse vortex generators (TVG) and longitudinal vortex generators (LVG) [72]. Transverse vortices are two-dimensional flows with axes normal to the flow direction, while longitudinal vortices rotate around an axis in the streamwise direction, implying a three-dimensional swirling flow. When pressure losses are taken into account, LVG are found to have an advantage over TVG in terms of global mixing and heat transfer

performances [73]. Also, Fiebig [72] indicated that longitudinal vortices can significantly increase local and average heat transfer coefficients in the whole channel, while the heat transfer enhancement by transverse vortices is restricted for the case of steady-state laminar flow.

This work focuses on the study of passive LVG and their unique capability in heat transfer enhancement through the generation of large scale longitudinal vortices. This secondary enhancement is a result of the combination of the main mechanisms of heat transfer intensification: the reduction of the laminar sub layer thickness near the wall, the development of three-dimensional turbulent layers and the swirl movement of the streamwise vortex that enhances convective transfer [74, 75].

An early study for a circular cylinder in cross flow with delta-winglet vortex generators was conducted by Johnson and Joubert [76], which seem to be the first article deliberating the influence of vortex generators on heat transfer in 1969. Global heat transfer results were frustrating whereas local Nusselt number increases about 200% due to local thermal mixing.

As a developing work to Johnson and Joubert, Edwards and Alker [77] experimentally studied cubes and delta-winglet vortex generators in a fully developed duct flow. Parametric effects were addressed by changing the size and spacing of the protuberances. They pointed that cubes reached a local Nusselt number peak of about 76% which ensured a higher intensification than delta-winglet vortex generators without providing any pressure drop data. Edwards and Alker [77] found that the performance of counter-rotating vortices is superior to co-rotating vortices.

A comprehensive survey of the protuberances effects on boundary layer flows was elucidated by Sedney [78]. Protrusions effects behaviors in laminar and turbulent boundary layers are analogous. The flow splits over the cusp and continuous longitudinal vortices are generated in a horseshoe pattern, which they may endure for more than 100 disturbance

heights downstream. Location and height of the lump are substantial, while the shape of the protuberance has a modicum effect on the secondary flow. Figure 22 shows three types of surface protuberances, where the locally horseshoe vortices are shown and the legs of the horseshoe vortex exemplify longitudinal vortices. The formed counter-rotating downstream vortices are analogous to those naturally generated by the cylinder-plate interference in Figure 21-a.

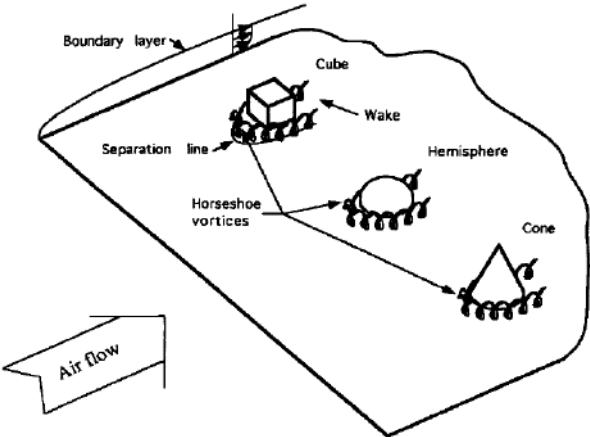


Figure 22 Some types of surface protrusions: cube, hemisphere and cone [71].

An experimental study was carried out by Shakaba et al. [79] concerning attitude of a single longitudinal vortex embedded in a developing boundary layer. They concluded that the streamwise vorticity was incessant and only reduced by the spanwise surface shear stress. Moreover, they pointed that simple eddy viscosity models would not accurately predict the perturbed boundary layer structure. In addition, and as a progress of their previous work, Mehta and Bradshaw [80] experimentally investigated multiple longitudinal vortices with common flow up in developing turbulent boundary layer. Considerable structural alterations in the turbulence were realized, leading them to claim that algebraic turbulence models cannot predict such flow structures.

When the transverse distance between leading edges is less than that of trailing edges, the configuration is known as common flow down (CFD) and vice-versa for common flow up (CFU) [81]. Common flow down vortices create down-wash in between, and up-wash flow in the outside regions. Along the downstream direction, the vortices' velocity vectors decrease while the distance between vortex cores increases which leads to the thinning of the thermal boundary layer [81].

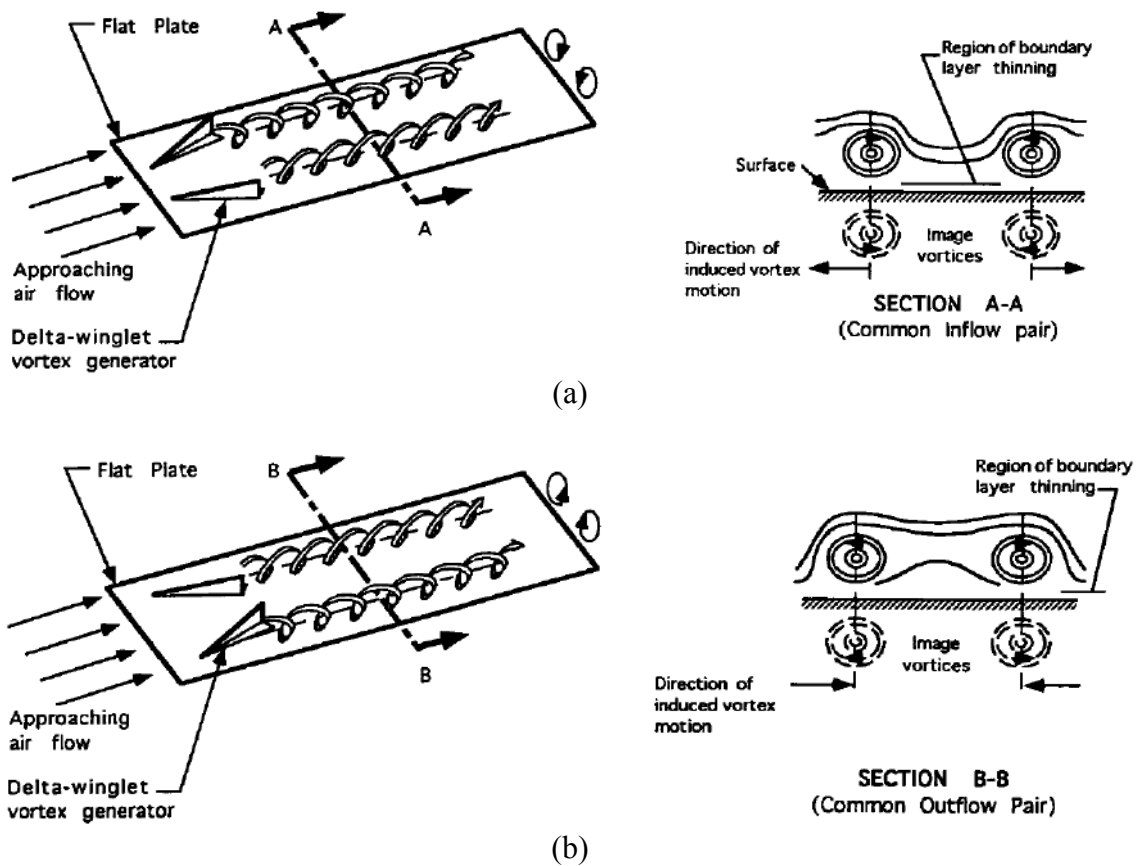


Figure 23 Schematic showing the longitudinal vortices configurations: (a) common flow down (common inflow pair) and (b) common flow up (common outflow pair) [71].

Another experimental heat transfer measurements for a single longitudinal vortex in turbulent boundary layer was performed by Eibeck and Eaton [82]. In the downwash region, a peak heat transfer enhancement of about 25% was recorded while it decreases as much as

15% in the upwash region. Also, they found that the generated vortex is deviated from its longitudinal trajectory due to the interaction between the vortex and the wall.

Mean flow measurements for common flow up and common flow down configurations embedded in a turbulent boundary layer were experimentally performed by Pauley and Eaton [83]. Wider region of thin boundary layer between the two vortices was achieved with the common flow down configuration. However, common flow up configuration behaved in a similar attitude adduced by Mehta and Bradshaw [80].

Fiebig et al. [84] perform numerically studied delta wings and delta-winglet pairs (DWP) in developing laminar flow between two parallel plates. Vortex generators angle of attack was varied from 10° to 50° for $500 < Re < 2000$. They deduced that the circular shaped vortex over a plate is distorted to an elliptical cross sectional shape due to the interaction of the vortices with the wall. In addition, this interaction produced vortex spreading for the common flow down configuration which in turns widened the thin boundary layer region between the two vortices. Delta-winglet pair seemed to have a better global performance for heat transfer enhancement over delta wing.

Tiggelbeck et al. [85] examined experimentally the heat transfer enhancement in a channel with double rows of punched delta-winglet pairs at $Re=4600$. The second row VG configuration was either set aligned or staggered relative to the first row. They used unsteady liquid crystal thermography (LCT) to extract local heat transfer, laser light sheet for flow visualization and load cell for drag measurements. An increase of about 60% in the heat transfer and 145% in pressure drop for the delta-winglet pairs in aligned configurations at an angle of attack of 45° was reached. The aligned configuration bestowed a better performance than that for staggered configuration.

Wu and Tao [86, 87] studied numerically the convection heat transfer in rectangular channel with a pair of rectangular winglet vortex generators at Reynolds numbers between

800 and 3000. They observed that the thickness of the rectangular-winglet vortex generator can decrease the heat transfer enhancement in the near region of the VG and has a little influence on friction. Also, they remarked that the pressure drop increases rapidly with the increase of the angle of attack. In addition, they deduced that the longitudinal vortices enable to enhance the global heat transfer of the channel, whereas transversal vortices can only enhance the local heat transfer of the channel. Delta-winglet pair (DWP) showed a better heat transfer performance than rectangular-winglet pair (RWP) and is more efficient for the same VG area.

Min et al. [88] experimentally investigated the performance of rectangular-winglet pair and octagonal-winglet pair (cutting the four corners of the rectangular-winglet shown in Figure 24) in rectangular channel.

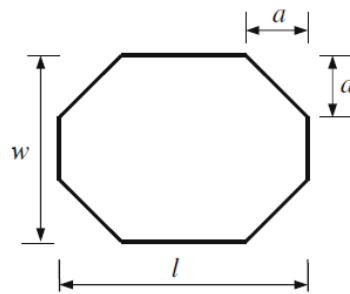


Figure 24 Modified rectangular winglet [88].

They found that octagonal-winglet pair induced a higher heat transfer with lower friction than that for rectangular-winglet pair at same VG area. They interpret their finding by claiming that higher heat transfer was achieved due to longer VG length for generating vortices, and lower friction due to the edge cuttings that tended to inhibit flow disturbance. The average Nusselt number increases with the angle of attack and angle of 55° shows about 50% increase when compared to a similar conditions empty channel.

Tian et al. [89] compared delta-winglet pair with rectangular-winglet pair for common flow down and common flow up configurations and deduced that delta-winglet pair in

common flow down geometry is more efficient than other configurations. Biswas et al. [90] studied the performance of a delta-winglet type VG and concluded that such VGs show great promise for enhancing the heat transfer in plate-fin heat exchangers.

Allison and Dally [91] recognized that winglets have been successfully used to improve heat transfer exchange of modern thermal systems since they can generate intensive longitudinal vortices with low pressure drop penalties.

In addition to the previous review, finding the optimum performance of a vortex generator depending on specific criteria is also critical. In fact, many parameters may alter the performance of the heat exchanger, thus varying the VG shape, angle of attack, position, composition with other types, Reynolds number, and many others is a field of consideration for many researchers.

Salviano et al. [92] studied the optimization of VG position and angles in a fin-tube compact heat exchanger using the genetic algorithm and results were evaluated using RSM. Salviano et al. [93] also numerically investigated the thermal-hydraulic performance optimization of inline and staggered LVGs in fin-tube heat exchangers for laminar flows. Seven independent input parameters for each VG were considered and results indicated that higher heat transfer augmentation was achieved by configuration optimization.

Lei et al. [94] studied the effect of changing the angle of attack for delta-winglet vortex generator between 10° and 50° , in addition to changing aspect ratio from 1 to 4 and the Reynolds number from 600 to 2600. Heat transfer enhancement by punched winglet-type VG arrays in fin-and-tube heat exchangers using numerical studies was investigated by He et al. [95]. They varied the VG angle of attack and spacing between staggered VGs and concluded that the heat transfer and pressure drop increase as angle of attack increases.

Lemouedda et al. [96] examined an optimization of the angle of attack of delta-winglet VGs in plate-fin-and-tube heat exchangers using a combination among numerical analysis,

genetic algorithm and RSM. Angle of attack was varied between -90° and 90° for Reynolds numbers between 200 and 1200. They found that for the inline arrangement the common-flow-down (CFD) configuration is more suitable than the common-flow-up (CFU).

Wu and Tao [97] presented numerical simulation results for laminar flow (Reynolds numbers from 800 to 2000) heat transfer of the fin-and-tube surface with vortex generators at two angles of attack (30° and 45°). They found that the delta winglet with the attack angle of 45° enhances the heat transfer while increasing pressure drop. Also, Wu and Tao [98] studied experimentally and numerically the convective heat transfer on the top and bottom surfaces of a plain plate and four plates with delta winglet VG pair in laminar flow. The VG was directly punched from the plates at different angle of attacks (15° , 30° , 45° and 60°). They deduced that the average Nusselt number of the plate with 60° angle of attack is slightly higher than that of 45° attack angle.

Yongsiri et al. [99] made numerical study of flow and heat transfer in channel with various inclined detached ribs for turbulent flow ($Re=4000$ to 24000). The angle of attack examined was varied from 0° to 165° and it was revealed that for high Reynolds number the inclined ribs with 60° and 120° yield to a comparable heat transfer performance over other angles. While for low Reynolds number, the effect of angle of attack was not significant.

1.8 Objective and outline of this research work

Various previous parametric studies have been made concerning vortex generators alignments, positions, angle of attack and other factors. Most of these studies were oriented towards having a combination between LVGs and other passive technique in laminar flow or relatively low turbulent Reynolds numbers without studying the absolute effect of the LVG at a wide range of Reynolds numbers. Previous studies did not include the effect of changing the inclination angle while preserving the same frontal area. Therefore, numerical and

experimental analyzes for the effects of varying the inclination angle of vortex generators on the flow structure and thus on the heat transfer mechanism over a wide range of Reynolds number should be discussed.

The present work focuses on designing a better aerodynamic VG shape that can provide the same heat transfer with a reduced pressure drop. The new VG increases the global total enhancement over a wide range of Reynolds numbers. Inclination optimization is also conducted through this study with the addition of hemispherical protrusions downstream the new VG. The aim of this study is to numerically analyze the effect of the new VG geometry on the flow structure and thus on the heat transfer mechanism. The numerical model used is validated and compared by a thorough experimental study. Hence, the objective of this PhD is to study the thermal performance and the flow structural characteristics of multi-scale vortices in a plate-fin heat exchanger.

After presenting a synoptic literature review on the flow behavior and thermal hydraulics of longitudinal vortex generators used in fin-plate heat exchangers in Chapter 1, Chapter 2 presents some of the numerical methods used in turbulent flows modeling. Also, experimental setup and relevant instrumentations used for flow visualization and analysis in addition to the test benches utilized in this work are discussed in Chapter 2. Chapter 3 deals with an experimental study of rectangular-winglet pair to study the effect of longitudinal vortices on the flow structure between two parallel plates using the stereoscopic particle image velocimetry (SPIV) new technology. In Chapter 4, numerical study using computational fluid dynamics software is conducted to validate the numerical model used for the turbulent flows. After validating the turbulence model for simulating turbulent flow, numerical simulations are performed to design a new vortex generator which ensures a better total enhancement and enhanced flow structural mechanism are discussed in Chapter 5. Chapter 6 deals with the optimization of the new vortex generator configuration using

response surface methodology (RSM). The parameters that the new vortex generator is optimized on are the Reynolds number and the inclination angle for which results are obtained numerically. In Chapter 7, hemispherical protrusions are added to the channel with the new vortex generator in different locations, where computational fluid dynamic software is used to elucidate the new flow structure and study the thermal hydraulic impact, while last Chapter is devoted to the concluding and future work remarks. Chapters 3 to 7 are presented as either published paper (Chapter 5), submitted paper or to be submitted papers.

Chapter 2

Methods and Materials

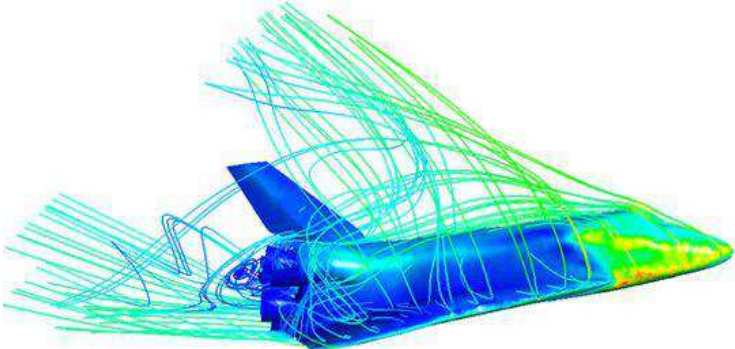
2.1 Introduction

Research in fluid mechanics mainly depends on three types of scientific activities: experiments, analyses and simulations. The scientific research can either rely on one of the three types or combines two and maybe three types of activities. If experimental or simulation method is chosen solely for a scientific research, results quality may not be high enough due to many factors. Contributing factors may result from many error sources that are briefly discussed in subsequent sections. While integrating more than one activity might offer further solid results. Sobieski [100] declared that: “It has been assumed that an experiment is the most important stage of research and that a virtual model has to be based on experimental data. This assumption follows from the general principle that a simulation model is of value when it conforms to real world observation“. In the present work, numerical model used is validated using experimental activity and this chapter present concise sections addressing numerical and experimental setups in the domain of fluid mechanics.

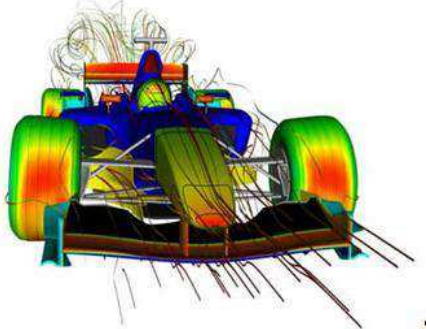
2.2 Computational fluid dynamics

Computational Fluid Dynamics (CFD) is an important branch of fluid mechanics. As its name indicates, computation refers to numerical algorithms solved by a computer, fluid refers to gas or liquid and dynamics refers to the motion of that fluid, thus, it is the science for modeling the fluid motion in a medium using mathematical algorithms. Since fluid flows are governed by partial differential equations representing mass, momentum and energy

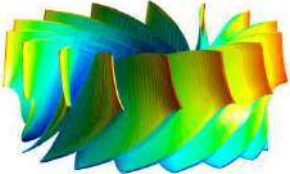
conservation laws, CFD is the art of replacing the system of partial differential equations by a set of algebraic equations solved by computers. It uses numerical methods and algorithms to solve fluid flow problems. CFD becomes popular since experimental methods are very expensive, time consuming and involve too much labor. Many reasons drive researchers to perform CFD numerical simulations. It is cheap, since they only need electricity, license and researcher brain matter. CFD simulations are flexible, since adjusting computerized model is much easier, cheaper, faster and simpler than real prototype one. It provides profound analysis, because one can analyze special and physically unreachable zones, in addition to visualizing streamlines, velocity and pressure contours and many others. CFD is precise; it is considered a robust tool for modeling fluid flows due to the refined enhancement of numerical techniques for modeling. Also, CFD is a multitask tool that can be used in aerodynamic modeling in addition to internal combustion engines, turbomachinery, fluid-structure interaction and plenty others. Figure 25 presents some of the CFD applications that are used in many industrial fields, civil, environmental and others.



(a)



(b)



(c)

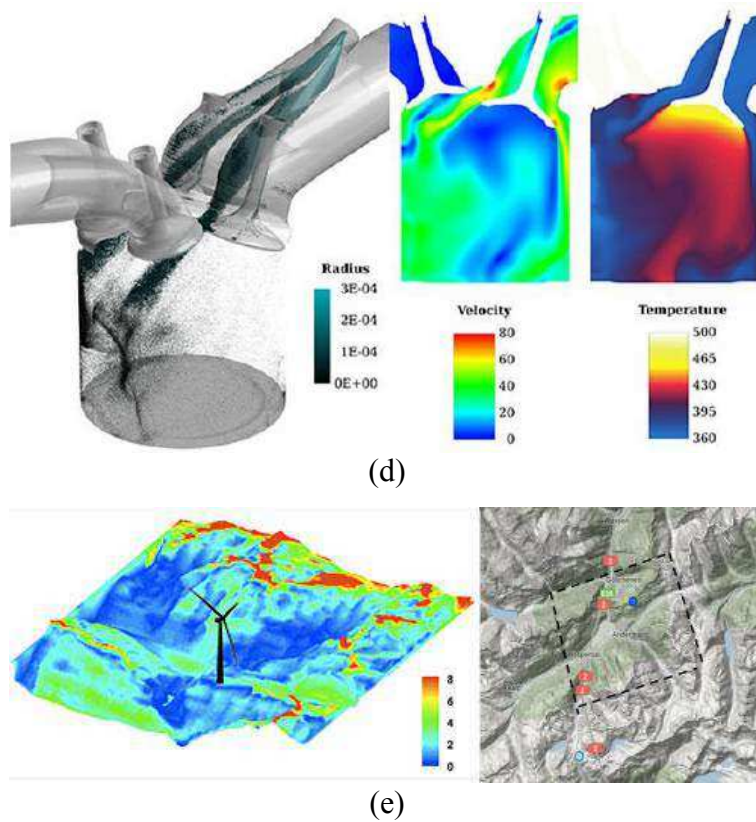


Figure 25 Some CFD applications in industrial and environmental fields: (a) aerospace [101], (b) automotive [102], (c) turbomachinery [103], (d) Internal combustion engines [104], (e) wind farm planning [105].

2.2.1 Governing equations

In order to solve a CFD case in fluid mechanics, two types of solution methods exist: finite volume method (FVM) and finite difference method (FDM). FVM is the most common approach used in CFD simulation, where the governing equations are solved over discrete control volumes. FVM dominates FDM due to its high accuracy, while FDM is used for approximating the solution. Many commercial programs can be used for CFD simulations.

When applying Newton's second law on a fluid flow, Navier-Stokes equation is obtained. Partial differential equations define the mass, momentum and energy. In this study, the flow is considered incompressible and steady state. Thus, the study is time independent, and the fluid has constant density and viscosity. The flow field is governed by the three-

dimensional (3D) steady-state Reynolds averaged Navier-Stokes (RANS) equations. The continuity and momentum equations for an incompressible Newtonian fluid are:

$$\frac{\partial u_i}{\partial x_i} = 0 \quad (2.1)$$

$$u_j \frac{\partial u_i}{\partial x_j} = -\frac{1}{\rho} \frac{\partial p}{\partial x_i} + \nu \frac{\partial^2 u_i}{\partial x_j \partial x_j} - \frac{\partial \overline{u'_i u'_j}}{\partial x_j} \quad (2.2)$$

where the term $-\overline{u'_i u'_j}$ is the Reynolds stress tensor resulting from the averaging procedure on the nonlinear convective terms in the momentum equations. The heat transfer is computed by solving the energy equation:

$$\frac{\partial}{\partial x_i} [u_i (\rho E + p)] = \frac{\partial}{\partial x_i} (\lambda_{eff} \frac{\partial T}{\partial x_i}) \quad (2.3)$$

where E is the total energy and λ_{eff} the effective thermal conductivity.

The software used for the flow computation is the ANSYS Fluent 15, which is based on an Eulerian approach to solve the Cauchy equations through cell-centered finite volume discretization. The code computes the conservation equations for mass and momentum in addition to the energy equation for flows involving heat transfer. Turbulence models allow the calculation of the mean flow without first calculating the full time-dependent flow field. Turbulence model must have wide applicability, accuracy, simplicity and time frugal.

2.2.2 Turbulence models

There is a variety of turbulence models which can be split into the following distribution [106]:

- Spalart-Allmaras model
- κ - ε models
 - Standard κ - ε model
 - Renormalization-group (RNG) κ - ε model
 - Realizable κ - ε model

- κ - ω models
 - Standard κ - ω model
 - Shear-stress transport (SST) κ - ω model
- Transition κ - κ - ω model
- Transition SST model
- v^2 -f model
- Reynolds stress models (RSM)
 - Linear pressure-strain RSM model
 - Quadratic pressure-strain RSM model
 - Low-Re stress-omega RSM model
- Detached eddy simulation (DES) model
 - Spalart-Allmaras RANS model
 - Realizable κ - ε RANS model
 - SST κ - ω RANS model
- Large eddy simulation (LES) model
 - Smagorinsky-Lilly subgrid-scale model
 - WALE subgrid-scale model
 - Dynamic Smagorinsky model
 - Kinetic-energy transport subgrid-scale model

Many researchers performed numerical simulations to study and analyze the thermal hydraulic performance of vortex generators in enhanced heat exchangers. Various turbulence models were used to model transverse and longitudinal vortices in turbulent flows. Two of the commonly used turbulence models for studying flow and heat transfer downstream VGs are the re-normalization-group (RNG) κ - ε model and shear-stress transport (SST) κ - ω model. These two models have been widely used in considerable studies concerning this research topic [92, 99, 107, 108, 109, 110, 111].

The re-normalization-group (RNG) κ - ε model was developed by Yakhot et al. [112, 113] using re-normalization group (RNG) method to renormalize the Navier-Stokes equations in order to capture the effects of small scale motion in a turbulent flow. In standard κ - ε model,

the turbulent diffusion is accounted only at a specific scale, since eddy viscosity is resolved from a single length scale. This trend is not realistic since all scales of motion will contribute to the turbulent diffusion. The modified κ - ε model solves this problem and involves different scales of motion to the production term. The RNG κ - ε model shows fundamental improvements over the standard κ - ε model and enhances the final solution [114], where the effects of turbulence of strong streamline curvature, vortices and swirl effect are taken in account [115]. The equations for the turbulence kinetic energy κ and its dissipation rate ε are:

$$\rho \frac{\partial}{\partial x_i} (\kappa u_i) = \frac{\partial}{\partial x_j} \left(\sigma_k \mu_{eff} \frac{\partial \kappa}{\partial x_j} \right) + \rho C_\mu \frac{k^2}{\varepsilon} \Sigma^2 - \rho \varepsilon \quad (2.4)$$

$$\rho \frac{\partial}{\partial x_i} (\varepsilon u_i) = \frac{\partial}{\partial x_j} \left(\sigma_\varepsilon \mu_{eff} \frac{\partial \varepsilon}{\partial x_j} \right) - \rho C_{1\varepsilon} C_\mu \Sigma^2 - \rho C_{2\varepsilon} \frac{\varepsilon^2}{k} - R_\varepsilon \quad (2.5)$$

where the model constants are $C_\mu=0.0845$, $C_{1\varepsilon}=1.42$ and $C_{2\varepsilon}=1.68$. $\sigma_k, \sigma_\varepsilon$ are the turbulent Prandtl number for κ and ε respectively and μ_{eff} is the effective viscosity. The additional term R_ε is given by [116]:

$$R_\varepsilon = \frac{\rho C_\mu \gamma^3 \left(1 - \frac{\gamma}{4.38} \right) \varepsilon^2}{1 + 0.012 \gamma^3} \frac{1}{k} \quad (2.6)$$

with $\gamma = k\Sigma/\varepsilon$ and Σ is the modulus of the mean strain rate tensor.

The shear-stress transport (SST) κ - ω model developed by Menter [117] solves two additional partial differential equations: a modified version of the κ equation used in κ - ε model and a transport one for ω . Also, the shear stress transport (SST) combines the better of two worlds: the use of κ - ω formulation in the inner parts of the boundary layer and it switches to a κ - ε behavior in the free-stream, thus avoiding the κ - ω sensitivity to the inlet free-stream turbulence properties. In addition, it is characterized by its good behavior in adverse pressure gradients and separating flows while attaining accuracy and reliability [118].

The SST and standard κ - ω models are alike with the subsequent refining:

- A blending function is employed to multiply the standard κ - ω and the transformed κ - ε models by it and those two models are added with each other. The standard κ - ω model is actuated when the value of the blending function is equal to one in the near-wall region. On the other hand, the transformed κ - ε model is initiated when the blending function is zeroed in location far from the surface.
- The ω equation in the SST form includes a damped cross-diffusion derivative term.
- The description of the turbulent viscosity is altered to include the transport of the turbulent shear stress.
- The constants used in modeling are not alike.

The preceding attributes give the SST κ - ω model additional accuracy and reliability thus providing it an advantage over the standard κ - ω model.

The SST κ - ω model transport equations which have the same form as the standard κ - ω model are:

$$\rho \frac{\partial}{\partial x_i} (\kappa u_i) = \frac{\partial}{\partial x_j} \left(\Gamma_k \frac{\partial \kappa}{\partial x_j} \right) + \tilde{G}_k - Y_k \quad (2.7)$$

and

$$\rho \frac{\partial}{\partial x_i} (\omega u_i) = \frac{\partial}{\partial x_j} \left(\Gamma_\omega \frac{\partial \omega}{\partial x_j} \right) + G_\omega - Y_\omega + D_\omega \quad (2.8)$$

where \tilde{G}_k is the production of turbulence kinetic energy due to mean velocity gradients, G_ω is the generation of ω , Γ_k and Γ_ω are respectively the effective diffusivity of κ ; $\Gamma_k = \mu + \frac{\mu_t}{\sigma_k}$ and $\Gamma_\omega = \mu + \frac{\mu_t}{\sigma_\omega}$, Y_k and Y_ω are the dissipation of κ and ω due to turbulence respectively, D_ω is the cross-diffusion, σ_k, σ_ω are the inverse effective Prandtl number for κ and ω respectively and μ_t is the turbulent viscosity. For detailed discussion of these equations refer to [118].

For spatial discretization of the convective terms, a scheme of double precision and second order upwind is used to consecutively solve the flow equations for both models [119].

Central-difference and second order accuracy are selected for the diffusion terms. The Coupled algorithm is used for the pressure-velocity coupling with the pseudo transient option. Pseudo transient method option is a form of implicit under-relaxation for steady-state cases. It allows the user to obtain solutions faster and more robustly.

2.2.3 Numerical error sources

The reliability of CFD simulations highly relies on the convenient setting of numerical simulation parameters and boundary conditions. Acquiring CFD results from a software is relatively not considered an arduous task, but how can we ensure that the results are good enough and can be trusted? Thus, comprehending the source of errors or inaccuracies and uncertainties that can emerge in simulation is a necessity. The definitions of these terms related to CFD simulation are given by the American Institute of Aeronautics and Astronautics (AIAA) as [120]:

- Error: a recognizable deficiency in any phase or activity of modeling and simulation that is not due to lack of knowledge.
- Uncertainty: a potential deficiency in any phase or activity of the modeling process that is due to lack of knowledge.

In addition, the European Research Community on Flow, Turbulence and Combustion (ERCOFTAC) provides seven different error and uncertainty sources [121]:

1. Model error and uncertainties: the difference between the real flow and the mathematical model utilized. Errors from turbulence modeling are the most spread errors in this category.
2. Discretization or numerical error: the difference between exact and numerical solutions of the mathematical model, with a limited resolution in time and space.

3. Iteration or convergence error: the difference between exact and iterative solutions of the discretized equations.
4. Round-off error: limitations of computer digits available to store for a given value.
5. Code errors: not intended programming errors in the implementation of models (Software bugs) or compiler errors.
6. Application uncertainties: due to complex application, inaccuracy is introduced, since precise data needed for the simulation is not always available.
7. User errors: due to the application of the code in a less-than-accurate or improper manner and may show up as modeling and discretization errors. Also, inconvenient boundary conditions, inappropriate setting of parameter values and badly chosen model are considered user errors. In addition, computer aided design (CAD) geometry related errors, improper grid generation, CFD setup and post-processing are among the user errors.

For detailed description of these errors, reader may refer to the reference [122].

2.3 Experimental study

The definition of experiment is wide and has changed in responses to changing norms and practices within particular fields of study, while experimental research tightens this definition to the experiments dealing with scientific research field such as fluid mechanics. Experiments in fluid mechanics are considered a very important part of investigating flow structure characteristics. Experiments can supplement theoretical studies, modelling of flow field and numerical simulations. In addition, experiments can be utilized to confirm, validate or develop theoretical or numerical results. Experimental fluid mechanics belongs to pillars of research seeking for an ideal knowledge in this domain. Figure 26 shows a scheme

representing the three pillars of research in fluid mechanics: theory, numerical simulations and experiments [123].

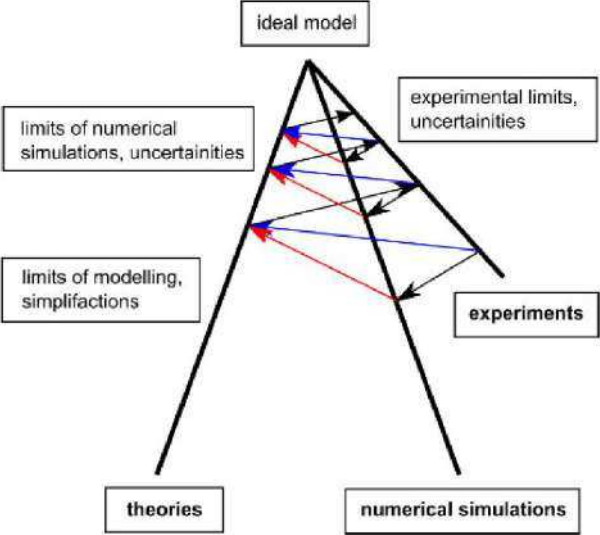


Figure 26 A scheme of pillars of basic research in fluid mechanics [123].

2.3.1 Instrumentation

Experiments should be designed to consider several approaches to obtain the final result. Many factors have to be considered when selecting an experimental method [124]: experience in the use of instruments; knowledge of calibration methods and awareness of the different errors to which instruments are subject; understanding of the relative merits and limitations of alternate instrumentations and their applicability to different experimental situations.

A variety of experimental measurement instrumentation exists in laboratories to measure fluid and thermodynamic properties in test benches, flow structure characteristics and visualization and many others. Tunnels are used to study the effect of a fluid moving past solid objects. The flow velocity can be measured using hot-wire anemometry, Laser Doppler Velocimetry (LDV), vortex shedding or many other techniques. Pressure measurement methods also can vary from barometers, manometers, transducers, pitot and others. Flow

streamlines may be visualized using smoke machines and flow structure can be illuminated and captured using some special techniques such as Particle Image Velocimetry (PIV). And so on, many other flow properties can be obtained using many other instrumentations and methods.

In this section, techniques used and instrumentations exercised in this work is only presented briefly. For further information regarding the instrumentations and measurement methods in fluid mechanics, reader may refer to Rathakrishnan [125].

2.3.1.1 Laser Doppler anemometry

Laser Doppler velocimetry (LDV) is the technique of using the Doppler shift in a laser beam to measure the velocity in transparent or semi-transparent fluid flows. When testing gaseous fluid flows, this technique is known as Laser Doppler Anemometry (LDA). It is a widely used in fluid dynamic investigations and considered an accepted tool used for more than three decades. LDA is advantageous to use in fluid experiments since it is a non-intrusive measuring device that has high spatial and temporal resolution and able to measure reversing flows with no need of any calibration. It consists of a continuous wave laser, transmitting optics including the beam splitter and focusing lens, receiving optics involving a focusing lens, an interference filter and a photodetector, a signal conditioner and a signal processor. The working principle of LDA system is elucidated in Figure 27.

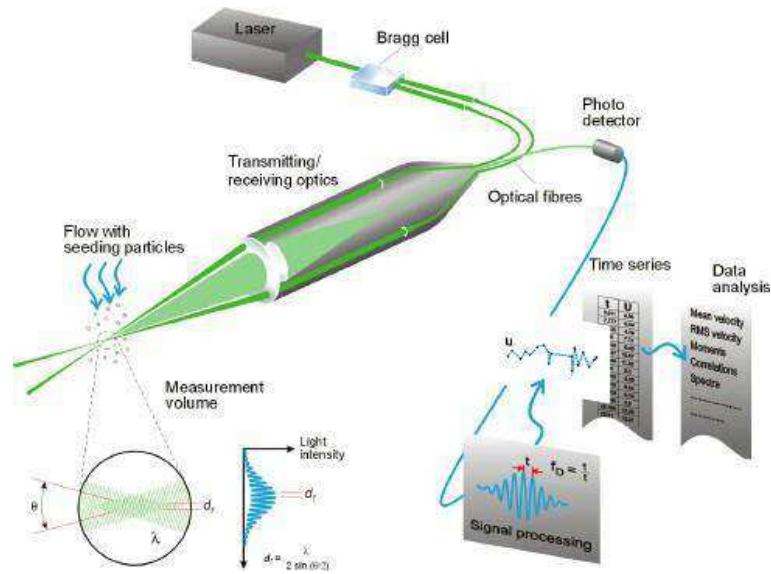


Figure 27 Measurement principle of LDA by Dantec Dynamics© [126].

Measuring with LDA is absolute, linear with velocity and requires no pre-calibration. Two collimated, monochromatic, and coherent laser beams are crossed in the flow of the fluid being measured. The two equal intensity beams are obtained by splitting a single beam using a Bragg cell, thus ensuring coherence between the two. A Bragg cell is a glass crystal with a vibrating piezo crystal attached, in which it generates acoustical waves acting like an optical grid.

A transmitting optics focuses the parallel beams in the probe to intersect at the focal point of the laser beam in the probe volume, where they interfere and generate a set of straight fringes. The splitted parallel beams in the probe, focused beams, and the probe volume are presented in Figure 28.

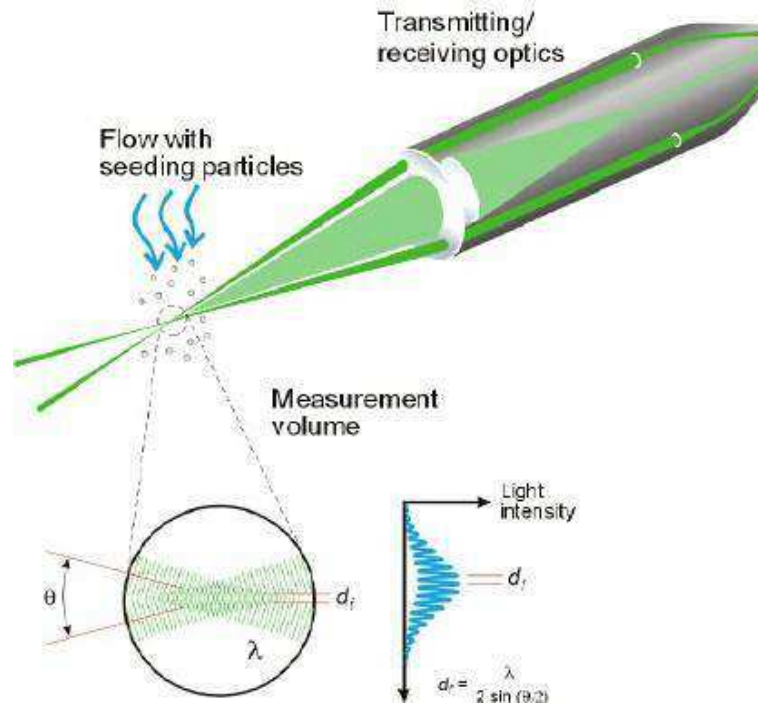


Figure 28 The probe and probe volume by Dantec Dynamics© [126].

The light intensity is modulated due to interference between the laser beams, which produces parallel planes of high light intensity called fringes. As particles entrained in the fluid pass through the fringes, they scatter light proportional to the light intensity that is then collected by a receiving optics and focused on a photodetector. An interference filter mounted before the photodetector filtrates the required wavelength to remove ambient light noise. The reflected or scattered light contains a Doppler shift which is proportional to the velocity component perpendicular to the bisector of the two laser beams. The reflected light fluctuates in intensity in which the frequency of fluctuation is equivalent to the Doppler shift between the incident and scattered light, and is thus proportional to the particle velocity.

Two velocity components can be measured using LDA with two additional beams added in the optics perpendicular to the first two beams. In addition, this technique enables the measurement of all three velocity components by two separate probes measuring two and

one components. Different wavelengths with three photodetectors are used to separate the measured components. A compact transmitting unit that can transmit up to six beams is utilized in modern LDA systems by Dantec [126].

2.3.1.2 Particle image velocimetry

Previous studies, limited by single-point velocity measurement techniques, measure the single-point local dissipation rate or averaged over a finite volume, thus being limited to a local or mean estimation of the fluid structure characteristics over a narrow region. Intrusive complex probes are generally unsuitable for complex flows and LDA technique has sampling limitations in addition to a limited studied space. Particle image velocimetry (PIV) is a whole-flow-field technique providing instantaneous velocity vector measurements in a cross section of a flow. PIV is a non-intrusive technique that measures the velocities ranging from zero to supersonic of micron-sized particles in a flow. The velocity vectors are derived from subsections of the target area of the particle seeded flow by measuring the movement of particles between two light pulses.

The flow is illuminated at the target area with a laser light sheet and the camera lens images the target area onto the sensor array of a digital camera which is able to capture both light pulses in separate image frames as presented in Figure 29.

The images are chopped into small subsections called interrogation areas just after the two light pulses sequence is recorded. The interrogation areas (IA) from each image frame (named as I_1 and I_2) are cross-correlated with each other. This correlation results in a single peak which identifies the common particle displacement (DX). Thus, particle displacement is measured precisely, and since the accurate time sequence of the two successive image frames is known, velocity is also achieved with sub-pixel interpolation. Then, by repeating the cross-

correlation for each interrogation area over the two image frames, a velocity vector map over the whole target area is acquired as shown in Correlation of two interrogation areas of the PIV system by Dantec Dynamics© .Figure 30.

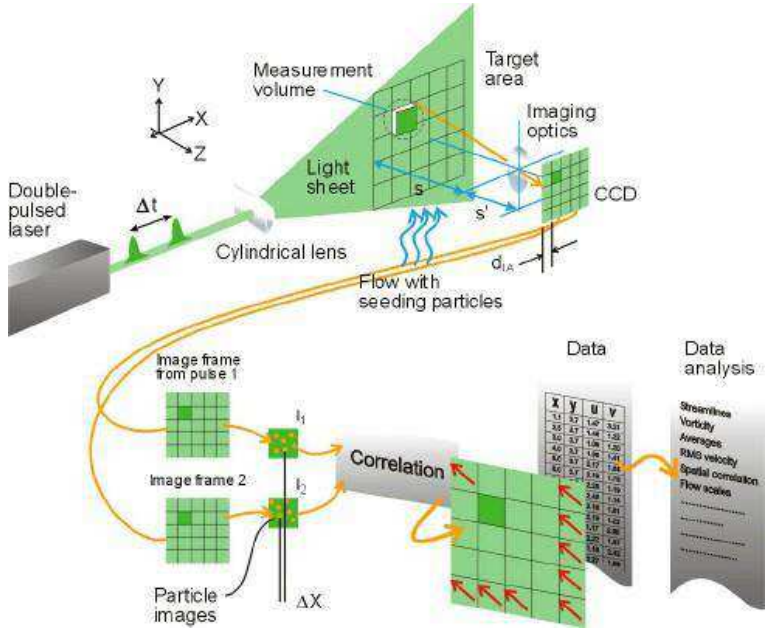


Figure 29 PIV measurement principle by Dantec Dynamics© [127].

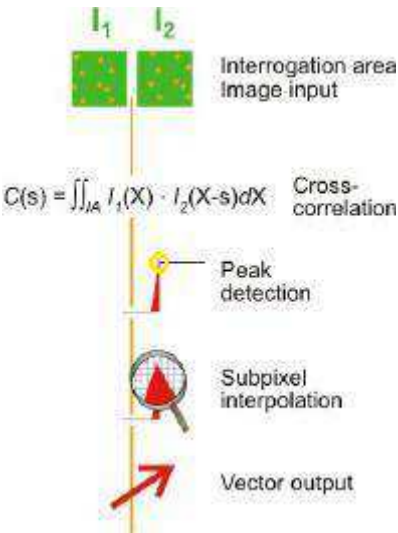


Figure 30 Correlation of two interrogation areas of the PIV system by Dantec Dynamics©

[127].

2.3.1.3 Stereoscopic particle image velocimetry

PIV measures two velocity components in a two dimensional plane (2D-2C) using a single camera. PIV may solve part of the problem, since PIV is not restricted over single-point measurements and 2D velocity fields are simultaneously obtainable. In applications where the circumferential velocity component, its derivatives and all derivatives along the circumferential direction are needed, PIV technique is inefficient since it lacks the capability to measure 3D velocity fields. Subsequently fully resolved 3-component velocity measurements are fundamental and SPIV (Stereoscopic particle image velocimetry) takes the advantage over other techniques.

SPIV uses the same mechanism as standard PIV but instead of having one camera to capture the plane of interest, two cameras at different angles are used as presented in Figure 31. SPIV technique is used to measure the three-component velocity field of the flow in the planar region illuminated by a laser light sheet. The fundamental principle behind SPIV is stereoscopic imaging of particles in an illuminated plane in the flow. Two cameras view the same plane at different angles and capture particle displacement images that contain the influence of the third velocity component.

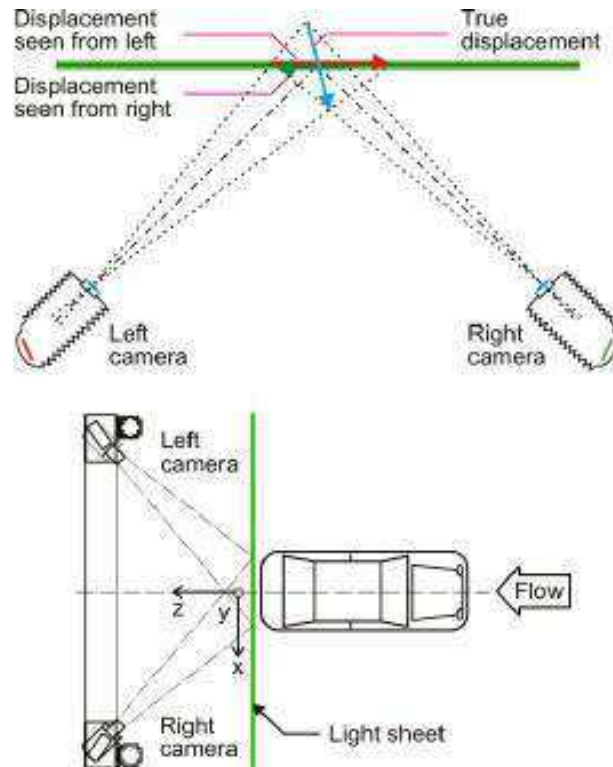


Figure 31 Two cameras technique for SPIV system by Dantec Dynamics© [127].

2.3.2 Experimental test benches

To study the structure and characteristics of a flow downstream the studied object configuration, wind tunnels are used as test bench. This study benefited from two test benches designed and developed by the Industrial Energy Department in École de Mines-Douai laboratories. The first wind tunnel test bench is named as Alpha-1, which already existed, and the second is named as Alpha-3, which was exclusively designed for the current and subsequent studies. This section is dedicated for the description and characterization of both wind tunnel test benches.

2.3.2.1 Alpha-1 test bench

Alpha-1 close-loop air channel test bench is illustrated by a Computer Aided Drawing (CAD) drawing in Figure 32. Air is sucked from the seeding room towards the test channel in

a closed loop circuit by means of a 2.3 kW centrifugal fan. The test section is 1200 mm in length, 500 mm in width and of height equal to 37.8 mm. To homogenize the flow upstream the test section, conditioning elements (honeycomb and convergent section) are used. The upper and lateral faces of the test section are made of transparent glass in order to allow particles illuminating and image acquisition. A convergent bend element is used to direct the airflow towards the PVC pipe. The main objective of this element is to make the rear test section wall transparent for cross-sectional data acquisition. Pressure and temperature sensors are used to account for the air thermo-physical properties effects on the measured flow rate. Required flow rate for the measurement is obtained by varying the rotational speed of the fan. In the seeding room, seeding particles are generated through a controlled combustion process of incense which produces about 1 μm mean diameter smoke particles [128] used as flow tracers.

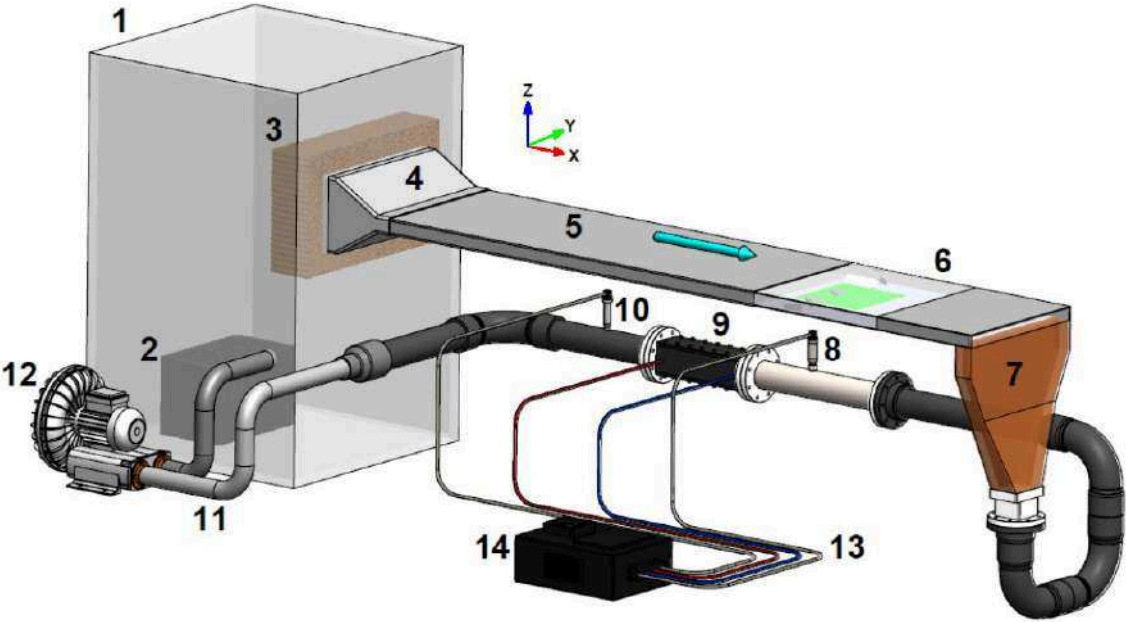


Figure 32 Alpha-1 experimental test bench: (1) Seeding room; (2) Particles generator; (3) Honeycomb; (4) Convergent section; (5) Upstream channel; (6) Test section (lateral and upper glazed windows); (7) Convergent 90° bend; (8) Absolute pressure transducer; (9) Laminar flowmeter; (10) Temperature probe; (11) PVC suction pipe; (12) Centrifugal fan; (13) Wirings and cables; (14) Micro-manometer; the cyan arrow indicates the air flow direction.

2.3.2.2 Alpha-3 test bench

The Alpha-3 test bench is similar in parts and instrumentation to Alpha-1 and a CAD drawing of Alpha-3 is shown in Figure 33. It is a close-loop air channel test bench where air is sucked from the seeding room towards the test channel by means of a 2.3 kW centrifugal fan. A bell-shape convergent section is used to decrease the turbulence at the inlet before adding a mesh screen to homogenize the flow at the inlet. Also, pressure and temperature sensors are used to account for the air thermo-physical properties effects on the measured flow rate. The rotational speed of the fan is changed in order to obtain the recommended measurement flow rate. Same particle generating technique as Alpha-1 test bench is used for flow tracing.

The main advancement utilized in Alpha-3 test bench is the test section part. The test section is 1280 mm in length, 185 mm in width and of height equal to 50 mm. The upper, lower and lateral faces of the test section are made of transparent thick Plexiglas in order to allow particles illuminating and image acquisition with no obstacles at any orientation. The whole test section part is designed to rotate by sealed swivel hinges. This design ensures fixed, non-moving measuring instrumentations when changing the plane of interest acquisition from vertical to horizontal and vice-versa. In other words, all appliances and instruments (LDA, laser source, cameras, etc.) do not move thus do not need any re-

calibration; instead, the test section is rotated for changing measuring planes. Figure 34 elucidate a CAD drawing of Alpha-3 swivel test section.

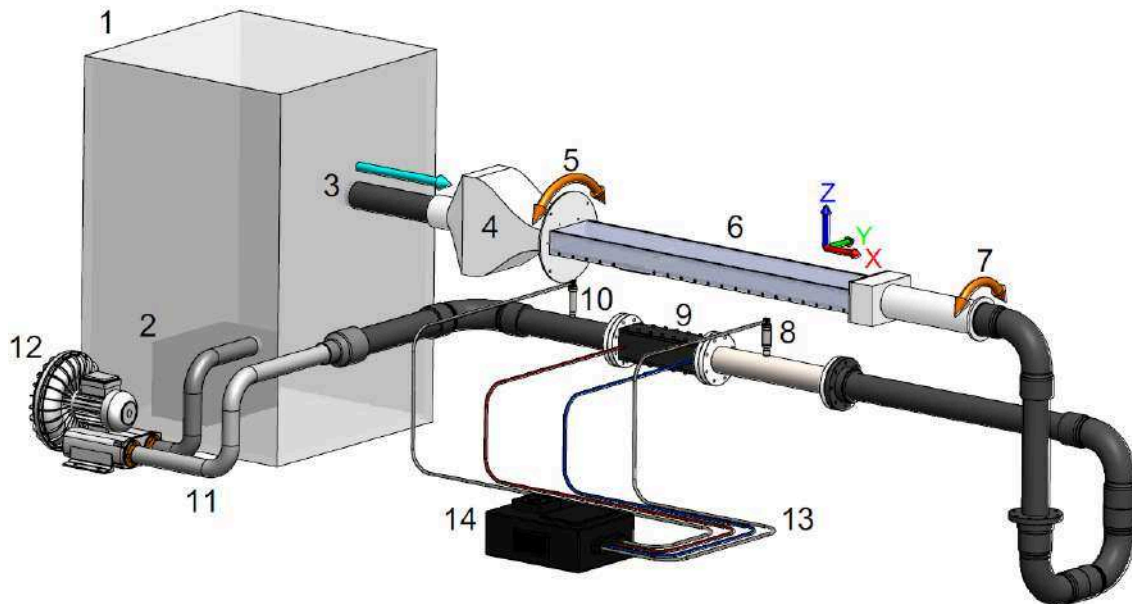


Figure 33 Alpha-3 experimental test bench: (1) Seeding room; (2) Particles generator; (3) Entrance pipe; (4) Bell-shape convergent section; (5) Swivel disk; (6) Test section (lateral, lower and upper Plexiglas walls); (7) Swivel hinge; (8) Absolute pressure transducer; (9) Diaphragm flowmeter; (10) Temperature probe; (11) PVC suction pipe; (12) Centrifugal fan; (13) Wirings and cables; (14) Micro-manometer; the cyan arrow indicates the air flow direction.

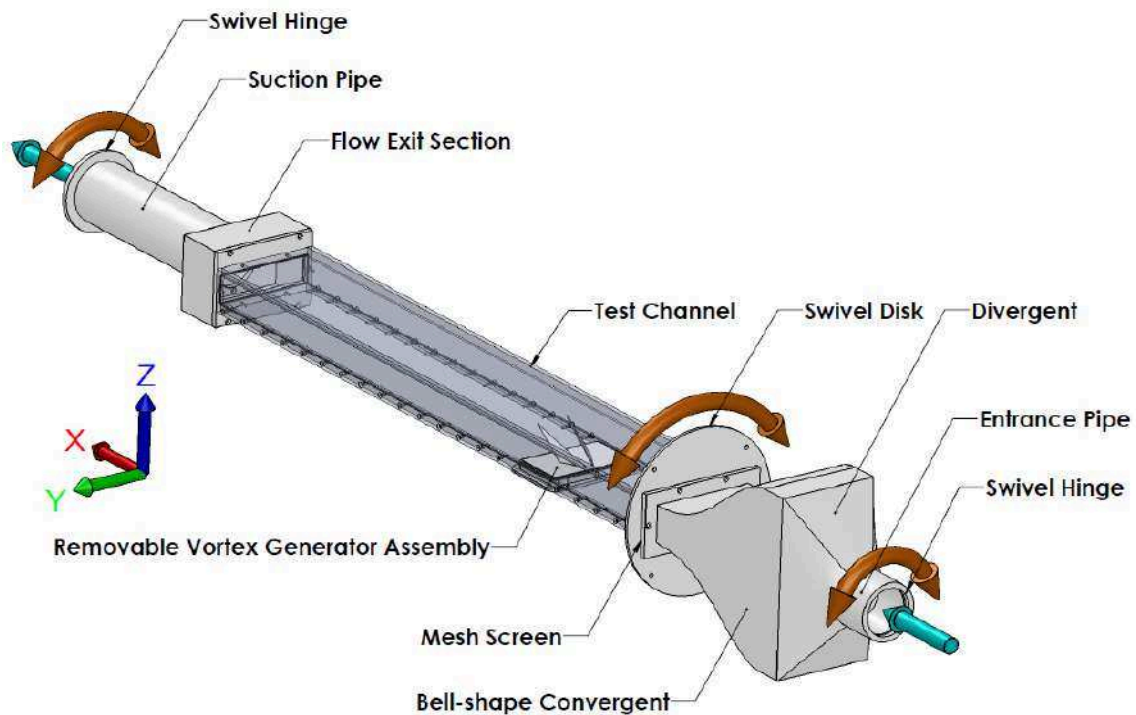


Figure 34 Detailed view for Alpha-3 swivel test section.

2.3.3 Experimental error sources

When performing an experiment to measure physical quantities such as velocity, temperature, heat flux or others, results errors may be encountered since it is impossible to make an exact measure. All experimental results contain errors and thus all experiments are imperfect. Just how imperfect they are depends on the kinds and contributions of errors made in the experiment. Three main types of errors may arise from an experimental study: human error, systematic error and random error.

Human errors are mistakes done by the experimenter by false setup, wrong reading of an instrument, calculation mistakes and many others. This type of error is not considered as a source of experimental error, since it is caused by the experimenter himself. But human errors are one of the main sources of false results and should be taken into account.

Systematic errors, as their name reveals, are errors caused by the design of the system and the way in which the experiment was performed. They arise due to imperfect equipment design and can be eliminated. Four kinds of systematic errors can be defined: instrumental errors such as flow disturbance by intrusive probes, bad calibration of instruments, nonlinear ranges of the instrument and other factors related to the instrument itself; observational errors; environmentally related errors such as changing the environmental conditions of an experiment; theoretical, due to simplification of the system or approximating the equations describing it.

Random errors are unpredictable errors caused by measurement fluctuations since no measurement can be made with infinite precision. Random errors will cause a series of measurements to be sometimes too large and other times too high. The effects of random errors on the physical quantity under investigation can often be determined since they can be quantified using statistical analysis, unlike systematic errors. These errors can be significantly reduced by averaging a sufficiently large number of data, since they behave in a fluctuating manner.

As a result, the Alpha-1 and Alpha-3 test benches induce both types of errors, systematic and random errors. Mal-orthogonality and misalignment of data acquisition system, formed from cameras and laser light source, with the test section can mutate the results. Manufacturing errors, assembly tolerances, crooked walls, laser refraction, external vibration, are all systematic error sources. Also, calibrating tolerances in calibration target and inaccurate positioning of the calibrating target are error sources.

2.4 Conclusion

Computational Fluid Dynamics is an excellent tool to quickly determining the performance of fluid dynamics devices and systems. But there is a very real possibility in

CFD of getting a solution that is completely wrong, even though the problem statement is correct. Understanding the role of CFD in the theoretical and numerical development process is critical. Also, validating with real world tests and experiments ensures that the final results meet expectations. Thus, the necessity of validating the turbulence model used in the study is evident for more reliable and solid results. But, CFD does not completely replace experiment, rather than the amount of experimentations and the overall cost can be significantly reduced. Table 2 submits a summary showing the differences between experiments and simulations [129].

Table 2 Differences between experiments and simulations [129].

Experiments	Simulations
Quantitative description of flow phenomena using measurements for: <ul style="list-style-type: none"> - One quantity at a time - Limited number of points and time - Laboratory scale model - Limited range of problems and operating conditions 	Quantitative prediction of flow phenomena using software for: <ul style="list-style-type: none"> - All desired quantities - High resolution in space and time - Actual flow domain - Virtually any problem and realistic operating conditions
Error sources: human, systematic and random errors.	Error sources: setup, modeling, discretization and iteration errors.
Equipment and personnel are difficult to transport	Software is portable, easy to use and modify.
<ul style="list-style-type: none"> - Expensive - Slow - Sequential - Single purpose 	<ul style="list-style-type: none"> - Cheap/cheaper - Fast/faster - Parallel - Multi-purpose

Chapitre 3

Analyse expérimentale par PIV stéréoscopique du développement de tourbillons longitudinaux à l'aval d'ailettes rectangulaires

Dans ce chapitre, une étude expérimentale est menée pour examiner les caractéristiques des tourbillons longitudinaux générés par des ailettes rectangulaires dans un écoulement turbulent établi en canal. Pour cela une rangée d'ailettes rectangulaires est disposée dans un canal à plaques planes parallèles. Un banc d'essais spécifiquement développé est utilisé et une chaîne de vélocimétrie par imagerie de particules stéréoscopique (S-PIV) permet de mesurer les trois composantes des champs de vitesse dans des plans bidimensionnels (PIV2D3C). L'analyse fine de l'écoulement est effectuée à un nombre de Reynolds $Re=4400$ (basé sur le diamètre hydraulique du canal).

Des mesures dans des plans horizontaux parallèles aux parois du canal sont effectuées afin d'analyser les caractéristiques globales de la vitesse moyenne et des fluctuations de l'énergie cinétique turbulente. La topologie et l'évolution des tourbillons longitudinaux générés en aval de la paire d'ailettes rectangulaires sont précisément quantifiées et présentées dans ce chapitre. Les résultats montrent par ailleurs la présence de tourbillons induits proches de l'axe médian ($y/H=0$) du canal. Concernant l'énergie cinétique turbulente, nous montrons que la composante longitudinale est supérieure aux composantes transversales et verticales, en particulier proche des winglets.

Experimental analysis by stereo-PIV of the development of streamwise vortices downstream of rectangular winglets

Mohammad Oneissi ^{a, b}, Elkhadim Bouhoubeiny ^a, Serge Russeil ^{a,*}, Daniel Bougeard ^a, Thierry Lemenand ^b, Charbel Habchi ^c

^a Mines Douai, EI, F59500 Douai, France

^b Angers University, ISTIA, LARIS EA 7315, Angers, France

^c Notre Dame University - Louaize, Mechanical Engineering Department, P.O. Box: 72 Zouk Mikael, Zouk Mosbeh, Lebanon

Abstract

Accurate experimental characterization of longitudinal vortices in channel flow induced by rectangular winglets is necessary to, validate, estimate and develop numerical models that can predict the impact of the flow structure on the heat transfer enhancement. For this aim, an experimental investigation is conducted to examine the characteristics of longitudinal vortices generated by rectangular winglets in fully developed turbulent channel flow. A row of rectangular winglet pairs is implemented in a parallel plate test bench channel. Stereoscopic Particle Image Velocimetry (SPIV) is used to harvest 3D instantaneous velocity fields in flow configuration of $Re=4400$ based on the channel's hydraulic diameter. Three-dimensional velocity components, velocity streamlines, topologies of Γ_2 function and normalized turbulent kinetic energy downstream the winglets are analyzed. It is shown that the flow properties are disturbed and a main vortex is generated in addition to induced vortices downstream the winglet

* Corresponding author.

Tel.: +33 3 27 71 23 88; fax: +33 3 27 71 29 15

Email address: serge.russeil@mines-douai.fr (S. Russeil)

pair. This study highlights the flow topologies and characteristics in horizontal streamwise planes and vertical cross-sections. Finally, this work provides an SPIV benchmark of the complex flow developing downstream rectangular winglet pair, where this configuration has been widely numerically studied

Keywords:

Rectangular winglet pair, longitudinal vortices, vortex generator, Stereoscopic Particle-Image Velocimetry (SPIV), plate-fin heat exchanger, parallel-plate channel

Nomenclature

H	Channel height, m	2D-PIV	2 Dimensional Particle Image Velocimetry
X	Longitudinal distance from VG trailing edge, m	3D-PIV	3 Dimensional Particle Image Velocimetry
Y	Transverse distance from channel mid-axis, m	3C-PIV	3 Components Particle Image Velocimetry
Z	Vertical distance from channel bottom wall, m	CCD	Charge-coupled device
Re	Reynolds number, dimensionless	CCW	Counter clock-wise
S	Domain	CFD	Computational Fluid Dynamics
M	Domain center	CW	Clock-wise
U	Mean flow velocity, m s^{-1}	DWP	Delta Winglet Pair
u_{rms}	Rms velocity component, m s^{-1}	KE_{tot}	Total turbulent kinetic energy, J
u	Flow longitudinal velocity component, m s^{-1}	KE_m	Mean kinetic energy, J
v	Flow transverse velocity component, m s^{-1}	LDA	Laser Doppler Anemometry
w	Flow vertical velocity component, m s^{-1}	LVG	Longitudinal Vortex Generator
$\bar{u}, \bar{v}, \bar{w}$	mean velocity components, m s^{-1}	Nd:YAG	Neodymium-doped Yttrium Aluminum Garnet
u', v', w'	Turbulent Fluctuations, m s^{-1}	PIV	Particle Image Velocimetry
\vec{u}_s	Velocity convection, m s^{-1}	rms	Root mean square
\vec{u}_m	Local velocity in a domain, m s^{-1}	RWP	Rectangular Winglet Pair
y^+	Dimensionless wall distance	SPIV	Stereoscopic Particle Image Velocimetry
U^+	Dimensionless Mean velocity profile with wall shear velocity	TKE	Turbulent kinetic energy
		TVG	Transverse Vortex Generator
Γ_1	Gamma-1 function	VG	Vortex Generator
Γ_2	Gamma-2 function		

1. Introduction

Plate-fin heat exchangers are widely used in various industrial fields such as heating, ventilating, and refrigeration system, automotive and aerospace industries, petrochemical industries, electronic components cooling and others [1, 2]. Since heat transfer coefficient for flow over a flat plate is relatively low due to the thick boundary layer, thinning the boundary layer is a must in order to achieve higher heat transfer coefficient in plate-fin heat exchangers. One technique used in plate-fin heat exchangers that strongly enhance the convective transport phenomena is transverse and longitudinal vortices which increase the velocity fluctuations and thinning the flow boundary layer leading to better heat transfer. Different types of vortices can be generated by either of the following methods:

- Flow separation behind vortex generators (VG), perturbators or turbulence promoters [3, 4],
- Surface curvature where the centrifugal force produces longitudinal vortices (Dean and Görtler instabilities) [5, 6],
- Laminar or turbulent jets (annular vortices) [7].

In this work, VG technique is used since it can be readily integrated into compact channels or plate-fin heat exchangers to improve the convective transfer between the high and low momentum fluids [8]. In addition to the vortices generated by VG, shear layers are formed on the front and rear edges of the generator [9], creating an energy transport that enhances the heat transfer locally and globally. High-velocity fluctuations caused by these shear layers, which can be characterized by the turbulent kinetic energy, may become unstable and lead to a self-sustained oscillatory flow [10].

Using VG, two enhancement methods can be distinguished: the active VG method [11] and the passive VG method [12]. Passive VG are more commonly used since they are

characterized by their efficiency, economy, manufacturing simplicity and maintenance ease, opposite to active VG which are energy consumers and less easy to implement. The passive VG have various types which include helical and twisted inserts [13], dimples or protrusions [14], cylindrical tubes [15], transverse vortex generators (TVG) [16], longitudinal vortex generators (LVG) [17, 18], plane or curved surface of VG [19, 20] or a combination of the above types [21]. Transverse vortices are two-dimensional flows with axes normal to the main flow direction, while longitudinal vortices rotate about an axis in the streamwise direction, implying a three-dimensional swirling motion. When pressure losses are taken into account, LVG are found to have an advantage over TVG in terms of global mixing and heat transfer performances [4].

VG winglet pairs exist in two configurations, one is the common flow down and the other is the common flow up. When the transverse distance between leading edges is less than that of trailing edges, the configuration is known as common flow down and vice-versa for common flow up [22]. Common flow up vortices create up-wash in between, and down-wash flow in the outside regions. Along the downstream direction, the magnitude of transverse velocity vectors decrease while the distance between vortex cores increases which leads to the thinning of the thermal boundary layer [22]. Tian et al. [23] studied both delta-winglet pair (DWP) and rectangular winglet pair (RWP) for common flow down and common flow up configurations and deduced that DWP in common flow down geometry is more efficient than other configurations.

A review on the surface heat transfer enhancement using longitudinal vortices is discussed by Jacobi and Shah [8], and concluded that the use of this type of vortices in heat exchanger applications shows promise. Lee et al [24] numerically investigated the heat transfer characteristics and turbulent structure in a three dimensional turbulent boundary layer with longitudinal vortices. They indicated that the disturbance of the boundary layer causes the best

heat transfer enhancement in the region where the flows were directed toward the walls while the vortex core was the region of relatively lower mixing. The performance of winglet type vortex generator in improving heat transfer was shown by Biswas et al [25]. It was found that a winglet pair has less pressure drop penalty than that of a single wing in addition to that winglet pairs could eliminate poor heat transfer zones.

When performing an experimental study, the flow characteristics are highly depending on the data extracted from the measurements. Many appliances have been used in channel flow experiments despite disparity in their accuracy. Also, accurate estimation of some parameters is fundamental for both laminar and turbulent flows. For example, precise prediction of the turbulence dissipation rate in turbulent flows is important in many industrial processes in order to analyze the micromixing process [26]. Previous studies, limited by single-point velocity measurement techniques, measures the single-point local dissipation rate, thus being limited to a local or mean estimation of the fluid structure characteristics over a narrow region. Techniques used can vary from the spatially aligned hot-wire probes [27] to laser Doppler anemometry (LDA) [28]. Such intrusive complex probes are generally unsuitable for complex flows and LDA technique has a limited studied regions. PIV may solve part of the problem, since PIV is not restricted over single-point measurements and 2D and even 3D velocity fields are simultaneously obtainable. Subsequently fully resolved 3-component velocity measurements are fundamental and SPIV takes the advantage over other techniques.

Many studies were conducted about the effect of rectangular winglet pairs in a channel. Most, if not even all, of these studies investigated the formation of longitudinal vortices by rectangular winglet pairs numerically. Thus, due to the high interest of such vortex generators by researchers, accurate experimental characterization in channel flow of longitudinal vortices induced by rectangular winglet pair is necessary to validate, estimate and develop numerical models that can predict the impact of flow structure on heat transfer enhancement. For this

intention, an experimental investigation is conducted to examine the characteristics of longitudinal vortices generated by a pair of rectangular winglets in common flow down configuration inside a developed channel flow. A row of rectangular winglet pairs is implemented in a parallel plate channel of height (H). Stereoscopic Particle Image Velocimetry (SPIV) is used to harvest 3D instantaneous velocity fields in flow configuration at $Re = 4400$. The methodology used for analyzing the flow characteristics downstream the VGs was divided into two parts: horizontal streamwise measurements over the length of the channel and vertical measurements in cross-sections at distinct locations. The test bench and stereoscopic PIV measurements are presented in Section 2. Analysis of flow characteristics in horizontal and vertical planes are discussed in Section 3, while Section 4 is devoted to the concluding remarks.

2. Experimental setup

2.1 Test bench

The experiments have been performed in the close-loop air channel test bench illustrated in Figure 1. Air is sucked from the seeding room towards the test channel in a closed loop circuit by means of a 2.3 kW centrifugal fan. The test section is 1200 mm in length, 500 mm in width and of height equal to 37.8 mm. To homogenize the flow upstream the test section, conditioning elements (honeycomb and convergent section) are used. The upper and lateral faces of the test section are made of transparent glass in order to allow particles illuminating and image acquisition. Downstream, a convergent bend element is used to direct the airflow towards a PVC pipe. The main objective of this element is to make the rear test section wall transparent for cross-sectional data acquisition. Pressure and temperature sensors are used to account for the air thermo-physical properties effects on the measured flow rate which is measured by means of a laminar flowmeter and located in the pipe system before the seeding room. Required

flow rate for the measurement is obtained by varying the rotational speed of the fan. In the seeding room, seeding particles are generated through a controlled combustion process of incense which produces about $1 \mu\text{m}$ mean diameter smoke particles [29] used as flow tracers.

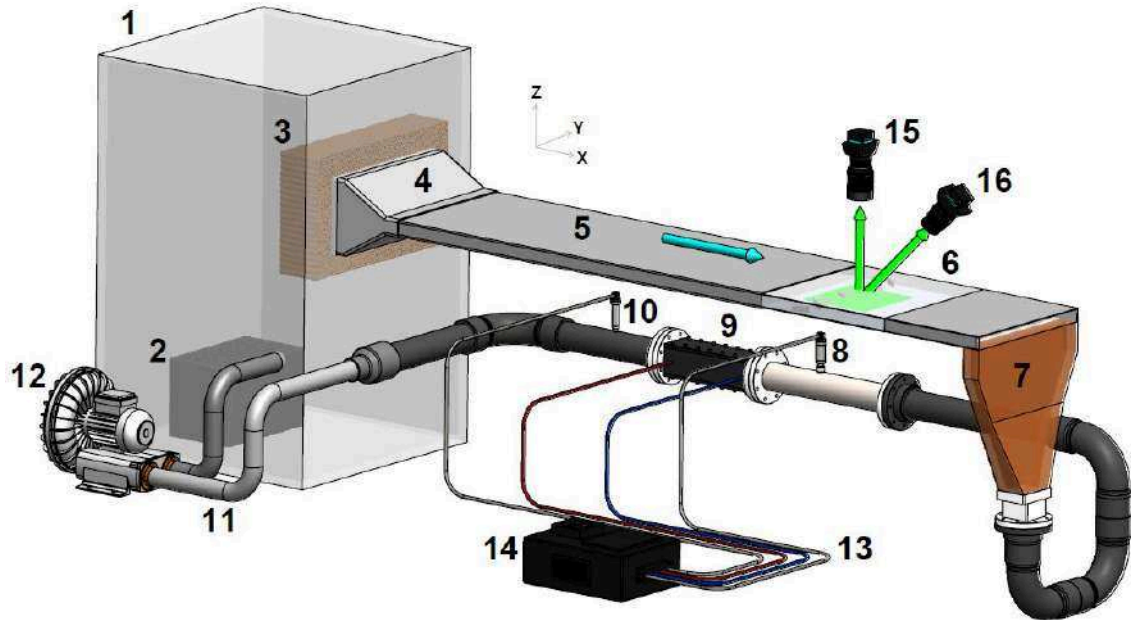


Figure 1 Experimental bench: (1) Seeding room; (2) Particles generator; (3) Honeycomb; (4) Convergent Section; (5) Upstream channel; (6) Test section (lateral and upper glazed windows); (7) Convergent 90° bend; (8) Absolute pressure transducer; (9) Laminar flowmeter; (10) Temperature probe; (11) PVC suction pipe; (12) Centrifugal fan; (13) Wirings and cables; (14) Micro-manometer; (15-16) Camera (position configuration for horizontal planes measurements)

A row of rectangular winglet pairs in common flow down configuration mounted on the bottom wall of the test section is used to generate longitudinal vortices in the test channel. The test section consists of four rectangular winglet pairs that produce four pairs of longitudinal vortices, see Figure 2. Only one pair of rectangular winglets at the middle of the test section is investigated in this study. Each rectangular winglet is $1.5H$ in length, $H/2$ in height and of thickness equal to 2 mm ($0.05H$). The winglets are installed normal to the channel bottom wall with an angle of attack of 30° from the incident flow and the distance between the leading edges

of each pair is 8 mm ($0.2H$). The upstream channel (Part-5 in Figure 1) is specifically designed to obtain a fully developed flow at the entrance of the test section. The RWP are manufactured by means of an Objet Alaris 30 Desktop 3D Printer using photopolymer jetting technology.

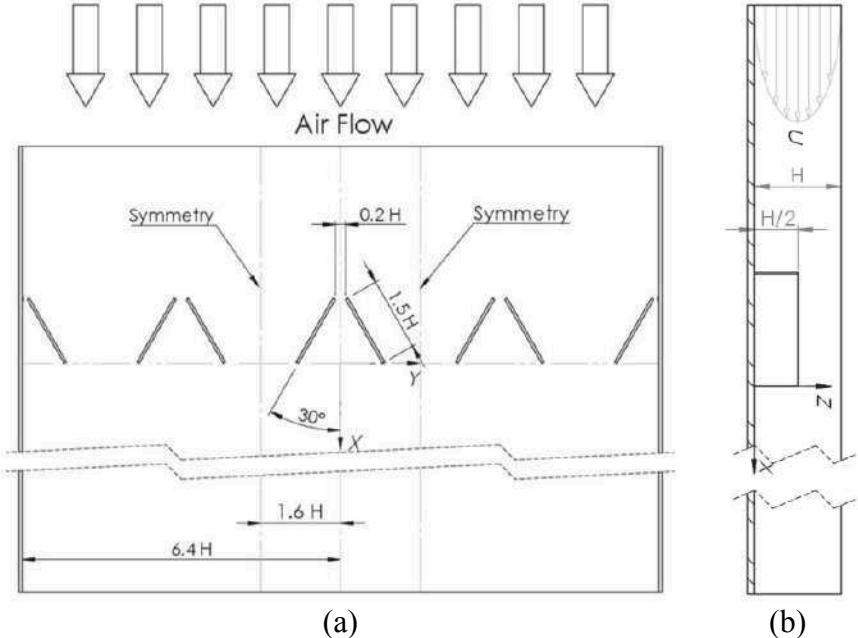


Figure 2 Geometrical characteristics of the rectangular winglet pairs test section (a) top view and (b) side view

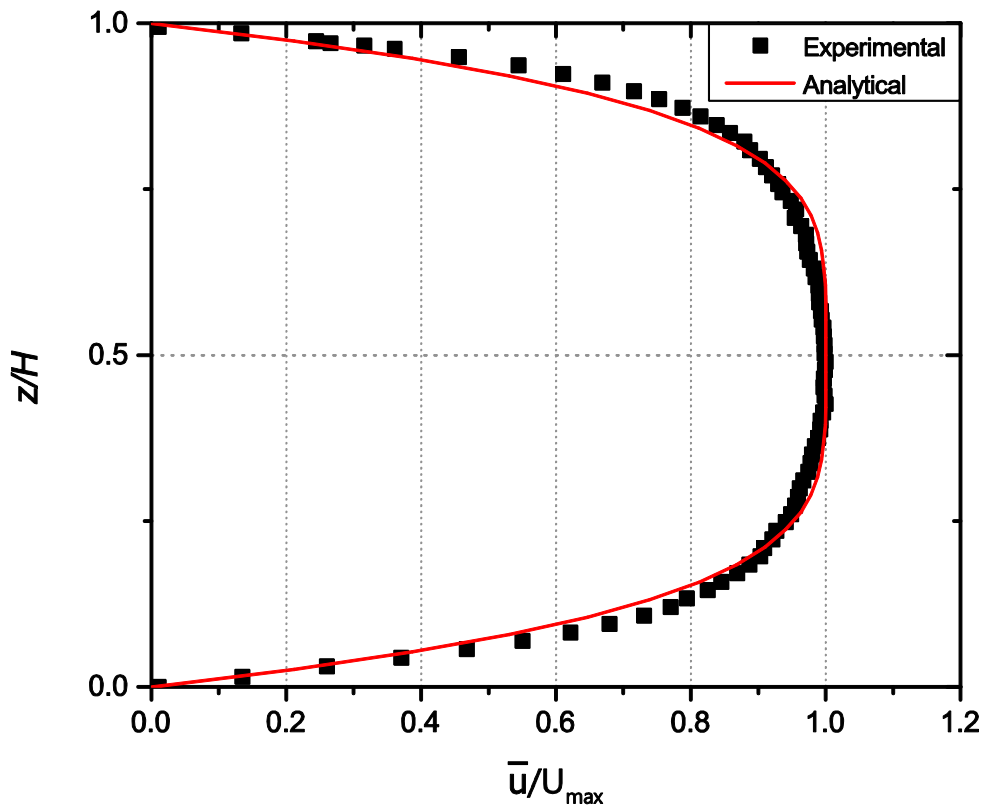
2.2 Inlet velocity profile measurement using LDA

LDA technique is used to determine the velocity profile at the test section inlet located at 120 mm upstream the trailing edge of winglet pairs. LDA is the technique of using the Doppler shift in a laser beam to measure the velocity in transparent or semi-transparent gaseous flows. Measuring with LDA is absolute, linear with velocity and requires no pre-calibration.

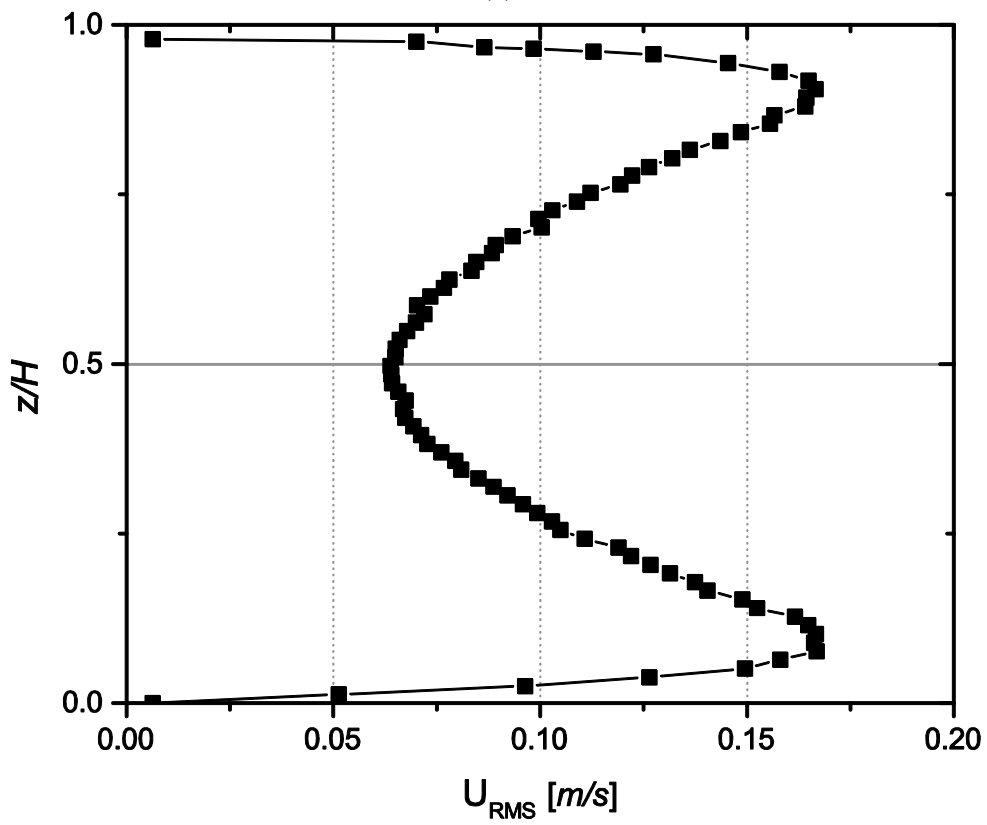
Measurements are made using a Dantec Dynamics© laser Doppler anemometry (LDA) system equipped with a 10 W argon-ion laser source and two BSA-enhanced signal-processing units (57N20 BSA and 57N35 BSA enhanced models); the measuring head is equipped with a 500 mm focal lens. The laser wavelength is 514.5 nm (green) and the shift frequency is 40 MHz (Bragg cell). The laser beam separation distance is 40 mm and its diameter before the lens is

3.8 mm; the beam intersection angle is 13.55° . The measurement volume of the LDA is positioned by a three-dimensional lightweight precision traversing system controlled via a PC. Precision of the measurement volume positioning system is $12.5 \mu\text{m}$. Measurement volume dimensions are $404 \mu\text{m}$ length, $48 \mu\text{m}$ width and height, and it contains 21 fringes spaced by $2.18 \mu\text{m}$. The data-acquisition rate is in the range 1–4 kHz.

Figure 3 represents the mean, root mean square (rms) and the non-dimensional velocity profiles for $\text{Re}=4400$. Mean velocity extracted from experimental results is compared with an analytical turbulent velocity profile between two parallel plates and shows a great agreement. The average error between experimental and analytical velocities is less than 2%. This analytical velocity profile is developed by Stigler [30] based on vorticity distribution between two parallel plates. Stigler velocity profile is better than the more usual power law velocity profiles which was derived only for flows in a pipe, since the derivative of the function does not tends to infinity at the boundaries, thus no infinite shear stress at the walls. In addition, it solves the Munson power law in which the derivative of the function at the middle of the channel does not tend to zero. Root mean square (rms) velocity profiles, also presented in Figure 3, are found to be symmetrical profiles, and highest values of velocity fluctuations are located in the vicinity of the test section upper and lower walls due to boundary layer turbulent flow.



(a)



(b)

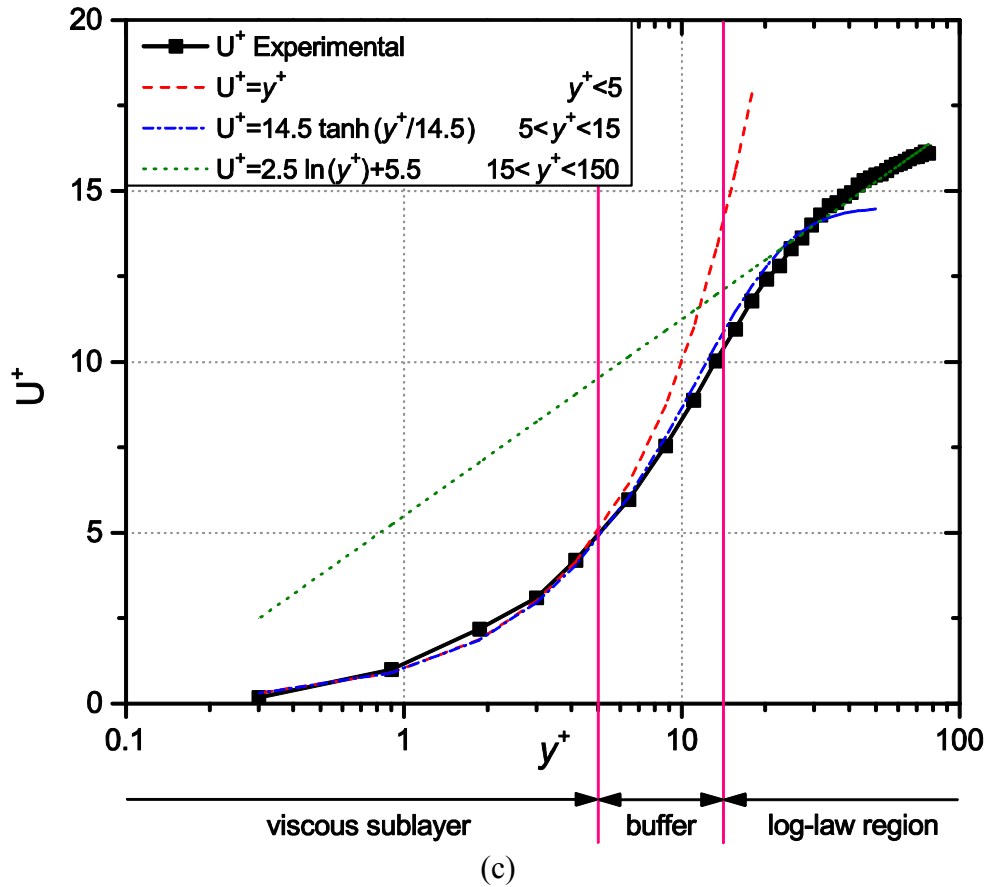


Figure 3 Velocity profiles at the test section inlet for $Re=4400$: (a) mean velocity from experimental data compared to analytical solution, (b) root mean square of experimental velocity (rms), (c) dimensionless mean velocity by lower wall shear velocity for experimental data compared to inner boundary layer laws.

Figure 3-c presents the mean U^+ velocity profile normalized by the wall-shear velocity as a solid line. Dotted lines represent the usual inner boundary layer laws of the wall at near wall regions in turbulent flow: the viscous sublayer where viscous shear dominates and can be modeled linearly and the overlap layer where viscous and inertial shears are important and can be modeled logarithmically. In this region, both experimental and the analytical results attain the same behavior showing that incoming flow is fully developed.

2.3 Stereoscopic PIV measurements

2D PIV is an imaging-based flow diagnostic technique that depends on seeding fluid flows with tiny tracer particles and observing the motion of these tracers to derive fluid velocity vectors. A sheet of laser light is used to illuminate the region of interest and the tracer particles scatter the light when they pass through. Stereoscopic PIV technique, which is also referred to as 2D3C-PIV, enables to measure the three-components of the flow velocity field. The fundamental principle behind SPIV is stereoscopic imaging of particles in a laser light illuminated plane in the flow. Two cameras view the same plane at different angles and capture particle displacement images that contain the influence of the third velocity component.

The SPIV system used in this work consists of a laser light source, two digital cameras and image-based processing software. The laser light is a double pulsed Neodymium-doped Yttrium Aluminum Garnet (Nd:YAG) laser with a wavelength of 532 nm. The pulse duration and energy level of the used laser is 10 ns and 120 mJ respectively at a frequency of 21 Hz. The cameras used are charge-coupled device (CCD) digital cameras with 4872×3248 pixels resolution and frequency of 4 Hz in single frame. Also, Scheimpflug systems are used to correct for the non-alignment of the objective camera axis (lens plane not parallel to the image plane), and sharpening the image [31]. Image processing and algorithms are calculated and managed by the DynamicStudio-4.2 software from DANTEC Dynamics.

In the present study, the three velocity field components are measured in two plane orientations:

- xy measurement planes, where the laser sheet is placed horizontally above the winglets row parallel to the bottom wall.
- yz measurement planes, where the laser sheet is placed vertically in cross-sections normal to the main flow direction at distinct locations.

2.3.1 Horizontal measurement planes

In the configuration of xy measurement planes, the laser is placed parallel to the channel walls, so that the laser light sheet is parallel to the main flow direction. The horizontal laser sheet is chosen to be located at $z/H = 0.6$ from the bottom wall (3 mm above the vortex generators). As shown in Figure 4 (left) the two cameras equipped with 60 mm Nikon lenses are placed above the test section to capture the flow velocity fields in the illuminated plane of interest. One camera is positioned perpendicular to the plane of interest while the second is tilted by 60° from the first to account for stereoscopic effect. As a result of this configuration, the 2D planar velocity components in the plane (u and v) are measured from the normal camera image. Using two cameras with the stereoscopic analysis, the three velocity components can be deduced.

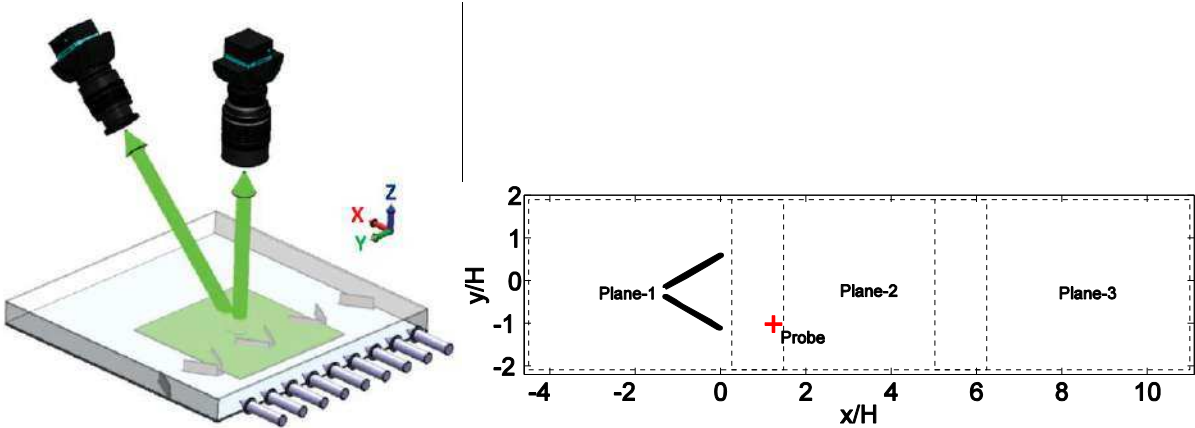


Figure 4 Horizontal measurement configuration (left) overlapped measurement planes (right)

Since the field of view of the camera system is limited, three xy successive measurement planes are needed to capture the velocity fields downstream the VG over the whole test section length. Overlapping planes are measured to ensure that there are no non-captured zones among the three planes as presented in Figure 4 (right). Each xy -plane covers an area of $23.4 \text{ cm} \times 15.6 \text{ cm}$ of the channel. Due to the movement of the camera system to capture each plane,

manufacturing tolerances, positioning uncertainties and other factors, a simple algorithm is used to correct for all these uncertainties.

In each measurement plane, 3000 images are captured with a sampling frequency of 2 Hz. Vector fields are calculated by means of an adaptive correlation algorithm using a multi-pass iteration procedure starting with an interrogation window of 128×128 pixels and decreased to 32×32 pixels. Every resulting instantaneous velocity field plane is meshed on $301 \times 201 = 60501$ elements with a spacing of 0.78 mm in both directions. A statistical analysis has to be performed to examine the convergence of mean and turbulent quantities according to the number of samples recorded in each measurement plane. For this aim, the variation of the measured mean and fluctuating velocity components are calculated in the VG's wake region at a given point named probe-2 shown in Figure 4 (right). Figure 5 represents the evolution of the mean velocity field components and their corresponding rms values at probe-2. It is observed that the relative scatter of velocity components values decreases with increasing the acquisition sample size. Such behavior was also reported by Uzol and Camci [32] who investigated the accuracy of ensemble averaged PIV data inside the wake region of a 2 row staggered array of circular cylinders using 2750 measurement samples. They demonstrated that the relative scatter was about 2% from the mean flow velocity when using 1000 samples out of the total of 2750 samples. Similarly Braza et al [33] performed 2D2C-PIV and 3 components-PIV (2D3C-PIV) measurements at low frequencies (4 Hz) as well as time resolved 2D2C-PIV at 1 kHz. They recorded 3000 and 2570 pairs of images for the 2D2C-PIV and 2D3C-PIV respectively in order to obtain converged turbulence statistics of the Reynolds averaged parameters. They showed that the variations of the mean flow and the correlation components were lower than 4%. In the present investigation, 3000 samples recorded in each plane are used to characterize the flow over the row of pair of rectangular winglets. If using 2500 samples, the variations of mean velocity components \bar{u} , \bar{v} and \bar{w} are found lower than 3%. This convergence criteria is found

to be in accordance with previously published results obtained by Uzol [32] and Braza et al [33].

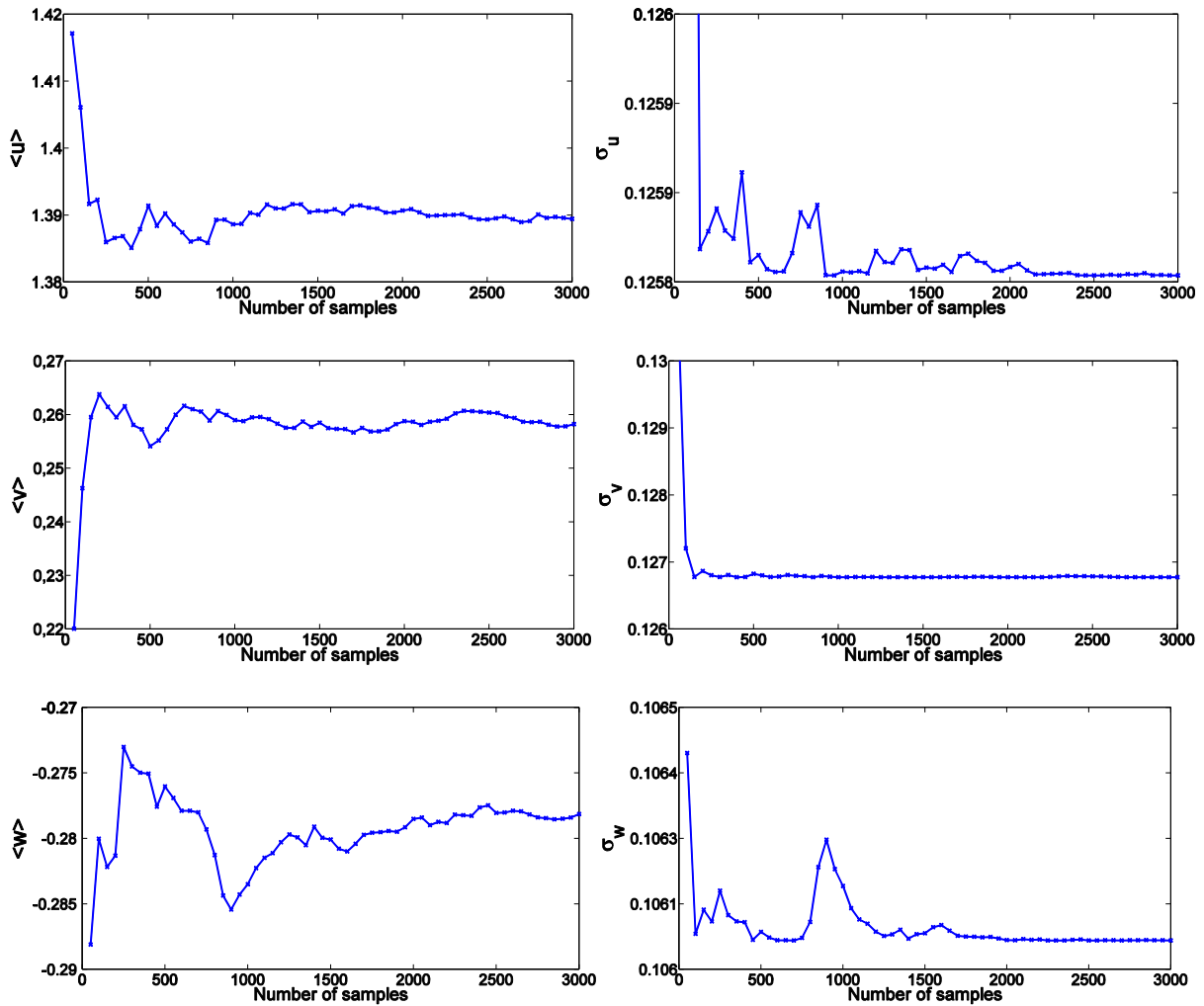


Figure 5 Statistical convergence graphs of the mean velocity components (left) and corresponding rms (right) at $Re=4400$

In order to further validate the present SPIV measurements, LDA measurements are also performed in the wake of the winglet pair. The longitudinal velocity profiles are determined at several locations downstream the vortex generator at $z/H = 0.6$ (which is the same height of the PIV xy measurement planes, i.e. 24 mm from bottom wall). A comparison between PIV and LDA measurements of longitudinal velocity profiles at a distance $X=H$ is presented in Figure 6. The mean velocity (\bar{u}) is normalized with the bulk mean flow velocity at $Re=4400$ (U) and

the rms values are normalized by its square (U^2). The results obtained from PIV and LDA longitudinal velocity measurements are found to be in an overall very good agreement. Higher differences of the values are noticed in some few local measuring points where extrema exist. Differences observed between PIV and LDA measurements are in acceptable ranges i.e. 3 % over most of the profile, the maximum local differences being less than 7% for the mean velocity and 9% for its corresponding rms.

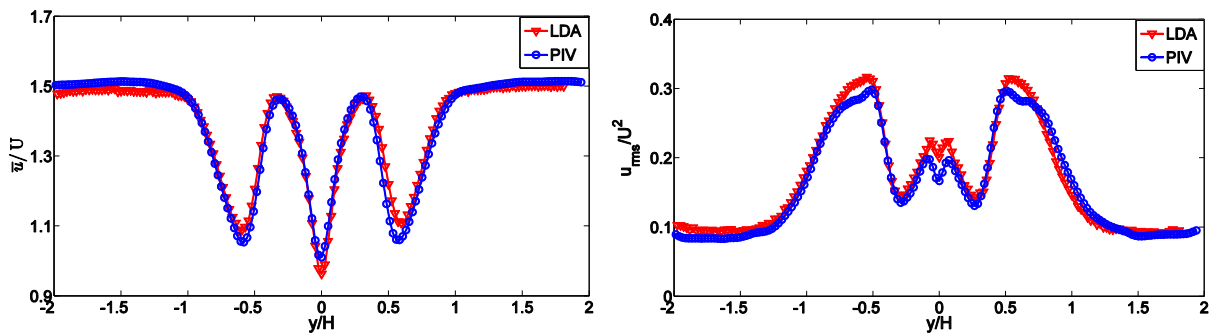


Figure 6 Mean velocity profiles (left) and their corresponding rms (right) comparison between PIV and LDA measurements for horizontal plane measurements at $Re=4400$

2.3.2 Vertical measurement planes

After measuring the velocity components in horizontal planes, vertical measurements at several cross sectional locations are conducted to examine the topology of the longitudinal vortices induced by the rectangular winglet pairs. To perform the vertical planes measurements, the laser sheet is directed transversally at each distance (X) as presented in Figure 7. Since the optical path is longer, zooming is needed for keeping good spatial resolution and thus the 60 mm lenses are now replaced by 135 mm Nikon lenses. Both cameras positions are rotated horizontally one being normal to the vertical laser sheet at the rear side of the channel test section and the second having a 45° tilt angle with the first. As a consequence of this setup, planar velocity components in the vertical plane (v and w) are measured while the normal component (u) is concluded from the second camera image. Using an adaptive correlation algorithm, the 3D velocity field components are obtained in several locations behind the winglet

pairs as demonstrated in Table 1. The final interrogation windows size used is 32×32 pixels with 50% of adjacent windows overlapping. In each PIV velocity field $230 \times 42 = 9660$ instantaneous velocity vectors are finally provided with a spatial resolution of 0.95 mm in both directions.

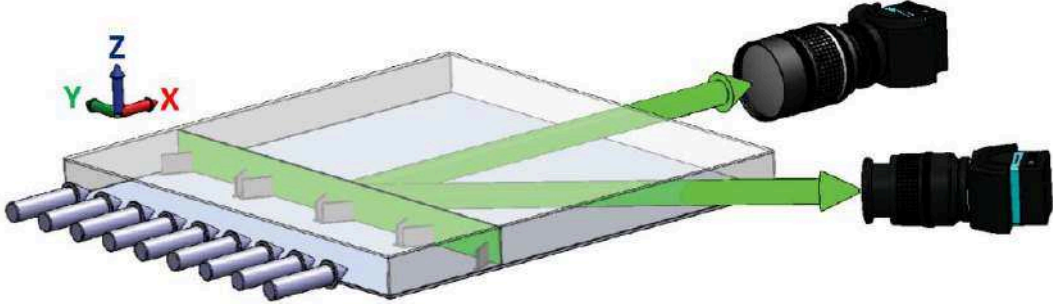


Figure 7 Vertical measurement configuration with the two cameras having 45° inclination angle.

Plane	X=0	X=H	X=3H	X=4H	X=5H	X=9H	X=10.5H
X (mm)	0	38	114	150	190	344	399
X = x/H	0	1.01	3.02	3.97	5.03	9.10	10.56

Table 1 Locations of the vertical laser sheet in yz-measurement vertical planes.

To examine the SPIV measurements and totally assess the quality of the stereoscopic process, a comparison between measured u velocity from horizontal plane (xy measurement in section 2.2.1) and deduced longitudinal velocity at a vertical measurement plane ($X=H$) is shown in Figure 8. Both mean longitudinal velocity and its corresponding rms show a good agreement between the measured and deduced values from two different experimental configurations. The mean difference for mean and rms longitudinal velocities is less than 6%.

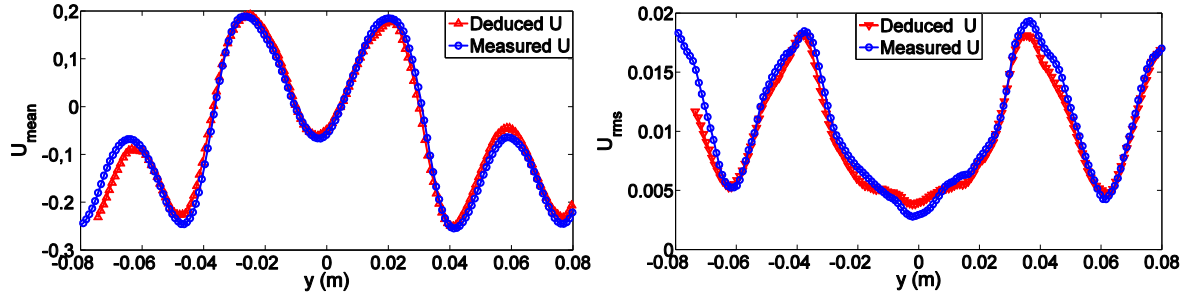


Figure 8 Comparison between measured (xy measurements) and deduced values on the vertical plane measurements (yz measurements) at $X=H$ and $Re=4400$, mean velocity profiles (left) and corresponding rms (right).

3. Results and discussion

Global characteristics of the mean velocity and turbulent kinetic energy fields in the horizontal plane (xy-measurement plane) are investigated first. Then, the topology and evolution of longitudinal vortices generated behind the rectangular winglet pair in vertical planes (yz-measurement plane) are examined.

3.1 Flow analysis in the horizontal plane

For horizontal plane, the mean and turbulent flow characteristics are investigated for Reynolds number $Re=4400$, in addition to the flow analysis. In order to investigate the flow topology in the horizontal plane xy ($z/H=0.6$ from bottom wall), the three mean velocity components \bar{u} , \bar{v} and \bar{w} are calculated by averaging 3000 instantaneous velocity fields as presented in section 2. Figure 9 shows the topologies of these velocity components. For the mean longitudinal velocity \bar{u} , the maximum values occur above the rectangular winglet pair and different areas of velocity variation are observed behind it. The main two areas of velocity deficit are associated to the evolution of longitudinal vortices in the wake region of each rectangular winglet, since in the vortex region the flow is dominated by transversal and normal

velocities and not the longitudinal velocity. We can also observe the same phenomenon near the symmetric axis after a distance $x/H=2$ corresponding to the development of the induced vortices, as presented in following paragraphs.

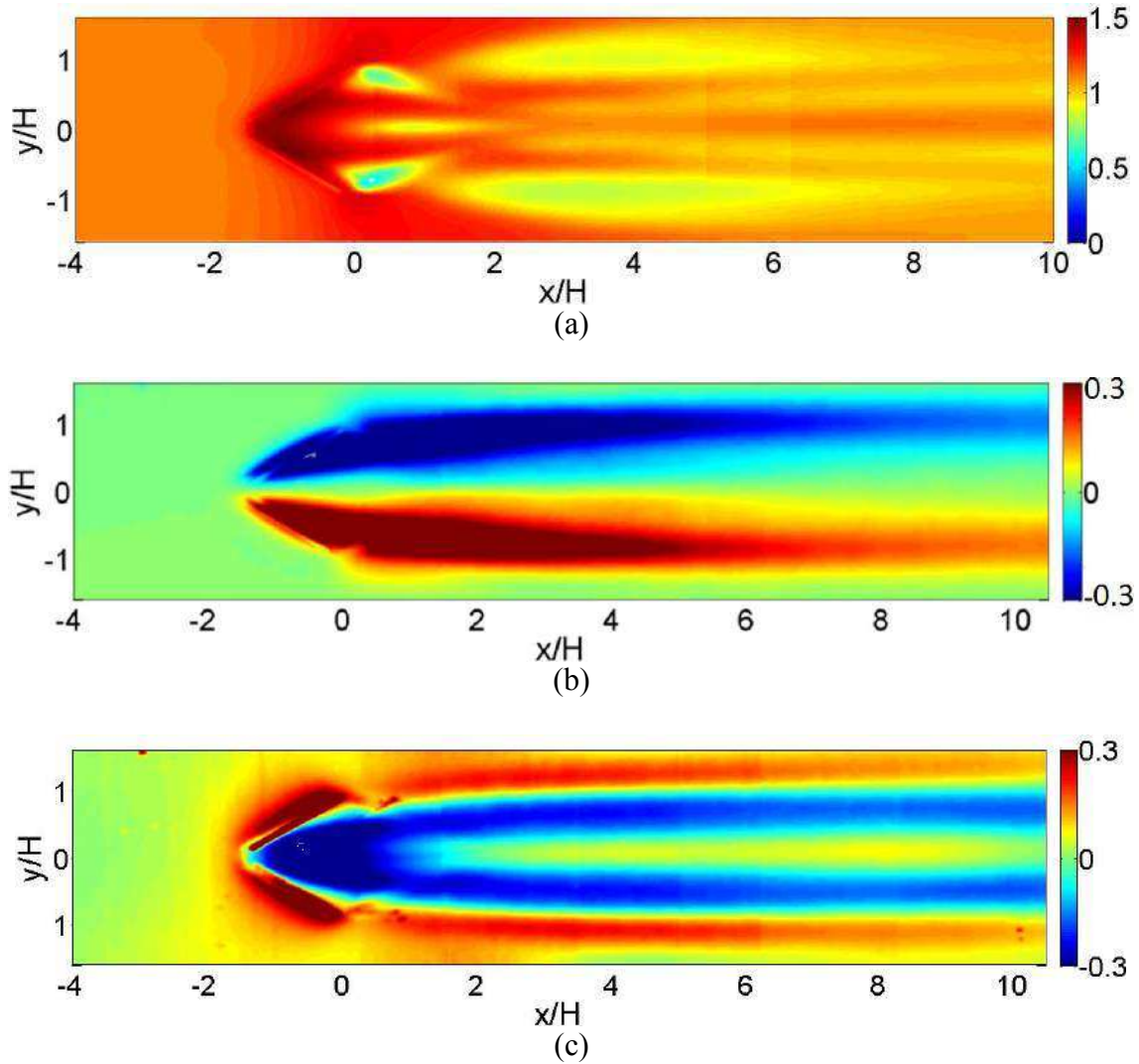


Figure 9 Mean flow velocity components on the horizontal plane for $Re = 4400$: (a) \bar{u} , (b) \bar{v} , (c) \bar{w} .

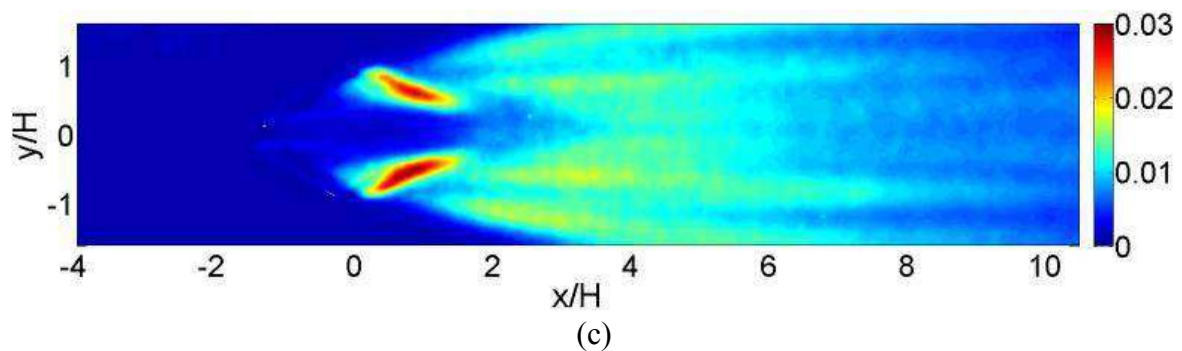
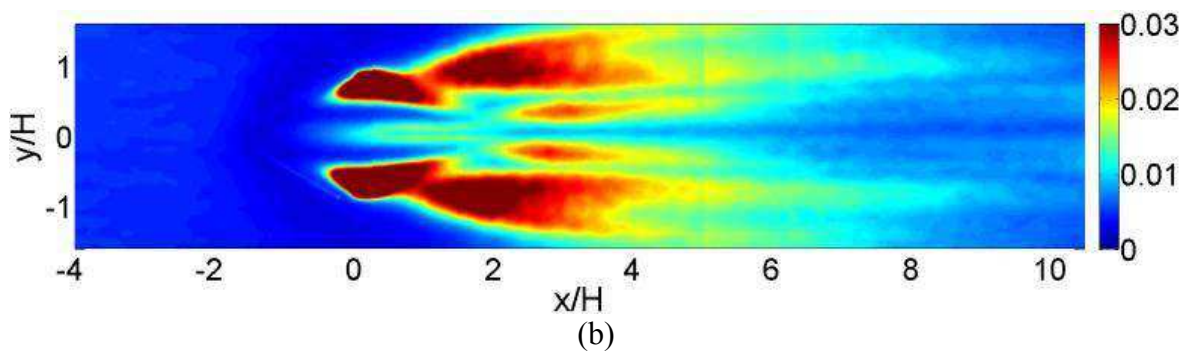
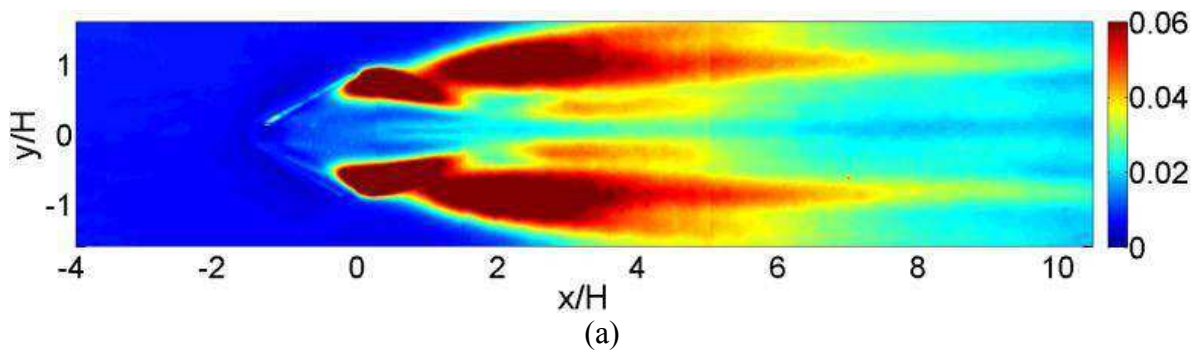
The distribution of the mean transverse velocity component \bar{v} is also symmetric, but the difference in contour colors is due to the opposite direction of each transverse velocity component in the wake region. It is shown in Figure 9 (b) that the largest region of transversal velocity component is directly behind the winglet pair due to flow separation. The vertical

component \bar{w} is compatible with the longitudinal component and leads to the same analysis. It can be seen that the flow is directed downward between the two winglets and then splits into two regions at $x/H=1$ separated by $y/H=0$ axis: each corresponds to the development of a main longitudinal vortex downstream a winglet. In each region, the up-wash flow is colored in red, the downwash effect is colored in blue and stagnation zone is colored in green. Thus, it's is clear that the longitudinal vortices generated downstream the rectangular winglet pair are a common down configuration vortices. Note that two stagnation zones can be observed in each region due to the main and induced vortices flows: the first one is developed at $x/H=0$ for the main vortex and the second developed at about $x/H=2$ for the induced vortex which shown to be rotating in opposite direction of the main vortex. Thus, for each region we can deduce that a main vortex is produced due to flow separation over the winglet in which it begins to develop after a distance $x/H=1$ from winglet trailing edge.

To investigate the turbulent characteristics of the flow, turbulent kinetic energy $\left[TKE = \frac{1}{2} (\overline{u'^2} + \overline{v'^2} + \overline{w'^2}) \right]$ and Reynolds stress tensor components $\frac{1}{2}\overline{u'^2}$, $\frac{1}{2}\overline{v'^2}$ and $\frac{1}{2}\overline{w'^2}$ are all computed from 3000 fluctuation velocity fields obtained in xy-measurement plane.

Figure 10 presents these turbulent quantities normalized with the square of mean flow velocity (U^2) at $Re=4400$. The distribution of the turbulent quantities are found clearly symmetric along the $y/H=0$ axis. Two high levels of the turbulent kinetic energy are observed in the near wake of each winglet corresponding to two peak values: a first peak is $TKE/U^2=0.095$ at location $x/H=0.6$ and the second is $TKE/U^2=0.073$ at $x/H=2$. Note that the color map scale for Figure 10 (a) is chosen with maximum value of 0.06 instead of 0.095 for higher graphic contrast resolution. Furthermore, energy dissipation is clearly observed downstream the winglet pair and the maximum level of turbulent energy decreases more than 20% after $x/H = 2$. The Reynolds components $\frac{1}{2}\overline{u'^2}$ and $\frac{1}{2}\overline{w'^2}$ behave in the same manner with

respect to global distribution characteristics of the turbulent kinetic energy. For the Reynolds transverse component $\frac{1}{2}\overline{w'^2}$, the maximum values are located behind the winglet at $x/H=0.6$. Also, the small fluctuating area near the middle axis $y/H=0$ of TKE and $\frac{1}{2}\overline{u'^2}$ is an evidence for the generation of the induced vortices shown in the following section. Longitudinal fluctuations component $\left(\frac{1}{2}\overline{u'^2}\right)$ in the wake region attributes 36.4% of the turbulent kinetic energy, while transversal $\left(\frac{1}{2}\overline{v'^2}\right)$ and vertical $\left(\frac{1}{2}\overline{w'^2}\right)$ components correspond to 30.6% and 33% respectively.



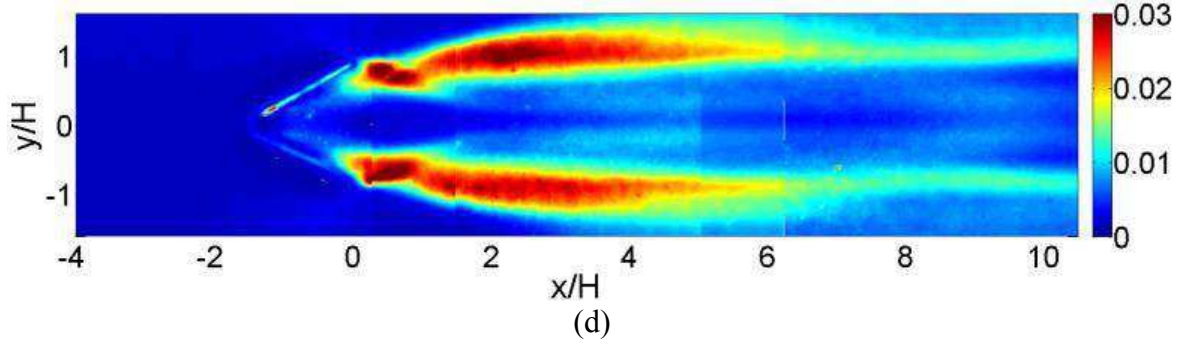


Figure 10 Topologies of the turbulent kinetic energy and the fluctuations of each component at $Re=4400$, (a) $TKE/U^2 = \frac{1}{2}(\overline{u'^2} + \overline{v'^2} + \overline{w'^2})$, (b) $\frac{1}{2}\overline{u'^2}/U^2$, (c) $\frac{1}{2}\overline{v'^2}/U^2$, (d) $\frac{1}{2}\overline{w'^2}/U^2$.

3.2 Flow analysis in the vertical planes

In this section, vertical flow configuration (yz -measurement planes) is analyzed allowing the examination of the characteristics of longitudinal vortices at several locations in the wake of the rectangular winglet pair. Figure 11 shows a detailed visualization of the 3D velocity fields at different measurement locations ($X= 0, H, 3H, 4H$ and $5H$), where the color map represent the normalized longitudinal velocity component (u) and the velocity vectors are the normalized planar components (v and w). The visualization of sections is restricted to $5H$ since velocity vectors and contours are not visually clear for further sections. Geometrical characteristics of longitudinal vortices created by winglet pair can clearly be seen. Main longitudinal vortex rotating direction at each vertical plane can be designated to be clock-wise for the left side vortex (upper side vortex in xy -horizontal plane) thus emphasizing previous examinations. Moreover, the main vortex effect on longitudinal velocity is obvious and low velocity regions are visible at the vortex cores and near the walls.

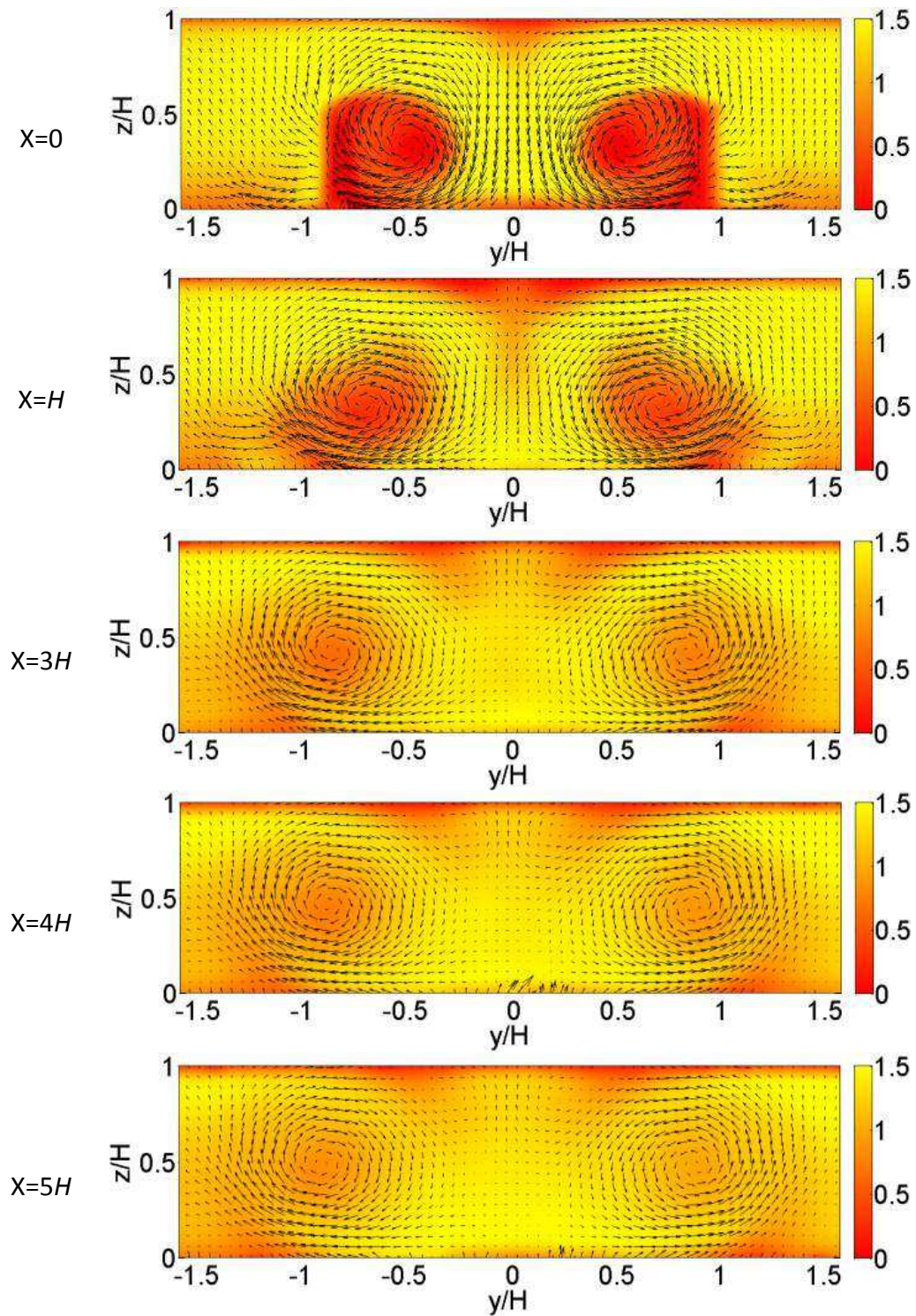
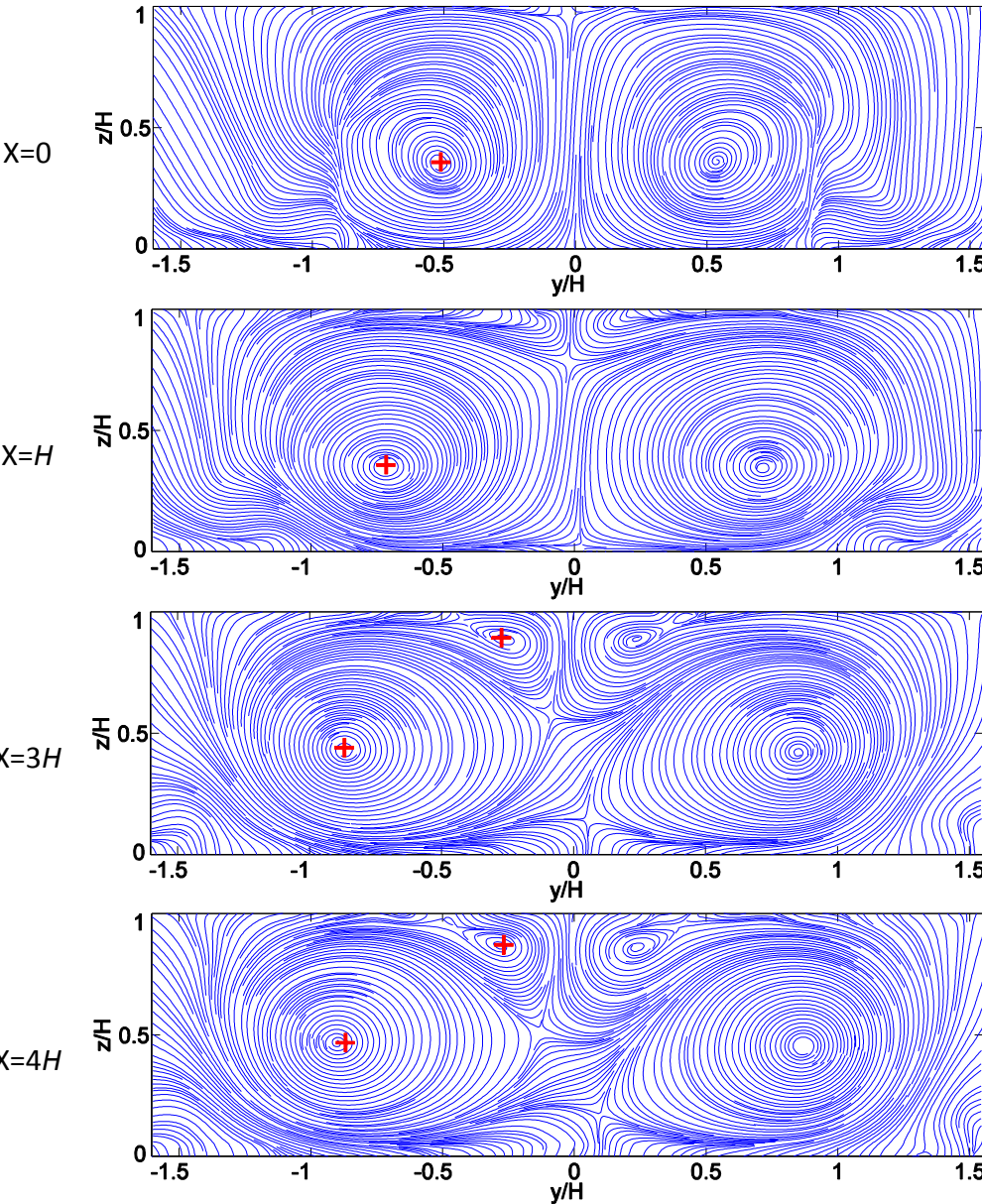


Figure 11 Normalized 3D components of the mean velocity fields downstream the winglet pair at $Re=4400$

In addition to the velocity fields, velocity streamlines with vortex core centers are presented in Figure 12. Main vortex is clearly visible and it can be seen that they are already

developed just after the VG ($X=0$). The main vortices remain more or less in the middle of the channel height but tend to move towards lateral walls. Two induced vortices are detected after $x/H=2$ (not presented here) near the upper wall near to $y/H=0$ axis. It can be deduced that the induced vortex is generated in a region between $X=H$ and $X=3H$ which supports previous inspections. In addition, each induced vortex rotates opposite to the associated main vortex due to the viscous forces applied by the main vortex inertial swirling flow. Further downstream topologies are not presented here since no valuable information can be extracted from it.



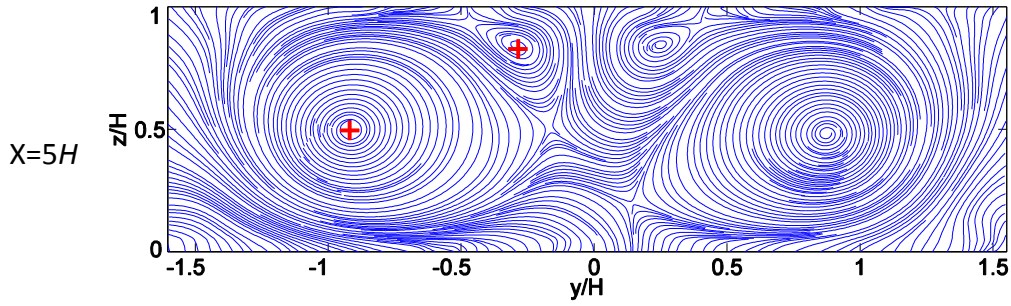


Figure 12 Mean velocity streamlines with vortex core centers downstream the winglet pair at $Re=4400$

To better examine the longitudinal velocity component, Figure 13 shows the mean velocity profiles in vertical planes through the vortex core. These profiles are characterized by a local minimum as crossing the vortex core. Since the vortex is growing with the channel length, the core of the main vortex is getting farther from the bottom wall, thus the vertical location of profile minimums reaches about the middle of the channel height at $X=4H$.

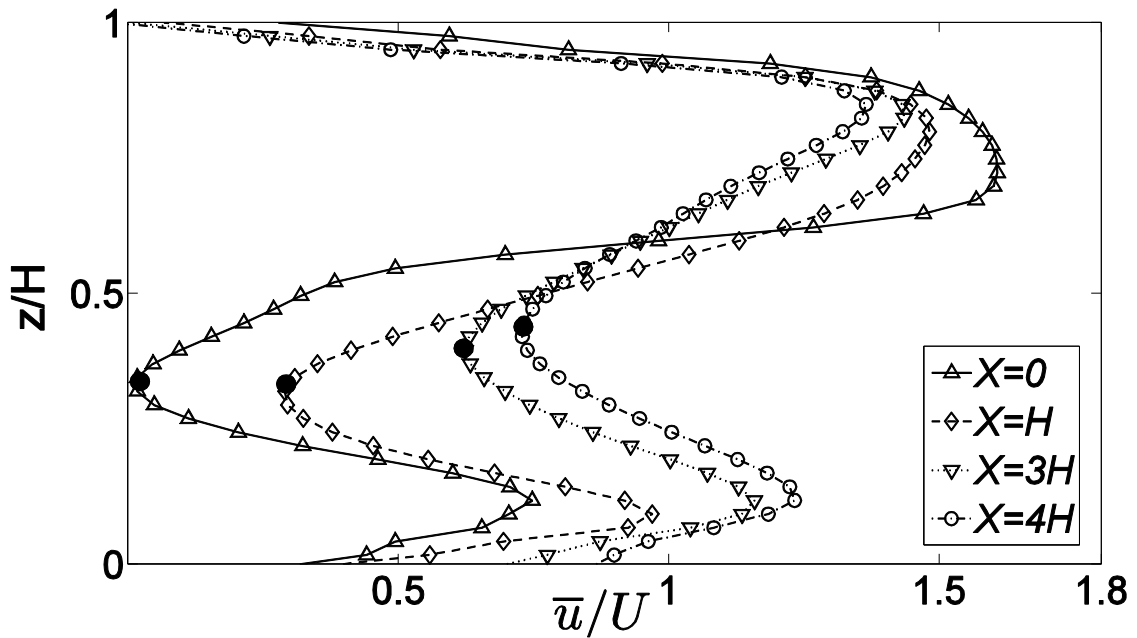


Figure 13 Normalized longitudinal velocity profiles at different planes for $Re=4400$

Streamlines are not considered a scientific tool for identifying vortices, thus a reliable tool that allows the core identification of vortices is a must. When dealing with vortex cores identification, the main drawback of Depardon et al. [34] approach is that scalar functions like Γ_1 (initially defined by Graftieaux et al. [35]) are not Galilean invariant: Γ_1 fails to identify the location of the center of a vortex that is convected with high velocity, whereas it is correctly identified in a reference frame moving with the convection velocity [36]. Thus, Favelier et al. [37] proposed a modified definition of Γ_1 named Γ_2 defined as Galilean invariant allowing extracting the rotational structure. The Γ_2 function, is defined at any location inside the flow domain by:

$$\Gamma_2(\mathbf{P}) = \frac{1}{S} \int_{M \in S} \frac{\overrightarrow{PM} \wedge (\overrightarrow{u_m} - \overrightarrow{u_s})}{\|\overrightarrow{PM}\| \cdot \|\overrightarrow{u} - \overrightarrow{u_m}\|} dS \quad (1)$$

where S is a domain with center M , $\overrightarrow{u_s} = \int_S U dS$ denotes the velocity convection and the relative velocity $\overrightarrow{u_m} - \overrightarrow{u_s}$ in a reference frame moving with the local velocity $\overrightarrow{u_m}$.

With this definition, it is clear that Γ_2 is Galilean invariant, dimensionless and ranging between -1 and 1. For two-dimensional incompressible flows, the inner core of a vortex is defined by the condition $|\Gamma_2| \geq 2/\pi$ and the maximum value is located at the center of the vortex. It is a top-hat function reaching its maximum value at the center of a vortex, and with large gradients at the boundary of the vortex [36].

In this study, Γ_2 criterion is employed in order to identify and track the main and induced vortices in the flow behind the winglet pair. The topologies of the Γ_2 function at different locations for Reynolds number $Re=4400$ are given in Figure 14. Main vortices are clearly visible associated with two induced vortices at the top ; which they sustain till $x/H=10$; and even others near bottom walls downstream each winglet which are not seen before using Γ_2 criterion.

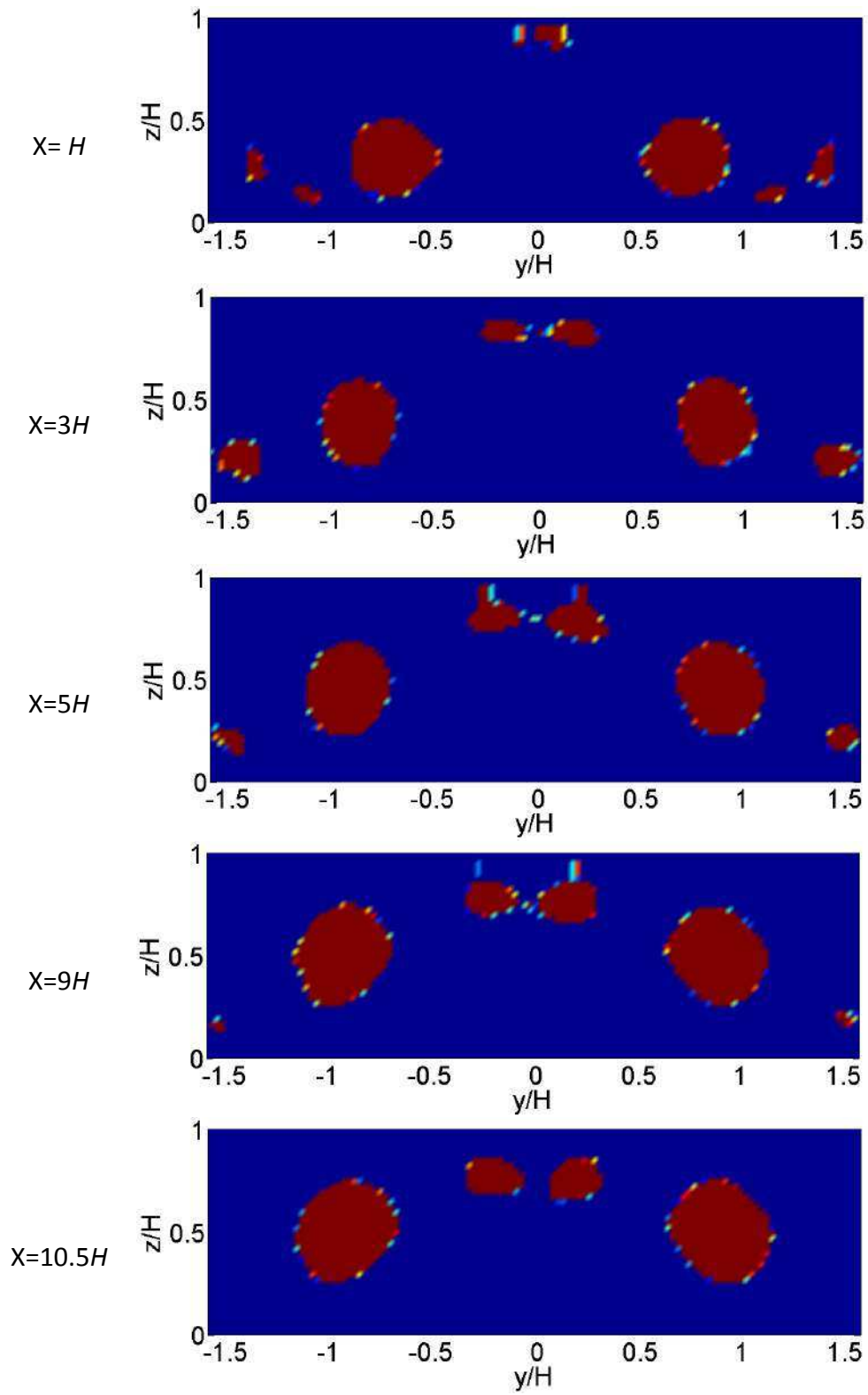


Figure 14 Topologies of Γ_2 function used for vortex identification downstream the winglet pair at $Re=4400$

In order to quantify the spatial evolution of the main and induced vortices behind the winglets, vortices cores are determined using the maximum values of Γ_2 function. Table 2 presents the planar coordinates of the main (named 1) and induced (named 2) vortices cores at each cross-section investigated downstream the VGs. The results clearly show that the main vortices moves away from the bottom wall. Note that, the Z_1 evolution of the main vortex core in vertical direction shows that the main vortex is moving towards the upper wall, while Y_1 shows that the main vortices are repelling from each other. Moreover, induced vortices are shown to be departing from the channel middle vertical axis in the horizontal direction Y while moving away from the top wall.

	X=0	X=H	X=3H	X=4H	X=5H	X=9H	X=10.5H
Y_1	-0.512	-0.716	-0.869	-0.894	-0.920	-0.920	-0.920
Z_1	0.370	0.370	0.445	0.470	0.496	0.546	0.546
Y_2	–	–	-0.273	-0.268	-0.287	-0.291	-0.306
Z_2	–	–	0.862	0.841	0.802	0.737	0.718

Table 2 Planer coordinates of the vortices centers at $Re=4400$ normalized by channel height H .

In addition to previous demonstration, turbulent kinetic energy $TKE = \frac{1}{2}(\overline{u'^2} + \overline{v'^2} + \overline{w'^2})$ is calculated using the fluctuating velocity fields deduced from the Reynolds decomposition. Figure 15 displays the normalized turbulent kinetic energy (by U^2) downstream the winglet pair at the locations $X=0, H$ and $3H$. In particular, it is observed that the highest turbulent kinetic energy zone is located in the wake region behind the winglet pairs due to the fluctuating swirl flow. These turbulent kinetic energy zones are located in the longitudinal

vortices flow region where high flow fluctuation exists. High values of kinetic energy decrease downstream the VG due to main and induced vortices dissipation.

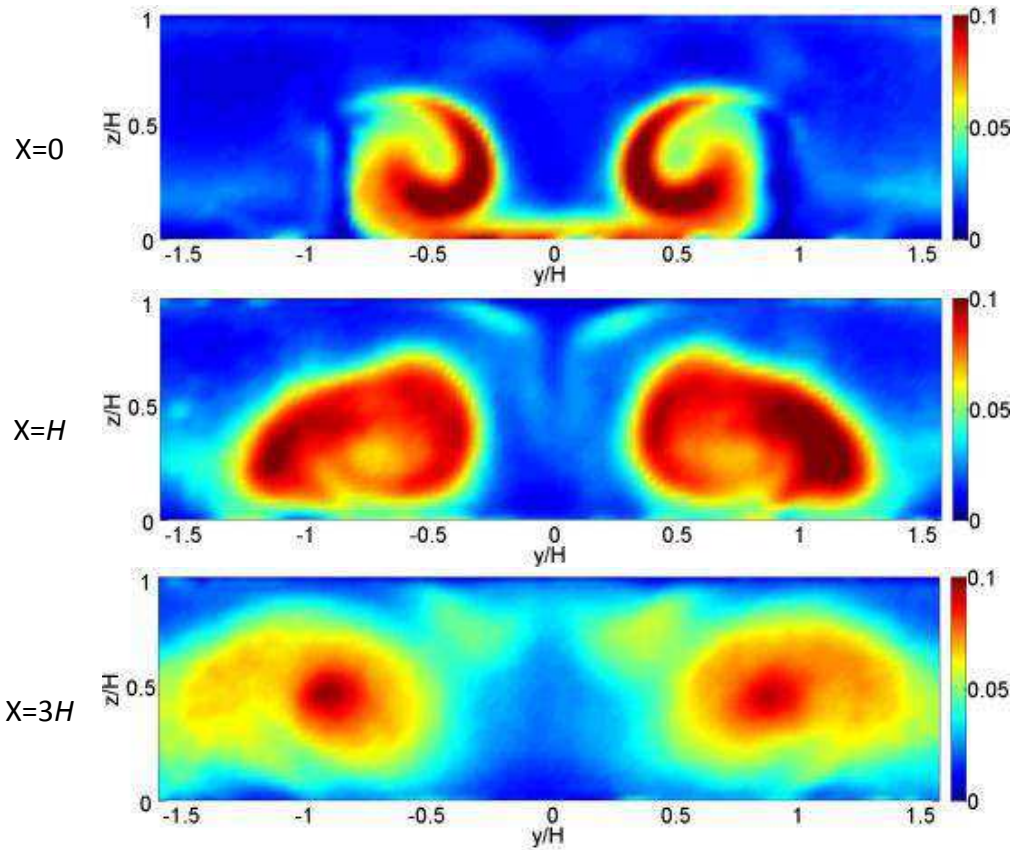


Figure 15 Normalized turbulent kinetic energy downstream the winglet pair at $Re=4400$

Also, integral turbulent kinetic energy is determined to examine the global impact of longitudinal vortices behind rectangular winglet pairs by integrating the TKE over the cross sectional area. It is important to study the global influence of VG and impact on heat transfer. Figure 16 gives the evolution of turbulent kinetic energy in successive cross-sections: TKE increases from 0.038 at $x/H=0$ to reach a maximum value of 0.055 at $x/H=3$, then to decrease to 0.035 at $x/H=11$. The increasing behavior of the TKE curve is caused by the increasing turbulence due to the vortex generator. When flow reaches the VG the flow separation is weak and thus the turbulent energy is low. After flow separation due to VG, the interaction of the

vortices causes the increase in turbulent energy until reaching its maximum value at $x/H=3$. Then, a decrease of the TKE is observed till reaching a value of 0.035 at $x/H=10.5$ due to the viscous dissipation of the vortices. Thus, such investigation may help the designer of heat exchanger to place tandem VGs downstream the first one in a position where the TKE decreases to a specific value. This placement of VG promotes the increase of TKE and thus enhancing heat transfer process.

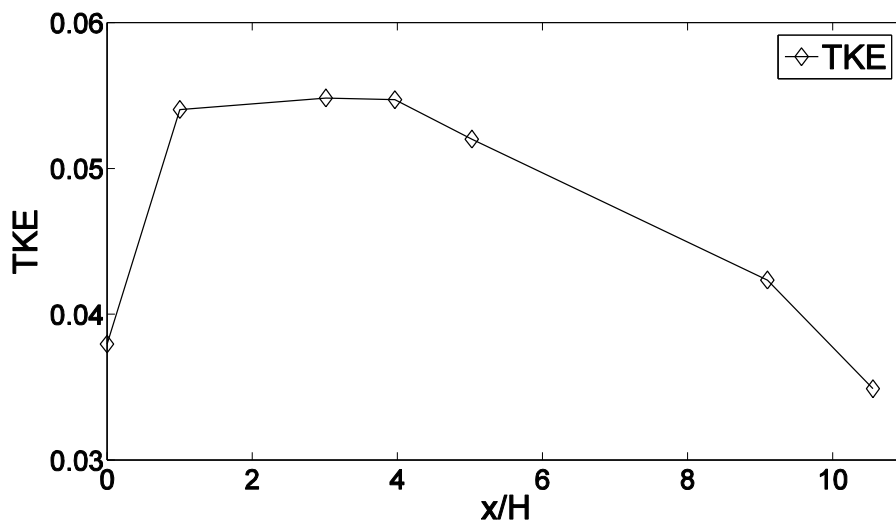


Figure 16 Evolution of the integral kinetic energy behind the winglet pair for $Re=4400$.

4. Conclusion

In this study, the characteristics of longitudinal vortices generated by rectangular winglet pairs in parallel plate fully-developed channel flow are experimentally investigated for Reynolds number $Re=4400$. The three components of velocity fields are obtained experimentally using Stereoscopic Particle-Image Velocimetry (SPIV) system. Horizontal streamwise planes measurements allow to analyze the global characteristics of mean velocity and turbulent kinetic energy fluctuations. Topology and evolution of longitudinal vortices generated downstream the rectangular winglet pair are quantified. Also, the fluctuating zones near the middle axis $y/H=0$ are an evidence for the formation of induced vortices in the channel.

It is also demonstrated that a domination of the longitudinal component over transverse and vertical components in the turbulent kinetic energy, particularly near the winglets. In addition, measurements in vertical cross-sections enabled the characteristic examination of longitudinal vortices at several locations downstream in the wake region. The evolution of longitudinal and induced vortices are presented for $Re=4400$. Normalized velocity components, velocity streamlines, topologies of Γ_2 function and normalized turbulent kinetic energy downstream the winglet pair are examined. Highest turbulent kinetic energy zone is identified in the wake region downstream the winglet pairs due to the fluctuating swirl flow and the interaction between vortices. These values of kinetic energy decrease downstream the channel due to main and induced vortices viscous dissipation.

Thus this work is very promising as the 3D velocity and fluctuating components are extracted experimentally and helps to clearly understand the generated vortices topologies. As well these results may be used to compare with numerical solutions in order to validate CFD models.

Future works may focus on the influence of Reynolds number on the development of longitudinal vortices. As main result, it should be explained that knowing the longitudinal evolution caused by longitudinal vortex generators helps researchers to design optimal enhancing devices because downstream zones of influence have been characterized. Also, link with heat transfer enhancement (wall interaction/core flow) should be discussed, in addition to mixing properties in core flow.

Acknowledgements

This work was partially funded by the ANR CarnotMINES “C.I.E.T.”. Authors would like to acknowledge Chrystèle Qaegeber-Evrard for her implication in the experimental work.

References

- [1] A. Ghanem, T. Lemenand, D. Della Valle and H. Peerhossaini, "Static mixers: Mechanisms, applications, and characterization methods - A review," *Chemical Engineering Research and Design*, vol. 92, no. 2, pp. 205-228, 2014.
- [2] J. Lin, "Review of research on low-profile vortex generators to control boundary-layer separation," *Progress in Aerospace Sciences*, vol. 38, pp. 389-420, 2002.
- [3] D. Dong and H. Meng, "Flow past a trapezoidal tab," *Journal of Fluid Mechanics*, vol. 510, pp. 219-242, 2004.
- [4] M. Fiebig, "Embedded vortices in internal flow: heat transfer and pressure loss enhancement," *International Journal of Heat and Fluid Flow*, vol. 16, pp. 376-388, 1995.
- [5] A. Ajakh, M. Kestoras, R. Toé and H. Peerhossaini, "Influence of forced perturbations in the stagnation region on Görtler instability," *The American Institute of Aeronautics and Astronautics Journal*, vol. 37, pp. 1572-1577, 1999.
- [6] C. Habchi, T. Lemenand, D. Della Valle and H. Peerhossaini, "Liquid/liquid dispersion in a chaotic advection flow," *International Journal of Multiphase Flow*, vol. 35, pp. 485-497, 2009.
- [7] W. Gretta and C. Smith, "The flow structure and statistics of a passive mixing tab," *Transactions of the ASME, Journal of Fluids Engineering*, vol. 115, pp. 255-263, 1993.
- [8] A. Jacobi and R. Shah, "Heat transfer surface enhancement through the use of longitudinal vortices: a review of recent progress," *Experimental Thermal and Fluid Science*, vol. 11, pp. 295-309, 1995.

- [9] J. Jones, "The calculation of paths of vortices from a system of vortex generators, and a comparison with experiment," Aeronautical Research Council, England, 1957.
- [10] A. Ghanem, C. Habchi, T. Lemenand, D. Della Valle and H. Peerhossaini, "Energy efficiency in process industry - High-efficiency vortex (HEV) multifunctional heat exchanger," *Renewable Energy*, vol. 56, pp. 96-104, 2013.
- [11] R. V. Westphal and R. D. Mehta, "Interaction of an oscillating vortex with a turbulent boundary layer," *Experiments in Fluids*, vol. 7, no. 6, pp. 405-411, 1989.
- [12] R. Webb and N. Kim, *Principles of Enhanced Heat Transfer*, New York: Wiley, 1994.
- [13] S. W. Chang, A. W. Lees and H.-T. Chang, "Influence of spiky twisted tape insert on thermal fluid performances of tubular air–water bubbly flow," *International Journal of Thermal Sciences*, vol. 48, pp. 2341-2354, 2009.
- [14] C. Habchi, S. Russeil, D. Bougeard, J. L. Harion, T. Lemenand, D. Della Valle and H. Peerhossaini, "Enhancing Heat Transfer in Vortex Generator-type Multifunctional Heat Exchangers," *Applied Thermal Engineering*, vol. 38, pp. 14-25, 2012.
- [15] S. Vintrou, D. Bougeard, S. Russeil, R. Nacereddine and J.-L. Harion, "Quantitative infrared investigation of local heat transfer in a circular finned tube heat exchanger assembly," *International Journal of Heat and Fluid Flow*, vol. 104, pp. 197-207, 2013.
- [16] C. Habchi, T. Lemenand, D. Della Valle and H. Peerhossaini, "Turbulence behavior of artificially generated vorticity," *Journal of Turbulence*, vol. 11, no. 36, pp. 1-28, 2010.
- [17] K. Kwak, K. Torii and K. Nishino, "Heat transfer and flow characteristics of fin-tube bundles with and without winglet-type vortex generators," *Experiments in Fluids*, vol. 33, no. 5, pp. 696-702, 2002.

- [18] C. Habchi, J. L. Harion, S. Russeil, D. Bougeard, F. Hachem and A. Elmarakbi, "Chaotic Mixing by Longitudinal Vorticity," *Chemical Engineering Science*, vol. 104, pp. 439-450, 2013.
- [19] R. Kamboj, P. S. Dhingra and P. G. Singh, "CFD Simulation of Heat Transfer Enhancement by Plain and Curved Winglet Type Vortex Generators with Punched Holes," *International Journal of Engineering Research and General Science*, vol. 2, no. 4, 2014.
- [20] G. Zhou and Z. Feng, "Experimental investigations of heat transfer enhancement by plane and curved winglet type vortex generators with punched holes," *International Journal of Thermal Sciences*, vol. 78, pp. 26-35, April 2014.
- [21] U. O. Ünal and M. Atlar, "An experimental investigation into the effect of vortex generators on the near-wake flow of a circular cylinder," *Experiments in Fluids*, vol. 48, no. 6, pp. 1059-1079, 2010.
- [22] M. Fiebig, "Vortex Generators for Compact Heat Exchangers," *Journal of Enhanced Heat Transfer*, Vols. 2(1-2), pp. 43-61, 1995.
- [23] L. Tian, Y. He and Y. Lei, "Numerical Study of Fluid Flow and Heat Transfer in a Flat Plate Channel with Longitudinal Vortex Generators by Applying Field Synergy Principle Analysis," *International Communications in Heat and Mass Transfer*, vol. 36, no. 2, pp. 111-120, 2009.
- [24] S. Lee, H. Ryou and Y. Choi, "Heat transfer in a three dimensional turbulent boundary layer with longitudinal vortices," *Journal of Heat Transfer*, vol. 124, pp. 1521-1534, 1999.

- [25] G. Biswas, K. Torii, D. Fujii and K. Nishino, "Numerical and experimental determination of flow structure and heat transfer effects of longitudinal vortices in a channel," *International Journal of Heat and Mass Transfer*, vol. 39, no. 16, pp. 3441-3451, 1996.
- [26] J. Sheng, H. Meng and R. Fox, "A large eddy PIV method for turbulence dissipation rate estimation," *Chemical Engineering Science*, vol. 55, pp. 4423-4434, 2000.
- [27] Y. Andreopoulos and A. Honkan, "Measurement in Science and Technology," *Experimental techniques for highly resolved measurements of rotation, strain, and dissipation rate tensors in turbulent flows*, vol. 7, pp. 1462-1476, 1996.
- [28] H. Hussein and R. Martinuzzi, "Energy balance for turbulence flow around a surface mounted cube placed in a channel," *Physics of Fluids*, vol. 56, pp. 764-780, 1995.
- [29] B. Wang, S. Lee and K. Ho, "Chemical composition of fine particles from incense burning in a large environmental chamber," *Atmospheric Environment*, vol. 40, pp. 7858-7868, 2006.
- [30] J. Štigler, "Introduction of the analytical turbulent velocity profile between two parallel plates," in 148, Svratka, Czech Republic, 2012.
- [31] A. K. Prasad and K. Jensen, "Scheimpflug stereocamera for particle image velocimetry in liquid flows," *Applied Optics*, vol. 34, no. 30, pp. 7092-7099, 1995.
- [32] O. Uzol and C. Camci, "The effect of sample size, turbulence intensity and the velocity field on the experimental accuracy of ensemble averaged PIV measurements," in 4th International Symposium on Particle Image Velocimetry, Göttingen, Germany, 2001.
- [33] M. Braza, R. Perrin and Y. Hoarau, "Turbulence properties in the cylinder wake at high reynolds numbers," *Journal of Fluids and Structures*, vol. 22, pp. 757-771, 2006.

- [34] S. Depardon, J. Lasserre, L. Brizzi and J. Boree, "Instantaneous skin-friction pattern analysis using automated critical point detection on near-wall PIV data," *Measurement Science and Technology*, vol. 17, no. 7, pp. 1659-1669, 2006.
- [35] L. Graftieaux, M. Michard and N. Grosjean, "Combining PIV, POD and vortex identification algorithms for the study of unsteady turbulent swirling flows," *Measurement Science and Technology*, vol. 12, pp. 1422-1429, 2001.
- [36] A. Berson, M. Michard and P. Blanc-Benon, "Vortex identification and tracking in unsteady flows," *Comptes Rendus Mecanique*, vol. 337, pp. 61-67, 2009.
- [37] T. Favelier, M. Michard and N. Grosjean, "Développement d'un critère d'identification de structures tourbillonnaires adapté aux mesures de vitesse par PIV," in *Proc. 9ème Congrès Francophone de Vélocimétrie Laser*, Bruxelles, 2004.

Chapitre 4

Étude comparative de simulations numériques et mesures expérimentales de générateurs de vorticit   à paires d'ailettes rectangulaires

Dans ce chapitre, une comparaison est effectu  e entre des simulations num  riques et une   tude exp  rimentale de la structure de l'  coulement de tourbillons longitudinaux g  n  r  s par des paires d'ailettes rectangulaires dans un canal    plaques planes    $Re=4400$. Les m  mes dimensions que le banc exp  rimental et les m  mes conditions aux limites sont simul  es avec ANSYS Fluent 15.0. Deux mod  les de turbulence sont mis en   uvre dans cette   tude : les mod  les (SST) « shear-stress transport » $k - \omega$ et (RNG) « re-normalisation group » $k - \epsilon$.

Les r  sultats du profil de vitesse obtenus    partir des simulations sont compar  s localement avec les r  sultats exp  rimentaux pr  c  dents obtenus par techniques LDA et PIV. La simulation obtenue avec le mod  le de turbulence SST $k - \omega$ montre une bonne concordance avec les donn  es exp  rimentales, alors que le mod  le de turbulence RNG $k - \epsilon$ ne pr  sente aucune correspondance. Les   valuations globales des topologies sont ensuite effectu  es pour validation suppl  mentaire des mod  les. Les topologies des composantes de vitesse horizontale ainsi que la topologie d'  nergie cin  tique turbulente    un plan horizontal pr  d  fini sont inspect  es. Le mod  le de turbulence SST $k - \omega$ montre une excellente correspondance avec les r  sultats exp  rimentaux : les deux topologies (obtenues exp  rimentalement et num  riquement) sont quasiment identiques. D'autre part, le mod  le de turbulence RNG $k - \epsilon$ ne montre aucune coh  rence avec les r  sultats exp  rimentaux. En plus

des comparaisons de topologies horizontales, des comparaisons verticales sont également effectuées pour un examen plus approfondi des simulations des caractéristiques de tourbillons longitudinaux dans la région de sillage. Les topologies de la fonction Γ_2 sont utilisées pour identifier et suivre les tourbillons principaux et induits dans l'écoulement en aval de la paire d'ailettes. Le modèle de turbulence SST $k - \omega$ prédit et identifie avec précision l'emplacement des vortex générés, le nombre de tourbillons générés (principaux et induits) ainsi que leur position relative. Le modèle de turbulence RNG $\kappa - \epsilon$ ne peut prédire que la génération des tourbillons principaux, mais il ne parvient pas à prédire les tourbillons induits.

Le but de cette étude est de valider quel modèle de turbulence prédit correctement la structure d'écoulement des tourbillons longitudinaux dans un canal à plaques planes.

Nous montrons que le modèle de turbulence SST $k - \omega$ affiche une supériorité sur le modèle RNG $k - \epsilon$ dans la prédiction des caractéristiques des structures d'écoulement de tourbillons longitudinaux dans un canal à plaques planes. De plus, le modèle SST $k - \omega$ est capable de capturer les tourbillons induits. Ainsi, le modèle de turbulence SST $k - \omega$ excelle dans la prévision de telles structures d'écoulement et par conséquent est préférable dans la modélisation des tourbillons longitudinaux dans les écoulements turbulents.

Comparison between numerical simulation and experimental study of rectangular-winglet pair vortex generator

Mohammad Oneissi^{a, b}, Charbel Habchi^c, Serge Russeil^{a, *}, Daniel Bougeard^a, Thierry Lemenand^b

^a Mines Douai, EI, F59500 Douai, France

^b Angers University, ISTIA, LARIS EA 7315, Angers, France

^cNotre Dame University - Louaize, Mech. Eng. Dep., P.O. Box: 72 Zouk Mikael, Zouk Mosbeh, Lebanon

Abstract

Vortex generators (VG) are widely used in heat exchangers for augmenting the heat transfer from fin plates to the working fluid. Therefore, understanding the development of longitudinal vortices in turbulent channel flows has a high importance for many research applications. When using numerical simulations, the choice of an appropriate turbulence model that can better predict the flow structure downstream a VG is fundamental. In the present study, three-dimensional numerical simulations, with two different commonly-used turbulence models, are performed for channel flow containing rectangular-winglet pairs (RWP) and compared to experimental data. The shear-stress transport (SST) κ - ω model and the re-normalization-group (RNG) κ - ε model are used for modeling turbulence. Validation is conducted by comparing the flow structure topologies obtained from numerical simulations with previously investigated experiments.

* Corresponding author.

Tel.: +33 3 27 71 23 88; fax: +33 3 27 71 29 15

Email address: serge.russeil@mines-douai.fr (S. Russeil)

Such study highlights the importance of properly choosing a suitable turbulence model that can predict realistic flow structure for longitudinal vortices. Finally it is found that the SST κ - ω shows superiority over the RNG κ - ε turbulence model in predicting flow structure characteristics of longitudinal vortices.

Keywords:

Rectangular winglet pair; vortex generator; longitudinal vortices; turbulence model; stereoscopic particle image velocimetry.

Nomenclature

B	Channel width, m
D_h	Hydraulic diameter, m
Re	Reynolds number
H	Channel height, m
L	Channel length, m
X	Streamwise distance, m
Y	Spanwise distance, m
Z	Normal distance from bottom wall, m
U	Mean flow velocity, m s^{-1}
u	Flow velocity in x direction, m s^{-1}
v	Flow velocity in y direction, m s^{-1}
w	Flow velocity in z direction, m s^{-1}

Abbreviations

CFD	Computational Fluid Dynamics
LDA	Laser Doppler Anemometer
LVG	Longitudinal Vortex Generator
PIV	Particle Image Velocimetry
RWP	Rectangular Winglet Pair
RNG	Re-normalization Group
SST	Shear-Stress Transport
TKE	Turbulent Kinetic Energy
TVG	Transverse Vortex Generator
VG	Vortex Generator

Greek letters

μ	Dynamic viscosity, Pa s
ν	Kinematic viscosity, $\text{m}^2 \text{s}^{-1}$
ρ	Fluid density, kg m^{-3}
Γ_2	Gamma-2 function
κ	Turbulence kinetic energy
ε	Dissipation rate
ω	Specific dissipation rate
Σ	modulus of the mean strain rate tensor, s^{-1}

Introduction

Heat exchangers are involved in tremendous industrial applications all over the world. Enhancing the performance of heat exchange process has been a substantial field for researches over decades where many active, passive and compound techniques arose. Passive technique, and especially vortex generators, was highlighted in the domain of enhanced heat exchangers and took its place in plenty of research studies. This importance is due to many reasons such as efficiency, industry, economy and maintenance supremacy of passive methods, vortex generators (VG) are widely used in this field. Longitudinal vortex generators (LVG) are found to have an advantage over transverse vortex generators (TVG) in terms of global mixing and heat transfer performances [1], and rectangular-winglet pair involved such vortex generators.

In order to investigate the flow structure of these vortex generators, three types of scientific activities exist: experiments, analyses and simulations. Experiments in fluid mechanics are considered a very important part of investigating flow structure characteristics. They can supplement theoretical studies, modelling of flow field and numerical simulations. Computational fluid dynamics (CFD) simulation is widely used in fluid dynamics research topics involving heat transfer with use of numerical methods and algorithms to solve fluid flow problems. Since experimental methods are very expensive, time consuming and involve too much labor, simulation study becomes popular. Many reasons drive researchers to perform CFD numerical simulations. CFD simulations are flexible; since adjusting computerized model is much easier, cheaper, faster and simpler than real prototype one. CFD simulations can provide profound analysis; because one can analyze special and physically unreachable zones, in addition to visualizing streamlines, velocity and pressure contours and many others. CFD is

precise; it is considered a multitask robust tool for modeling fluid flows due to the refined enhancement of numerical techniques for modeling.

Thus, depending on experimental investigation in thermal hydraulic studies may last many years and with the progress of computer technology combined to the improvement of advanced numerical models, many thermo-fluid researchers found their way in the track of numerical simulations. Fiebig et al. [2] perform numerically studied delta wings and delta-winglet pairs (DWP) in developing laminar flow between two parallel plates. Vortex generators angle of attack was varied from 10° to 50° for $500 < Re < 2000$. They deduced that the circular shaped vortex over a plate is distorted to an elliptical cross sectional shape due to the interaction of the vortices with the wall. In addition, this interaction produced vortex spreading for the common flow down configuration which in turns widened the thin boundary layer region between the two vortices. Delta-winglet pair seemed to have a better global performance for heat transfer enhancement over delta wing.

Wu and Tao [3, 4] studied numerically the convection heat transfer in rectangular channel with a pair of rectangular-winglet vortex generators at Reynolds numbers between 800 and 3000. They observed that the thickness of the rectangular-winglet vortex generator can decrease the heat transfer enhancement in the near region of the VG and has a little influence on friction. Also, they remarked that the pressure drop increases rapidly with the increase of the angle of attack. In addition, they deduced that the longitudinal vortices enable to enhance the global heat transfer of the channel, whereas transversal vortices can only enhance the local heat transfer of the channel. Delta-winglet pair showed a better heat transfer performance than rectangular-winglet pair (RWP) and is more efficient for the same VG area.

Many numerical simulations to study and analyze the thermal hydraulic performance of vortex generators in enhanced heat exchangers have been performed. Various turbulence models were used to model transverse and longitudinal vortices in turbulent flows. Two of the

commonly used turbulence models are the re-normalization-group (RNG) κ - ε model and the shear-stress transport (SST) κ - ω model. These two models have been widely used in considerable studies concerning this research topic [5, 6, 7, 8, 9, 10, 11].

In simulating turbulent flows, the selection of appropriate turbulence model plays a massive role in the prediction of the hydraulic performance and thus convective heat transfer. For this reason, and since the most commonly used models for modeling turbulent flow separation by vortex generators are the RNG κ - ε and SST κ - ω models, this paper focuses on comparing these two models prediction topologies with an experimental study done by Oneissi et al. [12] to validate turbulence models.

Oneissi et al. [12] investigated longitudinal vortices formed by rectangular-winglet pairs in parallel plate turbulent channel flow to examine the flow structure characteristics. A row of rectangular winglet pairs was implemented in a parallel plate test bench channel. Stereoscopic Particle Image Velocimetry (SPIV) was used to harvest three dimensional (3D) instantaneous velocity fields in flow configuration of $Re=4400$ based on the channel's hydraulic diameter. Normalized 3D components, velocity streamlines, topologies of Γ_2 function and normalized turbulent kinetic energy downstream the winglets at the same Reynolds number were also examined. For detailed information regarding the experimental setup, settings and analysis, refer to Oneissi et al. [12].

The goal behind this study is to validate commonly used turbulence numerical models that can predict the impact of the vortex generators on the flow structure characteristics. The numerical method, computational domain and mesh sensitivity analysis are presented in Section 2. Comparison of flow topologies in horizontal and vertical planes between experimental and CFD simulations are presented in Section 3. Section 4 is devoted to the concluding remarks.

1. Problem description

1.1 Numerical model

Three-dimensional (3D) numerical simulations of the flow and heat transfer in a parallel plate channel with new vortex generators is carried out for laminar and turbulent regimes. The following assumptions are used for the numerical simulations:

- Three-dimensional fluid flow and heat transfer are steady.
- Flow is incompressible
- Fluid properties are constant.
- Radiation heat transfer, body forces and viscous dissipation are neglected.

Based on the above assumptions, the channel flow is governed by the 3D steady-state Reynolds-averaged Navier-Stokes (RANS) equations. The continuity and momentum equations for an incompressible Newtonian fluid are:

$$\frac{\partial u_i}{\partial x_i} = 0 \quad (1)$$

$$u_j \frac{\partial u_i}{\partial x_j} = -\frac{1}{\rho} \frac{\partial p}{\partial x_i} + \nu \frac{\partial^2 u_i}{\partial x_j \partial x_j} - \frac{\partial \overline{u'_i u'_j}}{\partial x_j} \quad (2)$$

where the term $-u'_i u'_j$ is the Reynolds stress tensor resulting from the averaging procedure on the nonlinear convective terms in the momentum equations. The heat transfer is computed by solving the energy equation:

$$\frac{\partial}{\partial x_i} [u_i (\rho E + p)] = \frac{\partial}{\partial x_i} (\lambda_{eff} \frac{\partial T}{\partial x_i}) \quad (3)$$

where E is the total energy and λ_{eff} the effective thermal conductivity.

All computations are performed using ANSYS Fluent 15 code based on an Eulerian approach to solve the Cauchy equations through cell-centered finite volume discretization [10]. Mass and momentum conservation equations are solved by the code in addition to the energy equation for flows involving heat transfer [13]. Turbulence models allow the calculation of the

mean flow without first calculating the full time-dependent flow field. Turbulence model must have wide applicability, accuracy, simplicity and time frugality.

The re-normalization-group (RNG) κ - ε model was developed by Yakhot et al. [14, 15] using re-normalization group (RNG) method to renormalize the Navier-Stokes equations in order to capture the effects of small scale motion in a turbulent flow. In standard κ - ε model, the turbulent diffusion is accounted only at a specific scale, since eddy viscosity is resolved from a single length scale. This trend is not realistic since all scales of motion will contribute to the turbulent diffusion. The modified κ - ε model solves this problem and involves different scales of motion to the production term. The RNG κ - ε model shows fundamental improvements over the standard κ - ε model and enhances the final solution [16], where the effects of turbulence of strong streamline curvature, vortices and swirl effect are taken in account [17]. The equations for the turbulence kinetic energy κ and its dissipation rate ε are:

$$\rho \frac{\partial}{\partial x_i} (\kappa u_i) = \frac{\partial}{\partial x_j} \left(\sigma_k \mu_{eff} \frac{\partial \kappa}{\partial x_j} \right) + \rho C_\mu \frac{k^2}{\varepsilon} \Sigma^2 - \rho \varepsilon \quad (4)$$

$$\rho \frac{\partial}{\partial x_i} (\varepsilon u_i) = \frac{\partial}{\partial x_j} \left(\sigma_\varepsilon \mu_{eff} \frac{\partial \varepsilon}{\partial x_j} \right) - \rho C_{1\varepsilon} C_\mu \Sigma^2 - \rho C_{2\varepsilon} \frac{\varepsilon^2}{k} - R_\varepsilon \quad (5)$$

where $C_\mu=0.0845$, $C_{1\varepsilon}=1.42$, $C_{2\varepsilon}=1.68$, σ_k and σ_ε are the turbulent Prandtl number for κ and ε respectively, and μ_{eff} is the effective viscosity. The additional term R_ε is given by [18]:

$$R_\varepsilon = \frac{\rho C_\mu \gamma^3 \left(1 - \frac{\gamma}{4.38} \right) \varepsilon^2}{1 + 0.012 \gamma^3} \frac{1}{k} \quad (6)$$

with $\gamma = k\Sigma/\varepsilon$ and Σ is the modulus of the mean strain rate tensor.

Shear-stress transport (SST) κ - ω model developed by Menter [19] is also used in this study for turbulent flows. This model solves two additional partial differential equations, a modified version of the turbulence kinetic energy equation κ used in κ - ε model and a transport one for the specific dissipation ω . Also, the shear-stress transport combines the use of κ - ω

formulation in the inner parts of the boundary layer and the switching to a κ - ε behavior in the free-stream thus avoiding the κ - ω sensitivity to the inlet free-stream turbulence properties. In addition, it is characterized by its good behavior in adverse pressure gradients and separating flows while attaining accuracy and reliability [20].

The preceding attributes give the SST κ - ω model additional accuracy and reliability thus providing it an advantage over the standard κ - ω model. Moreover, the SST κ - ω model was used by many researchers in previous works that gave a fair matching with experimental results [6, 21]. Therefore, the SST κ - ω turbulence model is adopted in the present study.

This approach necessitates assessment of the wall adjacent cell size analogous to the dimensionless wall distance y^+ lower than 4, ensuring that the viscous sublayer is meshed.

The SST κ - ω model transport equations are:

$$\rho \frac{\partial}{\partial x_i} (\kappa u_i) = \frac{\partial}{\partial x_j} \left(\Gamma_\kappa \frac{\partial \kappa}{\partial x_j} \right) + \tilde{G}_\kappa - Y_\kappa \quad (7)$$

$$\rho \frac{\partial}{\partial x_i} (\omega u_i) = \frac{\partial}{\partial x_j} \left(\Gamma_\omega \frac{\partial \omega}{\partial x_j} \right) + G_\omega - Y_\omega + D_\omega \quad (8)$$

where

\tilde{G}_κ is the production of turbulence kinetic energy due to mean velocity gradients,

G_ω is the generation of ω ,

Γ_κ is the effective diffusivity of κ ; $\Gamma_\kappa = \mu + \frac{\mu_t}{\sigma_\kappa}$,

Γ_ω is the effective diffusivity of ω ; $\Gamma_\omega = \mu + \frac{\mu_t}{\sigma_\omega}$,

Y_κ is the dissipation of κ due to turbulence,

Y_ω is the dissipation of ω due to turbulence,

D_ω is the cross-diffusion,

$\sigma_\kappa, \sigma_\omega$ are the turbulent Prandtl number for κ and ω respectively,

μ_t is the turbulent viscosity. For detailed discussion of these equations refer to [20].

Low Reynolds correction and near-wall treatment are activated for SST κ - ω and RNG κ - ε turbulence models respectively. Double precision and second order upwind are used to consecutively solve the flow equations for spatial discretization of the convective terms [22]. Central-difference and second order accuracy are selected for the diffusion terms. The Coupled algorithm is used for the pressure-velocity coupling with the pseudo transient option which is a form of implicit under-relaxation for steady-state cases. Pseudo option allows the user to obtain solutions faster and more robustly.

1.2 Computational domain

A parallel plate channel similar to that experimented by Oneissi et al. [12] is modeled using ANSYS workbench. Oneissi et al. [12] test section consisted of four rectangular winglet pairs that produce four pairs of longitudinal vortices. This configuration permits to take the assumption of two axes of symmetry; the first is at the channel center and the other at one side of the middle winglet pair. Therefore, only one rectangular-winglet vortex generator is investigated in this study. The channel streamwise direction is defined as x, spanwise direction as y and z for the vertical direction.

Figure 1 presents an isometric view showing the simulated channel boundary conditions. The channel height $H=38.6$ mm is considered a baseline dimension with breadth $B=1.6H$ and length $L=11H$. Each rectangular winglet is $1.5H$ in length, $H/2$ in height and thickness equals to 2 mm ($0.05H$). The winglets are normal to the channel bottom wall with an angle of attack of 30° from the incident flow and the distance separating the leading edges of each pair is 8 mm ($0.2H$).

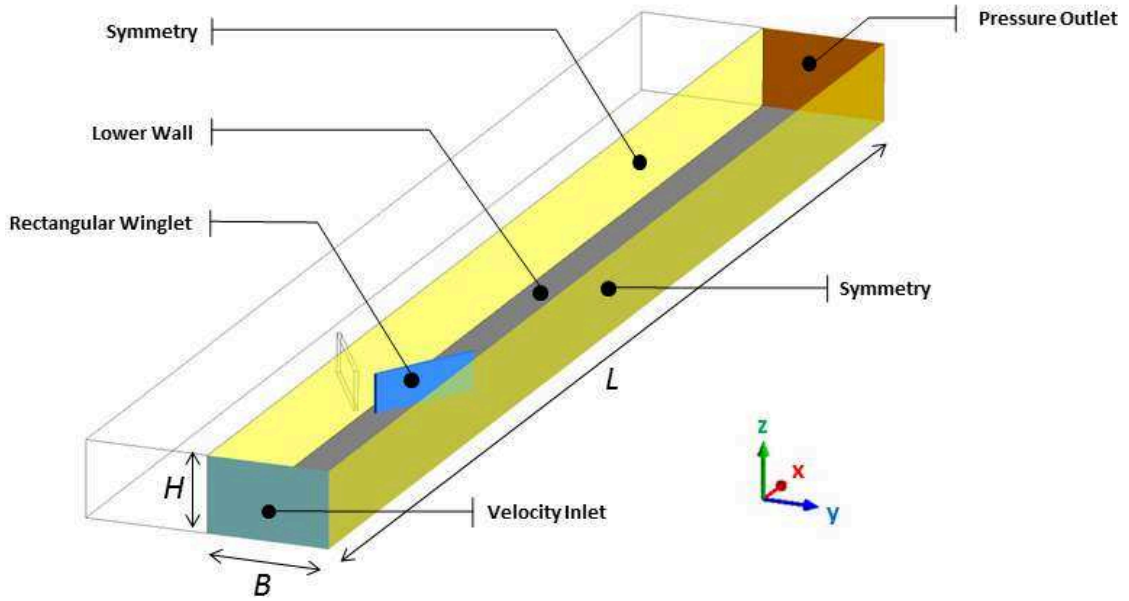


Figure 1 Isometric view of the computational domain showing the boundary conditions.

The Reynolds number is calculated based on the channel hydraulic diameter $D_h = 2H$ and $Re=4400$. The velocity inlet boundary condition is set as a user defined function (UDF). The inlet velocity profile function is similar to that extracted from Laser Doppler Anemometry (LDA) in Oneissi et al. [12] study shown in Figure 2.

The analytical velocity profile used was developed by Stigler [23] based on vorticity distribution between two parallel plates. Stigler velocity profile fits realistic results better than the power law velocity profiles that was derived for pipe flows, since the derivative of the function does not tend to infinity at the boundaries, thus no infinite shear stress at the walls. In addition, Stigler analytical solution solves the Munson power law in which the derivative of the function at the middle of the channel does not tend to zero. Stigler's analytical profile is defined as [23]:

$$\frac{U}{U_{max}} = 1 - \left[\frac{|2z - H|}{H} \right]^{n+1} \quad (9)$$

$$n = \frac{H^2(P_1 - P_2)}{4L\mu U_{mean}} - 2 \quad (10)$$

where

U is the longitudinal velocity value (m.s^{-1}),

U_{max} is the maximum velocity profile value (m.s^{-1}),

H is the channel height (m),

z is the vertical distance from the bottom wall (m), $0 \leq z \leq H$,

n is a pressure drop depending constant ($n=3.4$ in this study)

μ is the dynamic viscosity (Pa.s),

U_{mean} is the mean flow velocity (m.s^{-1}),

$P_1 - P_2$ is the pressure drop (Pa).

This expression can be used for both laminar and turbulent velocity profiles.

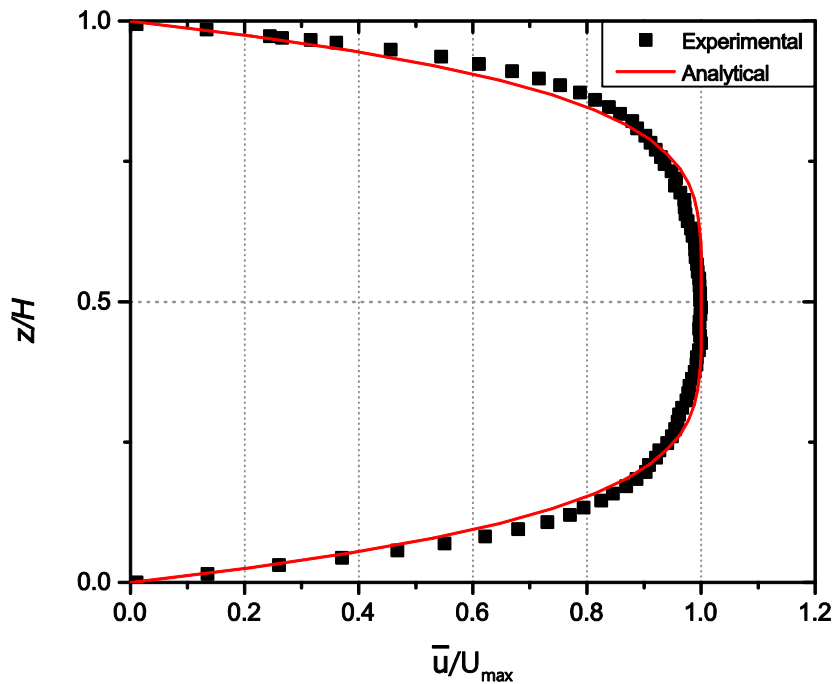


Figure 2 Mean velocity at the test section inlet for $Re=4400$ from experimental data compared to analytical solution [12].

Pressure outlet condition has been set for the outlet with a zero gauge pressure. In this work, the heat transfer is not a point of interest and thus, energy equation is disabled. Turbulence

intensity at the inlet has a dramatic influence on local and global results in turbulent flows. Proper turbulence intensity has to be chosen and in this study, turbulence intensity equal to 3% is selected. First, it is in the range of the moderate wind tunnel intensities (1%–5%). Second, this value for the turbulence intensity was used in recent papers [24, 25]. Also, the turbulence length scale, taken as a fraction of the inlet hydraulic diameter D_h , can be chosen equal to $0.07D_h$ as used in similar flow configurations.

1.3 Mesh sensitivity study

Mesh used in this work is based on a previous study done by Oneissi et al. [24] where a non-uniform mesh with polyhedral cells is used for the computational domain. All walls in the channel are treated with 10 inflation layers with 40 μm first layer thickness for attaining an acceptable y^+ value. Same insensitive mesh parameters set by Oneissi et al. [24] is conducted in this study. Table 1 presents the channel model mesh information used within this work.

Table 1 Mesh information

Maximum element size (mm)	1.30
Wall zizing (mm)	0.90
Type of mesh	Polyhedral
Number of elements	2,491,334
Inflation (mm)	40 μm –10 L
Maximum y^+	0.40

2. Results and discussion

2.1 Local comparison

In order to validate and detect the best turbulence model that can predict the generation of longitudinal vortices formed by rectangular winglet pair, local comparison with previously experimentally extracted results by Oneissi et al. [12] are made. Oneissi et al. [12] made a comparison between PIV and LDA measurements of longitudinal velocity profiles at a longitudinal distance $x=H$ downstream the VG trailing edge and vertical distance $z=24$ mm from the bottom wall. Longitudinal velocity profile is extracted from numerical simulation by both turbulence models at the same locations to compare with these previous experimental results. Figure 3 demonstrates a comparison between longitudinal mean velocity profiles (\bar{u}) normalized by the bulk velocity (U) extracted from experimental results with a 10% error and numerical simulations results. The normalized velocity profile (\bar{u}/U) obtained by numerical simulation using SST $\kappa\text{-}\omega$ turbulence model is shown to be in good correspondence with experimental results. The average error between simulation results and experimental results is less than 5% with a maximum error at the channel center line of about 14%. Similar global behavior of velocity profile is obtained for RNG $\kappa\text{-}\epsilon$ turbulence model with no correspondence to local values. It can be seen that the RNG $\kappa\text{-}\epsilon$ turbulence model could not predict the longitudinal velocity at the specified location because the average error is higher than 15%. However, this comparison is not enough to judge or even validate both turbulence models. Further comparison of flow structure characterization and flow topologies should be conducted to compare from a global and wider scope.

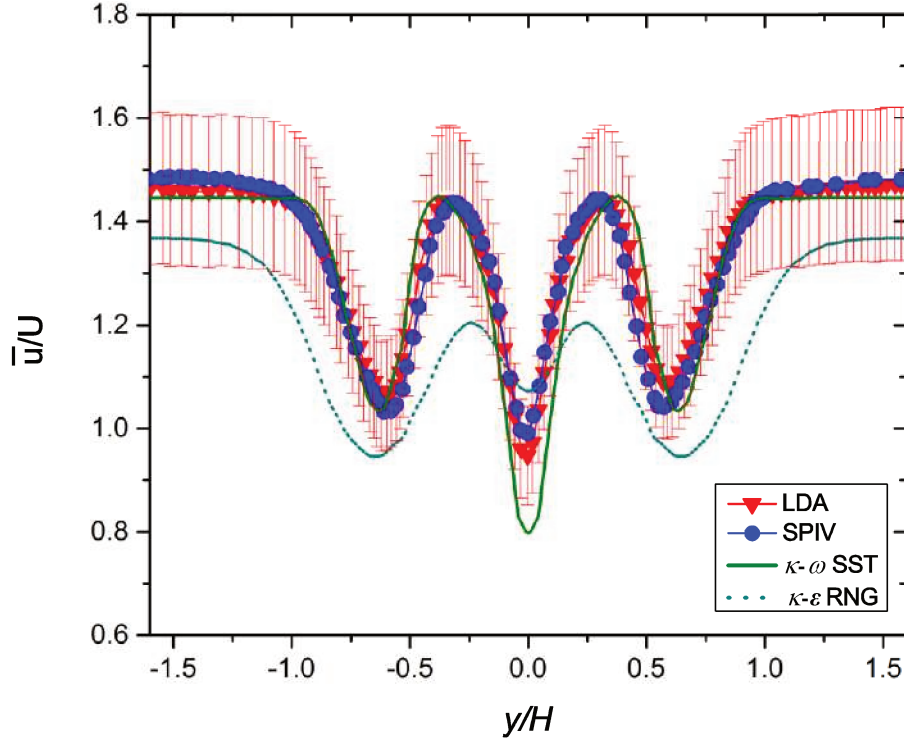


Figure 3 Comparison between normalized mean velocity profiles extracted from experimental results (with 10% error) and numerical simulations.

2.2 Flow structure comparison in the horizontal plane

Since local comparison of mean velocity profile is not a sufficient criterion to validate which turbulence model is able to better predict the flow structure downstream a longitudinal vortex generator, flow structure in horizontal plane of both models are compared with experimental results throughout this section. Mean and turbulent flow characteristics are investigated for Reynolds number $Re=4400$. In order to investigate the flow topology in the horizontal plane xy ($z=24$ mm from bottom wall), first, the three mean velocity components \bar{u} , \bar{v} and \bar{w} are compared with experimental topologies obtained by Oneissi et al. [12] using stereo-PIV system which were calculated by averaging 3000 instantaneous velocity fields. Second, to investigate the turbulent characteristics of the flow, turbulent kinetic energy is also compared.

2.2.1 Comparison with SST κ - ω turbulence model

Results obtained by numerical simulation are post-processed using ANSYS CFD-Post to ensure same normalizations, scales and color maps used by Oneissi et al. [12]. Figure 4 compares the topologies of velocity components in the horizontal plane at $Re = 4400$. On each picture, the upper half of the image represents the experimental results obtained by Oneissi et al. [12] denoted by SPIV item, while the bottom half demonstrates topology obtained from numerical simulation, indicated by CFD note.

From the CFD topology for the mean longitudinal velocity \bar{u} , the maximum values occur above the rectangular winglet pair and different areas of velocity variation are observed behind it. The main two areas of velocity deficit are associated to the evolution of longitudinal vortices in the wake region of each rectangular winglet. We can also observe the same phenomenon near the symmetric axis after a distance $x/H=2$ corresponding to the development of the induced vortices. This coincides with the experimental topology description reported by Oneissi et al. [12] and both halves may not be distinguished as symmetry. The topologies of the mean transverse velocity component \bar{v} obtained from experimental and numerical results are also symmetric. Figure 4 (b) shows that the transversal velocity component \bar{v} is embedded in region behind the winglet pair due to flow separation and dissipates along the channel in a manner similar to experimental data. Figure 4 (c) shows the vertical component \bar{w} obtained by CFD and experiments and show a great correspondence between both activities. It can be seen that the flow is directed downward between the two winglets and then splits into two regions: two main longitudinal vortices in the two regions separated by $y/H=0$ axis. In each region, the up-wash flow is colored in red, the downwash effect is colored in blue and stagnation zone is colored in green. A main vortex is produced due to flow separation over the winglet and rotates in a clock-wise (CW) direction and an induced vortex rotating counter clock-wise (CCW) is beginning to develop after a distance $x/H=2$ from winglet trailing edge. Both, experimental and

numerical results are in excellent correspondence with each other and show almost non-distinguishable flow topologies.

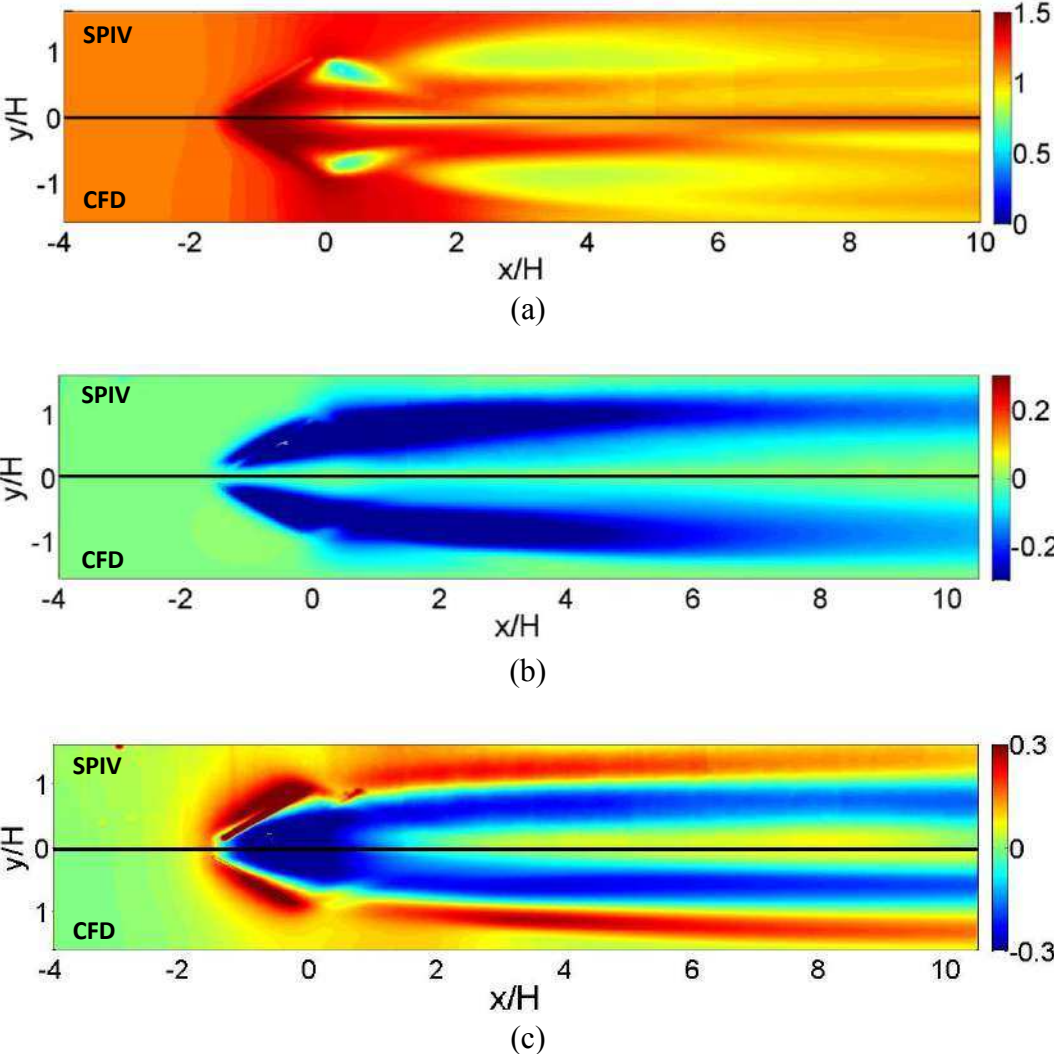


Figure 4 Comparison of mean flow velocity components in the horizontal plane at $Re = 4400$ and $z=24$ mm from bottom wall: (a) \bar{u} , (b) \bar{v} , (c) \bar{w} , upper section from experimental results and lower section from numerical simulations using SST $\kappa\text{-}\omega$ turbulence model.

Turbulent kinetic energy is computed to investigate the turbulence characteristics comparison. Figure 5 shows a comparison of the turbulent kinetic energy topology, normalized with the square of bulk mean flow velocity (U^2), between experimental results (denoted by SPIV) and numerical simulation (denoted by CFD) at $Re=4400$. Both figures are not totally

symmetric but they are in relatively good correspondence especially when extracting turbulent kinetic energy. SST κ - ω turbulence model seems to have good agreement with experimental results for primary vortex but, it does not reproduce that for secondary vortex, especially some differences appear from x/H higher than 3.

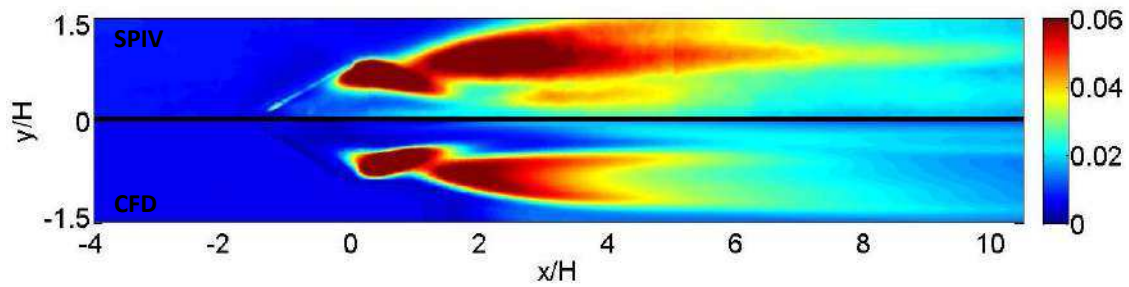


Figure 5 Comparison of the normalized turbulent kinetic energy topologies at $Re=4400$ and $z=24$ mm from bottom wall, between experimental results (upper section) and numerical simulation using SST κ - ω turbulence model (lower section).

2.2.2 Comparison with RNG κ - ϵ turbulence model

A similar strategy is followed in this section for comparing experimental results with RNG κ - ϵ turbulence model results. Figure 6 presents comparison of mean velocity components (\bar{u} , \bar{v} , \bar{w}) in horizontal plane between experimental results extracted by Oneissi et al. [12] and numerical results obtained using RNG κ - ϵ turbulence model at $Re=4400$ and $z=24$ mm from bottom wall. The simulation results globally show a poorer match with experimental data.

For the mean longitudinal velocity (\bar{u}), different velocity topologies are observed between experiment and simulation. It is observed from the CFD topology section that no induced vortices are predicted to be developed. The topologies of the mean transverse velocity component (\bar{v}) obtained from experimental and numerical results are rather different. Figure 6 (b) shows that the transversal velocity component (\bar{v}) is totally trapped in region directly behind the winglet pair in which it dissipates rapidly after a distance $x/H=4$. The vertical component

(\bar{w}) obtained by CFD is shown in Figure 6 (c) and also do not show any correspondence with experimental results. It can be seen that the RNG κ - ϵ turbulence model could not predict the induced vortices and only one stagnation zone line is shown in the lower half unlike real case. Only a main vortex is predicted to be produced due to flow separation over the winglet and rotates in a clock-wise (CW) direction when using RNG κ - ϵ turbulence model.

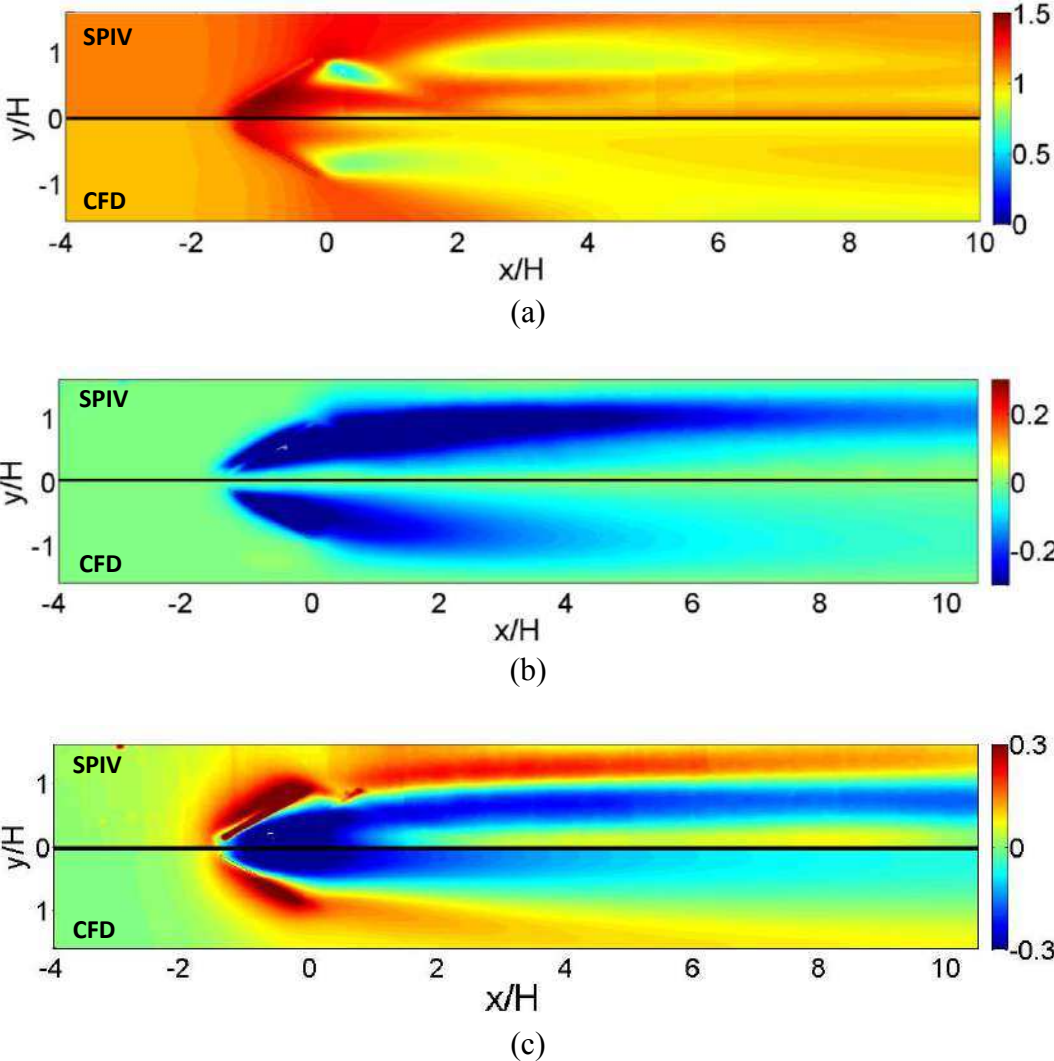


Figure 6 Comparison of mean flow velocity components in the horizontal plane at Re=4400 and z=24 mm from bottom wall: (a) \bar{u} , (b) \bar{v} , (c) \bar{w} , upper section from experimental results and lower section from numerical simulations using RNG κ - ϵ turbulence model.

Figure 7 presents a comparison of the normalized turbulent kinetic energy topologies between experimental results and numerical simulation using RNG $\kappa\text{-}\varepsilon$ turbulence model at $\text{Re}=4400$ and $z=24$ mm from bottom wall. Unlike the SST $\kappa\text{-}\omega$ turbulence model case, both figures are totally unsymmetrical with absolutely no correspondence. RNG $\kappa\text{-}\varepsilon$ turbulence model could not predict the turbulent kinetic energy even in an approximate manner.

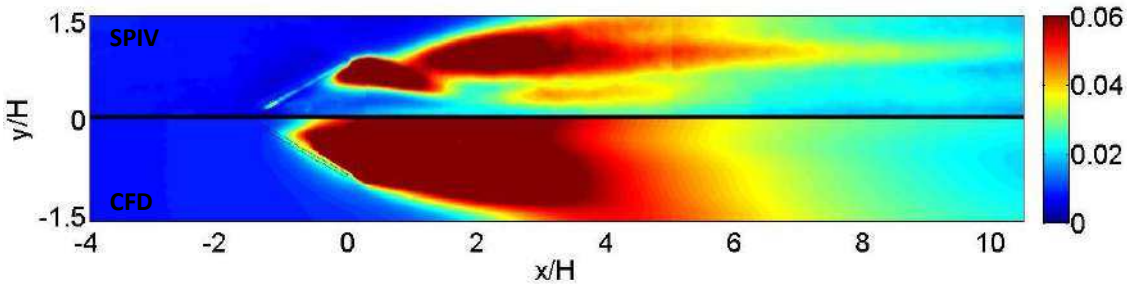


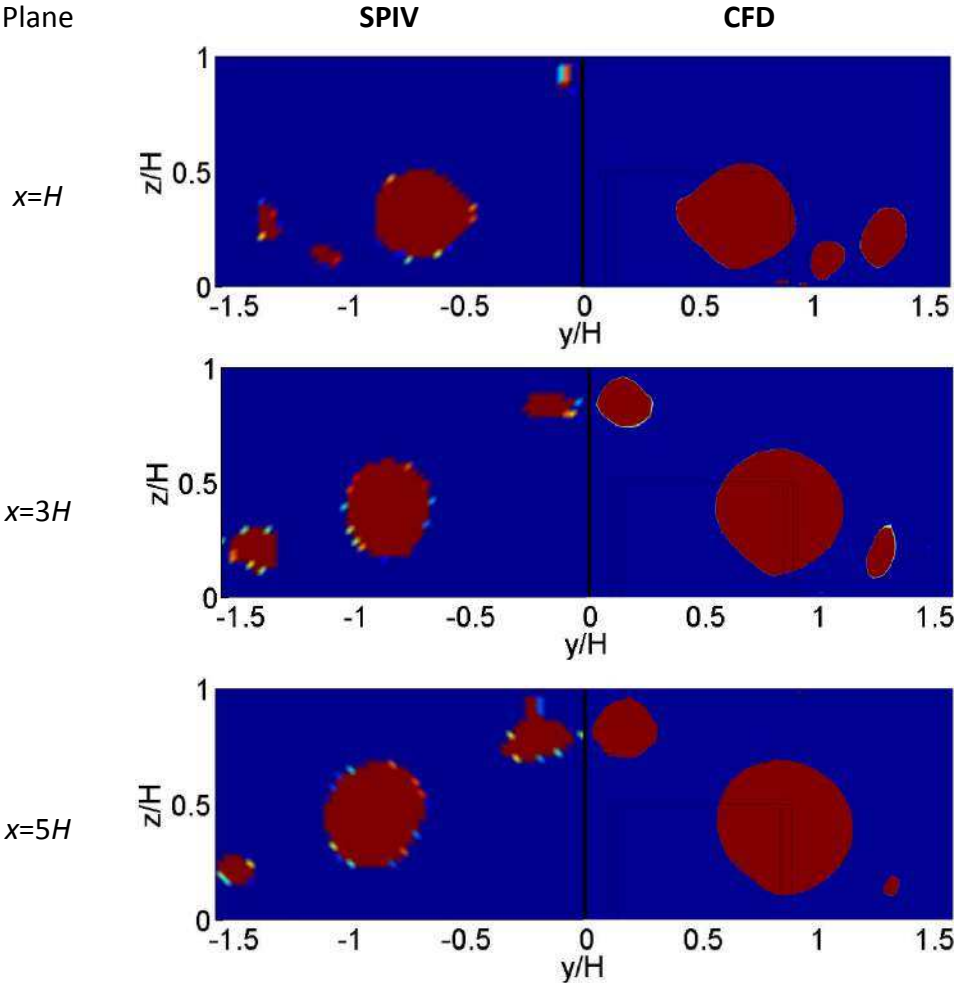
Figure 7 Comparison of the normalized turbulent kinetic energy topologies at $\text{Re}=4400$ and $z=24$ mm from bottom wall, between experimental results (upper section) and numerical simulation using RNG $\kappa\text{-}\varepsilon$ turbulence model (lower section).

2.3 Flow structure comparison in vertical planes

In addition to the topologies comparison in horizontal plane, topologies in vertical planes are conducted for further examination of the turbulence models prediction of longitudinal vortices characteristics at several locations in the wake region. In this section, Γ_2 criterion proposed by Favelier et al. [26] and employed by Oneissi et al. [12] to identify and track the main and induced vortices in the flow behind the winglet pair is also used to validate turbulence model predictions. Comparing topologies of the Γ_2 function with SST $\kappa\text{-}\omega$ turbulence model and RNG $\kappa\text{-}\varepsilon$ turbulence model at different locations ($x= H, 3H, 5H, 9H$ and $10.5H$) are respectively illustrated in Figure 8 and Figure 9.

It is clearly shown from Figure 8 that the SST $\kappa\text{-}\omega$ turbulence model accurately predicts and identifies the generated vortices location at different locations, while Figure 9 shows that

the RNG $\kappa\text{-}\varepsilon$ turbulence model could not predict the generation of vortices. The RNG $\kappa\text{-}\varepsilon$ turbulence model only predict the formation of one main vortex that developed along the channel, but it fails at predicting any induced vortices. Whereas, the SST $\kappa\text{-}\omega$ turbulence model precisely predict the number of generated vortices and the relative position of these vortices. Figure 8 shows that SST $\kappa\text{-}\omega$ turbulence model predicts one main vortex in addition to two induced vortices near the bottom wall of the channel at a distance $x=H$. Also, for the other planes, the SST $\kappa\text{-}\omega$ turbulence model accurately predict main and induced vortices numbers and locations.



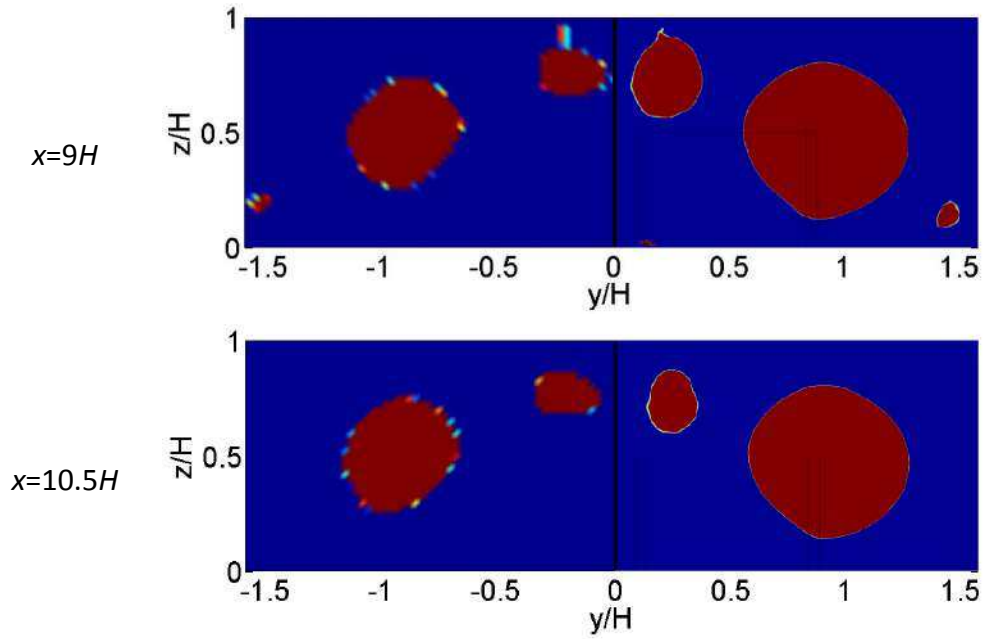
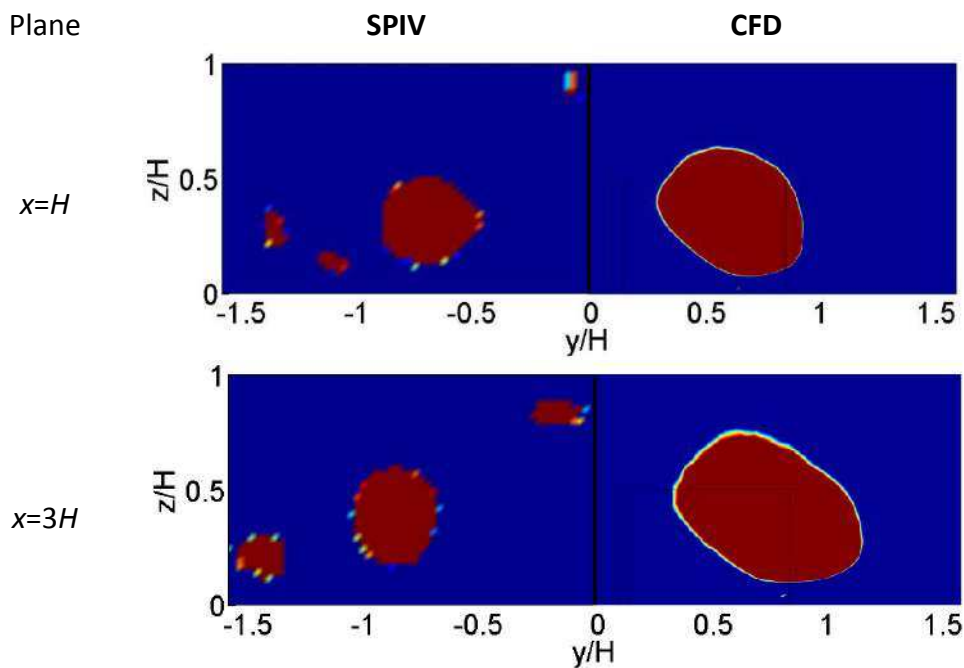


Figure 8 Comparison of Γ_2 function topologies used for vortex identification downstream the winglet pair at $Re=4400$ between experimental results (left section) and numerical simulation using SST $\kappa\text{-}\omega$ turbulence model (right section).



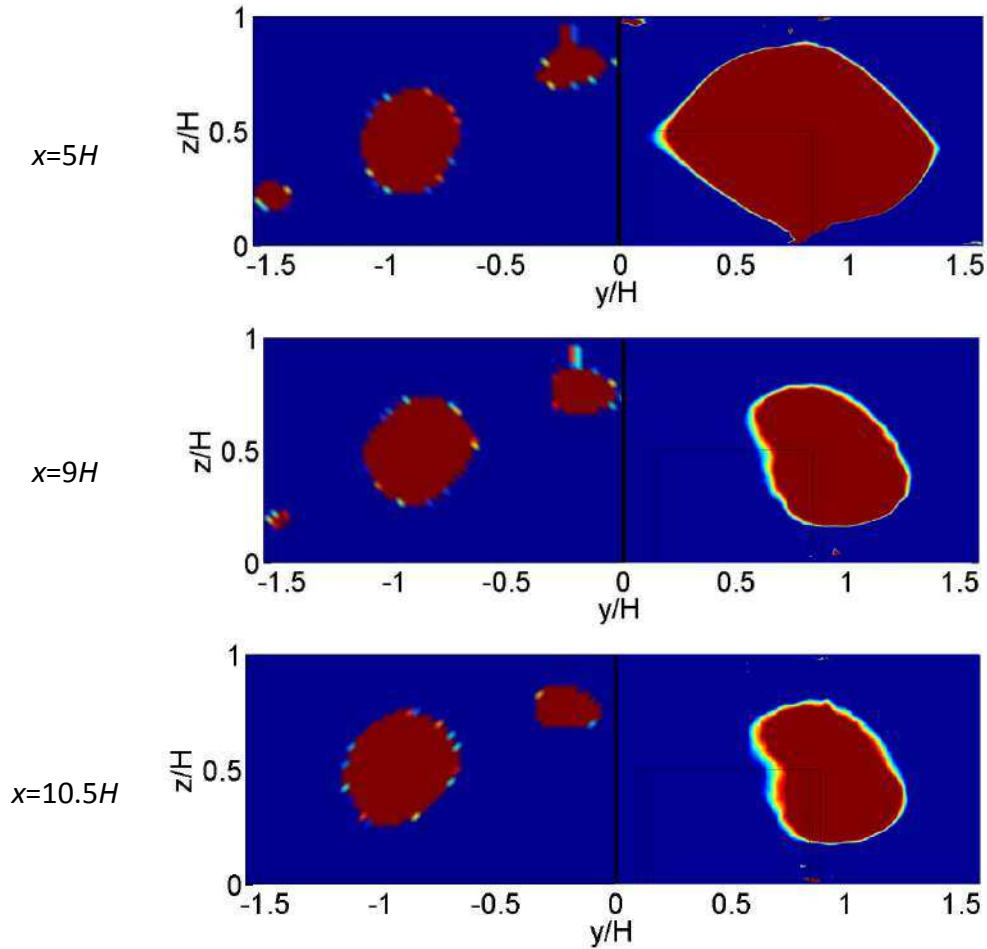


Figure 9 Comparison of Γ_2 function topologies used for vortex identification downstream the winglet pair at $Re=4400$ between experimental results (left section) and numerical simulation using RNG $\kappa\text{-}\epsilon$ turbulence model (right section).

3. Conclusion

In this work, a comparison between numerical simulation and previous experimental study of flow structure characteristics of longitudinal vortices generated by rectangular winglet pairs in parallel plate-fin channel is investigated at $Re=4400$. The aim of this study is to validate which turbulence model properly predicts the flow structure of longitudinal vortices in a parallel plate channel. Similar channel dimensions as the experimental test-bench with the same boundary conditions are modeled in ANSYS Fluent 15.0 CFD software. Two turbulence models are conducted within this investigation: the SST $\kappa\text{-}\omega$ turbulence model and the RNG $\kappa\text{-}\epsilon$

turbulence model. The obtained results of the velocity profile from the simulations are compared locally with formerly experimental results extracted using both LDA and SPIV techniques. Simulation adopted on SST $\kappa\text{-}\omega$ turbulence model shows a good correspondence with experimentally extracted data, while RNG $\kappa\text{-}\varepsilon$ turbulence model do not show any harmony. Global topologies evaluations are then carried on for further model validations. Horizontal velocity components topologies in addition to the turbulent kinetic energy topology at a predefined horizontal plane are inspected. The SST $\kappa\text{-}\omega$ turbulence model shows excellent correspondence with experimental results where both topologies (obtained experimentally and numerically) are almost non-distinguishable from each other. On the other hand, the RNG $\kappa\text{-}\varepsilon$ turbulence model shows no consistency at all with experimental results. In addition to the horizontal topologies comparisons, vertical comparisons are also conducted for further examination of the turbulence models prediction of longitudinal vortices characteristics at several locations in the wake region. Topologies of Γ_2 function are used to identify and track the main and induced vortices in the flow behind the winglet pair at different longitudinal locations. The SST $\kappa\text{-}\omega$ turbulence model accurately predicts and identifies the generated vortices location at different planes, the number of generated vortices (main and induced) as well as their relative positions. The RNG $\kappa\text{-}\varepsilon$ turbulence model could only predict the generation of main vortices, but it fails at predicting any induced vortices.

This study shows a superiority of the SST $\kappa\text{-}\omega$ turbulence model over the RNG $\kappa\text{-}\varepsilon$ turbulence model in predicting flow structure characteristics of longitudinal vortices in a parallel plate channel. Also, the SST $\kappa\text{-}\omega$ turbulence model is able to capture the induced vortices and therefore shall be used for predicting multi-scale vortices. Thus, the SST $\kappa\text{-}\omega$ turbulence model may excel in predicting such flow structures and consequently preferred to be used in modeling longitudinal vortices in turbulent flows.

References

- [1] M. Fiebig, "Embedded Vortices in Internal Flow: Heat Transfer and Pressure Loss Enhancement," *International Journal of Heat and Fluid Flow*, vol. 16, no. 5, pp. 376-388, 1995.
- [2] M. Fiebig, U. Brockmeier, N. K. Mitra and T. Guntermann, "Structure of Velocity and Temperature Fields in Laminar Channel Flows with Longitudinal Vortex Generators," *Numerical Heat Transfer, Part A*, vol. 15, pp. 281-302, 1989.
- [3] J. T. W. Wu, "Numerical Study on Laminar Convection Heat Transfer in a Rectangular Channel with Longitudinal Vortex Generator. Part A: Verification of field synergy principle," *International Journal of Heat and Mass Transfer*, vol. 51, no. 5, pp. 1179-1191, 2008.
- [4] J. M. Wu and W. Q. Tao, "Numerical Study on Laminar Convection Heat Transfer in a Channel with Longitudinal Vortex Generator. Part B: Parametric Study of Major Influence Factors," *International Journal of Heat and Mass Transfer*, vol. 51, pp. 3683-3692, 2008.
- [5] L. O. Salviano, D. J. Dezan and J. I. Yanagihara, "Optimization of winglet-type vortex generator positions and angles in plate-fin compact heat exchanger: Response Surface Methodology and Direct Optimization," *International Journal of Heat and Mass Transfer*, vol. 82, pp. 373-387, 2015.
- [6] K. Yongsiri, P. Eiamsa-ard, K. Wongcharee and S. Eiamsa-ard, "Augmented heat transfer in a turbulent channel flow with inclined detached-ribs," *Case Studies in Thermal Engineering*, vol. 3, pp. 1-10, 2014.

- [7] X.-Y. Tang and D.-S. Zhu, "Flow structure and heat transfer in a narrow rectangular channel with different discrete rib arrays," *Chemical Engineering and Processing: Process Intensification*, vol. 69, pp. 1-14, 2013.
- [8] X.-Y. Tang and D.-S. Zhu, "Experimental and Numerical Study on Heat Transfer Enhancement of a Rectangular Channel with Discontinuous Crossed Ribs and Grooves," *Chinese Journal of Chemical Engineering*, vol. 20, no. 2, pp. 220-230, 2012.
- [9] M. Hatami, D. Ganji and M. Gorji-Bandpy, "Experimental and numerical analysis of the optimized finned-tube heat exchanger for OM314 diesel exhaust exergy recovery," *Energy Conversion and Management*, vol. 97, pp. 26-41, 2015.
- [10] C. Habchi, S. Russeil, D. Bougeard, J. L. Harion, T. Lemenand, D. Della Valle and H. Peerhossaini, "Enhancing Heat Transfer in Vortex Generator-type Multifunctional Heat Exchangers," *Applied Thermal Engineering*, vol. 38, pp. 14-25, 2012.
- [11] S. Eiamsa-ard and P. Promvong, "Numerical study on heat transfer of turbulent channel flow over periodic grooves," *International Communications in Heat and Mass Transfer*, vol. 35, no. 7, pp. 844-852, 2008.
- [12] M. Oneissi, E. Bouhoubeiny, S. Russeil, D. Bougeard, T. Lemenand and C. Habchi, "Experimental analysis by stereo-PIV of the development of streamwise vortices downstream of rectangular winglets," *Journal X*, vol. xx, no. x, pp. xxx-xxx, 2016.
- [13] I. ANSYS, "Turbulence Models," in *ANSYS Fluent 12.0 Theory Guide*, April 2009, pp. 1-3;27.
- [14] V. Yakhot and S. Orszag, "Renormalization group analysis of turbulence:(i) basic theory," *Journal of Scientific Computing*, vol. 1, pp. 3-51, 1986.

- [15] V. Yakhot, S. Orszag, S. Thangam, T. Gatski and C. Speziale, "Development of turbulence models for shear flows by a double expansion technique," *Physics of Fluids A*, vol. 4, no. 7, pp. 1510-1520, 1992.
- [16] B. Launder and D. Spalding, "The numerical computation of turbulent flows," *Computer Methods in Applied Mechanics and Engineering*, vol. 3, no. 2, pp. 269-289, 1974.
- [17] D. Choudhury, "Introduction to the Renormalization Group Method and Turbulence Modeling," Fluent Inc, Technical memorandum TM-107, 1993.
- [18] H. Versteeg and W. Malalasekera, *An Introduction to Computational Fluid Dynamics: The Finite Volume Method*, second ed., New York: Prentice Hall, 1995, p. 520.
- [19] F. Menter, "Two-equation eddy-viscosity turbulence models for engineering applications," *AIAA Journal*, vol. 32, pp. 1598-1605, 1994.
- [20] I. ANSYS, "Standard and SST k-w Models," in *ANSYS Fluent 15.0 Theory Guide*, April 2009, p. 4.31.
- [21] X.-Y. Tang and D.-S. Zhu, "Flow structure and heat transfer in a narrow rectangular channel with different discrete rib arrays," *Chemical Engineering and Processing: Process Intensification*, vol. 69, pp. 1-14, 2013.
- [22] R. Warming and R. Beam, "Upwind second-order difference schemes and applications in aerodynamic flows," *AIAA Journal*, vol. 14, no. 9, pp. 1241-149, 1976.
- [23] J. Štigler, "Introduction of the analytical turbulent velocity profile between two parallel plates," in 148, Svratka, Czech Republic, 2012.
- [24] M. Oneissi, C. Habchi, S. Russeil, D. Bougeard and T. Lemenand, "Novel design of delta winglet pair vortex generator for heat transfer enhancement," *International Journal of Thermal Sciences*, vol. 109, pp. 1-9, 2016.

- [25] M. Nacer-Bey, S. Russeil and B. Baudoin, "PIV visualizations to the flow structure upstream of the tubes in a two-row plate-fin-and-tube heat exchanger," in Proceeding of the 4th International Conference on Compact Heat Exchangers and Enhancement Technology for the Process Industries, Grete Island, Greece, pp. 63-68, September 29-October 3, 2003.
- [26] T. Favelier, M. Michard and N. Grosjean, "Développement d'un critère d'identification de structures tourbillonnaires adapté aux mesures de vitesse par PIV," in Proc. 9ème Congrès Francophone de Vélocimétrie Laser, Bruxelles, 2004.

Chapitre 5

Conception nouvelle d'un générateur de vorticité à paires d'ailettes triangulaires pour l'amélioration du transfert de chaleur

Dans ce chapitre, des simulations numériques tridimensionnelles de deux configurations de générateurs de vorticité sont effectuées pour analyser l'amélioration du transfert de chaleur dans un échangeur de chaleur à plaques parallèles et ailettes. Les écoulements laminaires sont simulés pour des nombres de Reynolds 270, 540 et 1080. Le flux turbulent est modélisé à l'aide du modèle SST $k - \omega$ et validé avec des corrélations et des données expérimentales. Le but de ce travail est de produire une configuration plus aérodynamique qui réduit les pertes de charges et améliore le transfert de chaleur et les performances de mélange. La configuration IPWP est ensuite imaginée et présentée en modifiant la géométrie et l'orientation des ailettes du cas de référence représenté par la configuration DWP. Le générateur de vorticité IPWP présente de meilleures performances en ce qui concerne la vorticité et la chute de pression par rapport au cas DWP, pris comme configuration de base, sur un large éventail de nombres de Reynolds allant du laminaire au turbulent. Le maximum du coefficient de frottement pour IPWP est 50% inférieur à celui obtenu pour DWP. L'intensité de la vorticité pour IPWP est augmentée de 30% par rapport à la configuration de base. Cette amélioration est atteinte grâce au mécanisme de génération de tourbillons présenté par la configuration IPWP. Les tourbillons créés par chaque paire d'ailettes sont au nombre de six pour le cas DWP et de dix pour l'IPWP, l'interaction de ces tourbillons augmente positivement le processus d'échange de chaleur. Ainsi,

les résultats actuels sont très prometteurs puisque le facteur d'amélioration thermique est augmenté de 6% pour le générateur de vorticité IPWP par rapport au cas DWP.



Novel design of delta winglet pair vortex generator for heat transfer enhancement



Mohammad Oneissi^{a, b, c}, Charbel Habchi^d, Serge Russeil^{b, *}, Daniel Bougeard^b, Thierry Lemenand^c

^a Lebanese International University, Mechanical Engineering Department, Beirut, Lebanon

^b Mines Douai, El, F59500, Douai, France

^c Angers University, ISTIA, LARIS EA 7315, 49000, Angers, France

^d Notre Dame University – Louaize, Mechanical Engineering Department, P.O. Box: 72, Zouk Mikael, Zouk Mosbeh, Lebanon

ARTICLE INFO

Article history:

Received 22 August 2015

Received in revised form

22 May 2016

Accepted 24 May 2016

Available online 2 June 2016

Keywords:

Heat transfer enhancement

Winglet pair

Vortex generator

Plate-fin heat exchanger

Parallel-plate channel

Numerical simulation

ABSTRACT

Heat transfer is a naturally occurring phenomenon that can be greatly enhanced with the aid of vortex generators (VG). Three-dimensional numerical simulations of longitudinal vortex generators are performed to analyze heat transfer enhancement in parallel plate-fin heat exchanger. The shear-stress transport (SST) $\kappa\text{-}\omega$ model is adopted to model the flow turbulence. Empirical correlations from the open literature are used to validate empty channel simulations. First, numerical simulations are conducted for the classical delta winglet pair (DWP) which is introduced as the reference case in this study. Then, an innovative VG configuration, named inclined projected winglet pair (IPWP), is examined and it shows superior performance relative to the DWP. The IPWP exhibits similar heat transfer rates than that of the DWP but with lower pressure drop penalty due to its special aerodynamic design. The local performance is analyzed based on the streamwise distribution of Nusselt number and friction coefficient criteria in addition to vorticity. This study highlights the different mechanisms involved in the convective heat transfer intensification by generating more vortices using more aerodynamic VG shape while decreasing the pressure drop penalty.

© 2016 Elsevier Masson SAS. All rights reserved.

1. Introduction

The use of vortex generators (VG) in the various industrial fields is widespread ranging from compact heat exchangers to aeronautics [1–4]. In the field of heat exchangers, the role of the VG is the enhancement of the heat exchange process between the wall and the working fluid. This enhancement relies on generating a secondary flow in form of complex streamwise and transverse vortices. The vortices disrupt the growth of the boundary layer and eventually serve in enhancing the heat transfer [5]. For this intention, two enhancement methods can be implemented: the active VG method and the passive VG method [6]. Passive VG are more commonly used since they are characterized by their efficiency, economy, manufacturing simplicity and maintenance ease, opposite to active VG which are energy consumers and less easy to

implement. These VG have various types which include helical and twisted inserts [7,8], dimples or protrusions [9,10], cylindrical tubes [11–14], transverse vortex generators (TVG) [10,15,16], longitudinal vortex generators (LVG) [17–23], plane or curved surface of VG [24,25] or a combination of the above types [10,22,26–29].

Transverse vortices are two-dimensional flows with axes normal to the flow direction, while longitudinal vortices rotate about an axis in the streamwise direction, implying a three-dimensional swirling flow. When pressure losses are taken into account, LVG are found to have an advantage over TVG in terms of global mixing and heat transfer performances [30].

This paper focuses on the study of LVG and their unique capability in heat transfer enhancement through the generation of large scale longitudinal vortices. This enhancement is a result of the combination of the main mechanisms of heat transfer intensification: the reduction of the laminar sub layer thickness near the wall, the development of three-dimensional turbulent layers and the swirl motion of the streamwise vortices that enhances convective transfer [31,32].

* Corresponding author. DEI, Mines Douai, 941 rue Charles Bourseul, BP 10838, 59508 Douai Cedex, France. Tel.: +33 03 27 71 23 88.

E-mail address: serge.russeil@mines-douai.fr (S. Russeil).

Nomenclature			
A	cross-sectional area	T_s	surface temperature, K
B	channel width, m	U	mean flow velocity across the cross section, $m\ s^{-1}$
C_p	specific heat at constant pressure, $J\ (kgK)^{-1}$	u	flow velocity in x direction, $m\ s^{-1}$
D_h	hydraulic diameter, m	v	flow velocity in y direction, $m\ s^{-1}$
f	Fanning friction factor, <i>dimensionless</i>	w	flow velocity in z direction, $m\ s^{-1}$
H	channel height, m	x_v	distance of wingtips from the channel entrance, m
h	convective heat transfer coefficient, $W\ (m^2K)^{-1}$	z	Vortex generator height, m
j	Colburn factor, <i>dimensionless</i>	<i>Greek letters</i>	
k	thermal conductivity, $W(mK)^{-1}$	μ	dynamic viscosity, Pa s
L	channel length, m	ν	kinematic viscosity, $m^2\ s^{-1}$
l	Vortex generator span, m	ρ	fluid density, $kg\ m^{-3}$
\dot{m}	mass flow rate, $kg\ s^{-1}$	β	angle of attack, $^\circ$
Nu	Nusselt number, <i>dimensionless</i>	<i>Abbreviations</i>	
Pe	Péclet number = $Re\ Pr$, <i>dimensionless</i>	VG	Vortex Generator
Po	Poiseuille number, <i>dimensionless</i>	DWP	Delta Winglet Pair
Pr	Prandtl number, <i>dimensionless</i>	RWP	Rectangular Winglet Pair
ΔP	pressure drop, Pa	IPWP	Inclined Projected Winglet Pair
q''	heat flux	LVG	Longitudinal Vortex Generator
Re	Reynolds number, <i>dimensionless</i>	TVG	Transverse Vortex Generator
s	distance between tips of winglet pair, m	CFD	Computational Fluid Dynamics
$T_{b,x}$	bulk temperature at position x , K	SST	Shear-Stress Transport
T_i	inlet temperature, K	TEF	Thermal Enhancement Fraction, <i>dimensionless</i>
T_o	outlet bulk temperature, K		

Winglet pairs exist in two configurations, one is the common flow-down and the other is the common flow-up. When the transverse distance between leading edges is less than that of trailing edges, the configuration is known as common flow-down and vice-versa [33]. Common flow-down vortices create down-wash in between, and up-wash flow in the outside regions. Along the streamwise direction, the vortices' velocity vectors decrease while the distance between vortex cores increases which leads to the thinning of the thermal boundary layer [33]. Tian et al. [34] compared delta-winglet pair (DWP) with rectangular winglet pair (RWP) for common flow-down and common flow-up configurations and deduced that DWP in common flow-down geometry is more efficient than other configurations. Biswas et al. [5] studied the performance of a delta winglet type VG and concluded that such VGs show great promise for enhancing the heat transfer in plate-fin heat exchangers. Meanwhile, common flow-up configuration also seems to be important to study as future work in some applications. In fact, Jain et al. [35] proposed a common flow-up configuration delta winglet that causes significant separation delay, reduced form drag and removes the zones of poor heat transfer.

The present work focuses on designing a better aerodynamic VG shape that can provide the same heat transfer with a reduced pressure drop when compared to the DWP as a reference case. The new VG increases the global thermal enhancement with an average of about 6% and the averaged global pressure drop decreases by about 10% over a wide range of Reynolds numbers. Moreover, the effect of the new VG geometry on the flow structure and thus on the heat transfer mechanism is analyzed.

The numerical method, computational domain and mesh sensitivity analysis are presented in the problem statement in section 2. Numerical validation, global performance followed by local examination of the heat transfer phenomena and compactness comparison are discussed in section 3. Finally, section 4 is devoted to the concluding remarks.

2. Problem statement

2.1. Numerical model

The flow field is governed by the three-dimensional (3D) steady-state Reynolds averaged Navier-Stokes (RANS) equations. The continuity and momentum equations for an incompressible Newtonian fluid are:

$$\frac{\partial u_i}{\partial x_i} = 0 \quad (1)$$

$$u_j \frac{\partial u_i}{\partial x_j} = -\frac{1}{\rho} \frac{\partial p}{\partial x_i} + \nu \frac{\partial^2 u_i}{\partial x_j \partial x_j} - \frac{\partial u'_i u'_j}{\partial x_j} \quad (2)$$

where the term $-u'_i u'_j$ is the Reynolds stress tensor resulting from the averaging procedure on the nonlinear convective terms in the momentum equations.

The heat transfer is governed by the energy equation given below:

$$\frac{\partial}{\partial x_i} [u_i (\rho E + p)] = \frac{\partial}{\partial x_i} \left(\lambda_{eff} \frac{\partial T}{\partial x_i} \right) \quad (3)$$

where E is the total energy and λ_{eff} the effective thermal conductivity.

The solver used for the flow computation is the ANSYS Fluent 15, which is based on an Eulerian approach to solve the Cauchy equations through cell-centered finite volume discretization [10]. The code computes the conservation equations for mass and momentum in addition to the energy equation [36]. Turbulence models allow the calculation of the mean flow without first calculating the full time-dependent flow field.

In this study, for laminar flows ($Re = 270, 540$ and 1080) the laminar model is used whereas for turbulent flows ($Re = 2800,$

4600, 7700, 10,800, 16,200, 21,600 and 30,000) the shear-stress transport (SST) κ - ω model developed by Menter [37] is used. This turbulence model solves two additional partial differential equations; a modified version of the turbulence kinetic energy equation κ used in κ - ϵ model and a transport equation for the specific dissipation ω . Also, the shear stress transport (SST) combines the use of κ - ω formulation in the inner parts of the boundary layer and the switching to a κ - ϵ behavior in the free-stream thus avoiding the κ - ω sensitivity to the inlet free-stream turbulence properties. In addition, this model is characterized by its good behavior in adverse pressure gradients and separating flows while attaining accuracy and reliability [38].

The preceding attributes give the SST κ - ω model additional accuracy and reliability thus providing an advantage over the standard κ - ω model. Moreover, the SST κ - ω model was used by several researchers in previous works and it shows a fair agreement with experimental results for flow configurations similar to the present study [39,40].

The use of the SST κ - ω model necessitates assessment of the wall adjacent cell size analogous to the dimensionless wall distance y^+ less than 4, ensuring that the viscous sublayer is meshed.

The SST κ - ω model transport equations are:

$$\rho \frac{\partial}{\partial x_i} (\kappa u_i) = \frac{\partial}{\partial x_j} \left(\Gamma_k \frac{\partial \kappa}{\partial x_j} \right) + \tilde{G}_k - Y_k \quad (4)$$

$$\rho \frac{\partial}{\partial x_i} (\omega u_i) = \frac{\partial}{\partial x_j} \left(\Gamma_\omega \frac{\partial \omega}{\partial x_j} \right) + G_\omega - Y_\omega + D_\omega \quad (5)$$

where

\tilde{G}_k is the production of turbulence kinetic energy due to mean velocity gradients,

G_ω is the generation of ω ,

Γ_k is the effective diffusivity of κ ; ($\Gamma_k = \mu + \frac{\mu_t}{\sigma_k}$),

Γ_ω is the effective diffusivity of ω ; ($\Gamma_\omega = \mu + \frac{\mu_t}{\sigma_\omega}$),

Y_k is the dissipation of κ due to turbulence,

Y_ω is the dissipation of ω due to turbulence,

D_ω is the cross-diffusion,

σ_k, σ_ω is the turbulent Prandtl number for κ and ω respectively, and

μ_t is the turbulent viscosity

For detailed discussion of these equations refer to the ANSYS Fluent 15.0 theory guide [38].

For spatial discretization of the convective terms, a scheme of double precision and second order upwind is used to consecutively solve the flow equations [41]. Central-difference and second order accuracy are selected for the diffusion terms. The Coupled algorithm is used for the pressure-velocity coupling with the pseudo transient option. Pseudo transient method option is a form of implicit under-relaxation for steady-state cases. It allows the user to obtain solutions faster and more robustly.

2.2. Computational domain

The channel dimensions used for the simulations are taken from a previously designed parallel plate channel with height H , breadth $B = 1.6H$ and of length $L = 13H$. An isometric view showing the boundary conditions is presented in Fig. 1.

The Reynolds number is calculated based on the hydraulic diameter $D_h = 2H$. A hydrodynamic and thermally developing flow is computed with a uniform inlet velocity profile and uniform inlet temperature equal to 300 K for a wide range of Reynolds numbers: 270, 540, 1080, 2800, 4600, 7700, 10,800, 16,200, 21,600 and

30,000. The Reynolds number variation is done by varying the mean flow velocity magnitude at the inlet. For the outlet, a constant pressure outlet condition has been set with a zero gauge pressure. Isothermal walls are set for both, upper and bottom walls, with a constant temperature of 350 K. All VG cases have been simulated as an adiabatic wall to highlight the effect of the flow structure on the convective heat transfer alone. For turbulent cases, the turbulence intensity on the inlet boundary has a dramatic influence on local and global results. Proper turbulence intensity has to be chosen and in this study, turbulence intensity equal to 3% is selected. This value is in the range of the moderate wind tunnel intensities (1%–5%) [42]. Also, the turbulence length scale, taken as a fraction of the inlet hydraulic diameter D_h [43,44], can be chosen equal to $0.07D_h$ as used in similar flow configurations [45] or choosing the turbulence intensity with the hydraulic diameter is also valid and gives same results.

The goal behind this study is to improve or at least maintain the heat enhancement while reducing pressure drop induced by the DWP (90° elevation angle with the bottom wall). Therefore, the same frontal area as that of the DWP is preserved but with an inclination angle relative to the channel wall. A downstream projection on a 30° inclined plane from the DWP bottom edge is depicted. To state the matter differently, if the DWP surface was inclined 30° about the lower edge and then an extrusion of the DWP is made in the downstream direction, then the result is an inclined projected winglet pair (IPWP). Fig. 2 shows the 2D geometry of the IPWP generated by the projection of the DWP contour profile and the 3D model of the IPWP is shown in Fig. 3.

2.3. Mesh sensitivity

Non-uniform mesh with polyhedral cells is used for the computational domain. In order to maintain an accepted low value for y^+ , all solid walls in the channel (fin walls and VG) are treated with 10 inflation layers with a first layer thickness of 40 μm . Mesh independency tests are carried out on an empty channel turbulent flow for the highest Reynolds number $Re = 21,600$.

Table 1 shows the model mesh configurations and sensitivity scheme respectively. In order to reach the mesh size adapted in the simulation, an arbitrary estimate of the size is implemented and then simulated. In the inflation column, the first number gives the first inflation layer thickness, while the second gives the number of inflation layers. The element size is then decreased by a factor of 1.30 until the error based on both global Nusselt number and friction coefficient is less than 2%. Thus, as it can be seen from Table 1, Mesh-4 is used for all the other simulations. This choice is due to the non-necessity of any further refinement since the error becomes smaller than 2% with this mesh. The y^+ for all of the cases has a value smaller than 2.

3. Numerical results and discussion

3.1. Numerical validation

Developing flow (velocity and temperature) case is simulated in the present work by applying uniform velocity and temperature profiles at the inlet boundary condition. The performance evaluation of the different configurations is divided into two main categories: global and local approaches.

Global Nusselt number is given by:

$$\overline{Nu} = \frac{D_h h}{k} = \frac{2Hh}{k} \quad (6)$$

where:

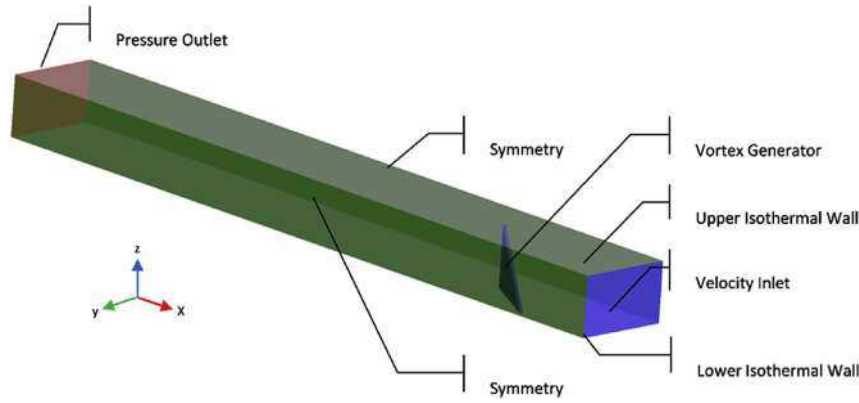


Fig. 1. Isometric view of the computational domain showing the boundary conditions.

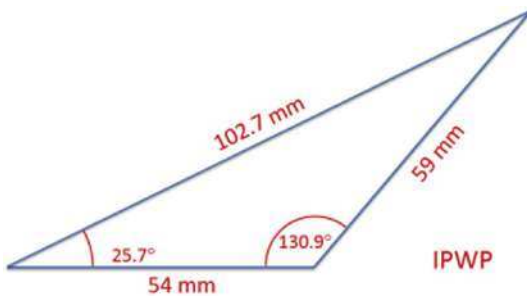


Fig. 2. 2D dimensions of the IPWP vortex generator.

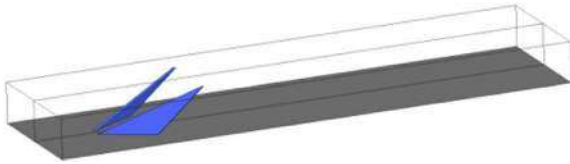


Fig. 3. 3D model of the IPWP vortex generator.

$$TEF = \frac{Nu}{Nu_0} \left(\frac{f}{f_0} \right)^{-\frac{1}{3}} \quad (10)$$

where the index “0” is for the case of empty channel.

Local Nusselt number at a given streamwise location x in the channel is given by:

$$Nu_x = \frac{D_h h_x}{k} = \frac{2Hq_x''}{k(T_s - T_{x,b})} \quad (11)$$

where:

$$T_{x,b} = \frac{\int_A \rho u C_p T dA}{\dot{m} C_p} = \frac{\int_A \rho u C_p T dA}{\rho u C_p dA} = \frac{1}{UA} \int_A u T dA \quad (12)$$

Local friction at a given streamwise location x in the channel is given by:

Table 1
Mesh study information.

Mesh	Maximum element size (mm)	Wall sizing (mm)	Number of elements	Inflation (mm)	Maximum y^+	Nu error (%)
1	3	2	276,321	10 μm –20L	1.55	–
2	2.3	1.5	439,539	20 μm –18L	0.94	5.95
3	1.7	1.15	713,156	30 μm –12L	0.92	3.13
4	1.3	0.9	1,299,018	40 μm –10L	0.82	1.17

$$h = \frac{\dot{m} C_p (T_o - T_{in})}{A_f (T_s - T_{avg})}$$

and

$$T_{avg} = \frac{T_o + T_{in}}{2}$$

Global friction factor is given by:

$$f = \frac{D_h \Delta P}{2L\rho U^2} = \frac{H\Delta P}{L\rho U^2} \quad (7)$$

where the pressure P is averaged over the flow cross section.

The thermal enhancement factor (TEF) is given by:

$$f_x = \frac{\Delta P}{P_{dynamic}} = \frac{2(P_{in} - P_x)}{\rho U^2} \quad (13)$$

For thermally and hydraulically developing laminar air flow, the results are validated for global Nusselt number using Stephan correlation [46], which is the integration of the local Nusselt number (Nu_x) on the channel length based on the bulk temperature at each position $T_{x,b}$. This correlation is valid in the range $0.1 \leq Pr \leq 1,000$ for parallel plate channels.

The local Nusselt number is given by:

$$Nu = \frac{D_h h}{k} = \frac{2H \cdot q''}{k(T_s - T_{x,b})} \quad (14)$$

where q'' is the heat flux at position x and

$$T_b = \frac{1}{UA} \int_A u.T.dA \tag{15}$$

$$Nu_{0-x} = \frac{1}{x} \int_0^x Nu_{(x)}.dx \tag{16}$$

$$Nu_{0-x} = 7.55 + \frac{0.024x^{*-1.14}}{1 + 0.0358x^{*-0.64}Pr^{0.17}} \tag{17}$$

where

$$x^* = \frac{x}{Pe.D_h} = \frac{x}{Re.D_h.Pr.D_h} \tag{18}$$

Local Nusselt number is expressed by the following analytical correlation based on the bulk temperature [46]:

$$Nu_x = 7.55 + 0.024 \frac{0.0179x^{*-1.78}Pr^{0.17} - 0.14x^{*-1.14}}{[1 + 0.0358x^{*-0.64}Pr^{0.17}]^2} \tag{19}$$

The relation that combines the Nusselt number based on the bulk temperature (Nu_x) and the one based on the entrance temperature can be set as:

$$Nu_{e(x)} = Nu_x e^{-\frac{kNu_x}{D_h.m\dot{c}_p}z} \tag{20}$$

Table 2 shows the global Nusselt numbers obtained from simulation compared to Stephan correlation [46] in laminar flow cases studied in this work. It shows that the Nusselt numbers obtained by simulation agrees fairly with that obtained by Stephan's correlation for laminar flow case.

A second approach is also adopted to validate the numerical results with those obtained experimentally by Tiggelbeck's experimental [47]. The results of interest are those dealing with a delta winglet pair (DWP) normalized to an empty channel. Tiggelbeck et al. [47] in their experiments found that the values of the normalized global Nusselt number and friction factor for $Re = 4600$ are equal to 1.49 and 1.91 respectively. Table 3 shows a comparison between numerical simulation and experimental results obtained by Tiggelbeck et al. [47] at $Re = 4600$. The last term corresponds to the thermal enhancement factor. The results are in a good agreement with each other with relatively low discrepancy and the numerical model seems reliable to predict flow and heat transfer characteristics.

3.2. Global performance analysis of vortex enhanced configurations

Fig. 4 plots the thermal enhancement factor for both IPWP and DWP configurations. This figure shows that the IPWP performance is always better than the DWP over the whole range of Reynolds numbers. For laminar flow the enhancement is relatively low (about 2%), while the enhancement is greater (about 6%) in the turbulent flow especially in the range of moderate Reynolds

Table 3

Normalized global Nusselt number, friction factor and thermal enhancement factor comparison between numerical simulation and experimental results at $Re = 4600$.

	Experiment	Simulation	Error (%)
Nu/Nu_0	1.49	1.56	4.69
f/f_0	1.91	1.95	2.09
$(Nu/Nu_0)(f/f_0)^{-1/3}$	1.2	1.25	4.17

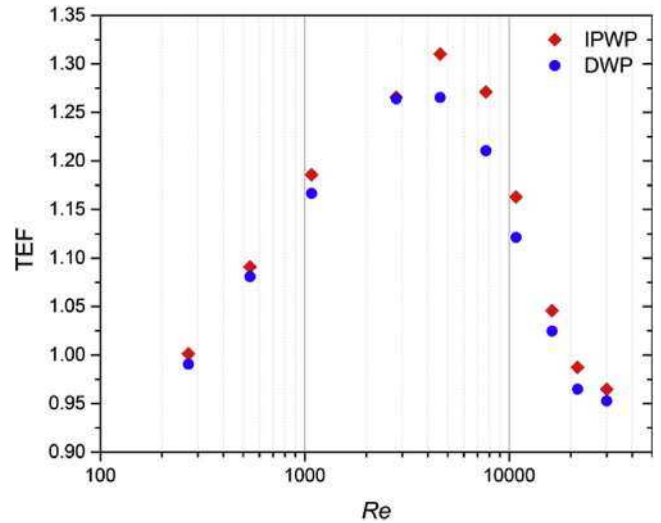


Fig. 4. Thermal enhancement factor (TEF) for DWP and IPWP configurations of vortex generator.

numbers between 4600 and 10,800.

This behavior is related to the difference in the local flow structures generated by the VGs at the different Reynolds numbers. For this aim, a detailed local analysis of the flow and heat transfer is conducted in the next section.

3.3. Local performance analysis

Subsequent to demonstrating the performance of the IPWP on the global scale, this section illustrates the performance from a local point of view. One case is discussed here, corresponding to a $Re = 4,600$, as Tiggelbeck et al. [47] experiment to understand the flow characteristics and to give an explanation of the heat transfer mechanisms.

Fig. 5 shows the streamwise evolution of the spanwise-averaged Nusselt number throughout the channel (see equation (11)). Friction coefficient and vorticity are illustrated respectively in Figs. 6 and 7. The left vertical dotted line with a filled triangle at the bottom of the graph represents the VG leading edge location connected to the bottom wall. The middle one designate for the separation of the bottom trailing edge with the bottom wall while the last vertical line represents the position where the IPWP vortex generator trailing edge separates from the upper wall.

Regarding the local Nusselt number behavior shown in Fig. 5, the IPWP local Nusselt number acts in an oscillatory manner on the

Table 2

Global Nusselt number comparison between simulation and correlations in the case of laminar flow.

Reynolds number Re	Nusselt number Nu	Stephan's correlation [46]	Error (%)
270	7.85	8.42	6.78
540	9.41	9.26	1.62
1080	11.58	10.78	7.41

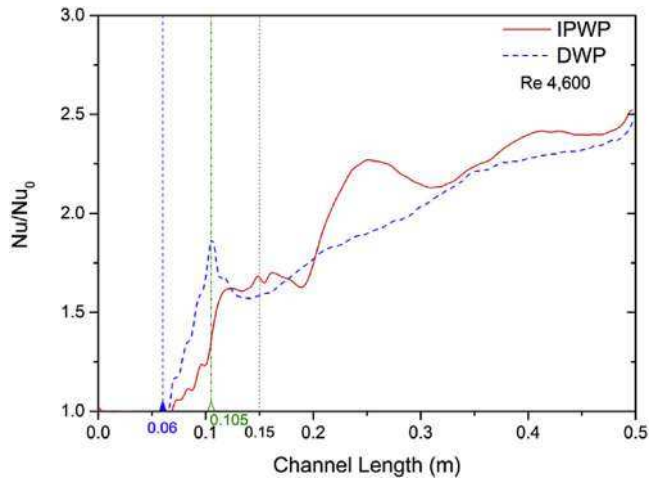


Fig. 5. Normalized local Nusselt number for the IPWP and DWP configurations.

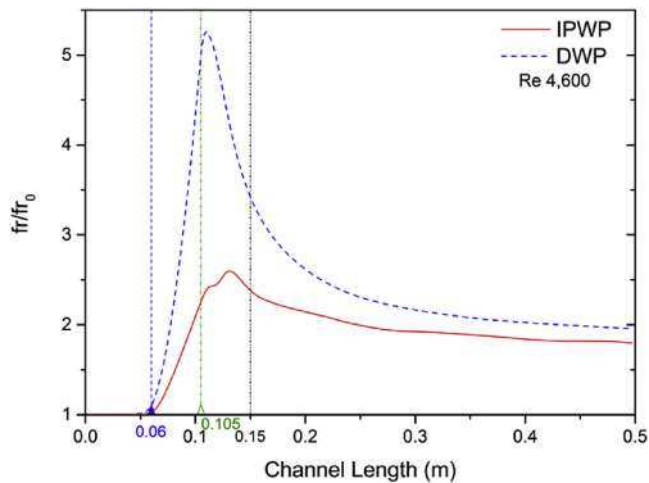


Fig. 6. Normalized local friction coefficient for the IPWP and DWP configurations.

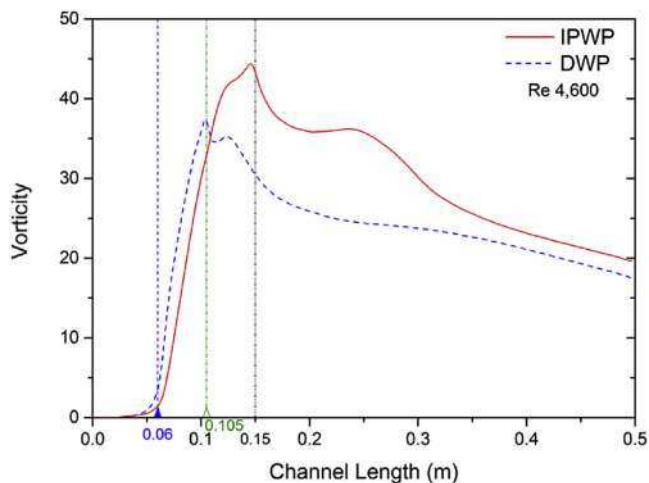


Fig. 7. Vorticity generated by the IPWP and DWP configurations.

contrary of DWP Nusselt number that runs smoothly monotonic downstream the VG. This non-trivial behavior is due to the

generation of several complex induced vortices in addition to the phenomena of moving vortex center across the channel that causes a complex interaction among vortices. Further explanation of this phenomenon is described in the next section. The local Nu in the IPWP is less than that of the DWP upstream the location of the VG but it gets greater than the DWP in the downstream region.

The normalized friction coefficient decreases from a value of 5.25 for a DWP vortex generator to 2.55 for IPWP one. This large decrease in the local friction coefficient is due to the inclination of the new VG configuration that decreases the pressure drop in the flow all along the channel. In addition to the superior performance of the IPWP from the friction point of view, Fig. 7 shows the better production of vorticity for the IPWP configuration over the DWP one. The vorticity produced from the IPWP is slightly lower upstream the VG but it is greatly enhanced in the downstream direction all along the channel, similarly to what has been observed for the local Nusselt number.

To summarize, based on local Nusselt number criterion, both configurations pertain to relatively similar values as shown in Fig. 5 with a small enhancement induced by the IPWP. Fig. 6 illustrates the local friction coefficient of the IPWP compared to the DWP. It's noticeable that the peak in the friction coefficient of the DWP is diminished by about 50% when compared to the IPWP. Moreover, Fig. 7 shows around 30% vorticity increase in the IPWP configuration with respect to the DWP. These better performances of the IPWP vortex generator over others necessitates a deep and detailed analysis of the heat transfer mechanism as discussed in the following section.

3.4. Flow structure and temperature distribution

For thorough examination of the occurring flow and heat transfer mechanisms, cross section planes are made to show the various streamlines and contours in different locations. Fig. 8 shows velocity streamlines and λ_2 contours at different planes for the DWP and IPWP configurations. The concept of λ_2 appeared when Jeong and Hussain [48] propose that a vortex corresponds to a region where two eigenvalues of the symmetric part of the square of the velocity gradient are negative. For further details regarding the identification of a vortex criterion (λ_2), reader may refer to Jeong and Hussain [48].

What is surprising from Fig. 8 is the fact that the IPWP generates more streamwise vortical flow structures than the DWP does. Also Fig. 8 enables to highlight the vortices location inside the channel for the IPWP. The increase in the number of streamwise vortices explains the increase in the Nusselt number and in the streamwise vorticity since more fluid particles are ejected from the near wall regions to the flow core.

For a detailed analysis, let's consider first the development of the vortices generated from a DWP vortex generator inside a parallel plate heat exchanger as presented in Fig. 9. Three vortices for a single VG are generated: a main vortex (a) is generated from the downstream fluid flow over the DWP vortex generator, a corner vortex (b) is developed after reaching the VG bottom trailing edge, and the third secondary vortex (c) is resulted due to the induced viscous force.

Fig. 10 illustrates the generation mechanism of the vortices for the IPWP configuration. A main clock-wise vortex (a) is generated from the downstream fluid flow over the sloped edge of the IPWP vortex generator. The VG base edge separates from the bottom wall of the heat exchanger first, thus producing a bottom counter clock-wise corner vortex (b). When moving downstream, the top edge of the VG separates from the upper wall leading for the generation of the upper counter clock-wise corner vortex (c). Two secondary vortices (d) and (e) are generated due to the induced viscous force

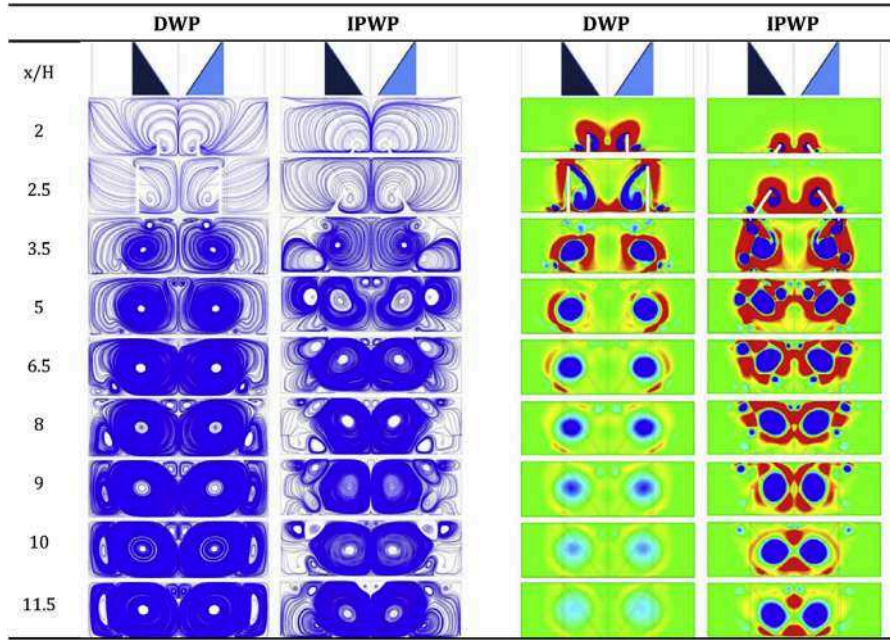
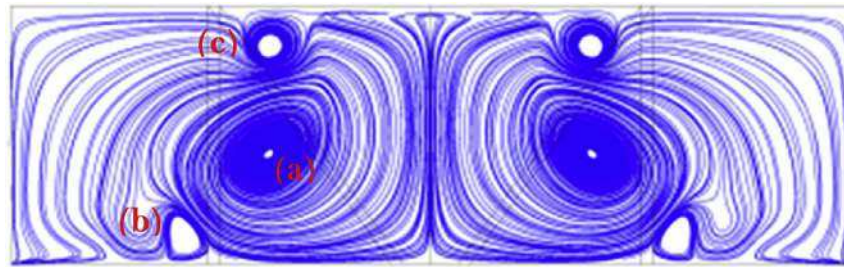


Fig. 8. Velocity streamlines (left) and λ_2 contours (right) for the DWP and IPWP configurations at different section planes.



of the primary vortices. One vortex (d) that rotates in the counter clock-wise direction is developed at the bottom surface and the other (e) at the upper one of the channel spins in the clock-wise direction. The change in vortex center location of the vortices (b) and (c) is established due to the swirl flow of vortex (a). This displacement of the vortices centers is due to the fluid viscous interaction with the main vortex flow. The viscous interaction force moves the center of small vortices in the direction of swirl flow, thus we can see that the centers of vortices (b) and (c) moves in the clockwise direction.

Fig. 8 also shows that the IPWP corner vortex (b) appears earlier than that for DWP but the main difference is that its size grows a lot while it moves towards the mid height of the channel and then towards the upper wall. While for the DWP case, the corner vortex (b) dissipates quite rapidly downstream when compared to the IPWP configuration. This is due to the difference in VG length where IPWP extends to a longer distance that DWP configuration does.

4. Conclusion

Three-dimensional numerical simulations of two configurations of vortex generators are performed to analyze heat transfer enhancement in parallel plate-fin heat exchanger. Laminar flow is

simulated for Reynolds numbers 270, 540 and 1080. Turbulent flow with the aid of the $\kappa-\omega$ SST model is modeled and validated with correlations and experimental data. The DWP configuration of Tiggelbeck et al. [47] is built-up on and used to validate the results obtained through simulations. The aim of this work is to produce a more aerodynamic configuration that reduces pressure drop and enhances heat transfer and mixing performances. IPWP configuration is then introduced by manipulating the winglets' geometry and orientation of the reference case represented by DWP configuration.

IPWP vortex generator shows better performance when compared to the DWP case, taken to be the reference configuration, over a wide range of Reynolds numbers from laminar to turbulent. The IPWP peak friction magnitude is 50% less than that in the DWP. Also the IPWP vorticity is increased by a value of 30% relative to the DWP configuration. Thus the thermal enhancement factor combining the heat transfer increase and the decrease in pressure loss is enhanced by about 6% in the case of the IPWP. This enhancement occurred due to the different vortex generation mechanisms exhibited by the IPWP. The number of vortices created by each pair of VG is six for the DWP case and it reaches ten for the IPWP one. The addition of those vortices positively altered the heat exchange process through the helical flow interaction between them. Thus the present results are very promising as the thermal

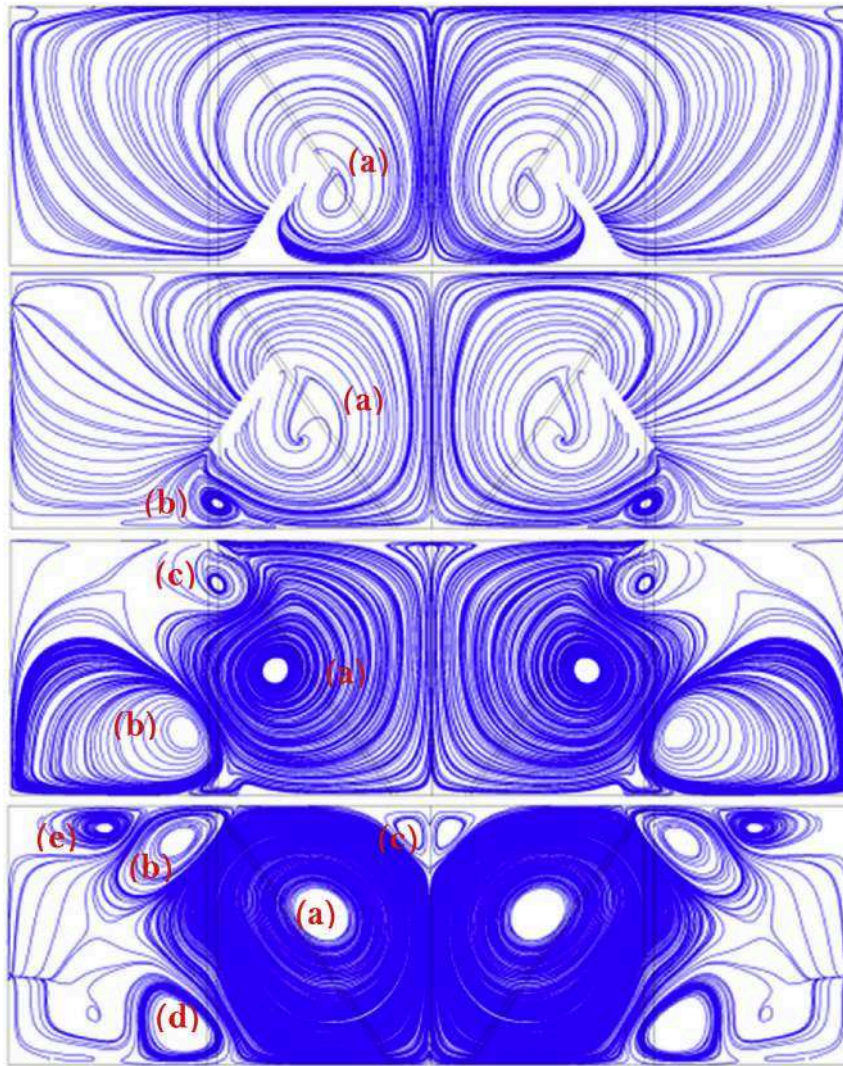


Fig. 10. Vortices developing mechanism for the IPWP at $x/H = 2.5, 3, 3.5$ and 8 from velocity inlet.

enhancement factor is found to be increased 6% for IPWP vortex generator compared to DWP case.

References

- [1] Lin J. Review of research on low-profile vortex generators to control boundary-layer separation. *Prog Aerosp Sci* 2002;38:389–420.
- [2] Islam MR, Hossain MA, Mashud M, Tanvir M. Drag reduction of a car by using vortex generator. *Int J Sci Eng Res* 2013;4(7).
- [3] Ghanem A, Lemenand T, Della Valle D, Peerhossaini H. Static mixers: mechanisms, applications, and characterization methods – a review. *Chem Eng Res Des* 2014;92(2):205–28.
- [4] Hatami M, Ganji D, Gorji-Bandpy M. Experimental investigations of diesel exhaust exergy recovery using delta winglet vortex generator heat exchanger. *Int J Therm Sci* 2015;93:52–63.
- [5] Biswas G, Torii K, Fujii D, Nishino K. Numerical and experimental determination of flow structure and heat transfer effects of longitudinal vortices in a channel flow. *Int J Heat Mass Transf* 1996;39(16):3441–51.
- [6] Webb R, Kim N. Principles of enhanced heat transfer. New York: Wiley; 1994.
- [7] Chang SW, Lees AW, Chang H-T. Influence of spiky twisted tape insert on thermal fluid performances of tubular air–water bubbly flow. *Int J Therm Sci* 2009;48:2341–54.
- [8] Gül H, Evin D. Heat transfer enhancement in circular tubes using helical swirl generator insert at the entrance. *Int J Therm Sci* 2007;46:1297–303.
- [9] Elyyan MA, Tafti DK. A novel split-dimple interrupted fin configuration for heat transfer augmentation. *Int J Heat Mass Transf* 2009;52:1561–72.
- [10] Habchi C, Russeil S, Bougeard D, Harion JL, Lemenand T, Della Valle D, et al. Enhancing heat transfer in vortex generator-type multifunctional heat exchangers. *Appl Therm Eng* 2012;38:14–25.
- [11] Tala J, Russeil S, Bougeard D, Harion J-L. Numerical analysis of the fin spacing effect on the horseshoe vortex system evolution in a two-rows finned-tube heat exchanger. *Int J Numer Methods Heat Fluid Flow* 2013;23(7):1136–54.
- [12] Vintrou S, Bougeard D, Russeil S, Nacereddine R, Harion J-L. Quantitative infrared investigation of local heat transfer in a circular finned tube heat exchanger assembly. *Int J Heat Fluid Flow* 2013;104:197–207.
- [13] Garcia A, Solano J, Vicente P, Viedma A. The influence of artificial roughness shape on heat transfer enhancement: corrugate tubes, dimpled tubes and wire coils. *Appl Therm Eng* 2012;35:196–201.
- [14] Wang J, Zhao Y. Heat and fluid flow characteristics of a rectangular channel with a small diameter circular cylinder as vortex generator. *Int J Therm Sci* 2015;92:1–13.
- [15] Habchi C, Lemenand T, Della Valle D, Peerhossaini H. Turbulence behavior of artificially generated vorticity. *J Turbul* 2010;11(36):1–28.
- [16] Khoshvaght-Aliabadi M, Zangouei S, Hormozi F. Performance of a plate-fin heat exchanger with vortex-generator channels: 3D-CFD simulation and experimental validation. *Int J Therm Sci* 2015;88:180–92.
- [17] Wu J, Tao W. Numerical study on laminar convection heat transfer in a channel with longitudinal vortex generator. Part B: parametric study of major influence factors. *Int J Heat Mass Transf* 2008;51:3683–92.
- [18] Saha P, Biswas G, Sarkar S. Comparison of winglet-type vortex generators periodically deployed in a plate-fin heat exchanger – a synergy based analysis. *Int J Heat Mass Transf* 2014;74:292–305.
- [19] Habchi C, Harion JL, Russeil S, Bougeard D, Hachem F, Elmarakbi A. Chaotic mixing by longitudinal vorticity. *Chem Eng Sci* 2013;104:439–50.
- [20] Habchi C, Lemenand T, Della Valle D, Al Shaer A, Peerhossaini H. Experimental study of the flow field behind a perforated vortex generator. *J Appl Mech Tech Phys* 2015;16:221–9.
- [21] Li L, Du X, Zhang Y, Yang L, Yang Y. Numerical simulation on flow and heat

- transfer of fin-and-tube heat exchanger with longitudinal vortex generators. *Int J Therm Sci* 2015;92:85–96.
- [22] Biswas G, Mitra N, Fiebig M. Heat transfer enhancement in fin-tube heat exchangers by winglet type vortex generators. *Int J Heat Mass Transf* 1994;37(2):283–91.
- [23] Deb P, Biswas G, Mitra N. Heat transfer and flow structure in laminar and turbulent flows in a rectangular channel with longitudinal vortices. *Int J Heat Mass Transf* 1995;38(13):2427–44.
- [24] Kamboj R, Dhingra PS, Singh PG. CFD simulation of heat transfer enhancement by plain and curved winglet type vortex generators with punched holes. *Int J Eng Res General Sci* 2014;2(4).
- [25] Zhou G, Feng Z. Experimental investigations of heat transfer enhancement by plane and curved winglet type vortex generators with punched holes. *Int J Therm Sci* April 2014;78:26–35.
- [26] He J, Liu L, Jacobi AM. Air-side heat-transfer enhancement by a new winglet-type vortex generator array in a plain-fin round-tube heat exchanger. *J Heat Transf* July 2010;132. pp. 071801–1 till 071801-9.
- [27] He Y, Han H, Tao YZ. Numerical study of heat-transfer enhancement by punched winglet-type vortex generator arrays in fin-and-tube heat exchangers. *Int J Heat Mass Transf* 2012;55:5449–58.
- [28] Wu J, Tao WQ. Investigation on laminar convection heat transfer in fin-and-tube heat exchanger in aligned arrangement with longitudinal vortex generator from the viewpoint of field synergy principle. *Appl Therm Eng* 2007;27: 2609–17.
- [29] Herpe J, Bougeard D, Russeil S, Stanciu M. Numerical investigation of local entropy production rate of a finned oval tube with vortex generators. *Int J Therm Sci* 2009;48:922–35.
- [30] Fiebig M. Embedded vortices in internal flow: heat transfer and pressure loss enhancement. *Int J Heat Fluid Flow* 1995;16(5):376–88.
- [31] Tiggelbeck S, Mitra N, Fiebig M. Flow structure and heat transfer in a channel with multiple longitudinal vortex generators. *Exp Therm Fluid Sci* 1992;5(4): 425–36.
- [32] Ghanem A, Habchi C, Lemenand T, Della Valle D, Peerhossaini H. Energy efficiency in process industry – high-efficiency vortex (HEV) multifunctional heat exchanger. *Renew Energy* 2013;56:96–104.
- [33] Fiebig M. Vortex generators for compact heat exchangers. *J Enhanc Heat Transf* 1995;2(1–2):43–61.
- [34] Tian L, He Y, Lei Y. Numerical study of fluid flow and heat transfer in a flat plate channel with longitudinal vortex generators by applying field synergy principle analysis. *Int Commun Heat Mass Transf* 2009;36(2):111–20.
- [35] Jain A, Biswas G, Maurya D. Winglet-type vortex generators with common-flow-up configuration for fin-tube heat exchangers. *Numer Heat Transf Part A* 2003;43:201–19.
- [36] I. ANSYS. Turbulence models. ANSYS fluent 12.0 theory guide. April 2009. p. 27.
- [37] Menter F. Two-equation eddy-viscosity turbulence models for engineering applications. *AIAA* 1994;32:1598–605.
- [38] I. ANSYS. Standard and SST k-w models. ANSYS fluent 12.0 theory guide. April 2009. p. 131–5.
- [39] Yongsiri K, Eiamsa-ard P, Wongcharee K, Eiamsa-ard S. Augmented heat transfer in a turbulent channel flow with inclined detached-ribs. *Case Stud Therm Eng* 2014;3:1–10.
- [40] Tanga X-Y, Zhu D-S. Flow structure and heat transfer in a narrow rectangular channel with different discrete rib arrays. *Chem Eng Process Process Intensif* 2013;69:1–14.
- [41] Warming R, Beam R. Upwind second-order difference schemes and applications in aerodynamic flows. *AIAA J* 1976;14(9). pp. 1241–2149.
- [42] Nacer-Bey M, Russeil S, Baudoin B. PIV visualizations to the flow structure upstream of the tubes in a two-row plate-fin-and-tube heat exchanger. In: *Proceeding of the 4th International conference on compact heat exchangers and enhancement technology for the process Industries*, Grete Island, Greece; September 29-October 3, 2003. p. 63–8.
- [43] Versteeg H, Mallasekera W. *Computational fluid Dynamics*. London: Longman Group; 1995.
- [44] Zikanov O. *Essential computational fluid Dynamics*. Hoboken: Wiley; 2010.
- [45] Naphon P, Kornkumjayrit K. Numerical analysis on the flow and heat transfer in the channel with V-shaped wavy lower plate. *Int Commun Heat Mass Transf* 2008;35:839–43.
- [46] Bejan A, Kraus A. *Heat transfer handbook*, vol. 1. New Jersey: Wiley; 2003. p. 395–438.
- [47] Tiggelbeck S, Mitra NK, Fiebig M. Comparison of wing-type vortex generators for heat transfer enhancement in channel flows. *J Heat Transf* 1994;116: 880–5.
- [48] Jeong J, Hussain F. On the identification of a vortex. *J Fluid Mech* 1995;285: 69–94.

Chapitre 6

Optimisation de l'angle d'inclinaison du générateur de vorticité IPWP « Inclined Projected Winglet Pair »

Dans ce chapitre, un grand nombre de simulations numériques tridimensionnelles correspondant à plus de dix configurations géométriques de générateurs de vorticité différents sont effectuées afin d'analyser les phénomènes d'intensification des transferts thermiques dans un échangeur de chaleur à plaques-ailettes parallèle.

Un modèle laminaire est utilisé pour les nombres de Reynolds 270, 540 et 1080, tandis que pour les écoulements turbulents un modèle $k - \omega$ est utilisé et validé à partir de résultats expérimentaux et de corrélations.

L'objectif de ce travail est de déterminer l'angle d'inclinaison optimal qui permet de réduire la perte de charge et intensifier le transfert de chaleur et les performances de mélange. Les configurations IPWP avec différents angles d'inclinaison (25°, 30°, 32°, 35°, 38°, 40°, 45°, 50°, 55° et 60°) sont ensuite présentées en modifiant la géométrie et l'orientation des « winglets ».

Afin d'expliquer les effets de l'angle d'inclinaison sur le transfert de chaleur et la perte de charge, une technique de surface de réponse (RSM) est utilisée pour analyser ces résultats au niveau global. La performance locale est analysée en étudiant la distribution des nombres de Nusselt locaux et du coefficient de frottement en complément de l'hélicité. On constate que l'IPWP avec un angle d'inclinaison dans la plage de 30° à 35° confère la meilleure performance globale par rapport à toutes les autres inclinaisons. La valeur du pic du

coefficient de frottement de la configuration IPWP-30 est de 50% inférieure à celle enregistrée par la configuration DWP de référence, et pour une inclinaison du VG encore plus forte on peut atteindre une diminution de ce pic de 70% (cas IPWP-60). Le coefficient de frottement moyen pondéré en surface par rapport au cas DWP diminue de 18% pour la configuration IPWP-30, atteignant environ 43% de diminution pour le cas IPWP-60. La configuration IPWP-30 présente l'augmentation maximale de l'hélicité moyenne avec une augmentation de 35,5% par rapport au cas DWP. De plus, nous montrons que le nombre de tourbillons à différentes échelles atteint huit (deux principaux et six vortex induits) pour la configuration IPWP-30 tandis que nous n'observons que deux tourbillons principaux pour d'autres configurations. Enfin, le « facteur d'amélioration thermique » est augmenté de 6% pour les générateurs de vortex IPWP-30 et IPWP-35 par rapport au cas DWP.

Cette étude met ainsi en évidence l'optimisation des échanges convectifs apportée par la configuration IPWP en se basant sur le facteur d'amélioration thermique (TEF), en fonction de l'angle d'inclinaison du VG.

Inclination Angle Optimization for “Inclined Projected Winglet Pair” Vortex Generator

Mohammad Oneissi ^{a,b}, Charbel Habchi ^c, Serge Russeil ^{a,*}, Daniel Bougeard ^a, Thierry Lemenand ^b

^a Mines Douai, EI, F59500 Douai, France

^b Angers University, ISTIA, LARIS EA 7315, Angers, France

^cNotre Dame University - Louaize, Mechanical Engineering Department, P.O. Box: 72 Zouk Mikael, Zouk Mosbeh, Lebanon

Abstract

Vortex generators (VG) are widely used in heat exchangers for augmenting the heat transfer from fin plates to the working fluid. In the present study, three-dimensional numerical simulations for longitudinal vortex generators (VG) are performed to examine the heat transfer enhancement in parallel plate-fin heat exchanger. The shear-stress transport (SST) κ - ω model is used for modeling turbulence. Inclination angle for a new VG configuration named Inclined Projected Winglet Pair (IPWP) proposed by Oneissi et al. [International Journal of Thermal Sciences, 109, 1-9, (2016)], was varied to study the effect of this angle on heat transfer. Response surface methodology (RSM) was used to deduce the inclination angle effects on heat transfer, pressure drop and vorticity from a global point of view. Based on the streamwise distribution of Nusselt number and friction coefficient criteria in addition to helicity, the local performance is also evaluated. Such study highlights the optimization for IPWP configuration involved in the convective heat transfer intensification, based on thermal enhancement factor (TEF), by varying the VG's inclination angle. Finally, it is found that the

* Corresponding author.

Tel.: +33 3 27 71 23 88; fax: +33 3 27 71 29 15

Email address: serge.russeil@mines-douai.fr (S. Russeil)

IPWP with inclination angle ranging from 30° to 35° exhibits the best global performance compared to other inclinations.

Keywords:

Heat transfer enhancement; winglet pair; vortex generator; plate-fin heat exchanger; parallel-plate channel; longitudinal vortices; numerical simulation; optimization.

Nomenclature

A	Cross-sectional area, m^2	U	Mean flow velocity, $m s^{-1}$
B	Channel width, m	u	Flow velocity in x direction, $m s^{-1}$
C_p	Specific heat at constant pressure, $J kg^{-1}K^{-1}$	v	Flow velocity in y direction, $m s^{-1}$
D_h	Hydraulic diameter, m	w	Flow velocity in z direction, $m s^{-1}$
f	Friction factor		
H	Channel height, m		
h	Convective heat transfer coefficient, $W m^{-2}K^{-1}$		
			Greek letters
		μ	Dynamic viscosity, Pa s
k	Thermal conductivity, $W m^{-1}K^{-1}$	ν	Kinematic viscosity, $m^2 s^{-1}$
L	Channel length, m	ρ	Fluid density, $kg m^{-3}$
\dot{m}	Mass flow rate, $kg s^{-1}$		Abbreviations
Nu	Nusselt number	VG	Vortex Generator
Pe	Péclet number= Re. Pr	DWP	Delta Winglet Pair
Po	Poiseuille number	RSM	Response Surface Methodology
Pr	Prandtl number	IPWP	Inclined Projected Winglet Pair
ΔP	Pressure drop, Pa	LVG	Longitudinal Vortex Generator
q''	Heat flux, $W m^{-2}$	TVG	Transverse Vortex Generator
Re	Reynolds number	CFD	Computational Fluid Dynamics
s	Distance between tips of winglet pair, m	SST	Shear-Stress Transport
$T_{b,x}$	Bulk temperature at position x, K	TEF	Thermal Enhancement Factor
T_i	Inlet temperature, K		
T_o	Outlet bulk temperature, K		
T_s	Surface temperature, K		

1. Introduction

Heat transfer intensification has been an essential subject for many years for several industrial applications, due to increasing demands and energy savings. Heat exchangers are considered one of the main and important issues in this domain since they are world widely used in power systems, air conditioning, aerospace industry and many other applications. In the field of heat exchangers, enhancing the heat transfer process between the fin and the working fluid is crucial for increasing efficiency and compactness. Convective heat transfer enhancement in a heat exchanger is accomplished by either active or passive methods [1]. Due to many reasons such as efficiency, industry, economy and maintenance supremacy of passive methods, vortex generators (VG) are widely used in this field. Various types of vortex generators exist that include helical and twisted inserts [2, 3], dimples or protrusions [4, 5], cylindrical tubes [6, 7], transverse vortex generators (TVG) [5], longitudinal vortex generators (LVGs) [8, 9], plane or curved surface of VG [10, 11] or a combination of the above types [12, 13]. LVGs are found to have an advantage over TVGs in terms of global mixing and heat transfer performances [14]. This paper focuses on the study of LVG and their unique capability in heat transfer enhancement through the generation of large scale longitudinal vortices.

Finding the optimum performance of a vortex generator depending on specific criteria is also critical. In fact, many parameters may alter the performance of the heat exchanger, thus varying the VG shape, angle of attack, position, composition with other types, Reynolds number, and many others is a field of consideration for many researchers. Saliviano et al. [15] studied the optimization of VG position and angles in a fin-tube compact heat exchanger using the genetic algorithm. Results were evaluated using direct optimization and by RSM. Lei et al. [16] studied the effect of changing the angle of attack for delta-winglet vortex generator between 10° and 50° , in addition to changing aspect ratio from 1 to 4 and the

Reynolds number from 600 to 2600. It was found that the delta-winglet vortex generator with an attack angle of 20° and an aspect ratio of 2 provides the best integrated performance over the range of Reynolds number computed. Heat transfer enhancement by punched winglet-type VG arrays in fin-and-tube heat exchangers using numerical studies was investigated by He et al. [12]. They varied the VG angle of attack and spacing between staggered VGs and concluded that the heat transfer and pressure drop increase as angle of attack increases. Lemouedda et al. [17] examined an optimization of the angle of attack of delta-winglet VGs in a plate-fin-and-tube heat exchangers using a combination among numerical analysis, genetic algorithm and RSM. Angle of attack was varied between -90° and 90° for Reynolds numbers between 200 and 1200. They found that for the inline arrangement the common-flow-down configuration is more suitable than the common-flow-up. Wu and Tao [8] presented numerical simulation results for laminar flow (Reynolds numbers from 800 to 2000) of heat transfer of the fin-and-tube surface with vortex generators at two angles of attack (30° and 45°). They found that the delta winglet with the attack angle of 45° enhances the heat transfer while increasing pressure drop. Also, Wu and Tao [18] studied experimentally and numerically the convective heat transfer on the top and bottom surfaces of a plain plate and four plates with delta winglet VG pair in laminar flow. The VG was directly punched from the plates at different angle of attacks (15° , 30° , 45° and 60°). They deduced that the average Nusselt number of the plate with 60° angle of attack is slightly higher than that of 45° attack angle. Yongsiri et al. [19] made numerical study of flow and heat transfer in channel with various inclined detached ribs for turbulent flow ($Re= 4000$ to 24000). The angle of attack examined was varied from 0° to 165° and it was revealed that for high Reynolds number the inclined ribs with 60° and 120° yield to a better (although comparable) heat transfer performance over other angles. However, for low Reynolds number, the effect of angle of attack was not significant.

Many optimization and parametric studies have been made concerning vortex generators alignments, positions, angles and other factors. Most of these studies were oriented towards having a combination between LVGs and tubes in laminar or relatively low Reynolds numbers without studying the absolute effect of the LVG. Thus, as a developing work of Oneissi et al. [20], the aim of this study is to analyze the effects of varying the inclination angle of the IPWP configuration on the flow structure and thus on the heat transfer mechanism over a wide range of Reynolds number. These effects are presented with response surface methodology (RSM) as a function of incidence angle (α) and Reynolds number (Re). RSM is a collection of statistical and mathematical techniques useful for developing, improving thus optimizing a case study, showing the response for changing several input variables. Direct optimization can be imposed on RSM showing the maximum or minimum of the function.

The numerical method, computational domain and mesh sensitivity analysis are presented in the problem description in Section 2. Numerical validation, global performance followed by local examination of the heat transfer phenomena are discussed in Section 3. Section 4 is devoted to the concluding remarks.

2. Problem description

2.1 Numerical model

Three-dimensional (3D) numerical simulations of the flow and heat transfer in a parallel plate channel with new vortex generators is carried out for laminar and turbulence regimes.

The following assumptions are used for the numerical simulations:

- Steady three-dimensional fluid flow and heat transfer.
- The flow is incompressible
- Fluid properties are constant.

- Radiation heat transfer, body forces and viscous dissipation are neglected.

Based on the above assumptions, the channel flow is governed by the 3D steady-state Reynolds-Averaged Navier-Stokes (RANS) equations. The continuity and momentum equations for an incompressible Newtonian fluid are:

$$\frac{\partial u_i}{\partial x_i} = 0 \quad (1)$$

$$u_j \frac{\partial u_i}{\partial x_j} = -\frac{1}{\rho} \frac{\partial p}{\partial x_i} + \nu \frac{\partial^2 u_i}{\partial x_j \partial x_j} - \frac{\partial \overline{u'_i u'_j}}{\partial x_j} \quad (2)$$

where the term $-\overline{u'_i u'_j}$ is the Reynolds stress tensor resulting from the averaging procedure on the nonlinear convective terms in the momentum equations. The heat transfer is computed by solving the energy equation:

$$\frac{\partial}{\partial x_i} [u_i (\rho E + p)] = \frac{\partial}{\partial x_i} (\lambda_{eff} \frac{\partial T}{\partial x_i}) \quad (3)$$

where E is the total energy and λ_{eff} the effective thermal conductivity.

All computations are performed using ANSYS Fluent 15 CFD code based on an Eulerian approach to solve the Cauchy equations through cell-centered finite volume discretization [5]. Mass and momentum conservation equations are solved by the code in addition to the energy equation for flows involving heat transfer [21]. Turbulence models allow the calculation of the mean flow without first calculating the full time-dependent flow field. Turbulence model must have wide applicability, accuracy, simplicity and time frugality.

Shear-stress transport (SST) κ - ω model developed by Menter [22] is used in this study for turbulent flows. This model solves two additional partial differential equations, a modified version of the turbulence kinetic energy equation κ used in κ - ε model and a transport one for the specific dissipation ω . Also, the shear stress transport combines the use of κ - ω formulation in the inner parts of the boundary layer and the switching to a κ - ε behavior in the

free-stream thus avoiding the κ - ω sensitivity to the inlet free-stream turbulence properties. In addition to that, it is characterized by its good behavior in adverse pressure gradients and separating flows while attaining accuracy and reliability [21].

The preceding attributes give the SST κ - ω model additional accuracy and reliability thus providing it an advantage over the standard κ - ω model. Moreover, the SST κ - ω model was used by many researchers in previous works that gave a fair matching with experimental results [19, 23]. Therefore, the SST κ - ω turbulence model is adopted in the present study.

This approach necessitates assessment of the wall adjacent cell size analogous to the dimensionless wall distance y^+ less than 4, ensuring that the viscous sublayer is meshed.

The SST κ - ω model transport equations are:

$$\rho \frac{\partial}{\partial x_i} (\kappa u_i) = \frac{\partial}{\partial x_j} \left(\Gamma_\kappa \frac{\partial \kappa}{\partial x_j} \right) + \tilde{G}_\kappa - Y_\kappa \quad (4)$$

$$\rho \frac{\partial}{\partial x_i} (\omega u_i) = \frac{\partial}{\partial x_j} \left(\Gamma_\omega \frac{\partial \omega}{\partial x_j} \right) + G_\omega - Y_\omega + D_\omega \quad (5)$$

where

\tilde{G}_κ is the production of turbulence kinetic energy due to mean velocity gradients,

G_ω is the generation of ω ,

Γ_κ is the effective diffusivity of κ ; $\Gamma_\kappa = \mu + \frac{\mu_t}{\sigma_\kappa}$,

Γ_ω is the effective diffusivity of ω ; $\Gamma_\omega = \mu + \frac{\mu_t}{\sigma_\omega}$,

Y_κ is the dissipation of κ due to turbulence,

Y_ω is the dissipation of ω due to turbulence,

D_ω is the cross-diffusion,

$\sigma_\kappa, \sigma_\omega$ are the turbulent Prandtl number for κ and ω respectively,

μ_t is the turbulent viscosity.

For detailed discussion of these equations refer to [21]. Double precision and second order upwind is used to consecutively solve the flow equations for spatial discretization of the convective terms [24]. Central-difference and second order accuracy are selected for the diffusion terms. The Coupled algorithm is used for the pressure-velocity coupling with the pseudo transient option which is a form of implicit under-relaxation for steady-state cases. Pseudo option allows the user to obtain solutions faster and more robustly.

2.2 Computational domain

In this study, x is defined as the streamwise direction, y as the spanwise direction and z for the fin pitch direction. Dimensions of the channel simulated are similar to Oneissi et al. [20] case taken from a previously designed experimental benchmark. A height $H=38.6$ mm, breadth $B=1.6H$ and length $L=13H$ are the main dimensions of this channel. An isometric view showing the boundary conditions are presented in Figure 1.

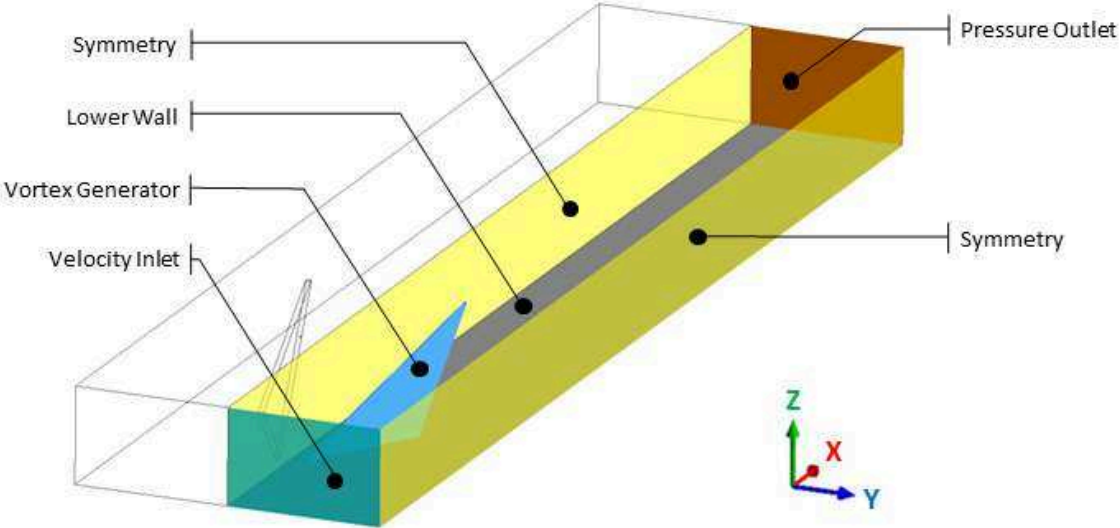


Figure 1 Isometric view of the computational domain showing the boundary conditions.

Figure 2 shows the dimensions of the delta winglet pair (DWP), the 30° inclined delta winglet pair (named as IPWP-30) and the 60° IPWP (named as IPWP-60) vortex generators. The same base and height dimensions are conserved for all VGs while the incident angle is varied for each IPWP. Note that the incident angle is the complementary angle of the inclination angle (Inclination angle (α) + Incident angle = 90°), since angle of incidence is measured from the base plane while angle of inclination is measured from the DWP vertical plane. These geometries are obtained by the frontal projection of the DWP on inclined planes from the base axis. The studied planes inclination angles are 0° for the DWP case (DWP corresponding to IPWP-0), 25° , 30° , 32° , 35° , 38° , 40° , 45° , 50° , 55° and 60° for the IPWP configurations.

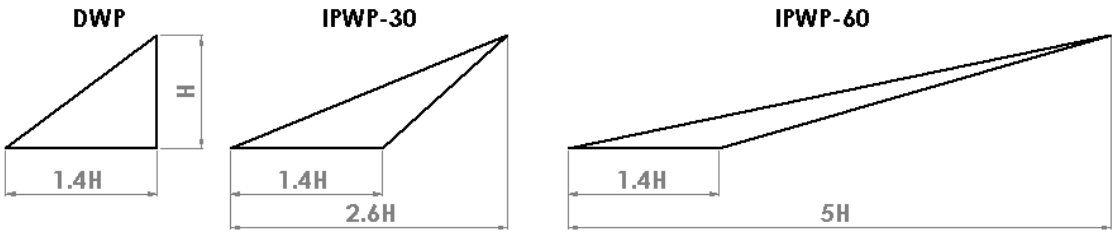


Figure 2 DWP (or IPWP-0), IPWP-30 and IPWP-60 geometric dimensions.

Figure 3 shows an isometric view of the IPWP-60 where the long projection is visible and may reach a length of 5H. Studied VGs length ranges between 1.4H for the DWP till 5H for the IPWP-60.

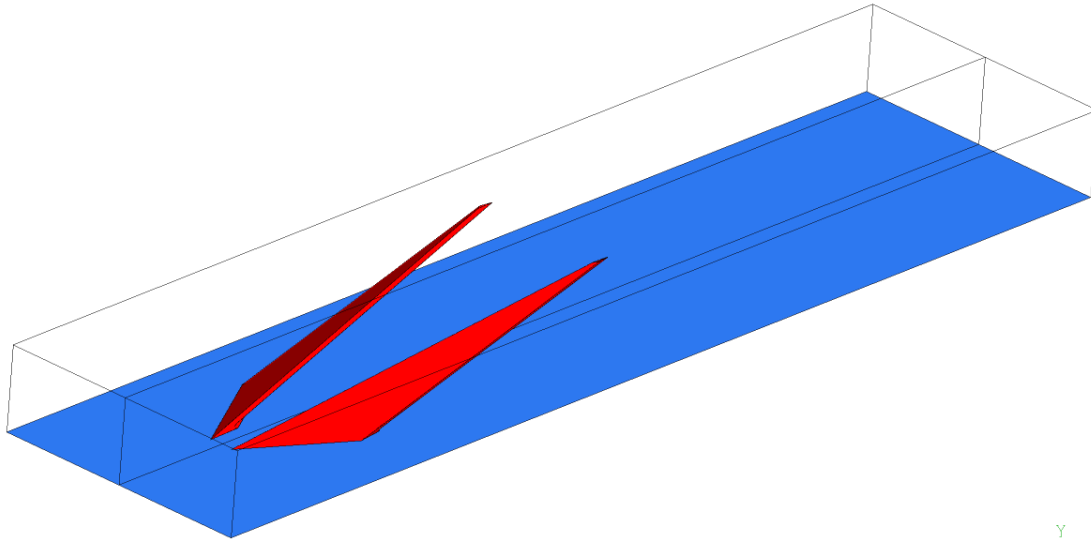


Figure 3 3D model of the IPWP-60 vortex generator.

The Reynolds number is calculated based on the hydraulic diameter $D_h = 2H$. A hydrodynamic and thermally developing flow is computed with a uniform inlet velocity profile and uniform inlet temperature equal to 300 K for all studied Reynolds numbers (270, 540, 1080, 2800, 4600, 7700, 10800, 16200, 21600 and 30000) while the velocity magnitude varies for each Reynolds number. A constant pressure outlet condition has been set for the outlet with a zero gauge pressure. Isothermal walls are set for both, upper and bottom, walls with a constant temperature of 350 K. All VG cases have been simulated as an adiabatic wall to highlight the effect of the flow structure on the convective heat transfer and exclude the varying VG surface area effects. Turbulence intensity at the inlet has a dramatic influence on local and global results in turbulent flows. Proper turbulence intensity has to be chosen and in this study, turbulence intensity equal to 3% is selected. First, it is in the range of the moderate wind tunnel intensities (1%–5%). Second, this value for the turbulence intensity was used in recent papers [20, 25]. Also, the turbulence length scale, taken as a fraction of the inlet hydraulic diameter D_h , can be chosen equal to $0.07D_h$ as used in similar flow configurations

or choosing the turbulence intensity with the hydraulic diameter is also valid and gives same results for our cases.

The goal behind this study is to analyze the effect of VG inclination angle on heat enhancement, pressure drop and vorticity while maintaining the same frontal area of the DWP case (90° elevation angle with the bottom wall). This means that if any of the VGs are projected on a transvers plane normal to the x-axis, it will produce the same projected shape and the same area. An area projection on 25° , 30° , 32° , 35° , 38° , 40° , 45° , 50° , 55° and 60° inclined planes of the DWP is depicted. To state the matter differently, if the DWP surface is inclined by an angle about the lower edge and then an extrusion of the DWP is made in the downstream direction, then the result is an inclined projected winglet pair (IPWP).

2.3 Mesh sensitivity study

Mesh used in this work is based on a previous study done by Oneissi et al. [20] where a non-uniform mesh with polyhedral cells is used for the computational domain. All walls in the channel are treated with 10 inflation layers with $40\ \mu\text{m}$ first layer thickness for attaining an acceptable y^+ value. Mesh independency is carried out on an empty channel turbulent flow where $Re=21600$ is used. Grids used for the mesh sensitivity are presented in Table 1. Procedure conducted to reach the mesh size adapted in the simulation is the following: arbitrary maximum element size is selected then decreased by a factor of 1.3 until the percent error based on both global Nusselt and friction coefficient reaches a value less than 2%. Thus, mesh-3 is used for all the simulations due to the non-necessity of any further refinement. Also, mesh validation with experimental results are already studied and depicted by Oneissi et al. [20] on the same configuration.

Table 1 Mesh study information.

Mesh	1	2	3
Maximum element size (mm)	2.30	1.70	1.30
Wall sizing (mm)	1.50	1.15	0.90
Type of mesh	Polyhedral	Polyhedral	Polyhedral
Number of elements	815,265	1,344,799	2,572,124
Inflation (mm)	20 μ m–18L	30 μ m–12L	40 μ m–10L
Maximum y^+	0.90	0.80	0.80
Error (%)	-	2.00	1.00

3. Results and discussions

3.1 Quantitative parameters and experimental validation

Developing flow (velocity and temperature) case is simulated by applying uniform velocity and temperature profiles at the inlet boundary condition. The performance evaluation of the different configurations is dismantled into two main categories, global and local approaches.

Global Nusselt number is given by:

$$\overline{Nu} = \frac{D_h h}{k} = \frac{2Hh}{k} \quad (6)$$

where $h = \frac{\dot{m}C_p(T_o - T_i)}{A_f(T_s - T_{avg})}$ is obtained from the energy balance on a control volume enclosing the channel, and $T_{avg} = \frac{T_o + T_{in}}{2}$ is the average temperature between the inlet and outlet.

Global friction factor is given by:

$$f = \frac{D_h \Delta P}{2L\rho U^2} = \frac{H\Delta P}{L\rho U^2} \quad (7)$$

The thermal enhancement factor (TEF) is given by:

$$TEF = \frac{Nu}{Nu_0} \left(\frac{f}{f_0} \right)^{-1/3} \quad (8)$$

where Nu_0 is the global Nusselt number for empty channel, Nu is the global Nusselt number for channel with VG, f_0 is the global friction coefficient for empty channel and f is the global friction coefficient for channel with VG.

Local Nusselt number at a given x location in the channel is given by:

$$Nu_x = \frac{D_h h_x}{k} = \frac{2Hq_x''}{k(T_s - T_{x,b})} \quad (9)$$

where:

$$T_{x,b} = \frac{\int_A \rho u C_p T dA}{\dot{m} C_p} = \frac{\int_A \rho u C_p T dA}{\rho u C_p dA} = \frac{1}{UA} \int_A u T dA \quad (10)$$

Local friction at a given x location in the channel is given by:

$$f_x = \frac{\Delta P}{P_{dynamic}} = \frac{2(P_{in} - P_x)}{\rho U^2} \quad (11)$$

For thermally and hydraulically developing laminar air flow, the results are validated for global Nusselt number using Stephan correlation [26]. It is the integration of the local Nusselt number (Nu_x) on the channel length and it is defined based on the bulk temperature at each position $T_{x,b}$. This correlation is valid in the range $0.1 \leq Pr \leq 1000$ for parallel plate channels.

The local Nusselt number is given by:

$$Nu = \frac{D_h h}{k} = \frac{2Hq''}{k(T_s - T_b)} \quad (12)$$

where q'' is the heat flux at position x and

$$T_b = \frac{1}{UA} \int_A u T dA \quad (13)$$

$$Nu_{0-x} = \frac{1}{x} \int_0^x Nu_{(x)} dx \quad (14)$$

and

$$Nu_{0-x} = 7.55 + \frac{0.024x^{*-1.14}}{1 + 0.0358x^{*-0.64}Pr^{0.17}} \quad (15)$$

where

$$x^* = \frac{x}{PeD_h} = \frac{x}{ReD_h PrD_h} \quad (16)$$

Local Nusselt number is expressed by the following analytical correlation based on the bulk temperature:

$$Nu_x = 7.55 + 0.024 \frac{0.0179x^{*-1.78}Pr^{0.17} - 0.14x^{*-1.14}}{[1 + 0.0358x^{*-0.64}Pr^{0.17}]^2} \quad (17)$$

The relation that combines the Nusselt number based on the bulk temperature (Nu_x) and the one based on the entrance temperature can be set as:

$$Nu_{e(x)} = Nu_x e^{-\frac{kNu_x}{D_h \dot{m} C_p} z} \quad (18)$$

This relation is used to validate the results for the laminar flow conditions. Table 2 shows the global Nusselt numbers obtained from simulation compared to correlation of Stephan [26] in laminar flow.

Table 2 Global Nusselt number comparison between simulation and correlation.

Reynolds number	Simulation results	Stephan's correlation [26]	Error (%)
270	7.85	8.42	6.80
540	9.41	9.26	1.60
1080	11.58	10.78	7.40

A second approach is adopted to validate the numerical results in turbulent flow regime for the case with VG. This approach is dependent on the proximity of the simulation results to Tiggelbeck's experimental results [27]. The results of interest are those dealing with a delta winglet pair (DWP) normalized to an empty channel. Tiggelbeck et al. [27] in their experiment found out that the values of the normalized global Nusselt number and friction factor at $Re=4600$ are equal to 1.49 and 1.91 respectively. The same channel dimensions, boundary conditions and post-processing of Tiggelbeck's [27] experiment are computed in the present study.

Table 3 shows a comparison between numerical simulation and experimental results obtained by Tiggelbeck et al. [27] at $Re=4600$. The first term corresponds to normalized Nusselt number, the second one is normalized friction factor and the third term corresponds to the thermal enhancement factor, defined in Eq. (8). The normalized results obtained from the simulations concur with that revealed by Tiggelbeck et al. [27]. The results are in a good agreement with each other with relatively low discrepancy, since error is less than 5%, and the numerical model is reliable to predict flow and heat transfer characteristics.

Table 3 Normalized global Nusselt number, friction factor and thermal enhancement factor comparison.

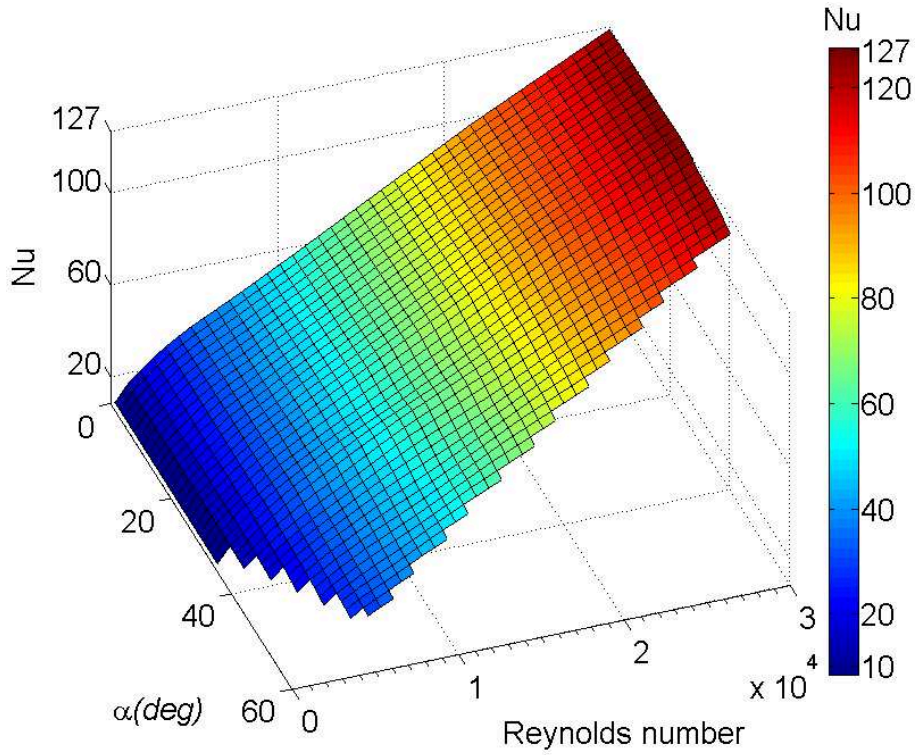
	Simulation results	Experiment results [27]	Error (%)
Nu/Nu_0	1.56	1.49	4.70
f/f_0	1.95	1.91	2.00
TEF	1.25	1.20	4.20

Since numerical simulations are close to ideal experiment, exhibited discrepancy between numerical simulations and experimental work can be mainly caused from the setup process difference between numerical simulation and experiment, in addition to data acquisition uncertainties and other factors.

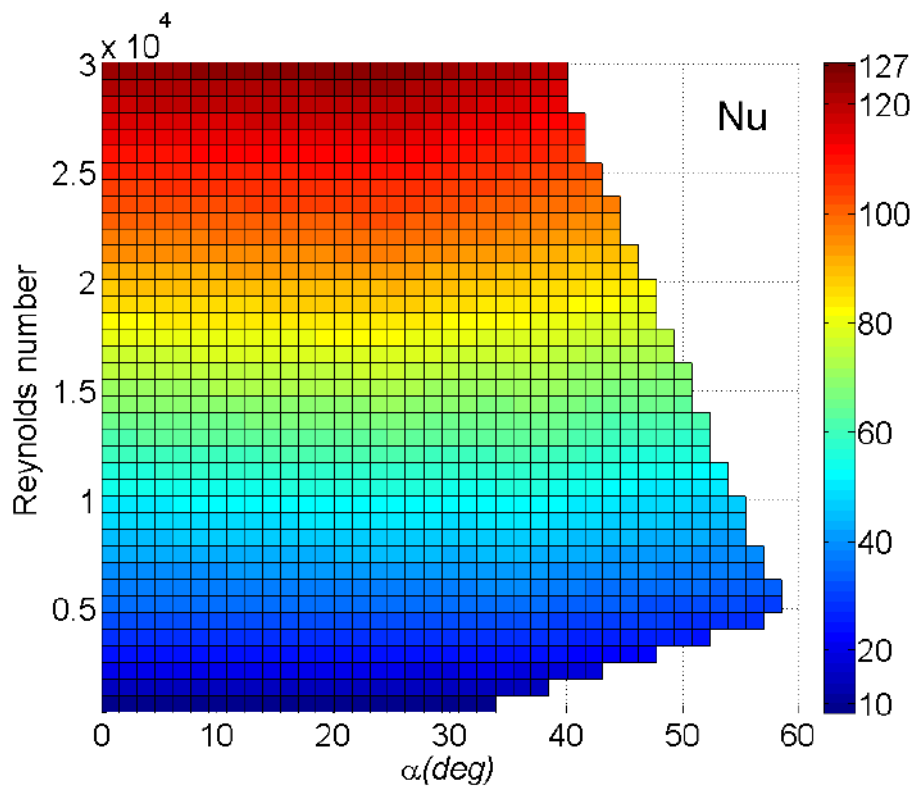
3.2 Global performances

Results obtained from more than 100 simulations covering a wide range of Reynolds numbers and different inclined projections of the VGs are plotted using response surface methodology (RSM).

The Nusselt number response surface representing the heat transfer due to IPWP different configurations is presented in Figure 4, function of Reynolds number and inclination angle (α). This figure shows a monotonic increase in Nusselt number as a function of Reynolds number. The Nusselt number increases from a value around 30 for $Re=5000$, 50 for $Re=10000$ and 127 for $Re=30000$. Otherwise, the Nusselt number is almost independent of the inclination angle, one can see nearly no change in the Nusselt number value when varying the inclination angle from 0° to 60° , i.e. the IPWP configuration does not increase the heat transfer compared to DWP configuration, since DWP and IPWP- 0° are the same geometry.



(a)



(b)

Figure 4 Response surface methodology (RSM) representing the Nusselt number of the IPWP function of Reynolds number and inclination angle (α): (a) Isometric view (b) Top view.

Figure 5 presents the RSM for the friction factor as a function of Reynolds number and angle of inclination (α). The plot clearly shows that the friction factor decreases as Reynolds number increases. Very high values of friction factor are depicted for relatively low laminar flow reaching a value of 0.16 at $Re=270$ and sharply decreases to reach a value of about 0.05 at $Re=2800$. For turbulent flow, the friction factor decreases gently from about 0.04 at $Re=4600$ until 0.025 at $Re=30000$.

In addition, Figure 5 also shows that the friction factor is so sensitive to the VG inclination (α). Friction factor decreases as VG inclination (α) increases, this is further inspected locally in the local performance section. The reason behind the diminishing of the friction factor with the increase of inclination angle is due to the more aerodynamic profile of the VG. When increasing inclination angle (α) (or decreasing the angle of incidence), profile or parasitic drag decreases which is a combination of the pressure or form drag and the skin friction drag. Pressure drag is caused by the separation flow from the VG body while skin friction drag is caused due to the viscous shear boundary layer over the VG body. When inclining the VG body, while maintaining the same frontal area, the pressure drag tends to decrease due to the more aerodynamic form, while the skin friction drag tends to increase due to the increase in immersed body surface area. The decrease of the form drag is more dominant than the increase of skin drag, leading to global decrease in the drag thus lower friction factor.

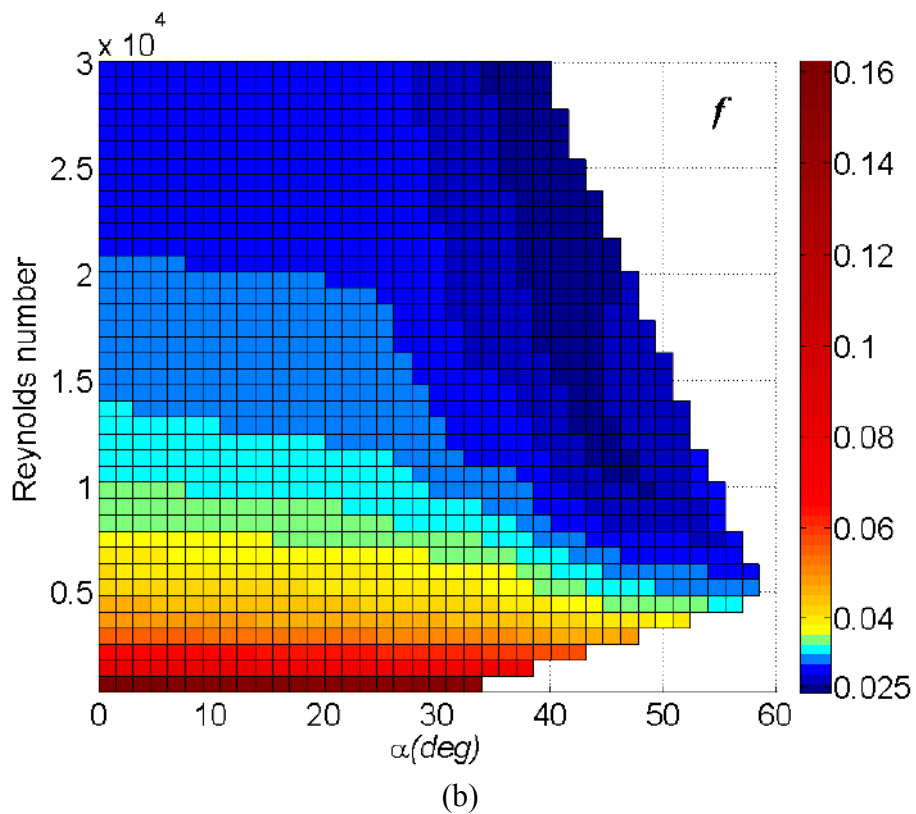
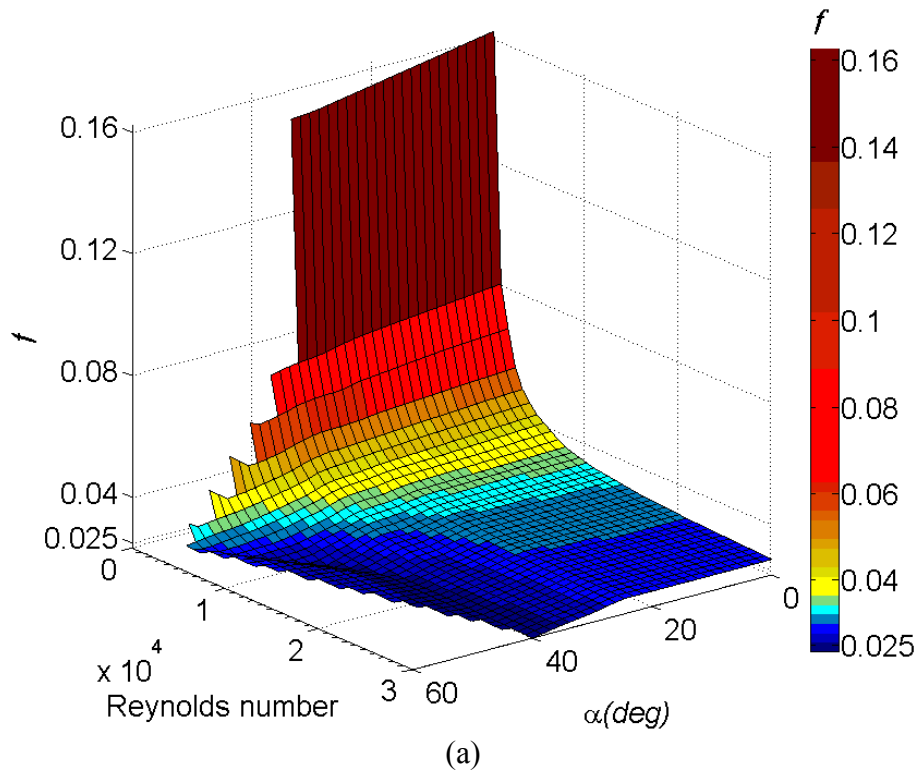
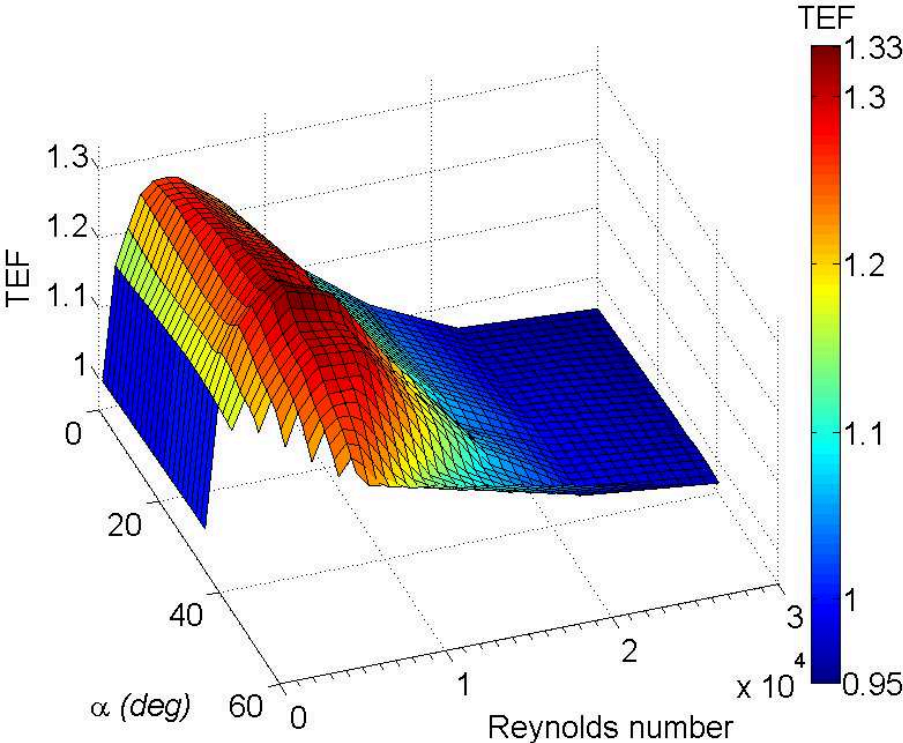


Figure 5 Response surface methodology (RSM) representing the friction factor of the IPWP function of Reynolds number and inclination angle (α): (a) Isometric view (b) Top view.

In addition to the Nusselt number and friction factor graphs, Figure 6 shows the response surface methodology performance of the IPWP based on the thermal enhancement factor criterion (TEF defined in Eq. (8)) as a function of Reynolds number and inclination angle (α). The RSM plot shows that the TEF increases rapidly with the increase of Reynolds number to reaches its maximum around $Re=5000$ zone. Then, TEF decreases gradually in slower manner to reach ineffective thermal enhancement after a Reynolds number about $Re\sim 15000$. Clearly, the zone of intensification for Reynolds number appears to be in the range [500–15000].

In addition, the RSM illustrates that the TEF is quietly affected by the inclination angle of the vortex generator reaching its maximum value in the region between 30° and 35° . It can be clearly shown that the maximum TEF for all the configurations studied is achieved in the near region of $Re=5000$. The global maximum TEF for the RSM, reaching a value of 1.33, is attained at an inclination angles between 30° and 35° at $Re\sim 4600$.



(a)

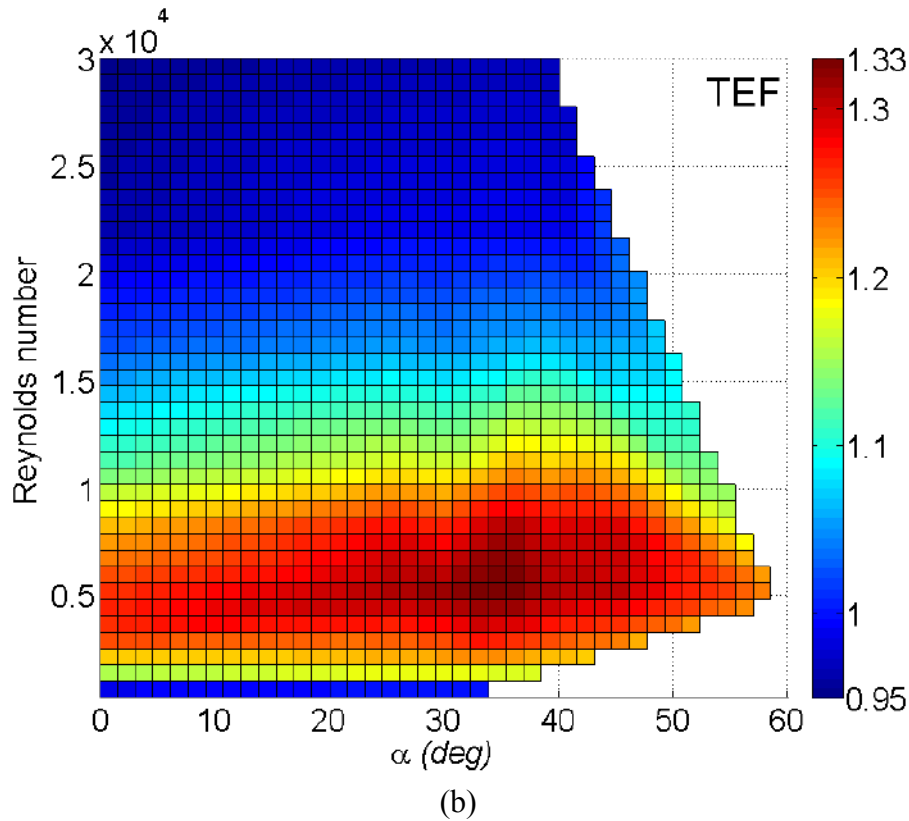


Figure 6 Response surface methodology (RSM) representing the thermal enhancement factor of the IPWP function of Reynolds number and inclination angle (α): (a) Isometric view (b) Top view.

3.3 Local performance

After demonstrating the performance of the IPWP with various angles of inclination (α) on the global scale, this section illustrates the performance from a local point of view leading to better understanding of the flow characteristics. The flow condition $Re=4600$ is chosen to illustrate the local performance, due to its domination from the global performance study.

From a local scope, the performance of the IPWP with various inclinations is demonstrated throughout this section and illustrated in Figure 7, Figure 8 and Figure 9, which represent respectively the normalized Nusselt number, the friction factor and the local helicity for four configurations of IPWP (30° , 40° , 50° and 60°) compared to DWP case. All VGs possess the same leading edge with the bottom fin and signified on each figure by the lower

filled triangle on the x-axis located at a distance $x=0.06$ m from the channel inlet. The other vertical lines with an upper filled triangle are the VGs trailing edges attached to the upper fin and denoted by the line type of each configuration.

Figure 7 shows the streamwise evolution of the normalized spanwise-averaged local Nusselt number Nu/Nu_0 throughout the channel. It can be seen that the normalized Nusselt numbers do not show any enhancement through the channel for the IPWP configurations compared to the reference case DWP, except for IPWP-30 which exhibits higher values most of the time. The DWP configuration shows a smooth increasing curve for the Nusselt number over the channel length, while inclined configurations behave in a fluctuating manner. These fluctuations are due to the multiscale vortices interaction which sometimes may built up and other times attenuate each other [20].

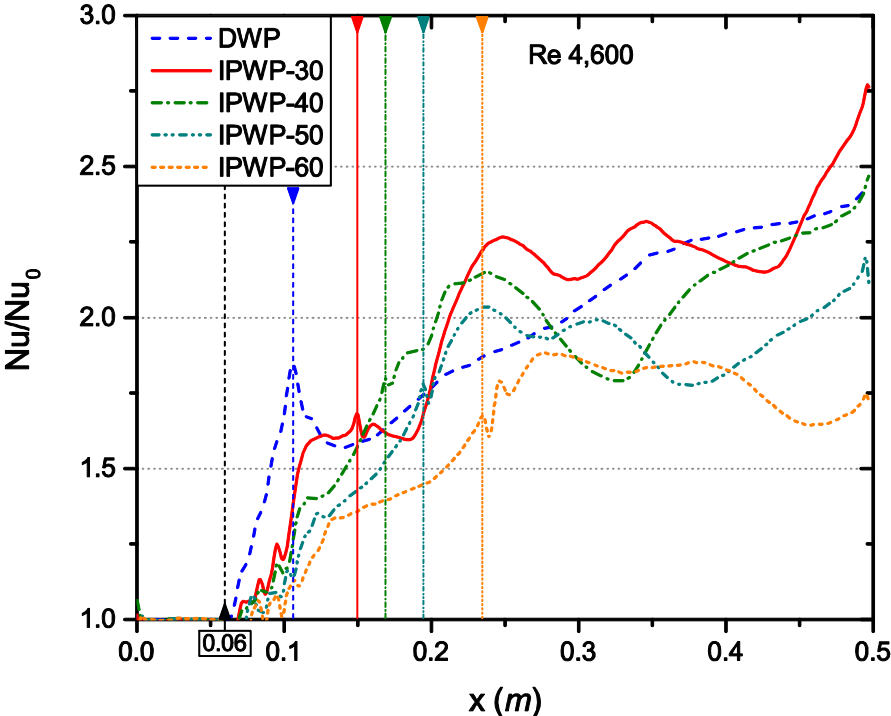


Figure 7 Normalized Nusselt number for the cases DWP and IPWP with inclinations.

Table 4 presents the normalized Nusselt number area weighted average values calculated from VG leading edge to the end of the channel. It can be seen that IPWP with inclinations in the range of 25° to 35° have the highest values of averaged Nusselt numbers, that represents an increase of 3.1% compared to DWP configuration. In addition, further increase of the inclination angle is seemed to be disadvantageous for the Nusselt number, since from an inclination of 40° the Nusselt number is diminished compared to DWP case. This Nusselt number decrease follows a monotonic tendency: the higher the inclination angle, the lower the heat transfer.

Table 4 Average normalized Nusselt number of different VG configurations and the percentage difference compared to DWP case, for Re=4600.

	DWP	IPWP -25	IPWP -30	IPWP -35	IPWP -40	IPWP -45	IPWP -50	IPWP -55	IPWP -60
Average value of Nu/Nu_0	1.94	2.00	2.00	2.00	1.88	1.84	1.74	1.68	1.58
Difference (%)	–	3.1	3.1	3.1	-3.1	-5.2	-10.3	-13.4	-18.6

Normalized friction coefficients f/f_0 are illustrated in Figure 8. DWP friction factor peak is severely suppressed when using IPWP configurations, showing a decrease by 50% for the IPWP-30. It can be shown that the more the inclination angle increases, the more the friction factor decreases, to reach about a 70% peak decrease for the IPWP-60. The decrease of the friction factor when the inclination angle increases is also observed on the whole longitudinal locations.

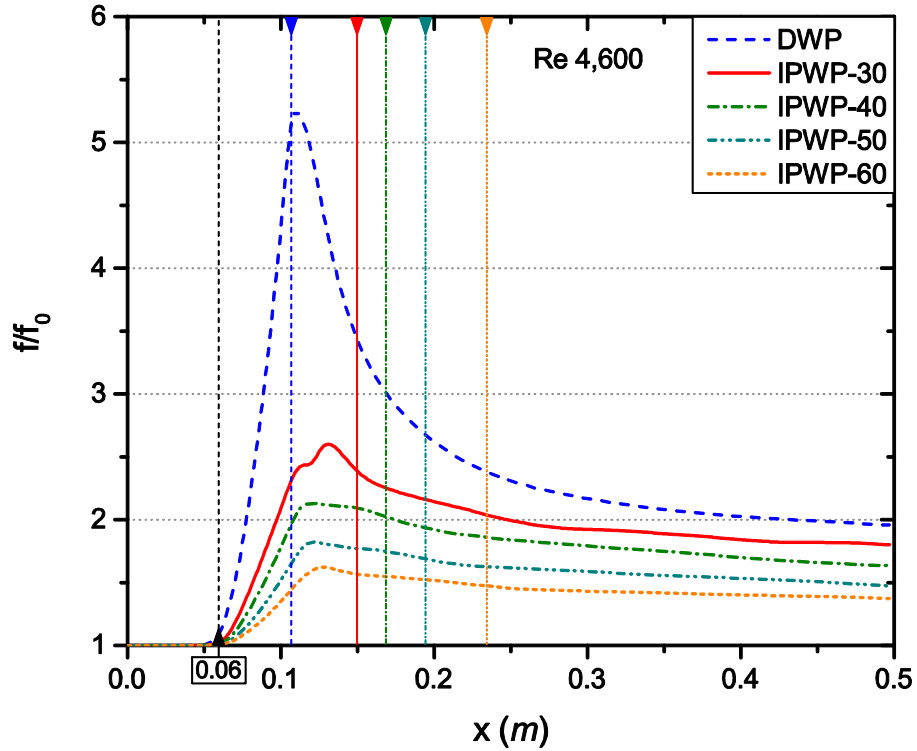


Figure 8 Normalized friction factor for the cases DWP and IPWP with inclinations.

Table 5 gives the peak and averaged values of the normalized friction factors of different VG configurations in addition to the percentage differences of these values compared to DWP configuration. Note that the friction factor average values are calculated from VG leading edge to the end of the channel. The area weighted average friction factor of DWP case is reduced by 18% for IPWP-30, reaching 43% decrease for the IPWP-60. The decrease of the friction factor with the increase of the inclination angle is a monotonic function under the studied operating conditions.

Table 5 Normalized friction values of different VG configurations and the percentage difference compared to DWP case (peak value and average value), for Re=4600.

DWP	IPWP							
	-25	-30	-35	-40	-45	-50	-55	-60

Peak value of f/f_0	5.25	2.94	2.60	2.34	2.13	1.98	1.82	1.71	1.62
Difference (%)	–	-44	-50	-55	-59	-62	-65	-67	-69
Average value of f/f_0	2.51	2.06	1.96	1.90	1.77	1.67	1.57	1.49	1.42
Difference (%)	–	-18	-22	-24	-29	-33	-37	-41	-43

The investigation of the flow effect is carried out by the study of helicity in this work, in order to remove the effect of high vorticity values near the walls. Helicity of IPWP configurations with four inclination angles and also DWP case is demonstrated in Figure 9. It shows that IPWP-30 configuration submits the highest helicity almost downstream the VG, always higher than DWP case. IPWP-60 provides the lowest values, lower than DWP case and IPWP-40 and IPWP-50 shows an increase of the helicity downstream the VG compared to DWP case over a short distance, until $x \approx 0.3m$.

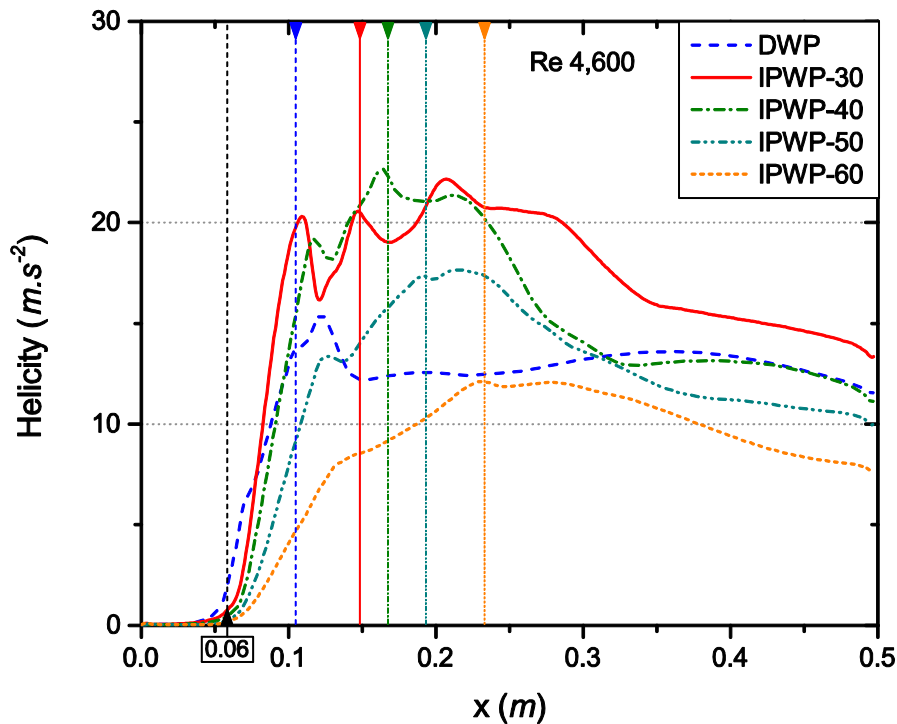


Figure 9 Local helicity for the cases DWP and IPWP with inclinations.

Table 6 shows the helicity profiles averaged from VG leading edge located at a distance $x=0.06$ m to the end of the channel for the different VG configurations, in addition to the percentage differences of helicity compared to DWP case. IPWP-30 provides the highest helicity profile along the channel of about 16.8 m/s^2 , with an augmentation of 35.5% it dominates over all other configurations in this aspect. From this inclination angle, when inclination angle increases, averaged vorticity rapidly decreases until reaching lower values than for DWP case from IPWP-50. The decrease attains 27.4% for the IPWP-60 relative to DWP performance.

Table 6 Helicity profiles averaged from VG leading edge located at a distance $x=0.06$ m from inlet of different VG configurations and the percentage difference compared to DWP case, for $Re=4600$.

	DWP	IPWP -25	IPWP -30	IPWP -35	IPWP -40	IPWP -45	IPWP -50	IPWP -55	IPWP -60
Average value of helicity (m.s^{-2})	12.4	16.3	16.8	16.2	14.9	13.8	12.3	10.9	9.0
Difference (%)	–	31.5	35.5	30.6	20.2	11.3	-0.8	-12.1	-27.4

3.4 Flow structure

From the global and local performances studies in the previous sections, it is obvious that the IPWP-30 and IPWP-35 configurations show performances that are prominent especially at $Re \sim 4600$. A study of the flow structure is established in this section at this Reynolds number to better understand the heat transfer process linked to the streamwise vortices.

According to Jeong and Hussain [28], a vortex corresponds to a region where two eigenvalues of the symmetric part of the square of the velocity gradient are negative; this is

the concept of λ_2 parameter which is used here in order to locate the streamwise vortices. For further details concerning the identification of a vortex criterion (λ_2), reader may refer to Jeong and Hussain [28].

Transversal section planes are performed to show the velocity streamlines and λ_2 contours in different locations downstream the VG. Four configurations that visualize the differences among are selected in this study, $\alpha=30^\circ, 40^\circ, 50^\circ$ and 60° . Figure 10 shows the velocity streamlines for the IPWP-30, IPWP-40, IPWP-50 and IPWP-60 configurations at different longitudinal planes.

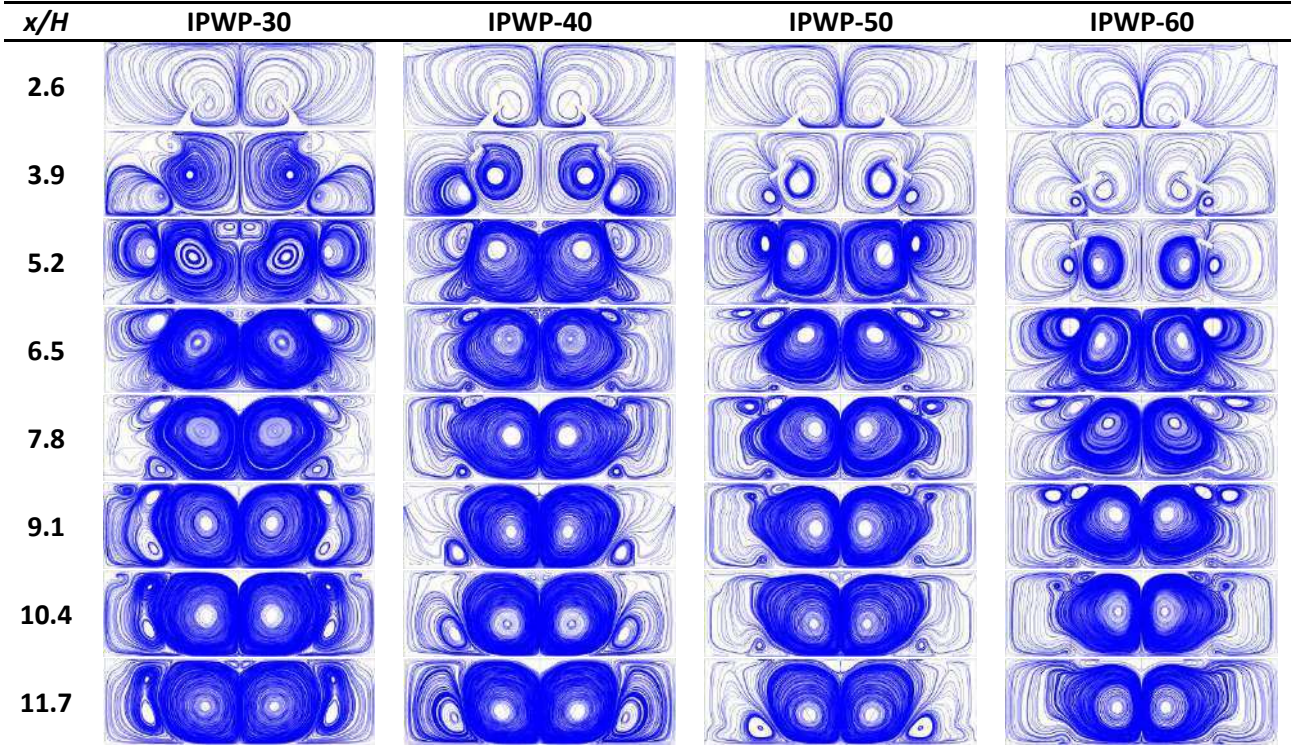


Figure 10 Velocity streamlines for the IPWP-30, IPWP-40, IPWP-50 and IPWP-60 for $Re=4600$ at different planes x/H between 2.6 and 11.7.

Figure 11 shows the λ_2 contours for the IPWP-30, IPWP-40, IPWP-50 and IPWP-60 configurations at different longitudinal planes. Figure 10 and Figure 11 enable to see the high

intensity and multiscale vortical structure predominance for the IPWP-30 over other configurations. Figure 10 and Figure 11 also enable to highlight the vortices location inside the channel for the IPWP configurations.

The interaction among the multiscale vortices created by the IPWP-30, leads to the permanence effect of the vortices in the downstream direction. Figure 10 and Figure 11 show that the vortices produced by IPWP-30 maintain their intensity for further distance compared to other inclined configurations.

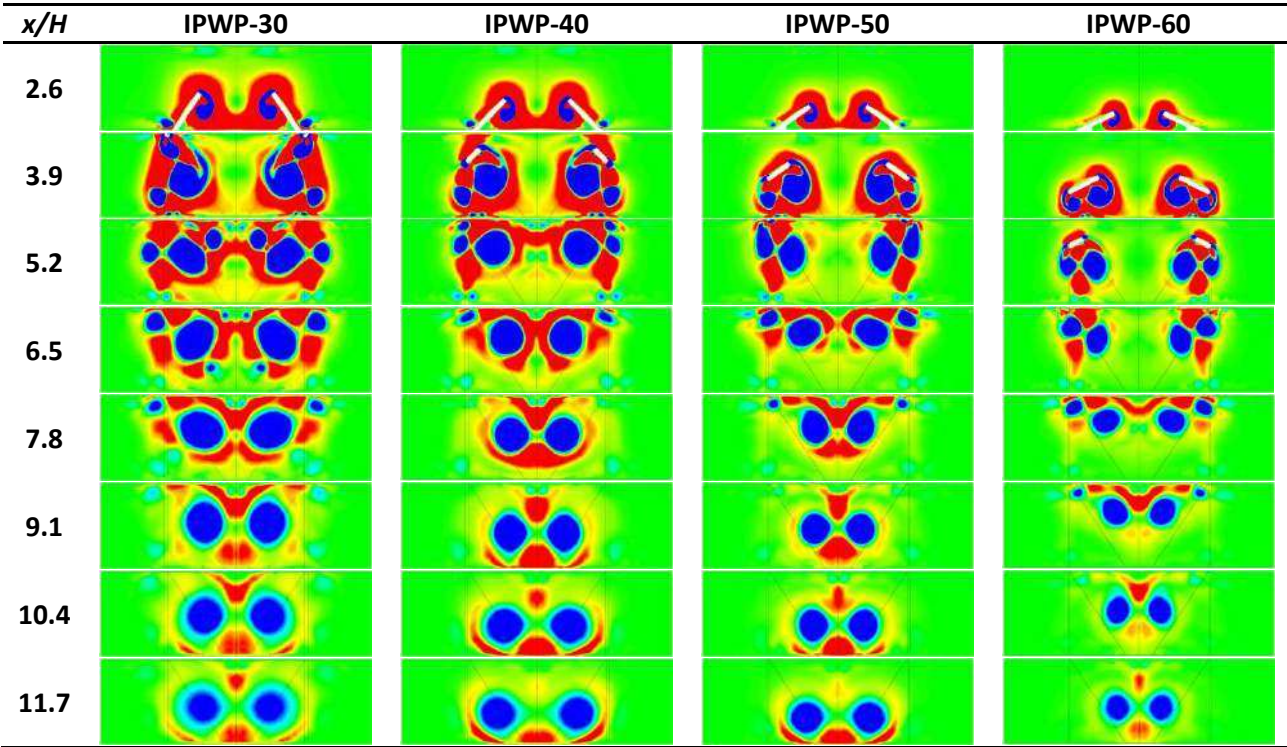


Figure 11 λ_2 contours for the IPWP-30, IPWP-40, IPWP-50 and IPWP-60 for $Re=4600$ at different planes x/H between 2.6 and 11.7.

In addition, Table 7 summarizes the number of primary and secondary vortices developed for each IPWP configuration that can be seen on Figure 10. It illustrates that the number of multiscale vortices for IPWP-30 reaches eight (two main and six induced vortices)

at a distance $x/H=11.7$. IPWP-40 and IPWP-50 reach a number of four vortices (two main and two induced vortices), while IPWP-60 produces only two vortices at a distance $x/H=11.7$. Reader may refer to Oneissi et al. [20] for further detailed description of the multiscale interaction mechanism among vortices.

Table 7 Primary and secondary vortices for IPWP configurations (for a pair of VGs) at $x/H=11.7$ for $Re=4600$.

	Primary vortices	Maximum secondary vortices
DWP	2	2
IPWP-30	2	6
IPWP-40	2	2
IPWP-50	2	2
IPWP-60	2	0

4. Conclusion

Numerous three-dimensional numerical simulations for more than ten configurations of vortex generators are performed to analyze heat transfer enhancement in parallel plate-fin heat exchanger. Laminar flows are simulated for Reynolds numbers 270, 540 and 1080, while turbulent flow is simulated for Reynolds numbers 2800, 4600, 7700, 10800, 16200, 21600 and 30000. Turbulent flow is modeled with the benefit of the $\kappa\text{-}\omega$ SST model and validated with correlations and experimental data. The DWP configuration of Tiggelbeck et al. [27] is built-up on and used to validate the results obtained through simulations.

The objective of this work is to identify the optimum inclination angle configuration that reduces pressure drop and enhances heat transfer and mixing performances. IPWP configurations with different inclination angles (0° , 25° , 30° , 32° , 35° , 38° , 40° , 45° , 50° , 55°)

and 60°) are then introduced by manipulating the winglets' geometry and orientation. The 0° case corresponds to the DWP configuration which is chosen as the reference case.

In order to explain the effects of inclination angle on heat transfer and pressure drop, response surface methodology (RSM) is used from a global scopes. Local performance is weighed based on the streamwise distribution of Nusselt number and friction coefficient criteria in addition to helicity. It is found that the IPWP with inclination angle in the range of 30° to 35° bestow better global performance than all other inclinations. The peak friction magnitude of IPWP-30 configuration is 50% less than that recorded by the DWP and further inclination of the VG may reach about a 70% peak decrease for the IPWP-60 case. The area weighted average friction compared to DWP case decreases 18% for IPWP-30 configuration, reaching about 43% decrease for the IPWP-60 case. IPWP-30 configuration exhibits the maximum intensification of averaged helicity with an augmentation of 35.5% compared to DWP case. In addition, it is illustrated that the number of multiscale vortices for IPWP-30 configuration reaches eight (two main and six induced vortices) while for other configurations it may suffice with two main vortices.

The present results are very promising as the thermal enhancement factor is found to be increased 6% for IPWP-30 and IPWP-35 vortex generators compared to DWP case. Such study highlights the optimization for IPWP involved in the convective heat transfer intensification, based on thermal enhancement factor (TEF), by varying the VG's inclination angle.

References

- [1] R. Webb and N. Kim, Principles of Enhanced Heat Transfer, 1994.
- [2] S. W. Chang, A. W. Lees and H.-T. Chang, "Influence of spiky twisted tape insert on thermal fluid performances of tubular air–water bubbly flow," International Journal of Thermal Sciences, vol. 48, pp. 2341-2354, 2009.
- [3] H. Gül and D. Evin, "Heat transfer enhancement in circular tubes using helical swirl generator insert at the entrance," International Journal of Thermal Sciences, vol. 46, pp. 1297-1303, 2007.
- [4] M. A. Elyyan and D. K. Tafti, "A novel split-dimple interrupted fin configuration for heat transfer augmentation," International Journal of Heat and Mass Transfer, vol. 52, pp. 1561-1572, 2009.
- [5] C. Habchi, S. Russeil, D. Bougeard, J. L. Harion, T. Lemenand, D. Della Valle and H. Peerhossaini, "Enhancing Heat Transfer in Vortex Generator-type Multifunctional Heat Exchangers," Applied Thermal Engineering, vol. 38, pp. 14-25, 2012.
- [6] J. Tala, S. Russeil, D. Bougeard and J.-L. Harion, "Numerical analysis of the fin spacing effect on the horseshoe vortex system evolution in a two-rows finned-tube heat exchanger," International Journal of Numerical Methods for Heat and Fluid Flow, vol. 23, no. 7, pp. 1136-1154, 2013.
- [7] S. Vintrou, D. Bougeard, S. Russeil, R. Nacereddine and J.-L. Harion, "Quantitative infrared investigation of local heat transfer in a circular finned tube heat exchanger assembly," International Journal of Heat and Fluid Flow, vol. 104, pp. 197-207, 2013.
- [8] J. Wu and W. Q. Tao, "Investigation on Laminar Convection Heat Transfer in Fin-and-Tube Heat Exchanger in Aligned Arrangement With Longitudinal Vortex Generator From

- the Viewpoint of Field Synergy Principle," *Applied Thermal Engineering*, vol. 27, pp. 2609-2617, 2007.
- [9] P. Saha, G. Biswas and S. Sarkar, "Comparison of winglet-type vortex generators periodically deployed in a plate-fin heat exchanger - A synergy based analysis," *International Journal of Heat and Mass Transfer*, vol. 74, pp. 292-305, 2014.
- [10] R. Kamboj, P. S. Dhingra and P. G. Singh, "CFD Simulation of Heat Transfer Enhancement by Plain and Curved Winglet Type Vortex Generators with Punched Holes," *International Journal of Engineering Research and General Science*, vol. 2, no. 4, pp. 648-659, 2014.
- [11] G. Zhou and Z. Feng, "Experimental investigations of heat transfer enhancement by plane and curved winglet type vortex generators with punched holes," *International Journal of Thermal Sciences*, vol. 78, pp. 26-35, 2014.
- [12] Y. He, H. Han, W. Tao and Y. Zhang, "Numerical study of heat-transfer enhancement by punched winglet-type vortex generator arrays in fin-and-tube heat exchangers," *International Journal of Heat and Mass Transfer*, vol. 55, pp. 5449-5458, 2012.
- [13] J. Herpe, D. Bougeard, S. Russeil and M. Stanciu, "Numerical investigation of local entropy production rate of a finned oval tube with vortex generators," *International Journal of Thermal Sciences*, vol. 48, pp. 922-935, 2009.
- [14] M. Fiebig, "Embedded Vortices in Internal Flow: Heat Transfer and Pressure Loss Enhancement," *International Journal of Heat and Fluid Flow*, vol. 16, no. 5, pp. 376-388, 1995.
- [15] L. O. Salviano, D. J. Dezan and J. I. Yanagihara, "Optimization of winglet-type vortex generator positions and angles in plate-fin compact heat exchanger: Response Surface Methodology and Direct Optimization," *International Journal of Heat and Mass*

- Transfer, vol. 82, pp. 373-387, 2015.
- [16] Y.-G. Lei, Y.-L. He, L.-T. Tian, P. Chu and W.-Q. Tao, "Hydrodynamics and heattransfer characteristics of a novel heat exchanger with delta-winglet vortex generators," *Chemical Engineering Science*, vol. 65, pp. 1551-1562, 2010.
- [17] A. Lemouedda, M. Breuer, E. Franz, T. Botsch and A. Delgado, "Optimization of the angle of attack of delta-winglet vortex generators in a plate-fin-and-tube heat exchanger," *International Journal of Heat and Mass Transfer*, vol. 53, pp. 5386-5399, 2010.
- [18] J. Wu and W. Tao, "Effect of longitudinal vortex generator on heat transfer in rectangular channels," *Applied Thermal Engineering*, vol. 37, pp. 67-72, 2012.
- [19] K. Yongsiri, P. Eiamsa-ard, K. Wongcharee and S. Eiamsa-ard, "Augmented heat transfer in a turbulent channel flow with inclined detached-ribs," *Case Studies in Thermal Engineering*, vol. 3, pp. 1-10, 2014.
- [20] M. Oneissi, C. Habchi, S. Russeil, D. Bougeard and T. Lemenand, "Novel design of delta winglet pair vortex generator for heat transfer enhancement," *International Journal of Thermal Sciences*, vol. 109, pp. 1-9, 2016.
- [21] I. ANSYS, "Turbulence Models," in *ANSYS Fluent 12.0 Theory Guide*, April 2009.
- [22] F. Menter, "Two-equation eddy-viscosity turbulence models for engineering applications," *AIAA Journal*, vol. 32, pp. 1598-1605, 1994.
- [23] X.-Y. Tanga and D.-S. Zhu, "Flow structure and heat transfer in a narrow rectangular channel with different discrete rib arrays," *Chemical Engineering and Processing: Process Intensification*, vol. 69, pp. 1-14, 2013.
- [24] R. Warming and R. Beam, "Upwind second-order difference schemes and applications in aerodynamic flows," *AIAA Journal*, vol. 14, no. 9, pp. 1241-149, 1976.

- [25] M. Nacer-Bey, S. Russeil and B. Baudoin, "PIV visualizations to the flow structure upstream of the tubes in a two-row plate-fin-and-tube heat exchanger," in Proceeding of the 4th International Conference on Compact Heat Exchangers and Enhancement Technology for the Process Industries, Grete Island, Greece, pp. 63-68, Sept. 29-Oct. 3, 2003.
- [26] A. Bejan, "Forced Convection: Internal Flows," Durham, North Carolina, Department of Mechanical Engineering and Materials Science, Duke University, 1995, pp. 395-438.
- [27] S. Tiggelbeck, N. K. Mitra and M. Fiebig, "Comparison of Wing-Type Vortex Generators for Heat Transfer Enhancement in Channel Flows," *Journal of Heat Transfer*, vol. 116, pp. 880-885, 1994.
- [28] J. Jeong and F. Hussain, "On the identification of a vortex," *Journal of Fluid Mechanics*, vol. 285, pp. 69-94, 1995.

Chapitre 7

Intensification des transferts thermiques d'un nouveau type de générateur de vorticit      paires d'ailettes en delta muni de protrusions dans un   changeur de chaleur    plaque et ailette

Dans ce chapitre, des simulations num  riques tridimensionnelles de g  n  rateurs de tourbillons longitudinaux munis de protrusions sont effectu  es afin d'  tudier les ph  nom  nes d'intensification des transferts dans les   changeurs de chaleur    plaque et ailettes. Les simulations num  riques en r  gime turbulent sont effectu  es en utilisant le mod  le $k - \omega$ SST. Ces simulations sont valid  es    partir de r  sultats exp  rimentaux et de corr  lations pour le nombre de Reynolds de 4600.

L'objectif de ce travail est d'augmenter la performance de la g  om  trie innovante IPWP. Dans un premier temps, des protrusions sont introduites dans le canal muni des DWP cr  ant ainsi les nouvelles g  om  tries DWP-PRO1 et DWP-PRO2. La configuration DWP-PRO1 pr  sente la meilleure performance. N  anmoins pour ces deux configurations, les augmentations de performances observ  es, transfert de chaleur et coefficient de frottement, ne sont pas tr  s cons  quentes. Dans un second temps, des protrusions sont mises    diff  rents endroits dans la configuration de canal munie de la g  om  trie IPWP, ce qui d  finit les g  om  tries IPWP-PRO 1, IPWP-PRO2, IPWP-HS et IPWP-M.

Ces nouvelles configurations : IPWP-PRO1 et IPWP-PRO2, n'entra  nent pas de meilleurs r  sultats concernant le transfert thermique par rapport    la g  om  trie « classique » IPWP. En revanche, l'IPWP-HS et IPWP-M augmentent le transfert

thermique par rapport à l'IPWP. En outre les résultats montrent que l'IPWP-M confère une meilleure performance que l'IPWP-HS.

Ainsi, les résultats actuels sont très prometteurs avec une amélioration du transfert thermique de 6,5% pour l'IPWP-M par rapport au DWP et une augmentation de 3% pour les deux configurations DWP-PRO1 et IPWP-M comparativement au DWP et IPWP respectivement.

Heat transfer enhancement of a novel delta winglet pair vortex generator with protrusions in parallel plate-fin heat exchanger

Mohammad Oneissi ^{a, b, c}, Charbel Habchi ^d, Serge Russeil ^{a,*}, Daniel Bougeard ^a, Thierry Lemenand ^b

^a Mines Douai, EI, F59500 Douai, France.

^b Angers University, ISTIA, LARIS EA 7315, Angers, France.

^c Lebanese International University LIU, Mechanical Engineering Dept., Beirut, Lebanon.

^d Notre Dame University-Louaize NDU, Mechanical Engineering Dept., Zouk Mikael, Lebanon.

Abstract

Vortex generators (VG) are known to be good enhancers of heat transfer. Heat transfer enhancement in parallel plate-fin heat exchanger is examined by performing three-dimensional numerical simulations of longitudinal vortex generators. The turbulence is modeled using the shear-stress transport (SST) $\kappa\text{-}\omega$ model. Hemi-spherical protrusions are inserted downstream new VG configuration designed by Oneissi et al. [International Journal of Thermal Sciences, 109, 1-9, (2016)] named inclined projected winglet pair (IPWP), in various locations, leading to the definition of six different configurations. Based on the streamwise distribution of Nusselt number and friction coefficient criteria in addition to vorticity, the local performance is analyzed. Some VGs with protrusions are examined and

* Corresponding author.

Tel.: +33 3 27 71 23 88; fax: +33 3 27 71 29 15

Email address: serge.russeil@mines-douai.fr (S. Russeil)

showed better performance relative to VGs standing alone. The present study highlights the different mechanisms involved in the convective heat transfer intensification by generating multiple interacting vortices, by adding protrusions with low pressure drop penalty. Finally, it is found that the IPWP with protrusions, set downstream in the middle, bestows better global performance than all other configurations.

Keywords

Heat transfer enhancement, winglet pair, vortex generator, protrusions, plate-fin heat exchanger, numerical simulation.

Nomenclature

A	Cross-sectional area, m ²	U	Mean flow velocity, m s ⁻¹
A _f	Fin area, m ²	u	Flow velocity in x direction, m s ⁻¹
B	Channel width, m	v	Flow velocity in y direction, m s ⁻¹
C _p	Specific heat at constant pressure, J kg ⁻¹ K ⁻¹	w	Flow velocity in z direction, m s ⁻¹
D _h	Hydraulic diameter, m	x _v	Distance of wingtips from the channel entrance, m
f	Friction factor	z	VG height, m
H	Channel height, m		
h	Convective heat transfer coefficient, W m ⁻² K ⁻¹		Greek letters
j	Colburn factor	μ	Dynamic viscosity, Pa s
k	Thermal conductivity, W m ⁻¹ K ⁻¹	ν	Kinematic viscosity, m ² s ⁻¹
L	Channel length, m	ρ	Fluid density, kg m ⁻³
l	VG span, m		
\dot{m}	Mass flow rate, kg s ⁻¹		Abbreviations
Nu	Nusselt number	VG	Vortex Generator
Pe	Péclet number= Re. Pr	DWP	Delta Winglet Pair
Po	Poiseuille number	RWP	Rectangular Winglet Pair
Pr	Prandtl number	IPWP	Inclined Projected Winglet Pair
ΔP	Pressure drop, Pa	LVG	Longitudinal Vortex Generator
q''	Heat flux, W m ⁻²	TVG	Transverse Vortex Generator
Re	Reynolds number	CFD	Computational Fluid Dynamics
s	Distance between tips of winglet pair, m	SST	Shear-Stress Transport
T _{x,b}	Bulk temperature at position x, K	TEF	Thermal enhancement factor
T _i	Inlet bulk temperature, K	PRO	Protrusion
T _o	Outlet bulk temperature, K	HS	High Spacing
T _s	Surface temperature, K	M	Middle

1. Introduction

Flow structure characteristics are fundamental for heat transfer augmentation in parallel plate-fin heat exchanger. In fact the amount of surface heat transfer augmentation is controlled by the topology of secondary flows, three-dimensionality, shear-layer reattachment and turbulence transport induced by the devices employed on the walls of the internal passages [1]. These devices may include cylindrical tubes [2, 3, 4], transverse vortex generators (TVGs) [5], longitudinal vortex generators (LVGs) [6, 7, 8, 9], plane or curved surface of VGs [10, 11], dimples or protrusions [1, 5, 12, 13, 14, 15, 16], or even a combination of the above types [5, 17, 18, 19].

These components are used in various industrial fields including electronics cooling, micro and macro-scale heat exchangers, combustion chambers, as well as others. This paper focuses on the addition of hemi-spherical protrusions downstream two types of LVGs, and on their unique capability in heat transfer enhancement through the generation of strongly interacting large scale longitudinal vortices. This enhancement is a result of the combination of the main mechanisms of heat transfer intensification: the reduction of the laminar sub layer thickness near the wall, the development of three-dimensional turbulent layers and the swirl movement of the streamwise vortex that enhances the convective transfer [20]. Protrusions downstream VGs show a significant effect on the heat transfer and especially on Nusselt number since they disturb the thin boundary layer at the wall, thus enhancing heat transfer [21]. Also, it is shown by Habchi et al. [21] that addition of hemispherical protrusions between the vortex generator arrays greatly enhances the heat transfer with only a small increase in pressure drop. This increase in local heat transfer is caused by increasing the

temperature gradients and vorticity very close to the heated wall. Ligrani et al. [1] reported that more extensive and stronger secondary flows are present over a much larger portion of the channel cross section when protrusions are added. Secondary flow generated by protrusions enhances the heat transfer augmentation. Hwang et al. [16] explained how a dimple-protrusion patterned wall affects the heat transfer characteristics. Xie et al. [22] showed in their investigation of flow and heat transfer in rectangular channel with dimple-protrusion geometry, that protrusions exhibit greater thermal enhancement with high friction cost than dimples do. Huang et al. [23] claimed that protrusions provide greater heat transfer enhancement than dimples do, in addition pressure drop penalty. Chen et al. [24] concluded that larger height of dimple-protrusion induces higher friction factor and Nusselt number.

The aim of the present study is to analyze the effect on the flow structure and heat transfer mechanisms of adding protrusions downstream two types of VGs. The numerical method, computational domain and mesh sensitivity analysis are presented in the problem statement in section 2. Numerical validation, global performance followed by local analysis of the heat transfer phenomena and compactness comparison are discussed in section 3. Finally section 4 is dedicated to the concluding remarks.

2. Problem description

2.1 Numerical model

The flow field is governed by the three-dimensional (3D) steady-state Reynolds Averaged Navier-Stokes (RANS) equations. The continuity and momentum equations for an incompressible Newtonian fluid are:

$$\frac{\partial u_i}{\partial x_i} = 0 \quad (1)$$

$$u_j \frac{\partial u_i}{\partial x_j} = -\frac{1}{\rho} \frac{\partial p}{\partial x_i} + \nu \frac{\partial^2 u_i}{\partial x_j \partial x_j} - \frac{\partial \overline{u'_i u'_j}}{\partial x_j} \quad (2)$$

where the term $\overline{u'_i u'_j}$ is the Reynolds stress tensor resulting from the averaging procedure on the nonlinear convective terms in the momentum equations, and the energy equation is:

$$\frac{\partial}{\partial x_i} [u_i (\rho E + p)] = \frac{\partial}{\partial x_i} (\lambda_{eff} \frac{\partial T}{\partial x_i}) \quad (3)$$

where E is the total energy and λ_{eff} the effective thermal conductivity.

The solver used for the flow computation is the code ANSYS Fluent 15, which is based on an Eulerian approach to solve the Cauchy equations through cell-centered finite volume discretization [5]. The code solves the conservation equations for mass and momentum in addition to the energy equation for flows involving heat transfer [25]. RANS turbulence models allow the calculation of the mean flow without first calculating the full time-dependent flow field.

For turbulent flows, $Re=4600$ is used in this study, the shear-stress transport (SST) $\kappa-\omega$ model developed by Menter [26] is often implemented. This model solves two additional

partial differential equations, a modified version of the turbulence kinetic energy equation κ used in κ - ε model and a transport one for the specific dissipation ω . Also, the shear stress transport (SST) combines the use of κ - ω formulation in the inner parts of the boundary layer and the switching to a κ - ε behavior in the free-stream thus avoiding the κ - ω sensitivity to the inlet free-stream turbulence properties [25]. In addition to that, it is characterized by its good behavior in adverse pressure gradients and separating flows while attaining accuracy and reliability [25].

The preceding attributes give the SST κ - ω model additional accuracy and reliability thus providing it an advantage over the standard κ - ω model. Moreover, the SST κ - ω model was used by many researchers in previous works that gave a fair matching with experimental results [27, 28].

This approach necessitates assessment of the wall adjacent cell size that insures a dimensionless wall distance y^+ lower than 5, ensuring that the viscous sublayer is meshed and solved.

The SST κ - ω model transport equations are:

$$\rho \frac{\partial}{\partial x_i} (\kappa u_i) = \frac{\partial}{\partial x_j} \left(\Gamma_k \frac{\partial \kappa}{\partial x_j} \right) + \tilde{G}_k - Y_k \quad (4)$$

$$\rho \frac{\partial}{\partial x_i} (\omega u_i) = \frac{\partial}{\partial x_j} \left(\Gamma_\omega \frac{\partial \omega}{\partial x_j} \right) + G_\omega - Y_\omega + D_\omega \quad (5)$$

where

\tilde{G}_k is the production of turbulence kinetic energy due to mean velocity gradients,

G_ω is the generation of ω ,

Γ_k is the effective diffusivity of κ ($\Gamma_k = \mu + \frac{\mu_t}{\sigma_k}$),

Γ_ω is the effective diffusivity of ω ($\Gamma_\omega = \mu + \frac{\mu_t}{\sigma_\omega}$),

Y_k is the dissipation of κ due to turbulence,

Y_ω is the dissipation of ω due to turbulence,

D_ω is the cross-diffusion,

σ_k, σ_ω are the turbulent Prandtl numbers for κ and ω respectively,

μ_t is the turbulent viscosity. For detailed discussion of these equations, the reader may refer to [25].

For spatial discretization of the convective terms, a scheme of double precision and second order upwind is used to consecutively solve the flow equations [29]. Central-difference and second order accuracy are selected for the diffusion terms. The coupled algorithm is used for the pressure-velocity coupling with the pseudo transient option [25]. Pseudo transient method option is a form of implicit under-relaxation for steady-state cases. It allows the user to obtain solutions faster and more robustly.

2.2 Computational domain

The channel dimensions used for the simulations are taken from a previously designed parallel plate channel with a height H , breadth $B=1.6H$ and a length $L=13H$. An isometric view showing the boundary conditions applied on the channel are presented in Figure 1.

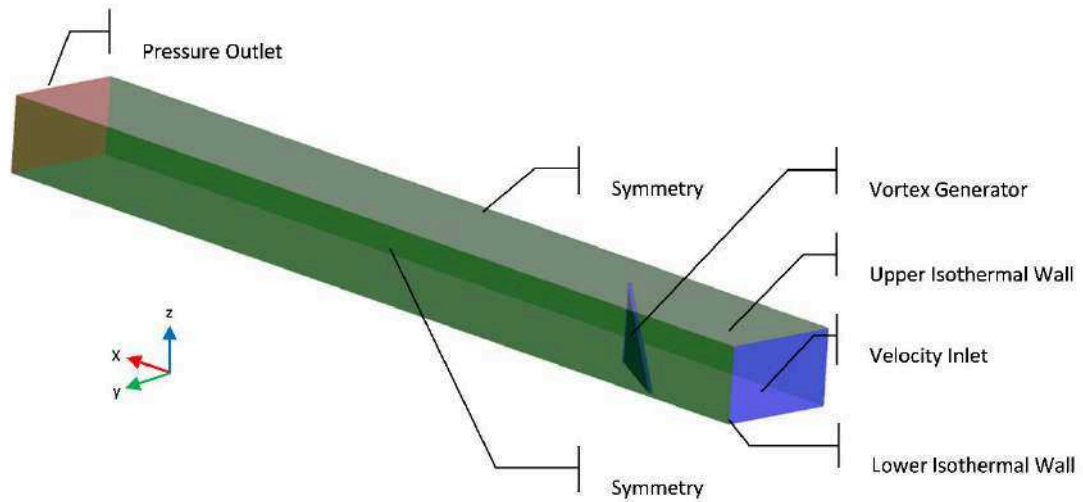


Figure 1 Isometric view of the computational domain showing the boundary conditions.

The Reynolds number, calculated based on the hydraulic diameter $D_h = 2H$, is taken equal to 4600. The reason behind selecting Reynolds equal to 4600 for this study is due to the high performance of such configuration at this Reynolds number [30]. The hydrodynamic and thermally developing flow is computed by means of a uniform inlet velocity profile and uniform inlet temperature equal to 300 K. Since factual simulations are the aim, realistic turbulence intensity is needed and inlet turbulence intensity equal to 3% is selected. First, it is in the range of the moderate wind tunnel intensities (1%–5%), thus being realistic to experimental test benches. Second, this value for the turbulence intensity was used in recent papers [31]. Also, the turbulence length scale, taken as a fraction of the inlet hydraulic diameter D_h [32, 33], can be chosen equal to $0.07D_h$ as used in similar flow configurations [34].

At the outlet, a constant pressure outlet condition has been set with a zero gauge pressure. Isothermal walls are set for both, upper and bottom walls, with a constant temperature of 350 K. All VGs cases have been simulated as an adiabatic wall as the purpose is to highlight the effect of the flow structure on the convective heat transfer.

2.2.1 DWP and IPWP configurations

Two types of vortex generators are used in this study: Figure 2 shows the dimensions of the classical Delta Winglet Pair (DWP) and the previously published Inclined Delta Winglet Pair (IPWP) vortex generators [30]. These dimensions are not for real scale heat exchanger channel, whereas they are prototypes compatible with existing wind tunnel test bench. Both configurations are implemented at an angle of attack equals to 30°. The same base and height dimensions are conserved for both VGs while the roll-up angle (angle between VG and lower wall) is decreased from 90°, for the DWP, to 30° for the IPWP. This geometry is obtained by the frontal projection of the DWP on a 30° inclined plane from the base axis.

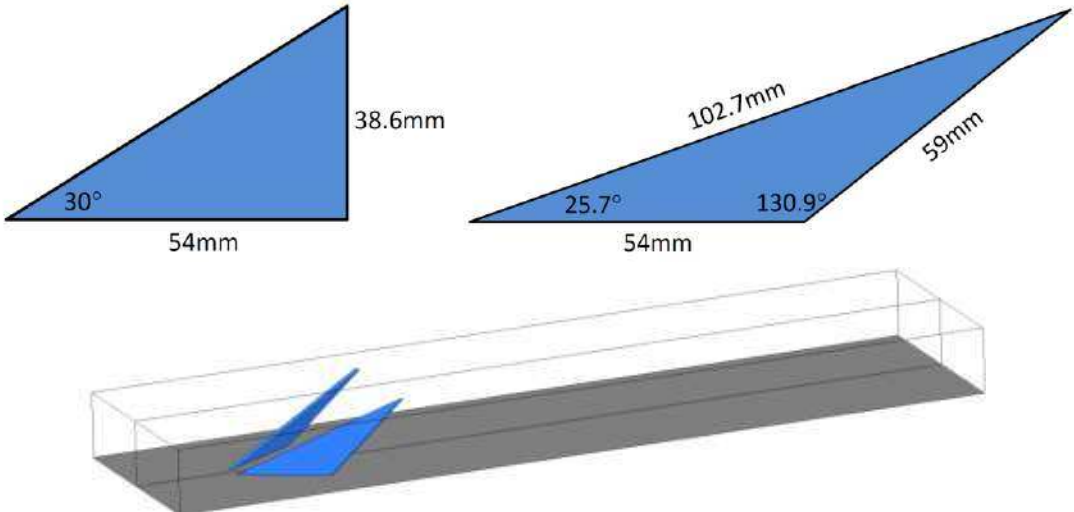


Figure 2 (a) DWP and IPWP geometry dimensions (b) 3D view for IPWP configuration.

The goal behind this study is to improve the heat transfer of the DWP and IPWP configurations at Reynolds number equals to 4600 by inserting protrusions downstream the VG and to compare with the IPWP performance that can be found in [30].

2.2.2 DWP with protrusion configurations

The approach studied throughout this section is the implementation of protrusions downstream the classical DWP configuration. Scaled dimensions of protrusions consisting of hemispheres of radius equal to one fourth of the channel height is implemented and located at a distance of three times the protrusion radius downstream the VG [21]. Figure 3 shows that the protrusions are located 30 mm downstream the VG trailing edge with a radius of 10 mm.

Two settings of hemispherical protrusions are selected and studied in this section. The first position of the protrusion, selected in the “idle region” of the swirling flow, is identified as DWP-PRO1. A protrusion in the shade of the DWP is named DWP-PRO2, as shown in Figure 5 **Error! Reference source not found.** Figure 4 is the streamline cross section plane of the channel downstream the DWP alone configuration studied by Oneissi et al. [30] presented to show the location of the protrusions as a function of transvers flows.

Also, Figure 5 shows the two configurations of DWP with protrusions: DWP-PRO1 is assigned to the DWP with 62 mm spanwise apart protrusions which is located in an inactive region of the swirling flow, while DWP-PRO2 is appointed to the DWP with 40 mm protrusions apart which interrupts the swirling flow of the main vortex as shown in Figure

5Error! Reference source not found.. Error! Reference source not found.Error!
Reference source not found.

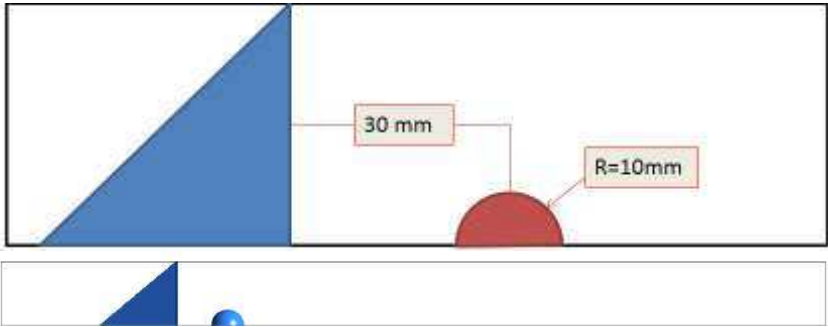


Figure 3 Dimensions of the protrusion downstream the DWP-PRO.

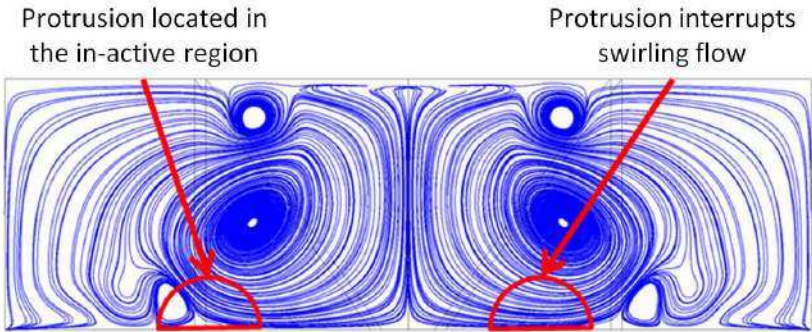
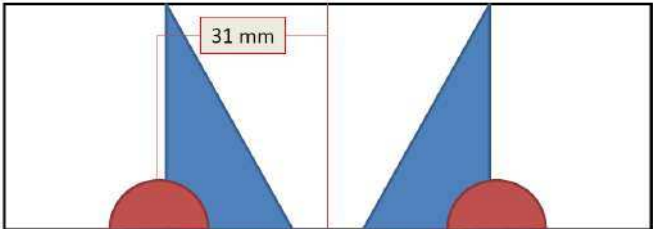


Figure 4 DWP-PRO1 (left) and PRO2 (right) positions with respect to the flow streamlines.



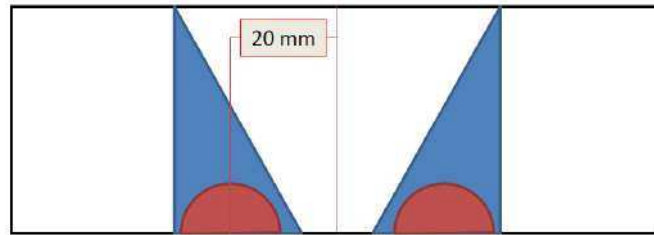


Figure 5 Geometries for VG with protrusion: DWP-PRO1 (top) and DWP-PRO2 (bottom).

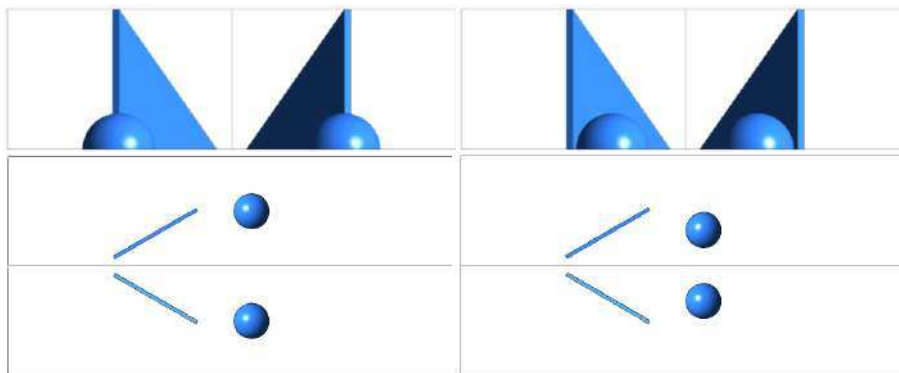


Figure 6 Front (top) and top views (bottom) of the DWP-PRO1 (left) and DWP-PRO2 (right).

2.2.3 IPWP with protrusion configurations

Another approach is also studied in this section by implementing a protrusion downstream the IPWP. The same protrusions implemented to the DWP configuration are used for the IPWP geometry. Thus, the protrusions are located 30 mm behind the VG lower corner edge with a radius of 10 mm. IPWP-PRO1 is assigned to the IPWP with 62 mm distant protrusions, while IPWP-PRO2 is appointed to the IPWP with 40 mm separated protrusions. Figure 7 shows 2D and 3D schematics of the IPWP PRO1 and IPWP PRO2 configurations.

In addition, two other protrusions are conducted in this section. The first setting IPWP-HS (HS for high spacing) goes for the same as the protrusions in the IPWP-PRO1 located in a

further downstream position. The second setting IPWP-M (M for middle), allocates a single protrusion at the plane of symmetry of the winglet pair positioned 30 mm behind the VG lower corner edge. Figure 8 shows 2D and 3D schematics of the IPWP-HS and IPWP-M configurations. Table 1 recapitulates the different VG configurations studied:

Table 1 Different VG configurations studied.

VG	PRO1	PRO2	HS	M
DWP	DWP-PRO1	DWP-PRO2	–	–
IPWP	IPWP-PRO1	IPWP-PRO2	IPWP-HS	IPWP-M

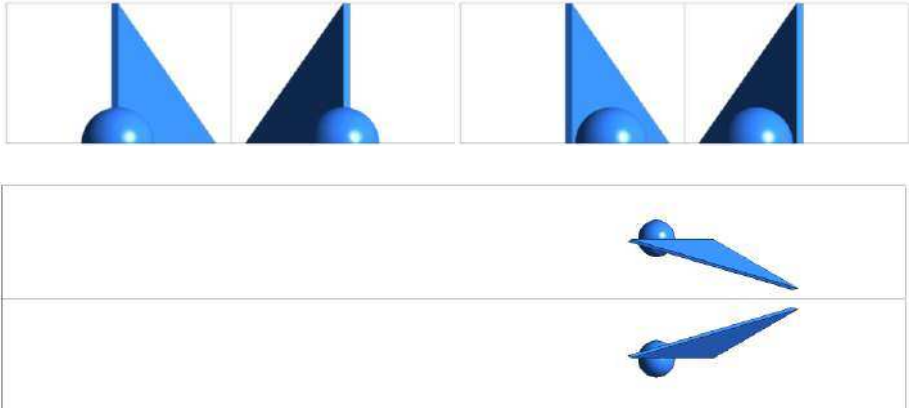


Figure 7 IPWP-PRO1 (top-left), IPWP-PRO2 (top-right) viewed from the aft, IPWP-PRO side view (middle), top view (bottom).

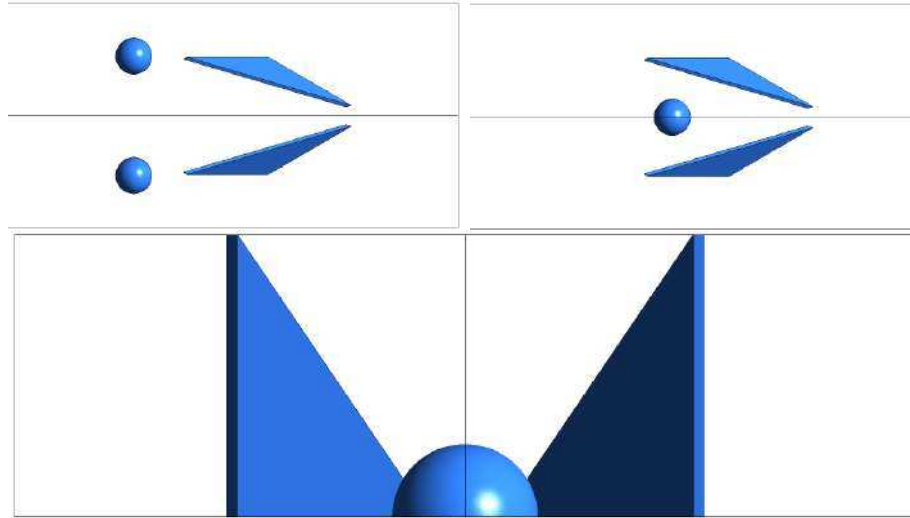


Figure 8 Top view for the IPWP-HS (top-left), IPWP-M (top-right), IPWP-M viewed from aft (bottom).

2.3 Mesh sensitivity study

Non-uniform mesh with polyhedral cells is used for discretization of the computational domain. In order to maintain an accepted low value for y^+ , all walls in the domain (channel and VG walls) are treated with ten inflation layers with a first layer thickness of $40 \mu\text{m}$. Mesh independency is carried out on an empty channel turbulent flow where $\text{Re}=21600$ which insures the mesh legitimacy at any lower Reynolds number.

Table 2 shows the different mesh densities used for the sensitivity study. In order to reach the mesh size adopted in the simulation, an arbitrary estimate of the element size is implemented, meshed and then the solution is computed. The element size is then decreased by a factor of 1.3 until the percent error based on both global Nusselt and friction coefficient is less than 2%. The error is calculated as following: $\text{Error} = (\overline{Nu}_{new} - \overline{Nu}_{old}) / \overline{Nu}_{old}$. Thus, as it can be observed from Table 2, mesh-3 is used for all the other simulations. This

choice is due to the non-necessity of any further refinement since the percent error becomes smaller than 2% after the 3rd mesh. All meshes have a y^+ value much lower than 5. This was obtained by using ten inflation layers of 40 μm first layer thickness (40 μm –10L) which ensure that the first cell is contained in the near wall viscous sub-layer insuring no wall function is used.

Table 2 Mesh study information.

Mesh	1	2	3
Maximum element size in volume (mm)	2.30	1.70	1.30
Element size on walls (mm)	1.50	1.15	0.90
Number of elements	440,123	715,789	1,300,245
Inflation (mm)	20 μm –18L	30 μm –12L	40 μm –10L
Maximum y^+	0.90	0.90	0.80
Error (%)	–	3.12	1.08

3. Results and discussion

3.1 Quantitative parameters and experimental validation

The performance evaluation of the different configurations is dismantled into two main categories, global and local approaches. Global Nusselt number is given by:

$$\overline{Nu} = \frac{D_h h}{k} = \frac{2Hh}{k} \quad (6)$$

where $h = \frac{\dot{m}c_p(T_o - T_i)}{A_f(T_s - T_{avg})}$ is obtained from the energy balance on a control volume enclosing the channel, and $T_{avg} = \frac{T_o + T_i}{2}$ is the average temperature between the inlet and outlet.

Global friction factor is given by:

$$f = \frac{D_h \Delta P}{2L\rho U^2} = \frac{H\Delta P}{L\rho U^2} \quad (7)$$

Analysis of the Nusselt number and the friction factor separately, do not give a clear idea of the global performance of the different geometries. Therefore, to compare the heat transfer efficiency of the different configurations for constant pumping power, the thermal enhancement factor (TEF) is introduced. The thermal enhancement factor is defined as the ratio of the heat exchanger (channel with VGs) convective heat transfer to that in an empty channel and represented as:

$$TEF = \frac{Nu}{Nu_0} \left(\frac{f}{f_0} \right)^{-1/3} \quad (8)$$

where Nu_0 is the global Nusselt number for empty channel, Nu is the global Nusselt number for channel equipped with VG, f_0 is the global friction coefficient for empty channel, f is the global friction coefficient for channel equipped with VG.

Spanwise averaged local Nusselt number at a given x location in the channel is given by:

$$Nu_{(x)} = \frac{D_h h_x}{k} = \frac{2Hq_x''}{k(T_s - T_{x,b})} \quad (9)$$

where q_x'' is the heat flux at position x and $T_{x,b}$ is the averaged bulk temperature in a cross sectional plane of the channel at position x and defined by:

$$T_{x,b} = \frac{\int_A \rho u C_p T dA}{\dot{m} C_p} = \frac{\int_A \rho u C_p T dA}{\rho u C_p dA} = \frac{1}{UA} \int_A u T dA \quad (10)$$

Spanwise averaged local friction factor at a given x location in the channel is given by:

$$f_{(x)} = \frac{\Delta P}{P_{dynamic}} = \frac{2(P_{in} - P_x)}{\rho U^2} \quad (11)$$

For thermally and hydraulically developing laminar air flow, the results are compared for global Nusselt number (not the usual definition presented in equation 6) using Stephan's correlation, (see equation 13) [35]. Stephan's correlation is used as a reference since it is the recommended analytical expression for overall Nusselt number in thermally and hydraulically laminar developing flow between two parallel-plate channels [35]. It is the integration of the local Nusselt number ($Nu_{(x)}$) over a specific length (from 0 to x) and it is defined based on the bulk temperature at each position $T_{x,b}$. This equation for global Nusselt number is valid in the range $0.1 \leq Pr \leq 1,000$ for parallel plate channels.

$$Nu_{0-x} = \frac{1}{x} \int_0^x Nu_{(x)} \cdot dx \quad (12)$$

Stephan's correlation is defined as:

$$Nu_{0-x} = 7.55 + \frac{0.024x^{*-1.14}}{1 + 0.0358x^{*-0.64} Pr^{0.17}} \quad (13)$$

where

$$x^* = \frac{x}{Pe \cdot D_h} = \frac{x}{Re_{D_h} \cdot Pr \cdot D_h} \quad (14)$$

Table 3 presents the global Nusselt numbers obtained from simulation compared to correlations of Stephan [35] in laminar flow and shows a good correspondence with a maximum error of 7.4%.

Table 3 Global Nusselt number comparison between simulation and correlations.

Reynolds number	Present simulation	Stephan's correlation [35]	Error (%)
270	7,85	8,42	6,80
540	9,41	9,26	1,60
1 080	11,58	10,78	7,40

A second approach is adopted to validate the numerical results in turbulent flow regime for the case with VG by comparing to Tiggelbeck's experimental results [36]. The results of interest are those dealing with a delta winglet pair (DWP) normalized to an empty channel. Tiggelbeck et al. [36] in their experiment found out that the values of the normalized global Nusselt number and friction factor for Re=4600 are equal to 1.49 and 1.91 respectively. The same channel dimensions, boundary conditions and post-processing as Tiggelbeck's [36] experiment are considered in the present study.

Table 4 shows a comparison between numerical simulation and experimental results obtained by Tiggelbeck et al. [36] for Re=4600. The results are in a good agreement with each other with relatively low discrepancy, since error between simulations and experiments is

always lower than 5%. The numerical model is reliable to predict flow and heat transfer characteristics.

Table 4 Normalized global Nusselt number, friction factor and thermal enhancement factor comparison for Re=4600.

	Simulation results	Experiment results [36]	Error (%)
Nu/Nu_0	1.56	1.49	4.7
f/f_0	1.95	1.91	2
$(Nu/Nu_0)(f/f_0)^{-1/3}$	1.25	1.2	4.2

Exhibited discrepancy between numerical simulations and experimental work can be mainly caused from the setup process difference between numerical simulation and experiment, in addition to data acquisition uncertainties and other factors.

3.2 Global performance analysis of protrusion enhanced configurations

Figure 9 shows the performance of the two DWP protrusion enhanced configurations based on the thermal enhancement factor (TEF) criterion for Reynolds number equal to 4600. Even though the enhancement is not firm, both types give better performance compared to DWP geometry that was already an interesting configuration when compared to the smooth channel case. All comparisons are conducted relative to the DWP geometry, which is taken as a baseline configuration.

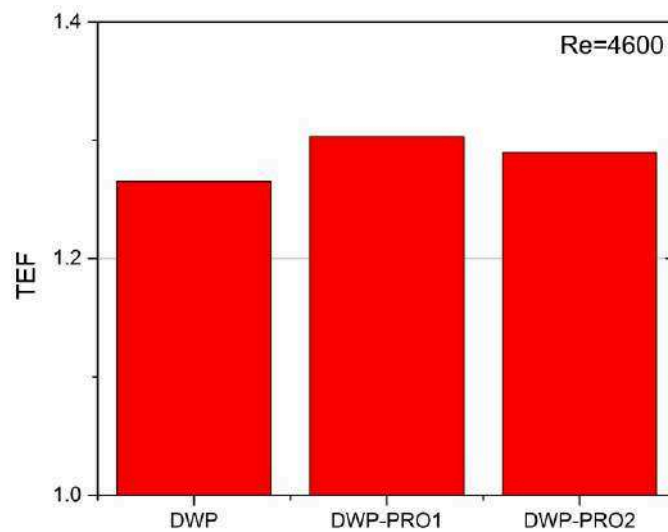


Figure 9 Performances of the DWP and DWP-PRO based on the TEF for $Re=4600$.

The several IPWP protrusion enhanced configurations thermal enhancement factors are presented in Figure 10 that shows the superiority of the IPWP-M over other IPWP types. It can be shown that both IPWP-PRO1 and IPWP-PRO2 enhance the heat transfer, but this enhancement is less than other configurations. When moving the protrusion more in a downstream direction (IPWP-HS) the heat transfer is more enhanced than the regular IPWP, but less than IPWP-M.

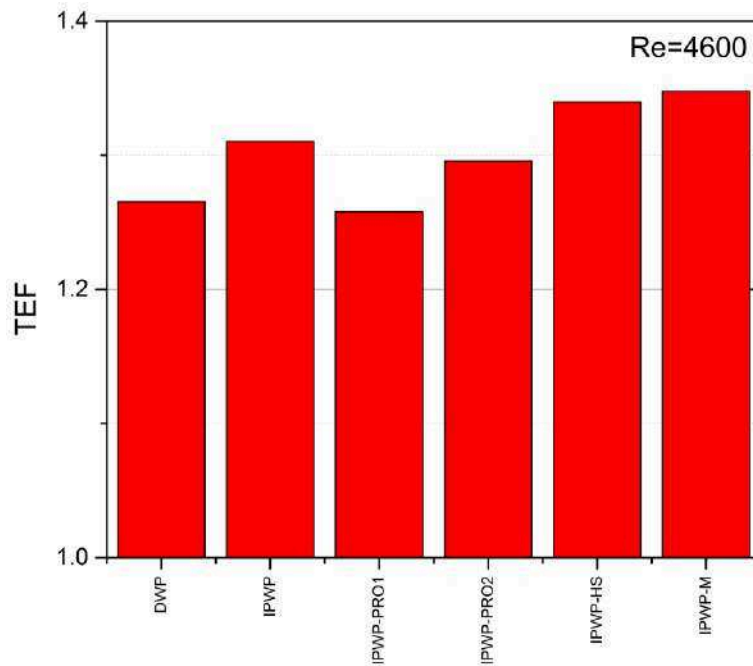


Figure 10 Performances of the various types of IPWP based on the TEF for Re=4600.

Percentages of TEF for all configurations compared to the baseline geometry DWP are listed in Table 5. Both IPWP-M and IPWP-HS give a better TEF compared to other configurations from DWP baseline configuration.

Table 5 Thermal enhancement fraction for all DWP and IPWP configurations studied for Re=4600.

	DWP	DWP-PRO1	DWP-PRO2	IPWP	IPWP-PRO1	IPWP-PRO2	IPWP-HS	IPWP-M
TEF	1.27	1.30	1.29	1.31	1.26	1.30	1.34	1.35
Enhancement relative to DWP (%)	–	2.4	1.6	3.1	-0.8	2.4	5.5	6.3

3.3 Streamwise evolution of performance parameters

Subsequent to demonstrating the performance of the DWP and IPWP configurations on the global scale, this section illustrates the performance from a streamwise averaged local point of view to understand the flow characteristics and the heat transfer mechanisms. The present local study is limited to the IPWP configurations due to its innovative character and improved performance compared to DWP ones. From a local scope, the performance of the IPWP with various protrusions is demonstrated throughout this section. IPWP-PRO1, IPWP-PRO2, IPWP-M and IPWP-HS are illustrated in Figure 11 through Figure 14.

Figure 11 and Figure 12 present the streamwise evolution of the spanwise-averaged Nusselt number throughout the channel (equation 9). Friction coefficient and vorticity are illustrated in Figure 13 and Figure 14 respectively. The left vertical dotted line with a filled triangle at the bottom of the graph is the VG leading edge connected to the bottom wall. The second one (from left) designates for the separation of the bottom trailing edge with the bottom wall. The bare vertical line represents the position where the VG trailing edge merges with the upper wall. While the vertical lines with filled circle at the bottom of the graph represents the position where the protrusion is inserted at the channel bottom wall.

It can be seen from Figure 11 that the normalized Nusselt number do not show any enhancement relative to IPWP baseline configuration through the channel for IPWP-PRO1 and IPWP-PRO2 configurations, where IPWP-PRO1 gives a better performance IPWP-PRO2. While IPWP-HS and IPWP-M grant a better Nusselt number compared to the IPWP as shown in Figure 12.

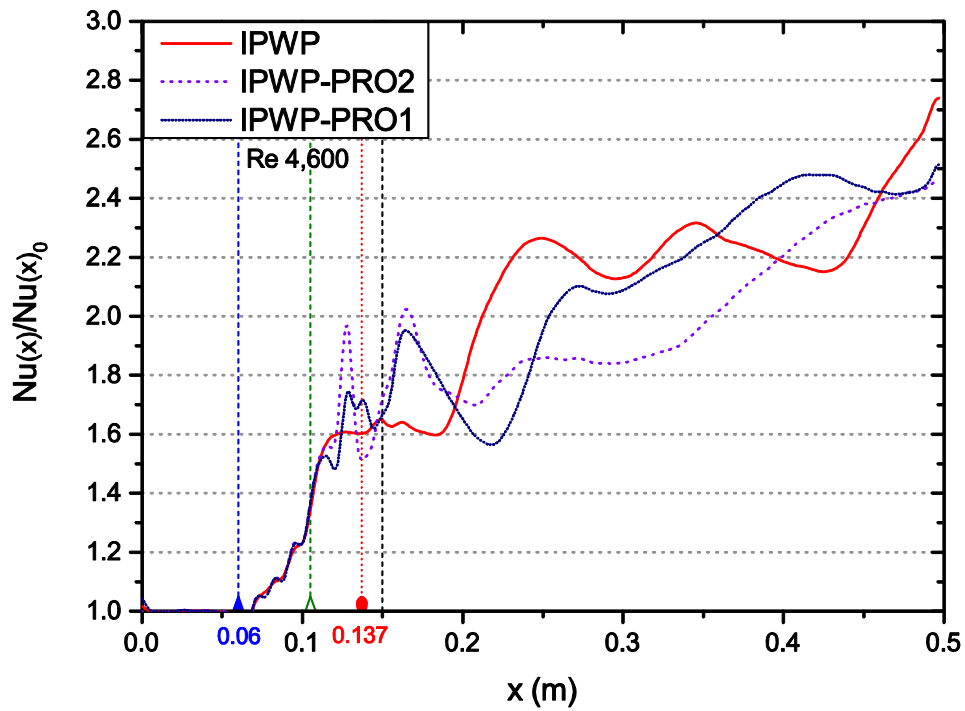


Figure 11 Streamwise evolution of normalized spanwise averaged Nusselt number for the IPWP and IPWP-PRO for $Re=4600$.

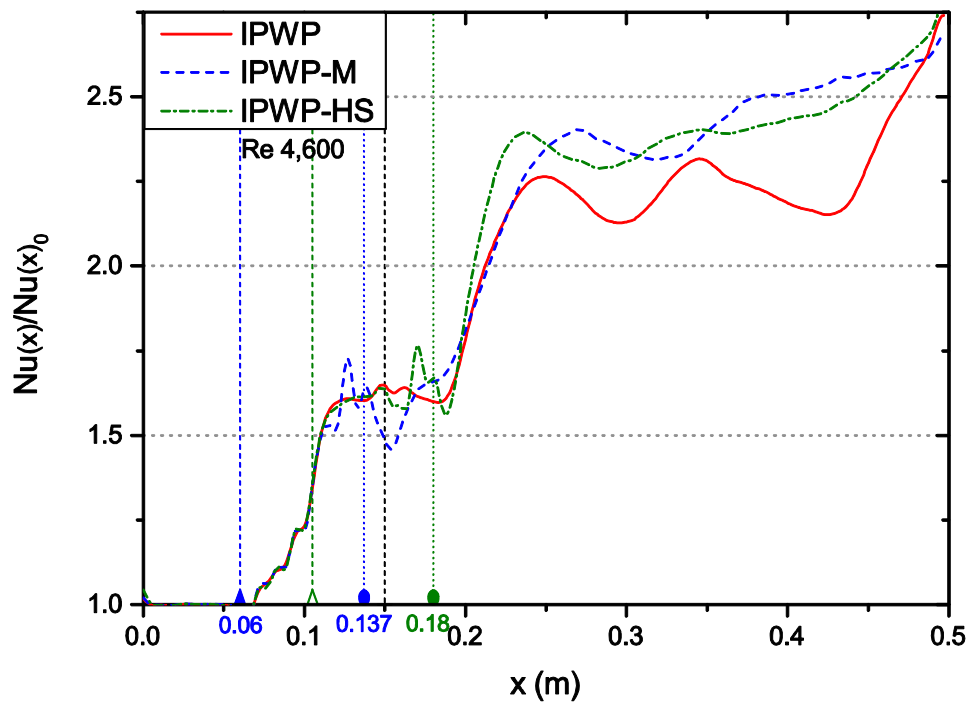


Figure 12 Streamwise evolution of normalized spanwise averaged Nusselt number for the IPWP and IPWP-M/HS for $Re=4600$.

The normalized spanwise averaged friction factor (Eq. 11) of IPWP-PRO1 and IPWP-PRO2 increases by 21% and 27% respectively at the peak as presented in Figure 13. The reason behind a 6% difference between IPWP-PRO1 and IPWP-PRO2 is that the protrusion in IPWP-PRO1 is located in an idle swirling flow, as previously shown in Figure 4, and disrupt the flow downstream of VGs more strongly. Besides, the principal increase of the f_x / f_{x0} value, upstream the peak, begins from the location of the protrusion, at $x=0.137$ m as shown in Figure 13. In the other hand, IPWP-HS and IPWP-M give a better result than IPWP-PRO1 and IPWP-PRO2 with an increase in the friction factor peak equal to only 4% and 9% respectively. The peak produced by the IPWP-HS configuration is moreover shifted further downstream, at $x=0.18$ m, which is located at the location of the protrusion in this case.

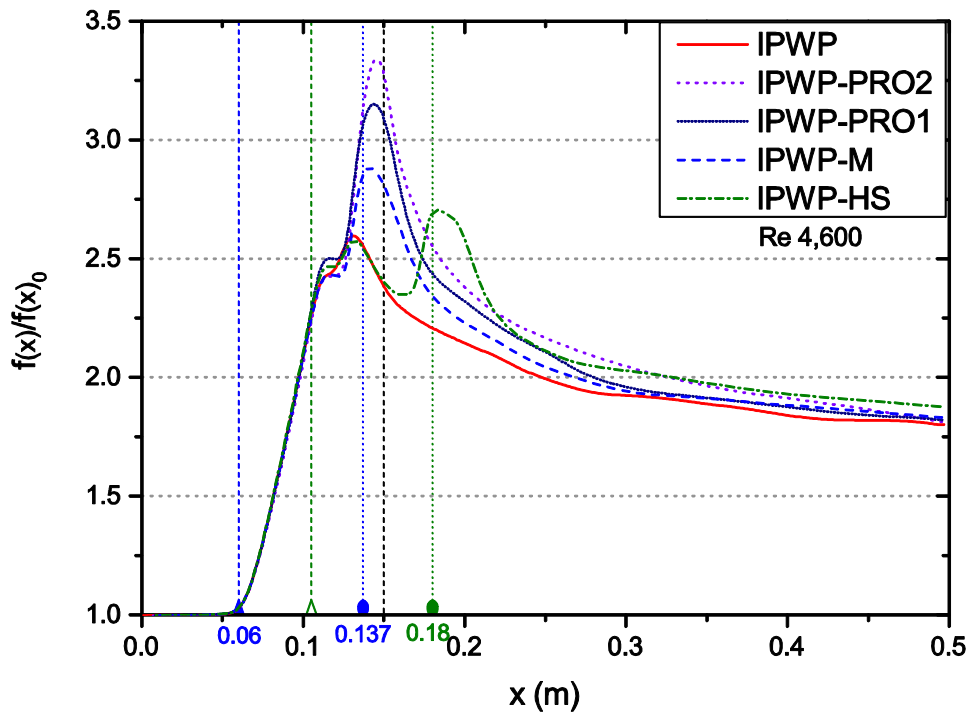


Figure 13 Streamwise evolution of normalized spanwise averaged friction number for the IPWP and IPWP protrusion enhanced configurations for $Re=4600$.

Vorticity of IPWP with protrusions is demonstrated in Figure 14. Vorticity is computed over cross sectional plane area at each local location (x) along the channel. Figure 14 shows that IPWP-HS and IPWP-M maintains almost the same averaged vorticity over the channel with the IPWP. It can be seen from Figure 14 that the vorticity increases at the protrusion location

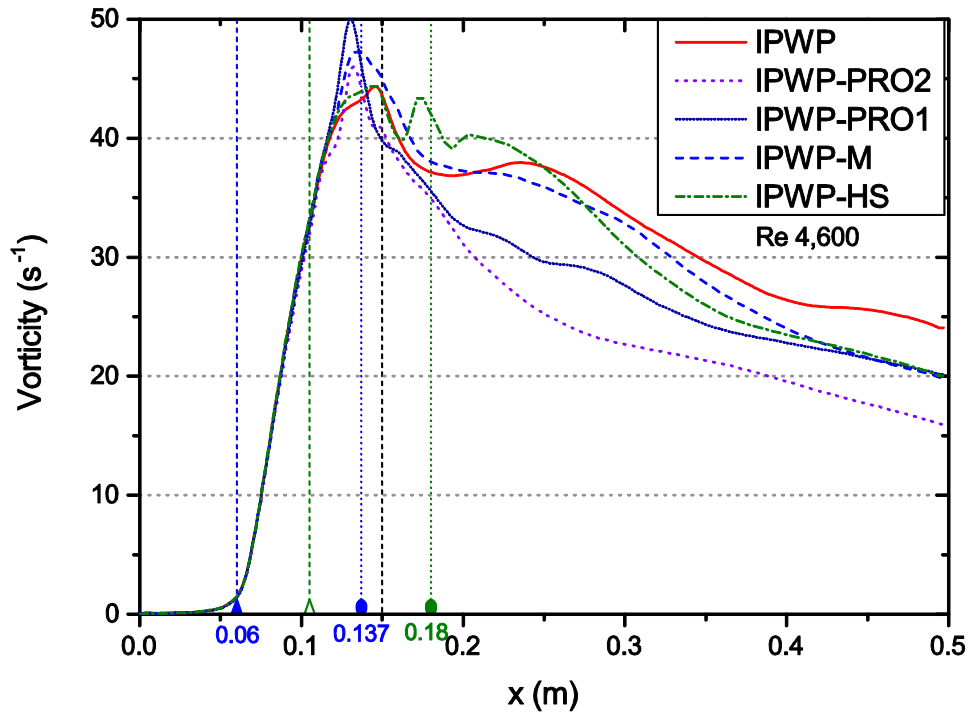


Figure 14 Streamwise evolution of normalized vorticity for the IPWP and IPWP protrusion enhanced configurations for $Re=4600$.

3.4 Flow structure

After presenting the VG configuration with protrusions and illustrating the results from the global and local scopes, it is obvious that the IPWP with protrusions performance is noticeable. For thorough examination of the occurring convective heat transfer mechanism, cross-section planes are made visualizing various streamlines and contours in different locations downstream VGs. Figure 15 and Figure 16 show velocity streamlines and temperature contours respectively at different planes downstream the IPWP, IPWP-HS and IPWP-M. These planes are located at different longitudinal distances measured from the VG leading edge where x/H of P1 to P15 are 2, 2.5, 2.7, 2.9, 3.1, 3.3, 3.5, 4, 4.5, 5, 6.5, 8, 9, 10 and 11.5 respectively. It is shown from Figure 15 that the same number of vortices is

maintained for the three configurations at most of the channel planes, except the regions just downstream protrusions. For IPWP-HS, in the region directly downstream the protrusions (after plane P9), an additional vortex is generated due to protrusion and sustains till plane P13. Whereas the IPWP-M protrusion (located at plane P6) generates two small vortices near the bottom wall at plane P7 and dissipates rapidly before plane P9. These two vortices are formed in a form of horseshoe vortex at the protrusion base near the bottom wall.

These results are analogous to that represented in Figure 16 that shows the effect of flow structure on the temperature distribution in these planes. For the IPWP-HS, the temperature distribution shows higher temperature zones just downstream the protrusions (at plane P10), which is a result of the newly generated vortices due to protrusions. The IPWP and IPWP-HS cases do not show any heat transfer distribution at the middle plane of the channel ($y/H=0$) on the bottom wall. This is because these configurations are a common flow down configurations that direct the flow in the down direction at the channel middle plane and thus, no significant high temperatures are indicated. For the IPWP-M case, the protrusion perturbs the downwash flow by producing the small two vortices and thus increasing the heat distribution in that region (plane P7 and plane P8).

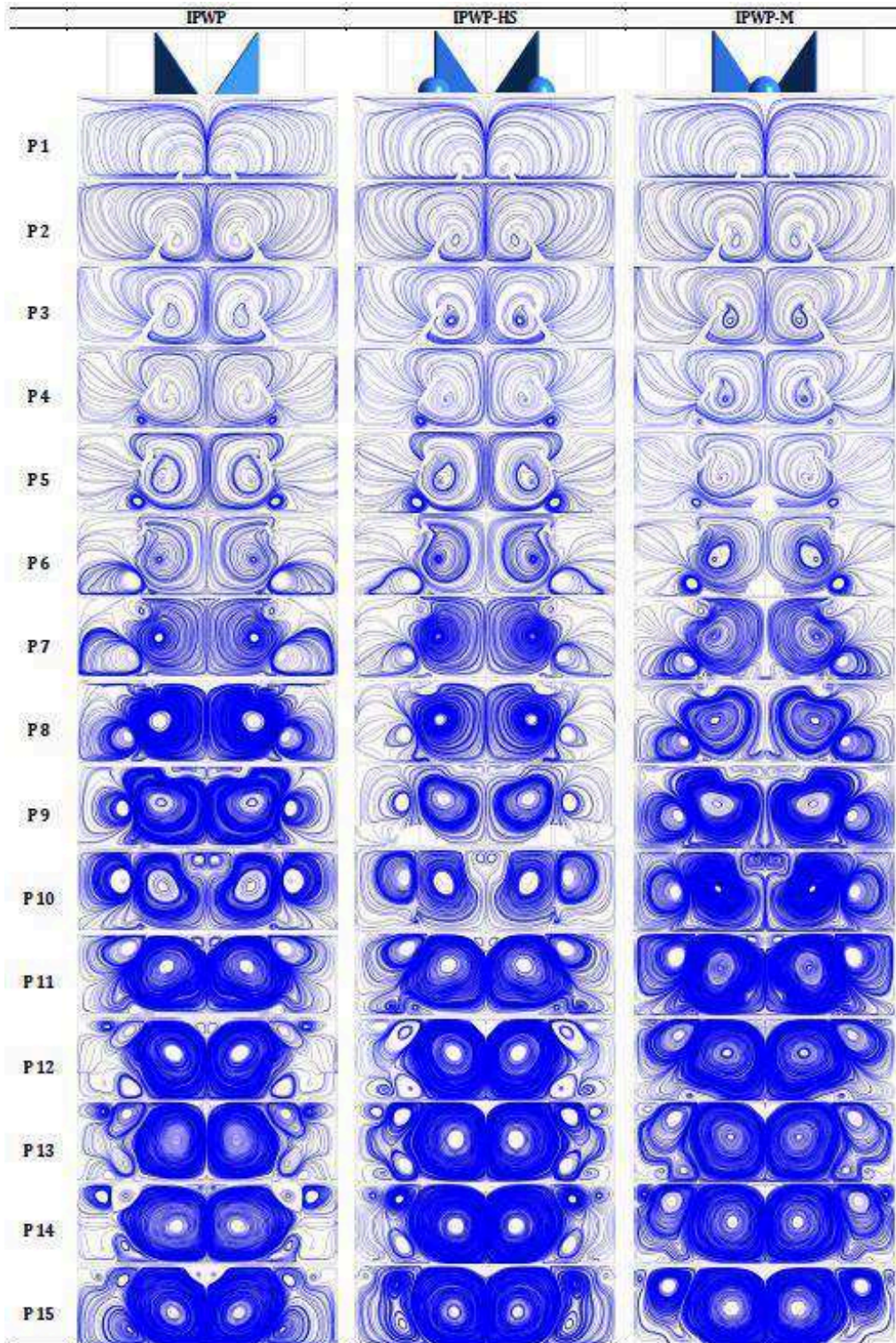


Figure 15 Velocity streamlines for the IPWP, IPWP-HS and IPWP-M configurations for $Re=4600$.

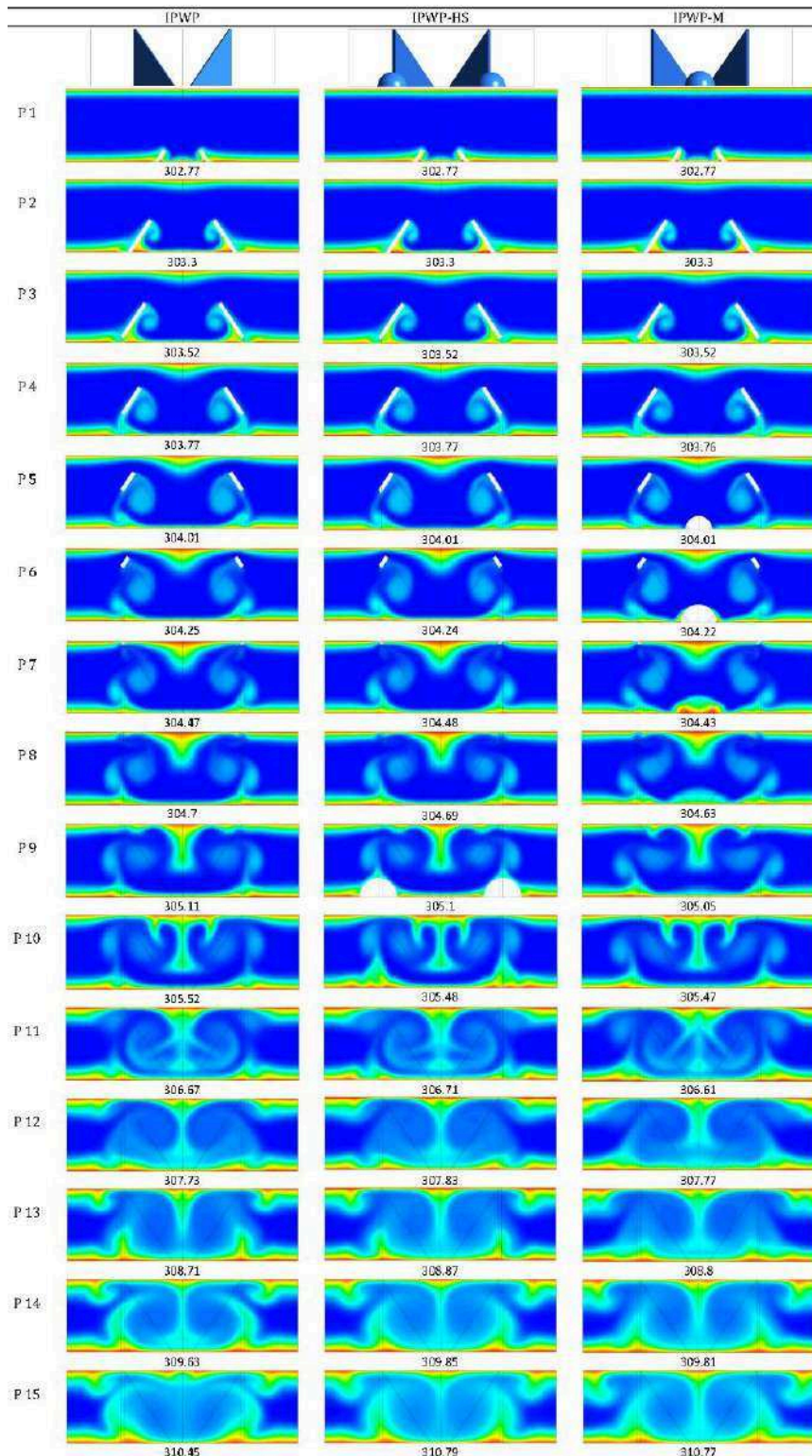


Figure 16 Temperature contours with area averaged temperature (below each section) for the IPWP, IPWP-HS and IPWP-M configurations for $Re=4600$.

4. Conclusion

Three-dimensional numerical simulations of longitudinal vortex generators combined with protrusions located downstream are performed to scrutinize heat transfer enhancement in parallel plate-fin heat exchanger. Turbulent flow with the aid of the $\kappa\text{-}\omega$ SST model is modeled and validated with correlations and experimental data at Reynolds number equal to 4600. The aim of this work is to assess the influence of protrusions and determine if they can further increase the thermal enhancement factor of the previously published innovative vortex generator IPWP.

Protrusions are introduced to the DWP resulting in the creation of the DWP-PRO1 and DWP-PRO2. Both configurations neither enhance the heat transfer nor friction factor drastically, while DWP-PRO1 having a better performance.

As well, protuberances are implemented with the IPWP at different locations, leading to the production of the IPWP-PRO1, IPWP-PRO2, IPWP-HS and IPWP-M.

These new formations end up with two effects:

- An un-assisting behavior that is originated from two formations: the IPWP-PRO1 and IPWP-PRO2 relative to IPWP baseline configuration, where both configurations do not outrun the regular IPWP in the total heat transfer enhancement.
- On the other hand, the IPWP-HS and IPWP-M escalate the heat transfer enhancement level. It is also revealed that the IPWP-M bestow a better performance than the IPWP-HS. Thus the present results are very promising

with 6.5% heat transfer enhancement for the IPWP-M compared to DWP and 3% increase for both DWP-PRO1 and IPWP-M compared respectively to DWP and IPWP geometries.

References

- [1] P. Ligrani, G. Mahmood, J. Harrison, C. Clayton and D. Nelson, "Flow structure and local Nusselt number variations in a channel with dimples and protrusions on opposite walls," *International Journal of Heat and Mass Transfer*, vol. 44, pp. 4413-4425, 2001.
- [2] J. Tala, S. Russeil, D. Bougeard and J.-L. Harion, "Numerical analysis of the fin spacing effect on the horseshoe vortex system evolution in a two-rows finned-tube heat exchanger," *International Journal of Numerical Methods for Heat and Fluid Flow*, vol. 23, no. 7, pp. 1136-1154, 2013.
- [3] S. Vintrou, D. Bougeard, S. Russeil, R. Nacereddine and J.-L. Harion, "Quantitative infrared investigation of local heat transfer in a circular finned tube heat exchanger assembly," *International Journal of Heat and Fluid Flow*, vol. 44, pp. 197-207, 2013.
- [4] A. Garcia, J. Solano, P. Vicente and A. Viedma, "The influence of artificial roughness shape on heat transfer enhancement: Corrugate tubes, dimpled tubes and wire coils," *Applied Thermal Engineering*, vol. 35, pp. 196-201, 2012.
- [5] C. Habchi, S. Russeil, D. Bougeard, J. L. Harion, T. Lemenand, D. Della Valle and H. Peerhossaini, "Enhancing Heat Transfer in Vortex Generator-type Multifunctional Heat Exchangers," *Applied Thermal Engineering*, vol. 38, pp. 14-25, 2012.
- [6] J. Wu and W. Tao, "Numerical study on laminar convection heat transfer in a channel with longitudinal vortex generator. Part B: Parametric study of major influence factors," *International Journal of Heat and Mass Transfer*, vol. 51, pp. 3683-3692, 2008.

- [7] P. Saha, G. Biswas and S. Sarkar, "Comparison of winglet-type vortex generators periodically deployed in a plate-fin heat exchanger - A synergy based analysis," *International Journal of Heat and Mass Transfer*, vol. 74, pp. 292-305, 2014.
- [8] C. Habchi, J. L. Harion, S. Russeil, D. Bougeard, F. Hachem and A. Elmarakbi, "Chaotic Mixing by Longitudinal Vorticity," *Chemical Engineering Science*, vol. 104, pp. 439-450, 2013.
- [9] C. Habchi, T. Lemenand, D. Della Valle, A. Al Shaer and H. Peerhossaini, "Experimental Study of the Flow Field Behind a Perforated Vortex Generator," *Journal Applied Mechanics and Technical Physics*, vol. 16, pp. 221-229, 2015.
- [10] R. Kamboj, P. S. Dhingra and P. G. Singh, "CFD Simulation of Heat Transfer Enhancement by Plain and Curved Winglet Type Vortex Generators with Punched Holes," *International Journal of Engineering Research and General Science*, vol. 2, no. 4, 2014.
- [11] G. Zhou and Z. Feng, "Experimental investigations of heat transfer enhancement by plane and curved winglet type vortex generators with punched holes," *International Journal of Thermal Sciences*, vol. 78, pp. 26-35, 2014.
- [12] M. A. Elyyan and D. K. Tafti, "A novel split-dimple interrupted fin configuration for heat transfer augmentation," *International Journal of Heat and Mass Transfer*, vol. 52, pp. 1561-1572, 2009.
- [13] M. A. Elyyan and D. K. Tafti, "Effect of Coriolis force in a rotating channel with dimples and protrusions," *International Journal of Heat and Fluid Flow*, vol. 31, pp. 1-18, 2010.

- [14] J. Lee and K.-S. Lee, "Correlations and shape optimization in a channel with aligned dimples and protrusions," *International Journal of Heat and Mass Transfer*, vol. 64, pp. 444-451, 2013.
- [15] Y. Chen, Y. Chew and B. Khoo, "Heat transfer and flow structure on periodically dimple-protrusion patterned walls in turbulent channel flow," *International Journal of Heat and Mass Transfer*, vol. 78, pp. 871-882, 2014.
- [16] S. D. Hwang, H. G. Kwon and H. H. Cho, "Heat transfer with dimple/protrusion arrays in a rectangular duct with a low Reynolds number range," *International Journal of Heat and Fluid Flow*, vol. 29, pp. 916-926, 2008.
- [17] J. He, L. Liu and A. M. Jacobi, "Air-Side Heat-Transfer Enhancement by a New Winglet-Type Vortex Generator Array in a Plain-Fin Round-Tube Heat Exchanger," *Journal of Heat Transfer*, vol. 132, pp. 071801-1 till 071801-9, 2010.
- [18] Y. He, H. Han, W. Tao and Y. Zhang, "Numerical study of heat-transfer enhancement by punched winglet-type vortex generator arrays in fin-and-tube heat exchangers," *International Journal of Heat and Mass Transfer*, vol. 55, pp. 5449-5458, 2012.
- [19] W. J.M. and T. W. Q., "Investigation on Laminar Convection Heat Transfer in Fin-and-Tube Heat Exchanger in Aligned Arrangement With Longitudinal Vortex Generator From the Viewpoint of Field Synergy Principle," *Applied Thermal Engineering*, vol. 27, pp. 2609-2617, 2007.
- [20] S. Tiggelbeck, N. Mitra and M. Fiebig, "Flow Structure and Heat Transfer in a Channel with Multiple Longitudinal Vortex Generators," *Experimental Thermal and Fluid*

- Science, vol. 5, no. 4, pp. 425-436, 1992.
- [21] C. Habchi, S. Russeil, D. Bougeard, J.-L. Harion, T. Lemenand, D. Della Valle and H. Peerhossaini, "Enhancing Heat Transfer in Vortex Generator-type Multifunctional Heat Exchangers," *Applied Thermal Engineering*, vol. 38, pp. 14-25, 2012.
- [22] Y. Xie, H. Qu and D. Zhang, "Numerical investigation of flow and heat transfer in rectangular channel with teardrop dimple/protrusion," *International Journal of Heat and Mass Transfer*, vol. 84, pp. 486-496, 2015.
- [23] Z. Huang, G. Yu, Z. Li and W. Tao, "Numerical study on heat transfer enhancement in a receiver tube of parabolic trough solar collector with dimples, protrusions and helical fins," *Energy Procedia*, vol. 69, pp. 1306-1316, 2015.
- [24] Y. Chen, Y. Chew and B. Khoo, "Heat transfer and flow structure on periodically dimple–protrusion patterned walls in turbulent channel flow," *International Journal of Heat and Mass Transfer*, vol. 78, pp. 871-882, 2014.
- [25] I. ANSYS, "Turbulence Models," in *ANSYS Fluent 12.0 Theory Guide*, April 2009.
- [26] F. Menter, "Two-equation eddy-viscosity turbulence models for engineering applications," *AIAA Journal*, vol. 32, pp. 1598-1605, 1994.
- [27] K. Yongsiri, P. Eiamsa-ard, K. Wongcharee and S. Eiamsa-ard, "Augmented heat transfer in a turbulent channel flow with inclined detached-ribs," *Case Studies in Thermal Engineering*, vol. 3, pp. 1-10, 2014.
- [28] X.-Y. Tanga and D.-S. Zhu, "Flow structure and heat transfer in a narrow rectangular channel with different discrete rib arrays," *Chemical Engineering and Processing:*

- Process Intensification, vol. 69, pp. 1-14, 2013.
- [29] R. Warming and R. Beam, "Upwind second-order difference schemes and applications in aerodynamic flows," *AIAA Journal*, vol. 14, no. 9, pp. 1241-149, 1976.
- [30] M. Oneissi, C. Habchi, S. Russeil, D. Bougeard and T. Lemenand, "Novel design of delta winglet pair vortex generator for heat transfer enhancement," *International Journal of Thermal Sciences*, vol. 109, pp. 1-9, 2016.
- [31] M. Nacer-Bey, S. Russeil and B. Baudoin, "PIV visualizations to the flow structure upstream of the tubes in a two-row plate-fin-and-tube heat exchanger," in *Proceeding of the 4th International Conference on Compact Heat Exchangers and Enhancement Technology for the Process Industries*, Grete Island, Greece, September 29 - October 3 - 2003.
- [32] H. Versteeg and W. Mallasekera, *Computational Fluid Dynamics*, London: Longman Group, 1995.
- [33] O. Zikanov, *Essential Computational Fluid Dynamics*, Hoboken: Wiley, 2010.
- [34] P. Naphon and K. Kornkumjayrit, "Numerical analysis on the flow and heat transfer in the channel with V-shaped wavy lower plate," *International Communications in Heat and Mass Transfer*, vol. 35, pp. 839-843, 2008.
- [35] A. Bejan, "Forced Convection: Internal Flows," Durham, North Carolina, Department of Mechanical Engineering and Materials Science, Duke University, 2003, pp. 395-438.
- [36] S. Tiggelbeck, N. K. Mitra and M. Fiebig, "Comparison of Wing-Type Vortex Generators for Heat Transfer Enhancement in Channel Flows," *Journal of Heat Transfer*, vol. 116, pp. 880-885, 1994.

Chapter 8

Conclusion and perspectives

The objective of this study was to investigate and design a new vortex generator (VG) for enhancing heat transfer in parallel plate-fin heat exchangers. Detailed overview about heat transfer enhancement techniques was presented in a literature review, in which are divided into three categories: passive, active and compound techniques. Passive techniques are more commonly used in heat exchangers since they are characterized by their efficiency, economy, ease of manufacturing and lower maintenance efforts. Vortex generators are one of the passive techniques that create secondary flows, disrupt the growth of the boundary layer and create swirling flows that enhance exchange between the walls and the core fluid, thus improving heat transfer.

Research in fluid mechanics mainly depends on three types of scientific activities: experiments, analyses and simulations. The scientific research can either rely on one of the three types or combines two and maybe three types of activities. If experimental or simulation method is chosen solely for a scientific research, results quality may not be high enough due to many factors. While integrating more than one activity might offer further solid results. Thus, computational fluid dynamics (CFD) governing equations, turbulence models and numerical error sources in addition to experimental instrumentations and error sources was all overviewed in Chapter-2.

Since performing experimental studies for newly designed VG is considered time and money consuming, numerical investigation using computational fluid dynamics simulations was conducted. The first goal was to choose and validate the turbulence numerical model to

be used in the study of longitudinal vortices. This validation was done using results extracted from experiment done on rectangular winglet pair (RWP) and compared to three-dimensional (3D) numerical simulation results.

The conducted experiment was presented in Chapter-3 and examined the characteristics of longitudinal vortices generated by rectangular winglets in fully developed turbulent channel flow. A row of rectangular winglets was implemented in parallel plate test bench channel, where stereoscopic particle image velocimetry (SPIV) was used to harvest the three components of velocity fields in two-dimensional (2D) planes. The flow analysis was conducted at $Re=4400$ based on the channel's hydraulic diameter. Measurement analysis of the global characteristics of mean velocity and turbulent kinetic energy fluctuations was obtained on horizontal streamwise planes. Topology and evolution of longitudinal vortices generated downstream the rectangular winglet pair were quantified. It was also demonstrated that a domination of the longitudinal component over transverse and vertical components in the turbulent kinetic energy, particularly near the winglets. Vertical cross-sectional measurements enabled the characteristic examination of longitudinal vortices at several locations downstream in the wake region. Normalized velocity components, velocity streamlines, topologies of I_2 function and normalized turbulent kinetic energy downstream the winglet pair were also examined.

The comparison between numerical simulation and previous experimental study of flow structure characteristics of longitudinal vortices generated by rectangular winglet pairs in parallel plate-fin channel was investigated in Chapter-4. Similar channel dimensions as previously experimented test-bench with the same boundary conditions were modeled in ANSYS Fluent 15.0 CFD software. Two turbulence models were conducted within this investigation: the shear-stress transport (SST) κ - ω model and the re-normalization-group (RNG) κ - ε model. The obtained results of the velocity profile from the simulations were

compared locally with experimental results extracted using both LDA and PIV techniques. Simulation adopted on SST $\kappa\text{-}\omega$ turbulence model showed a good correspondence with experimentally extracted data, while RNG $\kappa\text{-}\varepsilon$ turbulence model did not show any harmony. For further model validations, global topologies evaluations were also carried on. Horizontal velocity components topologies in addition to the turbulent kinetic energy topology at a predefined horizontal plane were inspected. The SST $\kappa\text{-}\omega$ turbulence model showed excellent correspondence with experimental results where both topologies (obtained experimentally and numerically) were almost identical. Otherwise, the RNG $\kappa\text{-}\varepsilon$ turbulence model showed no consistency at all with experimental results. Vertical comparisons were also conducted at several locations in the wake region. Topologies of Γ_2 function were used to identify and track the main and induced vortices in the flow behind the winglet pair at different longitudinal locations. The SST $\kappa\text{-}\omega$ turbulence model accurately predicted and identified the generated vortices location at different planes, the number of generated vortices (main and induced) as well as their relative positions. The RNG $\kappa\text{-}\varepsilon$ turbulence model could only predicted the generation of main vortices, but it failed in predicting induced vortices. It was shown that the SST $\kappa\text{-}\omega$ turbulence model showed a superior performance over the RNG $\kappa\text{-}\varepsilon$ turbulence model in predicting flow structure characteristics of longitudinal vortices in a parallel plate channel. Thus, the SST $\kappa\text{-}\omega$ turbulence model excelled in predicting such flow structures and consequently was chosen in modeling longitudinal vortices in turbulent flows.

After validating the turbulence model with experimental study, three-dimensional numerical simulations of two configurations of vortex generators were performed to analyze heat transfer enhancement in parallel plate-fin heat exchanger and presented in Chapter-5. Laminar flows were simulated for Reynolds numbers 270, 540 and 1080. Turbulent flow with the aid of the $\kappa\text{-}\omega$ SST model was modeled and validated with correlations and experimental

data. A more aerodynamic configuration that reduces pressure drop and enhances heat transfer and mixing performances was designed and named IPWP. IPWP vortex generator showed better performance with respect to vorticity and pressure drop when compared to the DWP case over a wide range of Reynolds numbers from laminar to turbulent. The IPWP peak friction magnitude was decreased 50% than that recorded by the DWP. Also the IPWP vorticity intensity was increased by a value of 30% from the baseline configuration level. This enhancement occurred due to the different vortex generation mechanism exhibited by the IPWP formation. The number of vortices created by each pair of VG was six for the DWP case and ten for the IPWP one. The addition of those vortices positively altered the heat exchange process through the helical flow interaction among them and the thermal enhancement factor was found to be increased 6% for IPWP vortex generator compared to DWP case.

After simulating the IPWP on arbitrary chosen inclination angle, the effect of inclination angle over a wide range of Reynolds numbers was studied and illustrated in Chapter-6. Reynolds numbers similar to the IPWP case study was also conducted while changing the inclination angle from 25° to 60°. The objective was to identify the optimum inclination angle configuration that reduces pressure drop and enhances heat transfer. IPWP configurations with different inclination angles (25°, 30°, 32°, 35°, 38°, 40°, 45°, 50°, 55° and 60°) were then introduced by manipulating the winglets' geometry and orientation. Response surface methodology (RSM) was used to show the effects of inclination angle on heat transfer and pressure drop from global scope. Local performance was weighed based on the streamwise distribution of Nusselt number and friction coefficient criteria in addition to helicity. It was found that the IPWP with inclination angle in the range of 30° to 35° submitted better global performance than all other inclinations. The peak friction magnitude of IPWP-30 configuration was 50% less than that recorded by the DWP and further

inclination of the VG reached about a 70% peak decrease for the IPWP-60 case. The area weighted average friction compared to DWP case decreased 18% for IPWP-30 configuration, reaching about 43% decrease for the IPWP-60 case. IPWP-30 configuration exhibited the maximum intensification of averaged helicity with an augmentation of 35.5% compared to DWP case. In addition, the number of multiscale vortices for IPWP-30 configuration reached eight (two main and six induced vortices) while for other configurations it sufficed with two main vortices. Also, thermal enhancement factor was found to be increased 6% for IPWP-30 and IPWP-35 vortex generators compared to DWP case.

Subsequent to previous founding, 3D numerical simulations of longitudinal VGs with protrusions were performed to increase the thermal enhancement fraction of the innovative vortex generator IPWP between parallel plates channel at $Re=4600$. Protrusions were first introduced to the DWP and resulted in two configurations: DWP-PRO1 and DWP-PRO2. Both configurations neither enhanced the heat transfer nor friction factor substantially, while DWP-PRO1 had a better performance than DWP-PRO2. As well, protuberances were implemented with the IPWP at different locations, leading to the production of the IPWP-PRO1, IPWP-PRO2, IPWP-HS and IPWP-M. These new formations resulted in two effects: an unassisting behavior that was originated from two formations: the IPWP-PRO1 and IPWP-PRO2. Both configurations did not outrun the regular IPWP in the total heat transfer enhancement. On the other hand the IPWP-HS and IPWP-M escalated the heat transfer enhancement level. It was also revealed that the IPWP-M showed a better performance than the IPWP-HS. The heat transfer was increased 6.5% for the IPWP-M compared to DWP and 3% increase for both: DWP-PRO1 and IPWP-M compared to DWP and IPWP respectively.

Finally, this study identified novel configuration design for longitudinal vortex generators in common flow up configuration. It relies on decreasing the pressure drop across the channel mainly caused by the VG and maintaining high intensity of multi-scaled vortices

that enhances the heat transfer and mixing performances. And as a future perspective, this study shows that passive techniques can still be developed and enhanced and opens a window for more new ideas to be investigated. For IPWP, many parameters may be changed, such as: changing the geometry dimensions, angle of attack, position, number of VGs, VG thickness, VG surface which can be altered to curved surface, and many other. Also, the influence of staggered or in lined VGs may be studied. In addition, protrusions shape, position, size, number can also be investigated. Thus the presented results are very promising and can open the door to different type and combinations of passive VGs in future work.

References

- [1] P. Stehlík, "Conventional versus specific types of heat exchangers in the case of polluted flue gas as the process fluid - A review," *Applied Thermal Engineering*, vol. 31, pp. 1-13, 2011.
- [2] A. Bergles, R. Webb and G. Junkan, "Energy Conservation Via Heat Transfer Enhancement," *Energy*, vol. 4, pp. 193-200, 1979.
- [3] A. Bergles, V. Nirmalan, G. Junkan and R. Webb, "Bibliography of Augmentation of Convective Heat and Mass Transfer, II, HTL-31," ISU-ERI-Ames-84221, Heat Transfer Laboratory, Iowa State University, Ames, IA, 1983.
- [4] A. Bergles, M. K. Jensen and B. Shome, "Bibliography on Augmentation of Convective Heat and Mass Transfer, Report HTL-23," Rensselaer Polytechnic Institute, Troy, NY, 1995.
- [5] A. Ghanem, C. Habchi, T. Lemenand, D. Della Valle and H. Peerhossaini, "Energy efficiency in process industry - High-efficiency vortex (HEV) multifunctional heat exchanger," *Renewable Energy*, vol. 56, pp. 96-104, 2013.
- [6] L. Jonghyeok and L. Kwan-Soo, "Friction and Colburn factor correlations and shape optimization of chevron-type plate heat exchangers," *Applied Thermal Engineering*, vol. 89, pp. 62-69, 2015.
- [7] Z. Astolfi-Filho, E. Basílio de Oliveira, J. Sélia dos Reis Coimbra and J. Telis-Romero, "Friction factors, convective heat transfer coefficients and the Colburn analogy for industrial sugarcane juices," *Biochemical Engineering Journal*, vol. 60, pp. 111-118, 2012.
- [8] W. Kays and A. London, *Compact Heat Exchangers*, 2nd Ed. ed., New York: McGraw-

Hill, 1964.

- [9] P. G. LaHaye, F. J. Neugebauer and R. K. Sakhuja, "A Generalized Prediction of Heat Transfer Surfaces," *Journal of Heat Transfer*, vol. 96, no. 4, pp. 511-517, 1974.
- [10] A. London, "Compact Heat Exchangers," *Mechanical Engineering*, ASME, vol. 86, pp. 31-34, 1964.
- [11] A. London and C. Ferguson, "Test Results of High-Performance Heat Exchanger Surfaces Used in Aircraft Intercoolers and Their Significance for Gas-turbine Regenerator Design," *Transactions of the ASME*, vol. 71, pp. 17-26, 1949.
- [12] R. Shah and A. London, "Laminar Flow Forced Convection in Ducts," Academic Press, 1978.
- [13] K. Stone, "Review of Literature on Heat Transfer Enhancement in Compact Heat Exchangers, Report ACRC TR-105," Urbana (IL), USA, 1996.
- [14] T. Cowell, "A general method for the comparison of compact heat transfer surfaces," *Journal of Heat Transfer*, vol. 112, no. 2, pp. 288-294, 1990.
- [15] J. Soland, J. Mack and W. Rohsenow, "Performance ranking of plate-fin heat exchanger surfaces," *Journal of Heat Transfer*, vol. 100, pp. 514-519, 1978.
- [16] R. Webb, "Performance evaluation criteria for use of enhanced heat transfer surfaces in heat exchanger design," *International Journal of Heat and Mass Transfer*, vol. 24, no. 4, pp. 715-726, 1981.
- [17] P. Promvong and C. Thianpong, "Thermal performance assessment of turbulent channel flows over different shaped ribs," *International Community Heat Mass Transfer*, vol. 35, pp. 1327-1334, 2008.
- [18] M. Rahimi, S. Shabanian and A. Alsairafi, "Experimental and CFD studies on heat

- transfer and friction factor characteristics of a tube equipped with modified twisted tape inserts," *Chemical Engineering and Processing: Process Intensification*, vol. 48, pp. 762-770, 2009.
- [19] A. Harvey, C. Ramshaw, D. Reay and , "Active enhancement methods," in *Process Intensification: Engineering for Efficiency, Sustainability and Flexibility*, Elsevier, 2013, pp. 69-74.
- [20] C.-A. Roulet, M.-C. Pibiri, R. Knutti and A. Weber, "Effect of chemical composition on VOC transfer through rotating heat exchangers," *Energy and Buildings*, vol. 34, no. 8, 2002.
- [21] "HRS Heat Exchangers, HRS Unicus Series," [Online]. Available: <http://www.hrs-heatexchangers.com>. [Accessed 1 September 2016].
- [22] A. Sowayan, "Effect of Bottom Wall Vibration on Heat Transfer Enhancement for a Square Cavity Domain," *Journal of Computational and Theoretical Nanoscience*, vol. 19, no. 3, pp. 889-892, 2013.
- [23] T. Wu and P. I. Ro, "Heat transfer performance of a cooling system using vibrating piezoelectric beams," *Journal of Micromechanics and Microengineering*, vol. 15, no. 1, pp. 213-220, 2005.
- [24] L. Cheng, T. Luan, W. Du and M. Xu, "Heat transfer enhancement by flow-induced vibration in heat exchangers," *International Journal of Heat and Mass Transfer*, vol. 52, pp. 1053-1057, 2009.
- [25] M. Jarrahi, C. Castelain and H. Peerhossaini, "Laminar Sinusoidal and Pulsatile Flows in a Curved Pipe," *Journal of Applied Fluid Mechanics*, vol. 4, no. 2, pp. 21-26, 2011.
- [26] "Acoustic Vibration, Morko America," [Online]. Available:

<http://www.morkoamerica.com>. [Accessed 12 October 2016].

- [27] Y. Diao, Y. Liu, J. Zhang, L. Guo, Y. Zhao and S. Wang, "Effect of electric field on the enhanced heat transfer characteristic of an evaporator with multilayered sintered copper mesh," *Journal of Electrostatics*, vol. 73, pp. 26-32, 2015.
- [28] G. Celata, A. Chiaradia, M. Cumo and F. D'Annibale, "Heat transfer enhancement by air injection in upward heated mixed-convection flow of water," *International Journal of Multiphase Flow*, vol. 25, pp. 1033-1052, 1999.
- [29] H. S. Dizaji and S. Jafarmadar, "Heat transfer enhancement due to air bubble injection into a horizontal double pipe heat exchanger," *International Journal of Automotive Engineering*, vol. 4, no. 4, pp. 902-910, 2014.
- [30] A.-R. A. Khaled, "Mathematical and Numerical Analysis of Heat Transfer Enhancement by Distribution of Suction Flows inside Permeable Tubes," *Mathematical Problems in Engineering*, pp. Article ID 953604, 11 pages, 2015.
- [31] P. Xua, B. Yu, S. Qiu, H. J. Poh and A. S. Mujumdar, "Turbulent impinging jet heat transfer enhancement due to intermittent pulsation," *International Journal of Thermal Sciences*, vol. 49, no. 7, pp. 1247-1252, 2010.
- [32] J. R. Matthew, E. M. Dede and S. N. Joshi, *Enhanced Two-Phase Impingement Technologies for Electronics Cooling*, IN 47907 USA: School of Mechanical Engineering, Purdue University, 585 Purdue Mall, West Lafayette, 2016.
- [33] S. M. Mousavizadeh, G. R. Ansarifard and M. Talebi, "Assessment of the TiO₂/water nanofluid effects on heat transfer characteristics in VVER-1000 nuclear reactor using CFD modeling," *Nuclear Engineering and Technology*, vol. 47, no. 7, pp. 814-826, 2015.

- [34] T.-C. Hung, W.-M. Yan, X.-D. Wang and C.-Y. Chang, "Heat transfer enhancement in microchannel heat sinks using nanofluids," *International Journal of Heat and Mass Transfer*, vol. 55, no. 9-10, pp. 2559-2570, 2012.
- [35] M. Levinbuk and L. Kustov, "New catalytic systems utilized to intensification of secondary oil-refining process without considerable revamping of available commercial units," *Chemie Ingenieur Technik*, vol. 73, no. 6, pp. 667-667, 2001.
- [36] L. Kiwi-Minsker and A. Renken, "Intensification of catalytic process by microstructured reactors," *Microchemical Engineering in Practice*, pp. 403-430, 2010.
- [37] A. Panov, R. Usmanova, V. Zaikov and G. Zaikov, "Intensification of dust removal process," *Journal of applied polymer science*, vol. 101, no. 5, pp. 3357-3360, 2006.
- [38] C. Kohlert, E. Reher and D. Bothmer, "Intensification of the calendering process with the help of wedge-shaped parts," *Advances in Polymer Technology*, vol. 6, no. 3, pp. 259-265, 1986.
- [39] A. Bergles, Techniques to Enhance Heat Transfer, in *Handbook of Heat Transfer*, 3rd ed., S. Kakac, A. E. Bergles, F. Mayinger and H. Yuncii, Eds., McGraw-Hill, New York, Chap.11, 1998.
- [40] A. L. Buxton and B. G. I. Dance, "ASM International," in *Surfi-Sculpt - Revolutionary surface processing with an electron beam*, ISEC Congress. St Paul, Minnesota, USA, 1-3 August 2005.
- [41] B. Köroğlu, N. Bogan and C. Park, "Effects of Tube Row on Heat Transfer and Surface Wetting of Microscale Porous-Layer Coated, Horizontal-Tube, Falling-Film Evaporator," *Journal of Heat Transfer*, vol. 135, no. 4, p. 11 pages, 2013.
- [42] F. Zhou, G. Demoulin, D. Geb and I. Catton, "Closure for a plane fin heat sink with

- scale-roughened surfaces for volume averaging theory (VAT) based modeling,"
International Journal of Heat and Mass Transfer, vol. 55, no. 25-26, pp. 7677-7685,
2012.
- [43] L. Ventola, F. Robotti, M. Dialameh, F. Calignano, D. Manfredi, E. Chiavazzo and P. Asinari, "Rough surfaces with enhanced heat transfer for electronics cooling by direct metal laser sintering," International Journal of Heat and Mass Transfer, vol. 75, pp. 58-74, 2014.
- [44] Y. Xuan and Q. Li, "Heat transfer enhancement of nanofluids," International Journal of Heat and Fluid Flow, vol. 21, no. 1, pp. 58-64, 2000.
- [45] Z. Jin-song, L. Zhong-yang, G. Xiang, N. Ming-jiang and C. Ke-fa, "Effect of particle loading on heat transfer enhancement in a gas-solid suspension cross flow," Journal of Zhejiang University-SCIENCE A, vol. 3, no. 4, pp. 381-386, 2002.
- [46] R. Webb and N. Kim, Principles of Enhanced Heat Transfer, New York: Wiley, 1994.
- [47] I. S. Park, "Numerical analysis for flow, heat and mass transfer in film flow along a vertical fluted tube," International Journal of Heat and Mass Transfer, vol. 53, no. 1-3, pp. 309-319, 2010.
- [48] M. Zeng, "Techniques of Heat Transfer Enhancements and their Applications," [Online]. Available: <http://gr.xjtu.edu.cn>. [Accessed 12 August 2016].
- [49] W. J. Dean, "Note on the motion of fluid in a curved pipe," Mathematika, vol. 6, no. 1, pp. 77-85, 1959.
- [50] S. Berger, L. Talbot and L. Yao, "Flow in curved pipes," Annual review of fluid mechanics, vol. 15, no. 1, pp. 461-512, 1983.
- [51] F. Jiang, K. Drese, S. Hardt, M. Küpper and F. Schönfeld, "Helical flows and chaotic

- mixing in curved micro channels," *AIChE Journal*, vol. 50, no. 9, pp. 2297-2305, 2004.
- [52] T. T. Chandratilleke and N. Nadim, *An Overview of Heat Transfer Phenomena*, S. N. Kazi, Ed., INTECH, 2012, pp. 125-150.
- [53] C. Habchi, T. Lemenand, D. Della Valle and H. Peerhossaini, "Liquid/liquid dispersion in a chaotic advection flow," *International Journal of Multiphase Flow*, vol. 35, no. 6, pp. 485-497, 2009.
- [54] "Helical Coil Heat Exchanger," SENTRY, [Online]. Available: <http://sentry-equip.com>. [Accessed 12 October 2016].
- [55] A. Briggs, C. Kelemenis and J. Rose, "Heat transfer and pressure drop during in-tube condensation from CFC-113/air mixtures using a wire insert," *Heat and Technology*, vol. 17, no. 2, pp. 57-61, 1999.
- [56] B. V. N. Ramakumar, J. D. Arsha and P. Tayal, "Tapered Twisted Tape Inserts for Enhanced Heat Transfer," *Journal of Heat Transfer*, vol. 138, no. 1, p. 9 pages, 2015.
- [57] M. Hajare, C. Deore, K. Kharde, P. Rawale and V. Dalvi, "REVIEW OF HEAT TRANSFER AUGMENTATION TECHNIQUES," *International journal of Engineering Research*, vol. 2, no. 2, pp. 293-300, 2014.
- [58] P. Chu, Y. L. He and W. Q. Tao, "Three-Dimensional Numerical Study of Flow and Heat Transfer Enhancement Using Vortex Generators in Fin-and-Tube Heat Exchangers," *Journal of Heat Transfer*, vol. 131, no. 9, p. 9 pages, 2009.
- [59] S. Ali, C. Habchi, S. Menanteau, T. Lemenand and J.-L. Harion, "Heat transfer and mixing enhancement by free elastic flaps oscillation," *International Journal of Heat and Mass Transfer*, vol. 85, pp. 250-264, 2015.
- [60] A. E. Bergles, "New Frontiers in Enhanced Heat Transfer," in *Advances in Enhanced*

- Heat Transfer," ASME, New York, p.1-8, 2000.
- [61] S. Acharya, R. G. Hibbs, Y. Chen and D. E. Nikitopoulos, "Mass/Heat Transfer in a Ribbed Passage with Cylindrical Vortex Generators: The Effect of Generator-Rib Spacing," *Journal of Heat Transfer*, vol. 122, no. 4, pp. 641-652, 2000.
- [62] V. Eliades, E. D. Nikitopoulos and S. Acharya, "Mass-Transfer Distribution in Rotating, Two-Pass, Ribbed Channels with Vortex Generators," *Journal of Thermophysics and Heat Transfer*, vol. 15, no. 3, pp. 266-274, 2001.
- [63] R. M. Manglik and A. E. Bergles, "Enhanced Heat Transfer in the New Millenium: A Review of the 2001 Literature," *Journal of Enhanced Heat Transfer*, vol. 11, no. 2, pp. 87-118, 2004.
- [64] Y. M. Zhang, G. M. Azad, J.-C. Han and C. P. Lee, "Turbulent Heat Transfer Enhancement and Surface Heating Effect in Square Channels with Wavy, and Twisted Tape Inserts with Interrupted Ribs," *Journal of Enhanced Heat Transfer*, vol. 7, no. 1, pp. 35-49, 2000.
- [65] V. Zimparov, "Enhancement of Heat Transfer by a Combination of Three-Start Spirally Corrugated Tubes with a Twisted Tape," *International Journal of Heat Mass Transfer*, vol. 44, no. 3, pp. 551-574, 2001.
- [66] H. Usui, Y. Sano and K. Iwashita, "Heat Transfer Enhancement Effects by Combined Use of Internally Grooved Rough Surfaces and Twisted Tapes," *Heat Transfer-Japanese*, vol. 13, no. 4, pp. 19-32, 1984.
- [67] Q. T. Zhou, S. Y. Ye, Y. H. Ou-Yang and N. Z. Gu, Combined Enhancement of Tube-Side Heat Transfer in Cast-Iron Air Preheater, in *Heat Transfer*, vol. 4, New York: Hemisphere Publishing, 1990, pp. 39-44.

- [68] A. K. Das, H. P. Kilty, P. J. Marto, A. Kumar and G. B. Andeen, "Dropwise Condensation of Steam on Horizontal Corrugated Tubes Using an Organic Self-Assembled Monolayer Coating," *Journal of Enhanced Heat Transfer*, vol. 7, no. 2, pp. 109-123, 2000.
- [69] T. Nishimura, K. Kunitsugu and A. M. Morega, "Fluid Mixing and Mass Transfer Enhancement in Grooved Channels for Pulsatile Flow," *Journal of Enhanced Heat Transfer*, vol. 5, no. 1, pp. 23-37, 1998.
- [70] S. C. Bhattacharya and D. Harrison, "Heat Transfer in a Pulsed Fluidized Bed," *Transactions of the Institution of Chemical Engineers*, vol. 54, pp. 281-286, 1976.
- [71] A. Jacobi and R. Shah, "Heat Transfer Surface Enhancement through the Use of Longitudinal Vortices: A Review of Recent Progress," *Experimental Thermal and Fluid Science*, vol. 11, pp. 295-309, 1995.
- [72] M. Fiebig, "Embedded Vortices in Internal Flow: Heat Transfer and Pressure Loss Enhancement," *International Journal of Heat and Fluid Flow*, vol. 16, no. 5, pp. 376-388, 1995.
- [73] M. Fiebig, "Embedded Vortices in Internal Flow: Heat Transfer and Pressure Loss Enhancement," *International Journal of Heat and Fluid Flow*, vol. 16, no. 5, pp. 376-388, 1995.
- [74] J. Lin, "Review of research on low-profile vortex generators to control boundary-layer separation," *Progress in Aerospace Sciences*, vol. 38, pp. 389-420, 2002.
- [75] J. Herpe, D. Bougeard, S. Russeil and M. Stanciu, "Numerical investigation of local entropy production rate of a finned oval tube with vortex generators," *International Journal of Thermal Sciences*, vol. 48, pp. 922-935, 2009.

- [76] T. R. Johnson and P. Joubert, "The Influence of Vortex Generators on Drag and Heat Transfer from a Circular Cylinder Normal to an Airstream," *Journal of Heat Transfer*, vol. 91, pp. 91-99, 1969.
- [77] F. J. Edwards and C. J. R. Alker, "The Improvement of Forced Convection Surface Heat Transfer Using Surface Protrusions in the Form of (A) Cubes and (B) Vortex Generators," in *Fifth International Heat Transfer Conference*, Tokyo, 1974.
- [78] R. Sedney, "A Survey of the Effects of Small Protuberances on Boundary-Layer Flows," *AIAA Journal*, vol. 11, pp. 782-792, 1973.
- [79] I. M. A. Shakaba, R. D. Mehta and P. Bradshaw, "Longitudinal Vortices Imbedded in Turbulent Boundary Layers. Part 1. Single Vortex," *Journal of Fluid Mechanics*, vol. 155, pp. 37-57, 1985.
- [80] R. D. Mehta and P. Bradshaw, "Longitudinal Vortices Imbedded in Turbulent Boundary Layers. Part 2. Vortex Pair with "Common Flow" Upwards," *Journal of Fluid Mechanics*, vol. 188, pp. 529-546, 1988.
- [81] M. Fiebig, "Vortex Generators for Compact Heat Exchangers," *Journal of Enhanced Heat Transfer*, Vols. 2(1-2), pp. 43-61, 1995.
- [82] P. A. Eibeck and J. K. Eaton, "Heat Transfer Effects of a Longitudinal Vortex Embedded in a Turbulent Boundary Layer," *Journal of Heat Transfer*, vol. 109, pp. 16-24, 1987.
- [83] W. R. Pauley and J. K. Eaton, "Experimental Study of the Development of Longitudinal Vortex Pairs Embedded in a Turbulent Boundary Layer," *AIAA Journal*, vol. 26, pp. 816-823, 1988.
- [84] M. Fiebig, U. Brockmeier, N. K. Mitra and T. Guntermann, "Structure of Velocity and

- Temperature Fields in Laminar Channel Flows with Longitudinal Vortex Generators," Numerical Heat Transfer, Part A, vol. 15, pp. 281-302, 1989.
- [85] S. Tiggelbeck, N. K. Mitra and M. Fiebig, "Experimental Investigations of Heat Transfer Enhancement and Flow Losses in a Channel with Double Rows of Longitudinal Vortex Generators," International Journal of Heat and Mass Transfer, vol. 26, pp. 2327-2337, 1993.
- [86] J. M. Wu and W. Q. Tao, "Numerical study on laminar convection heat transfer in a rectangular channel with longitudinal vortex generator. Part A: Verification of field synergy principle," International Journal of Heat and Mass Transfer, vol. 51, no. 5, pp. 1179-1191, 2008.
- [87] J. M. Wu and W. Q. Tao, "Numerical Study on Laminar Convection Heat Transfer in a Channel with Longitudinal Vortex Generator. Part B: Parametric Study of Major Influence Factors," International Journal of Heat and Mass Transfer, vol. 51, pp. 3683-3692, 2008.
- [88] C. Min, C. Qi, X. Kong and J. Dong, "Experimental Study of Rectangular Channel with Modified Rectangular Longitudinal Vortex Generators," International Journal of Heat and Mass Transfer, vol. 53, pp. 2023-3029, 2010.
- [89] L. Tian, Y. He and Y. Lei, "Numerical Study of Fluid Flow and Heat Transfer in a Flat Plate Channel with Longitudinal Vortex Generators by Applying Field Synergy Principle Analysis," International Communications in Heat and Mass Transfer, vol. 36, no. 2, pp. 111-120, 2009.
- [90] G. Biswas, K. Torii, D. Fujii and K. Nishino, "Numerical and Experimental Determination of Flow Structure and Heat Transfer Effects of Longitudinal Vortices in a Channel Flow," International Journal of Heat and Mass Transfer, vol. 39, no. 16, pp.

3441-3451, 1996.

- [91] C. Allison and B. Dally, "Effect of a delta-winglet vortex pair on the performance of a tube-fin heat exchanger," *International Journal of Heat and Mass Transfer*, vol. 50, no. 25-26, pp. 5065-5072, 2007.
- [92] L. O. Salviano, D. J. Dezan and J. I. Yanagihara, "Optimization of winglet-type vortex generator positions and angles in plate-fin compact heat exchanger: Response Surface Methodology and Direct Optimization," *International Journal of Heat and Mass Transfer*, vol. 82, pp. 373-387, 2015.
- [93] L. O. Salviano, D. J. Dezan and J. I. Yanagihara, "Thermal-hydraulic performance optimization of inline and staggered fin-tube compact heat exchangers applying longitudinal vortex generators," *Applied Thermal Engineering*, vol. 95, pp. 311-329, 2016.
- [94] Y.-G. Lei, Y.-L. He, L.-T. Tian, P. Chu and W.-Q. Tao, "Hydrodynamics and heattransfer characteristics of a novel heat exchanger with delta-winglet vortex generators," *Chemical Engineering Science*, vol. 65, pp. 1551-1562, 2010.
- [95] Y. He, H. Han, W. Tao and Y. Zhang, "Numerical study of heat-transfer enhancement by punched winglet-type vortex generator arrays in fin-and-tube heat exchangers," *International Journal of Heat and Mass Transfer*, vol. 55, pp. 5449-5458, 2012.
- [96] A. Lemouedda, M. Breuer, E. Franz, T. Botsch and A. Delgado, "Optimization of the angle of attack of delta-winglet vortex generators in a plate-fin-and-tube heat exchanger," *International Journal of Heat and Mass Transfer*, vol. 53, pp. 5386-5399, 2010.
- [97] J. Wu and W. Q. Tao, "Investigation on Laminar Convection Heat Transfer in Fin-and-

- Tube Heat Exchanger in Aligned Arrangement With Longitudinal Vortex Generator From the Viewpoint of Field Synergy Principle," *Applied Thermal Engineering*, vol. 27, pp. 2609-2617, 2007.
- [98] J. Wu and W. Tao, "Effect of longitudinal vortex generator on heat transfer in rectangular channels," *Applied Thermal Engineering*, vol. 37, pp. 67-72, 2012.
- [99] K. Yongsiri, P. Eiamsa-ard, K. Wongcharee and S. Eiamsa-ard, "Augmented heat transfer in a turbulent channel flow with inclined detached-ribs," *Case Studies in Thermal Engineering*, vol. 3, pp. 1-10, 2014.
- [100] W. Sobieski, "Relationships between cfd and experimental fluid mechanics," *Technical Sciences*, vol. 16, no. 3, pp. 169-178, 2013.
- [101] "Computational Fluid Dynamics is the Future," [Online]. Available: <http://cfd2012.com/aircraft-design.html>. [Accessed 1 September 2016].
- [102] "leap australia CFD blog," Courtesy of SAUBER PETRONAS Engineering AG, [Online]. Available: <http://www.computationalfluidynamics.com.au>. [Accessed 1 September 2016].
- [103] "HFM," Institute of Hydraulic Fluid Machinery, TU Graz, [Online]. Available: <http://www.hfm.tugraz.at>. [Accessed 1 September 2016].
- [104] "Digital Engineering," CONVERGE, [Online]. Available: <http://www.digitaleng.news>. [Accessed 1 September 2016].
- [105] "Laboratory for Energy Conversion," ETH Zurich, [Online]. Available: <https://www1.ethz.ch>. [Accessed 1 September 2016].
- [106] I. ANSYS, "Turbulence Models," in *ANSYS Fluent 12.0 Theory Guide*, April 2009, pp. 1-3;27.

- [107] X.-Y. Tang and D.-S. Zhu, "Flow structure and heat transfer in a narrow rectangular channel with different discrete rib arrays," *Chemical Engineering and Processing: Process Intensification*, vol. 69, pp. 1-14, 2013.
- [108] X.-Y. Tang and D.-S. Zhu, "Experimental and Numerical Study on Heat Transfer Enhancement of a Rectangular Channel with Discontinuous Crossed Ribs and Grooves," *Chinese Journal of Chemical Engineering*, vol. 20, no. 2, pp. 220-230, 2012.
- [109] M. Hatami, D. Ganji and M. Gorji-Bandpy, "Experimental and numerical analysis of the optimized finned-tube heat exchanger for OM314 diesel exhaust exergy recovery," *Energy Conversion and Management*, vol. 97, pp. 26-41, 2015.
- [110] C. Habchi, S. Russeil, D. Bougeard, J. L. Harion, T. Lemenand, D. Della Valle and H. Peerhossaini, "Enhancing Heat Transfer in Vortex Generator-type Multifunctional Heat Exchangers," *Applied Thermal Engineering*, vol. 38, pp. 14-25, 2012.
- [111] S. Eiamsa-ard and P. Promvonge, "Numerical study on heat transfer of turbulent channel flow over periodic grooves," *International Communications in Heat and Mass Transfer*, vol. 35, no. 7, pp. 844-852, 2008.
- [112] V. Yakhot and S. Orszag, "Renormalization group analysis of turbulence:(i) basic theory," *Journal of Scientific Computing*, vol. 1, pp. 3-51, 1986.
- [113] V. Yakhot, S. Orszag, S. Thangam, T. Gatski and C. Speziale, "Development of turbulence models for shear flows by a double expansion technique," *Physics of Fluids A*, vol. 4, no. 7, pp. 1510-1520, 1992.
- [114] B. Launder and D. Spalding, "The numerical computation of turbulent flows," *Computer Methods in Applied Mechanics and Engineering*, vol. 3, no. 2, pp. 269-289, 1974.

- [115] D. Choudhury, "Introduction to the Renormalization Group Method and Turbulence Modeling," Fluent Inc, Technical memorandum TM-107, 1993.
- [116] H. Versteeg and W. Malalasekera, An Introduction to Computational Fluid Dynamics: The Finite Volume Method, second ed., New York: Prentice Hall, 1995, p. 520.
- [117] F. Menter, "Two-equation eddy-viscosity turbulence models for engineering applications," AIAA Journal, vol. 32, pp. 1598-1605, 1994.
- [118] I. ANSYS, "Standard and SST k-w Models," in ANSYS Fluent 12.0 Theory Guide, April 2009, p. 4.31.
- [119] R. Warming and R. Beam, "Upwind second-order difference schemes and applications in aerodynamic flows," AIAA Journal, vol. 14, no. 9, pp. 1241-1249, 1976.
- [120] "Guide for the Verification and Validation of Computational Fluid Dynamics Simulations," American Institute of Aeronautics and Astronautics, AIAA G-077, 1998.
- [121] M. Casey and T. Wintergerste, Eds., European Research Community on Flow, Turbulance and Cumbastion, ERCOFTAC, Special Interest rroup on Quality and Trust in *Industrial CFD "Best Practice Guidelines"*, 2000.
- [122] K. Gungor, "Sources of errors for indoor air CFD simulations, Part 1," Ecolibrium, pp. 48-53, September 2015.
- [123] P. Šafařík, "Experimental Investigation in Fluid Mechanics - Its Role, Problems and Tasks," in EPJ Web of Conferences 45, 01118, 2013.
- [124] "Experimental methods, instrumentation, and laboratory practice," Hydrosience and Engineering, University of Iowa, Mechanics of Fluids and Transfer Processes, [Online]. Available: <http://www.iuhr.uiowa.edu>. [Accessed 5 September 2016].
- [125] E. Rathakrishnan, Instrumentation, Measurements, and Experiments in Fluids, New

York: CRC Press, 2007.

[126] "Measurement principles of LDA," DANTEC DYNAMICS, [Online]. Available:

<http://www.dantecdynamics.com>. [Accessed 5 September 2016].

[127] "Measurement Principles of PIV," DANTEC DYNAMICS, [Online]. Available:

<http://www.dantecdynamics.com>. [Accessed 5 September 2016].

[128] B. Wang, S. Lee and K. Ho, "Chemical composition of fine particles from incense burning in a large environmental chamber," *Atmospheric Environment*, vol. 40, pp. 7858-7868, 2006.

[129] D. Kuzmin, "Introduction to Computational Fluid Dynamic," Institute of Applied Mathematics, University of Dortmund, [Online]. Available:

<http://www.mathematik.uni-dortmund.de>. [Accessed 6 September 2016].

Thèse de Doctorat

Mohammad ONEISSI

Analysis of the flow structure and heat transfer enhancement in a rectangular channel with longitudinal vortices

Analyse des mécanismes d'intensification des transferts de chaleur dans un canal rectangulaire avec des tourbillons longitudinaux

Résumé

Ce travail de thèse repose sur la conception et l'étude d'un nouveau générateur de vorticit  (VG) permettant d'am liorer le transfert de chaleur dans des  changeurs de chaleur   plaques et ailettes. Un examen d taill  des techniques d'am lioration du transfert de chaleur est pr sent , elles se divisent en trois cat gories : les techniques passive, active et combin es. Les techniques passives sont plus couramment utilis es dans les  changeurs de chaleur car elles sont caract ris es par une meilleure efficacit ,  conomie, facilit  de fabrication et faible maintenance. Parmi les techniques passives, les g n rateurs de vorticit  cr ent des  coulements secondaires, cassent la croissance de la couche limite et cr ent des  coulements tourbillonnants qui am liorent l' change entre les parois et le fluide, intensifiant ainsi le transfert de chaleur.

Cette  tude bas e sur l'analyse des m canismes d'intensification, a permis de mettre en  vidence une nouvelle conception de configuration pour des g n rateurs de tourbillons longitudinaux avec pour r sultats une diminution des pertes de charges principalement caus es par le g n rateur de vorticit  et le maintien de tourbillons multi- chelles intenses qui am liorent les performances de transfert de chaleur et de m lange.

Mots cl s

G n rateur de vorticit , intensification des transferts de chaleur, ailette,  coulement en canal, simulation num rique, st reo PIV.

Abstract

The objective of this PhD thesis is to investigate and design a new vortex generator (VG) for enhancing heat transfer in parallel plate-fin heat exchangers. Detailed overview about heat transfer enhancement techniques was presented in a literature review, which are divided into three categories: passive, active and compound techniques. Passive techniques are more commonly used in heat exchangers since they are characterized by their efficiency, economy, ease of manufacturing and lower maintenance efforts. Vortex generators are one of the passive techniques that create secondary flows, disrupt the growth of the boundary layer and create swirling flows that enhance exchange between the walls and the core fluid, thus improving heat transfer.

Finally, based on the analysis of the thermal enhancement mechanisms, a novel configuration for longitudinal vortex generators in common flow up was identified. It relies on decreasing the pressure drop across the channel mainly caused by the vortex generators while maintaining high intensity of multi-scaled vortices that enhance the heat transfer and mixing performances.

Key Words

Vortex generator, heat transfer enhancement, vorticity, channel flow, CFD simulation, stereo PIV.